Carnegie Mellon University
MELLON COLLEGE OF SCIENCE

THESIS

SUBMITTED IN PARTIAL FULFILLMENT OF THE REQUIREMENTS
FOR THE DEGREE OF

DOCTOR OF PHILOSOPHY IN THE FIELD OF PHYSICS

TITLE: "Amplitude Analysis and Branching Fraction Measurement of $D^0 \to K^- \pi^+ \pi^0 \pi^0$

PRESENTED BY: Bai-Cian Ke

ACCEPTED BY THE DEPARTMENT OF PHYSICS

Roy Briere	08/21/17
ROY BRIERE, CHAIR PROFESSOR	DATE
Scott Dodelson	08/21/17
SCOTT DODELSON, DEPT HEAD	DATE

APPROVED BY THE COLLEGE COUNCIL

Rebecca Doerge	08/24/17
REBECCA DOERGE, DEAN	DATE

Amplitude Analysis and Branching Fraction Measurement of $D^0 \to K^-\pi^+\pi^0\pi^0$

by

Bai-Cian Ke

Submitted in partial fulfillment of the
requirements for the degree of
Doctor of Philosophy
at
Carnegie Mellon University
Department of Physics
Pittsburgh, Pennsylvania

Advised by Professor Roy Briere

August 11, 2017

Abstract

Utilizing the 2.93 fb^{-1} dataset at the $\psi(3770)$ resonance collected by the BESIII detector, we report the first amplitude analysis and absolute branching fraction measurement of $D^0 \to K^-\pi^+\pi^0\pi^0$. The $\psi(3770)$ resonance is near the $D\bar{D}$ threshold, where pair production of charm mesons enables precision measurements to be carried out. In particular, a double-tag technique reduces backgrounds and constrains the kinematics, which provides a 99% pure signal sample for amplitude analysis. Our partial wave analysis (PWA) technique only requires phase-space Monte-Carlo to simulate measurement efficiency. More than 60 amplitudes are tested and 26 significant amplitudes are found necessary to describe the structure. Furthermore, we use our PWA results to generate improved signal MC, and use this to replace signal events in the default MC. This "replaced MC" now gives us an accurate efficiency which allows us to extract the branching fraction. Using the updated information of measured structure to determine signal reconstruction efficiencies, we obtain $\mathcal{B}(D^0 \to K^-\pi^+\pi^0\pi^0) = (8.98 \pm 0.13(\mathrm{stat}) \pm 0.40(\mathrm{syst}))\%$.

Contents

Chapter 1

Introduction

In 1974, Samuel Ting, a Massachusetts Institute of Technology researcher, and his associates at the Brookhaven National Laboratory reported evidence of a new heavy particle they called the J [1]. Around the same time, Burton Richter and his team at the SLAC National Accelerator Laboratory reported a consistent result [2], naming it ψ. This particle with mass $m = 3.1$ GeV but surprisingly narrow width is now known as the J/ψ. Its discovery played a crucial role in the quark model, which was originally proposed with only three quarks (u, d, s). Later, it was proven that the J/ψ contains a new type of quark, the charm quark c, and is a $c\bar{c}$ bound state. This further provided support for the Glashow-Iliopoulos-Maiani mechanism [3, 4], which predicted the existence of a fourth quark as a partner to the strange quark. Each pair of quarks (u and d, c and s) is called a generation. Researchers working at the Fermi National Accelerator Laboratory (Fermilab) published evidence of the bottom quark in 1977 [5]. At this point, particle physicists anticipated the existence of the partner quark of bottom, known as the top quark. However, due to its unusually high mass, the top quark was not revealed until 1995, when Fermilab discovered it at the mass of 175 GeV [6, 7]. These six different types (or flavors) of quarks are the subject of "Flavor Physics" research.

An essential role in Flavor Physics is played by the weak interaction. The weak interaction is the only interaction capable of changing the flavor of quarks. Decays due to the weak interaction mainly lead to quarks decaying within their own generation ($d \to u$, $c \to s$, $t \to b$). In 1963, Nicola Cabibbo introduced the Cabibbo angle (θ_c) to allow for a reduced probability that strange quarks decay into up quarks [8]. After the fourth quark, the charm quark, was discovered in 1974, the Cabibbo angle was extended into a 2×2 Matrix, called the Cabibbo matrix, to represent the mixing of the weak and the mass eigenstates between u, d, s, and c quarks. Later, Kobayashi and Maskawa generalized the Cabibbo matrix into a 3×3 matrix, known as the Cabibbo-Kobayashi-Maskawa matrix (or CKM matrix), to preserve the universality of the weak interaction between three generations [9].

During recent years, heavy-quark hadrons ($c\bar{q}$, $b\bar{q}$, cqq', bqq') are a very topical field. Heavy-quark decays are considered to be an essential area to test the Standard Model through heavy-quark semileptonic, hadronic, and rare decays. In addition, they contain rich flavor physics, such as the mixing of the weak and the mass eigenstates.

The seven weakly-decaying ground-state hadrons (D^0, D^+, D_s^+, Λ_c^+, Ξ_c^+, Ξ_c^0, Ω_c^0), where c or s quarks must decay weakly to lighter quarks, are ideal places to investigate the weak interaction. Working with the BESIII collaboration, we focus on one large previously unmeasured four-body hadronic decay of the D^0 meson.

Since D mesons were discovered in 1976 by Mark I [10, 11], many measurements of D mesons have been performed. Today, most of the common, low-multiplicity D decay modes branching fractions are well-measured, but not all of them. The largest decay modes are Cabibbo-favored hadronic and semileptonic decay modes result from $c \to sW^+, W^+ \to u\bar{d}(l^+\nu_l)$ transitions, and even some of these Cabibbo-favored hadronic decay modes are still unmeasured.

Because D mesons are the lightest mesons containing a single charm quark, no strong decays are allowed, which makes D mesons a perfect place to study the weak decay of the charm quark. The charm quark preferentially decays into a strange quark via the weak interaction by emitting a W boson. The Cabibbo-favored hadronic decay of a W boson in the D meson decay can only contain the up and the anti-down quark due to energy conservation. Therefore, $\bar{K}n\pi$ modes are the most common hadronic decay modes of D mesons. There are three $D \to \bar{K}\pi$ modes, five $D \to \bar{K}\pi\pi$ modes, and seven $D \to \bar{K}\pi\pi\pi$ modes. Charge-conjugate states are implied throughout this analysis. All $\bar{K}\pi$ and $\bar{K}2\pi$ branching fractions have been measured, but only four of the seven $\bar{K}3\pi$. Some structure analyses have been published on $\bar{K}2\pi$ and $\bar{K}3\pi$ modes as well, listed in Tables 1.1, 1.2. Among those analyses, the Mark III collaboration published the latest structure analyses of four $D \to \bar{K}\pi\pi\pi$ decays, $K^-\pi^+\pi^+\pi^-$, $K_S\pi^+\pi^+\pi^-$, $K^-\pi^+\pi^+\pi^0$, and $K_S\pi^+\pi^-\pi^0$, with a total of 9.56 pb^{-1} data collected at the $\psi(3770)$ resonance [12]. However, $\bar{K}3\pi$ modes with at least two π^0s are unmeasured. Some components of these modes are implied from other results. For example, if $K_S\pi^+\pi^0\pi^-$ has a $K^{*-}\rho^+$ component, this can also lead to $K^-\pi^+\pi^0\pi^0$ by simply changing how the K^{*-} resonance decays.

The efficiency and resolution of π^0s are worse than that of charged particles, resulting in low statistics and higher backgrounds. However, BESIII has a sophisticated detector, mature software tools, and 2.93 fb^{-1} data at the $\psi(3770)$ resonance, which is just above the $D\bar{D}$ pair production threshold without enough energy even for extra pion. These advantages allow for study of the unmeasured $D^0 \to K^-\pi^+\pi^0\pi^0$ decay mode, which we believe is the largest unmeasured D meson branching fraction. The Electro-Magnetic Calorimeter (EMC) of the BESIII detector covers 93% of the solid angle and consists of CsI(TI) crystals, which precisely measures the energies and positions of photons. Since π^0 mesons are detected through the decay $\pi^0 \to \gamma\gamma$, the EMC in BESIII provides superior energy and position resolution of π^0 compared to Mark III, which is composed of lead-antimony alloy. We are, therefore, motivated to perform the first measurement of $D^0 \to K^-\pi^+\pi^0\pi^0$.

In this analysis, we present the amplitude analysis of the decay $D^0 \to K^-\pi^+\pi^0\pi^0$ and the measurement of its branching fraction with the 2.93 fb^{-1} $D\bar{D}$ threshold dataset collected by the BESIII detector at BEPCII. A DTag technique is essential throughout this whole analysis. There are types two types of samples used in the DTag technique: single tag and double tag samples. Double tag samples are used to provides a 99% pure signal sample for amplitude analysis (see Section 4.3). The results of amplitude analysis can provide an accurate structure of $D^0 \to K^-\pi^+\pi^0\pi^0$ and, consequently, an accurate measurement efficiency, comparing to the public MC. With the signal MC generated based on the amplitude analysis results, we can take advantage of both single tag and double tag samples to perform the first absolute branching fraction measurement of $D^0 \to K^-\pi^+\pi^0\pi^0$ (see Chapter 7).

Table 1.1: $D^0 \to \bar{K}n\pi$ Decay Modes. The $KK\pi$ modes are potential backgrounds to the $K^-\pi^+\pi^0\pi^0$ modes of interest to us.

Mode	PDG BF $\times 10^4$	Amplitude Analysis
$K^-\pi^+$	393 ± 4	N/A
$K_S\pi^0$	120 ± 4	N/A
$K^-\pi^+\pi^0$	1430 ± 80	MARK III[13], CLEO[14], E691[15]
$K_S\pi^+\pi^-$	285 ± 20	MARK III[13], CLEO[16], BaBar[17] ARGUS[18], E687[19]
$K_S\pi^0\pi^0$	91 ± 11	CLEO[20]
$K^-\pi^+\pi^0\pi^0$	—	—
$K^-\pi^+\pi^+\pi^-$	807 ± 23	MARK III[12][21], E691[22], BESIII[23]
$K_S\pi^+\pi^-\pi^0$	520 ± 60	MARK III[12], E691[22]
$K_S\pi^0\pi^0\pi^0$	—	—
$K_SK^{\mp}\pi^{\pm}$	$(36 \pm 5) + (22 \pm 4)$	—

Table 1.2: $D^+ \to \bar{K}n\pi$ Decay Modes.

Mode	PDG BF $\times 10^4$	Amplitude Analysis
$K_S\pi^+$	153 ± 6	—
$K^-\pi^+\pi^+$	946 ± 24	MARK III[13], CLEO-c[24]
$K_S\pi^+\pi^0$	724 ± 17	MARK III[13], BESIII[25]
$K^-\pi^+\pi^+\pi^0$	614 ± 16	MARK III[12], E691[22]
$K_S\pi^+\pi^+\pi^-$	305 ± 9	MARK III[12], E691[22]
$K_S\pi^+\pi^0\pi^0$	—	—

Chapter 2

Experimental Apparatus

2.1 The Beijing Electron Positron Collider II

The Beijing ElectronPositron Collider II (BEPCII) is a double-ring electron-positron collider, Figure 2.1, located in Beijing, People's Republic of China. With an upgrade finished in 2009, BEPCII has a design luminosity of $1 \times 10^{33}\text{cm}^{-2}\text{s}^{-1}$ at a center-of-mass energy of 3.77 GeV, a 100 times improvement over its predecessor. The design range of center-of-mass energy is $2.0 - 4.6$ GeV with a reduced luminosity of about $6 \times 10^{32}\text{cm}^{-2}\text{s}^{-1}$ at 3.0 and 4.2 GeV.

BEPCII was built in the existing tunnel with two storage rings of 237.5 m circumference. Each ring stores 93 bunches spaced by 8 ns or 2.4 m in multi-bunch mode and the bunch length is roughly 2 cm. Electrons and positrons, rotating in opposite directions, collide with a horizontal crossing angle of ± 11 mrad at the interaction point (IP), which centers on the BESIII detector. The new klystrons, new electron gun, new positron source and new injection scheme achieve a 200 mA/min recorded electron injection rate and a 50 mA/min recorded positron injection rate.

2.2 The Beijing Spectrometer III

The Beijing Spectrometer III (BESIII) is a general-purpose detector located in the interaction region at the BEPCII storage rings [26]. The BESIII detector, Figure 2.2, is cylindrically symmetric about the beam line and contains a helium-based, small-celled, multi-layer drift chamber (MDC), which measures momenta and specific ionization (dE/dx) of charged particles; plastic scintillator time-of-flight counters (TOF) for particle identification; an electro-magnetic calorimeter (EMC) of thallium-doped cesium iodide CsI(Tl) crystals, which is used to measure the energies and positions of photons; a super-conducting solenoidal magnet (SSM) with a field of 1 T; and a muon chamber (MUC) made of resistive plate counters (RPCs) for muon identification.

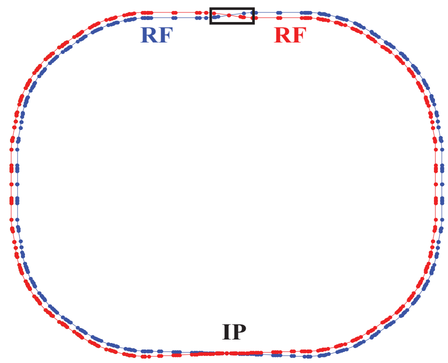

Figure 2.1: The schematic diagram of the BEPCII storage ring. Red and blue markers along the beam lines label the bending and focusing magnets. The beams cross over each other at the top (northern crossing point) and collide at the bottom (interaction point) with a horizontal crossing angle of ±11 mrad .

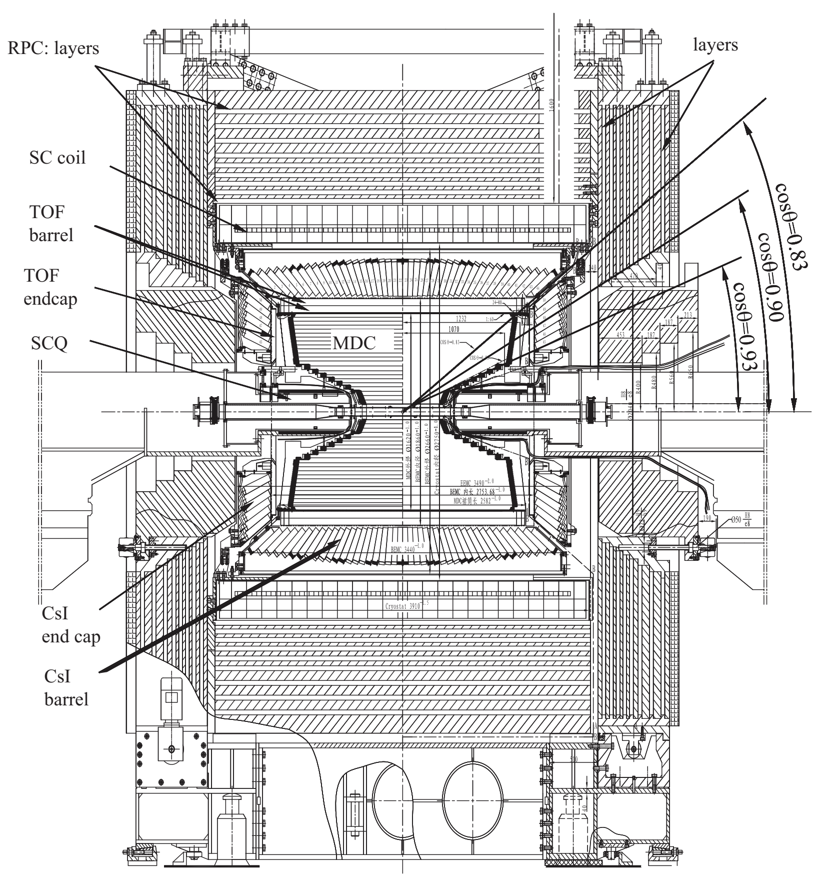

Figure 2.2: The schematic disgram of the BESIII detector. The electron and positron beams collide horizontally at the center of the diagram.

2.2.1 The Drift Chamber (MDC)

With a 59 mm inner radius, and a 810 mm outer radius, the BESIII drift chamber (MDC) is a small-celled multi-layer drift chamber operated using a helium-based gas mixture of 60%/40%, He-C_3H_8, and immersed in a 1T magnetic field. The MDC is used to measure the trajectories of charged particles and is optimized for efficiently tracking the relatively low momentum particles produced in the τ-charm energy region. The solid angle coverage of the MDC is $|\cos\theta| < 0.93$. Tracks pass through all 43 layers for $|\cos\theta| < 0.83$ and at least 20 layers for $0.83 < |\cos\theta| < 0.93$. The spatial resolution is about 130 mm averaged over the cell. The dE/dx resolution is about 6%, giving good π/K separation up to a momentum of 770 MeV/c, and the transverse momentum resolution is about 0.5% at 1 GeV/c. The MDC also produces signals for the level 1 triggers to select good physics events and reject various backgrounds.

2.2.2 The Time-Of-Flight (TOF)

The time-of-flight system (TOF) for particle identification (PID) is composed of a barrel part and two end caps. The barrel TOF is made of two layers of staggered scintillating bars. Each layer has 88 pieces of 5 cm thick, 2.4 m long plastic scintillators. Each end cap is made of a single layer of 48 fan-shaped, 5 cm thick, plastic scintillators. The barrel TOF covers the solid angle of $|\cos\theta| < 0.82$ while the end cap TOF covers $0.85 < |\cos\theta| < 0.95$. The time resolution is 80 ps in the barrel, and 110 ps in the end caps. The TOF also plays a role as the fast trigger for charged particles.

2.2.3 The Electro-Magnetic Calorimeter (EMC)

The Electro-Magnetic Calorimeter (EMC) is used to measure the energy and position of photons with a minimum cluster energy of 20 MeV. It has good e/π discrimination capability for momenta higher than 200 MeV/c. The EMC contains 6240 CsI(Tl) crystals in the barrel and end cap portions of the calorimeter. The EMC surrounds the TOF and covers 93% of the solid angle; the angular coverage of the barrel is $|\cos\theta| < 0.82$ and that of the end caps are $0.83 < |\cos\theta| < 0.93$. The energy and spatial resolutions at 1 GeV are 2.5% (5%) and 0.6 cm (0.9 cm), respectively, in the barrel (end cap).

2.2.4 The Super-Conducting Solenoidal Magnet (SSM)

Located outside of the electro-magnetic calorimeter, the Super-Conducting Solenoidal Magnet (SSM) is a 3.52 m long single-layer solenoid with a mean radius of 1.482 m. The SSM produces a 1 T magnetic field with a nominal current of 3369 A.

2.2.5 The Muon Chamber (MUC)

The Muon Chamber is used for particle identification, in particular to separate muons from charged π and other hadrons based on the penetration depth. The magnet return iron has nine layers of Resistive Plate Chambers (RPC) in the barrel and eight layers in the end cap to form a muon counter. The MUC covers 89% of the solid angle with 2 cm position resolution for the muons. Muons lose 160 MeV on average in the CsI crystals. The minimum muon momentum to trigger the MUC is 0.4 GeV/c.

Chapter 3

Amplitude Analysis

3.1 Probability Density Function and Likelihood Fit

This analysis concerns the decay of a "parent" particle into four "daughter" particles, e.g. $D^0 \to K^-\pi^+\pi^0\pi^0$. A four-body decay is in a five-dimensional space and the daughter particles' momenta are reconstructed for the probability density function. The normalized probability density function describes the likelihood of the amplitude modes as a function of daughter particles' four momenta and is given by

$$S(a_i, p_j) = \frac{\epsilon(p_j)|A(a_i, p_j)|^2 R_4(p_j)}{\int \epsilon(p_j)|A(a_i, p_j)|^2 R_4(p_j) dp_j}\,, \tag{3.1}$$

where the p_j are the daughter particles' four momenta and the a_i are the complex coefficients for amplitude modes. The $\epsilon(p_j)$ is the efficiency parameterized in terms of the daughter particles' four momenta. R_4 is the 4-body phase-space, defined as

$$R_4(p_j) = \delta^4(p_D - \sum_{\mu}^{4} p_\mu) \prod_{\mu}^{4} \frac{d^3 p_\mu}{(2\pi)^3 2E_\mu}\,. \tag{3.2}$$

$A(a_i, p_j)$ is the total amplitude and is represented as a coherent sum of amplitude modes:

$$A(a_i, p_j) = \sum_i a_i A_i(p_j)\,, \tag{3.3}$$

where the complex amplitudes a_i are written in the polar form as $\rho_i e^{i\phi_i}$, and the $A_i(p_j)$ are the amplitudes for each mode. The amplitude modes can be classified as two types, quasi-two-body and cascade. For a quasi-two-body amplitude mode, the D meson decays to two resonance states and thereafter each resonance state decays to two final daughter particles. A cascade amplitude mode is when the D meson decays to the first resonance state plus a final daughter particle, then the first resonance state decays to the second resonance state plus a final daughter particle, and finally the second resonance state decays to two final daughter particles. In both types, $A_i(p_j)$ can be modeled as

$$A_i(p_j) = P_i^1(p_j) P_i^2(p_j) S_i(p_j) F_i^1(p_j) F_i^2(p_j) F_i^D(p_j)\,, \tag{3.4}$$

where $F_i^D(p_j)$ is the Blatt-Weisskopf Barrier factor for the D meson. $P_i^{1,2}(p_j)$ and $F_i^{1,2}(p_j)$ are propagators and Blatt-Weisskopf Barrier factors, respectively, $(i = 1, 2)$ of the two resonance states for the quasi-two-body type or of the first and the second resonance states for the cascade type. $S_i(p_j)$ is the spin factor. Finally, the likelihood can be defined as

$$L = \prod_{j=1}^{N_s} S(a_i, p_j)\,, \tag{3.5}$$

where j indicates the selected events and N_s is the number of the selected events. Consequently, the log likelihood is given by

$$\begin{aligned} \ln L &= \sum_{j=1}^{N_s} \ln S(a_i, p_j) \\ &= \sum_{j=1}^{N_s} \ln \left(\frac{|A(a_i, p_j)|^2 R_4(p_j)}{\int \epsilon(p_j) |A(a_i, p_j)|^2 R_4(p_j) dp_j} \right) + \sum_{j=1}^{N_s} \ln \epsilon(p_j)\,. \end{aligned} \tag{3.6}$$

The normalization integration in the first term can be approximated by a phase-space Monte-Carlo integration obtained by summing over a phase-space Monte-Carlo sample,

$$\int \epsilon(p_j) |A(a_i, p_j)|^2 R_4(p_j) dp_j \approx \frac{1}{N_{g,ph}} \sum_{j=1}^{N_{s,ph}} |A(a_i, p_j)|^2\,, \tag{3.7}$$

where $N_{g,ph}$ is the number of generated phase-space events and $N_{s,ph}$ is the number of selected phase-space events. The basic concept behind is that the generated phase-space sample is "flat", and the efficiency is the "shape" after this phase-space sample is reconstructed by the detector.

For signal MC samples, the amplitude squared for each event should be normalized by the PDF generating the sample. The normalization integration using signal MC samples is given by

$$\int \epsilon(p_j) |A(a_i, p_j)|^2 R_4(p_j) dp_j \approx \frac{1}{N_{MC}} \sum_{j=1}^{N_{MC}} \frac{|A(a_i, p_j)|^2}{|A(a_i^{gen}, p_j)|^2}\,, \tag{3.8}$$

where a_i^{gen} are the parameters used to generate the signal MC sample. Considering the bias caused by particle identification, tracking, and π^0 data vs. MC efficiency differences, we introduce γ_ϵ to correct this bias,

$$\gamma_\epsilon(p) = \prod_i \frac{\epsilon_{i,data}(p_i)}{\epsilon_{i,MC}(p_i)}\,, \tag{3.9}$$

where i denote the four daughter particles. The values of $\epsilon_{i,data}(p_i)/\epsilon_{i,MC}(p_i)$ used in this analysis are listed in Appendix I. By weighting each signal MC event with γ_ϵ, the MC integration can be given by

$$\int \epsilon(p_j)|A(a_i,p_j)|^2 R_4(p_j)dp_j \approx \frac{1}{N_{MC}} \sum_j^{N_{MC}} \frac{|A(a_i,p_j)|^2\gamma_\epsilon(p_j)}{|A(a_i^{gen},p_j)|^2}\,. \tag{3.10}$$

Note that since the second term of Eq. 3.6 is independent of a_i and the normalization integration in the first term can be approximated by a phase-space Monte-Carlo integration, one can execute a Partial Wave Analysis (PWA) without knowing efficiency in advance.

3.2 Spin Factors

Considering a decay process $a \to bc$, we use the notation p_a, p_b, p_c as the momenta of particles a, b, c, respectively, and $r_a = p_b - p_c$. The spin projection operators are defined as

$$P^{(1)}_{\mu\mu'}(a) = -g_{\mu\mu'} + \frac{p_{a,\mu}p_{a,\mu'}}{p_a^2}\,, \tag{3.11}$$

$$P^{(2)}_{\mu\nu\mu'\nu'}(a) = \frac{1}{2}(P^{(1)}_{\mu\mu'}(a)P^{(1)}_{\nu\nu'}(a) + P^{(1)}_{\mu\nu'}(a)P^{(1)}_{\nu\mu'}(a)) + \frac{1}{3}P^{(1)}_{\mu\nu}(a)P^{(1)}_{\mu'\nu'}(a)\,. \tag{3.12}$$

The covariant tensors are given by

$$\tilde{t}^{(1)}_\mu(a) = -P^{(1)}_{\mu\mu'}(a)r_a^{\mu'}\,, \tag{3.13}$$

$$\tilde{t}^{(2)}_{\mu\nu}(a) = P^{(2)}_{\mu\nu\mu'\nu'}(a)r_a^{\mu'}r_a^{\nu'}\,. \tag{3.14}$$

A detailed discussion of spin factor can be found in reference [27]. We list the 10 kinds of spin factors used in this analysis in Table 3.1. Note that scalar, pseudo-scalar, vector, axial-vector and tensor states are denoted by S, P, V, A, T, respectively.

3.3 Blatt-Weisskopf Barrier Factors

The Blatt-Weisskopf barrier $F_i(p_j)$ is a barrier function for a two-body decay process, $a \to bc$. The Blatt-Weisskopf barrier depends on angular momenta and the magnitude of the momenta of daughter particles in the rest system of the mother particle. The definition is given by

$$F_L(q) = z^L X_L(q), \tag{3.15}$$

Table 3.1: Spin Factor for each decay chain. All operators, i.e. $\tilde{t}$, have the same definition as reference [27].

Decay Chain	$S(p)$
$D[S] \to V_1V_2$	$\tilde{t}^{(1)\mu}(V_1)\ \tilde{t}^{(1)}_{\mu}(V_2)$
$D[P] \to V_1V_2$	$\epsilon_{\mu\nu\lambda\sigma}p^{\mu}(D)\ \tilde{T}^{(1)\nu}(D)\ \tilde{t}^{(1)\lambda}(V_1)\ \tilde{t}^{(1)\sigma}(V_2)$
$D[D] \to V_1V_2$	$\tilde{T}^{(2)\mu\nu}\ \tilde{t}^{(1)}_{\mu}(V_1)\ \tilde{t}^{(1)}_{\mu}(V_2)$
$D \to AP_1, A[S] \to VP_2$	$p_1^{\nu}\ P^{(1)}_{\mu\nu}(A)\ \tilde{t}^{(1)\nu}_{(V)}$
$D \to AP_1, A[D] \to VP_2$	$\tilde{T}^{(1)\mu}(D)\ \tilde{t}^{(2)}_{\mu\nu}(A)\ \tilde{t}^{(1)\nu}(V)$
$D \to AP_1, A \to SP_2$	$\tilde{T}^{(1)\mu}(D)\ \tilde{t}^{(1)}_{\mu}(A)$
$D \to VS$	$\tilde{T}^{(1)\mu}(D)\ \tilde{t}^{(1)}_{\mu}(V)$
$D \to V_1P_1, V_1 \to V_2P_2$	$\epsilon_{\mu\nu\lambda\sigma}\ p^{\mu}_{V_1} r^{\nu}_{V_1}\ p^{\lambda}_{P_1}\ r^{\sigma}_{V_2}$
$D \to PP_1, P \to VP_2$	$p^{\mu}_{P_2}\ \tilde{t}^{(1)}_{\mu}(V)$
$D \to TS$	$\tilde{T}^{(2)\mu\nu}(D)\ \tilde{t}^{(2)}_{\mu\nu}(T)$

where L denotes the angular momenta, and $z = qR$, where q is the magnitude of the momenta of daughter particles in the rest system of the mother particle. For a process $a \to bc$, we define $s_i = E_i^2 - p_i^2$, $i = a, b, c$, such that

$$q^2 = \frac{(s_a + s_b - s_c)^2}{4s_a} - s_b \tag{3.16}$$

and R is the effective radius of the barrier used in BESIII MC generator (based on EvtGen), which is 3.0 GeV^{-1} and 5.0 GeV^{-1} for intermediate resonance and D meson, respectively. This value R is a typical value used by D physics. Further, this value will be varied as a source of systematics. The $X_L(q)$ are given by,

$$X_{L=0}(q) = 1, \tag{3.17}$$

$$X_{L=1}(q) = \sqrt{\frac{2}{z^2+1}}, \tag{3.18}$$

$$X_{L=2}(q) = \sqrt{\frac{13}{9z^4+3z^2+1}}, \tag{3.19}$$

3.4 Propagator

We use the relativistic Breit-Wigner function as the propagator for resonances $\bar{K}^{*0}$, K^{*-}, and $a_1(1260)^+$, and fix their width and mass to PDG values. The relativistic

Breit-Wigner function is given by

$$P(m) = \frac{1}{(m_0^2 - m^2) - i m_0 \Gamma(m)}\,, \tag{3.20}$$

where $m = \sqrt{E^2 - p^2}$ and m_0 is the rest mass of the resonance. $\Gamma(m)$ is given by,

$$\Gamma(m) = \Gamma_0 \left(\frac{q}{q_0}\right)^{2L+1} \left(\frac{m_0}{m}\right) \left(\frac{X_L(q)}{X_L(q_0)}\right)^2 , \tag{3.21}$$

where q_0 indicates the value of q when $s_a = m_0^2$. Resonances $\bar{K}_1(1270)^0$ and $K_1(1270)^-$ are also parameterized by the relativistic Breit-Wigner function but with constant width $\Gamma(m) = \Gamma_0$ because their large decay width may cause negative q_0. We parameterize ρ by the Gounaris-Sakurai lineshape [28], which is given by

$$P_{GS}(m) = \frac{1 + d\frac{\Gamma_0}{m_0}}{(m_0^2 - m^2) + f(m) - i m_0 \Gamma(m)}\,. \tag{3.22}$$

The function $f(m)$ is given by

$$f(m) = \Gamma_0 \frac{m_0^2}{q_0^3} \left[q^2 (h(m) - h(m_0)) + (m_0^2 - m^2) q_0^2 \left. \frac{dh}{d(m^2)} \right|_{m^2 = m_0^2} \right] , \tag{3.23}$$

where

$$h(m) = \frac{2q}{\pi m} \ln \left(\frac{m + 2q}{2 m_\pi} \right) , \tag{3.24}$$

and

$$\left. \frac{dh}{d(m^2)} \right|_{m^2 = m_0^2} = h(m_0) \left[(8 q_0^2)^{-1} - (2 m_0^2)^{-1} \right] + (2 \pi m_0^2)^{-1}\,. \tag{3.25}$$

The normalization condition at $P_{GS}(0)$ fixes the parameter $d = f(0)/(\Gamma_0 m_0)$. It is found to be

$$d = \frac{3 m_\pi^2}{\pi q_0^2} \ln \left(\frac{m_0 + 2 q_0}{2 m_\pi} \right) + \frac{m_0}{2 \pi q_0} - \frac{m_\pi^2 m_0}{\pi q_0^3}\,. \tag{3.26}$$

3.5 Fit Fraction

Since fit fraction (FF) is independent of the normalization, phase convention, and amplitude formalism, it provides a better way of comparing amplitudes among modes. The definition of the fit fraction for i^{th} amplitude is given by

$$\begin{aligned} FF_i &= \frac{\int |a_i A_i(p_j)|^2 R_4(p_j) dp_j}{\int |\sum_k a_k A_k(p_j)|^2 R_4(p_j) dp_j} \\ &\approx \frac{\sum_{j=1}^{N_{g,ph}} |a_i A_i|^2}{\sum_{j=1}^{N_{g,ph}} |\sum_k a_k A_k|^2}\,, \end{aligned} \tag{3.27}$$

where the integration is approximated by a Monte-Carlo integration with a phase-space Monte-Carlo sample. Comparing to Eq. 3.7, since fit fraction does not involve efficiency, the Monte-Carlo sample used here is at the generator level instead of at the reconstruction level.

As for the statitical uncertainty of fit fraction, it is not practical to analytically propagate the uncertainties of fit fractions from that of amplitudes and phases. So, we randomly perturb the variables determined in our fit (by a Gaussian-distributed amount controlled by the fit uncertainty and the covariance matrix) and calculate the fit fractions to determine the statistic uncertainties. We fit the distribution of each fit fraction with a Gaussian and the width of the Gaussian is defined as the uncertainty of the fit fraction. Figure 3.1 shows three typical examples of fit fraction distributions. Since fit fractions are always positive, when the mean values are close to zero, compared to their widths, the distributions are truncated. Empirically, they behave like truncated Gaussian functions.

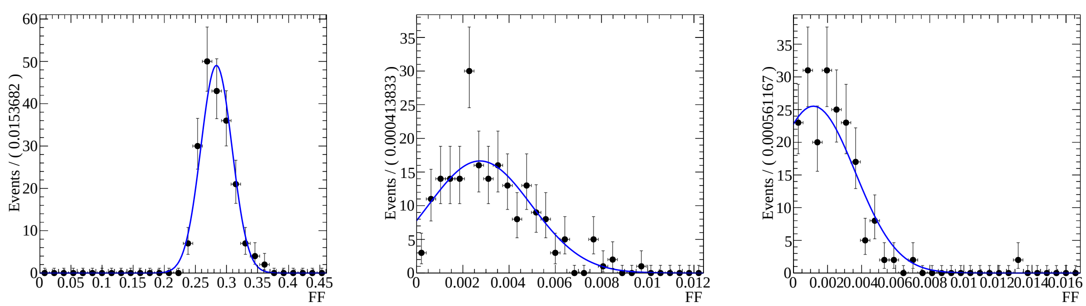

(a) $D^0 \to K^- a_1(1260)^+$, $a_1(1260)^+ \to \rho^+\pi^0[S]$

(b) $D^0 \to (K^-\pi^+)_S(\pi^0\pi^0)_T$

(c) $D^0 \to K^{*0}(\pi^0\pi^0)_S$

Figure 3.1: Fit fraction distributions by perturbing floating variables based on the covariance matrix. The distributions are fitted with Gaussian or truncated Gaussian functions if the mean values are close to zero comparing to their widths.

3.6 $K\pi$ S-Wave Formfactor

The kinematic modifications associated with $K\pi$ S-wave is modeled by a parameterization from scattering data [17, 29], which are described by a K_0^* Breit-Wigner along with an effective range non-resonant component with a phase shift:

$$A(m) = F \sin\delta_F e^{i\delta_F} + R \sin\delta_R e^{i\delta_R} e^{i2\delta_F} \,, \tag{3.28}$$

where

$$\delta_F = \phi_F + \cot^{-1}\left[\frac{1}{aq} + \frac{rq}{2}\right]$$
$$\delta_R = \phi_R + \tan^{-1}\left[\frac{M\Gamma(m_{K\pi})}{M^2 - m_{K\pi}^2}\right] ,$$

where a and r are the scattering length and effective interaction length, respectively. The parameters $F(\phi_F)$ and $R(\phi_R)$ are the magnitude (phase) for non-resonant state and resonance terms respectively. The definition of q and $\Gamma(m_{K\pi})$ can be found in Sections 3.3 and 3.4. The parameters M, F, ϕ_F, R, ϕ_R, a, r are fixed to the results of the $D^0 \to K_S\pi\pi$ analysis by BaBar [17], given in Table 3.3.

Table 3.3: Parameters of $K\pi$ S-Wave, by BaBar.

$M(\text{GeV}/c^2)$	1.463 ± 0.002
$\Gamma(\text{GeV}/c^2)$	0.233 ± 0.005
F	0.80 ± 0.09
ϕ_F	2.33 ± 0.13
R	1(fixed)
ϕ_R	-5.31 ± 0.04
a	1.07 ± 0.11
r	-1.8 ± 0.3

3.7 Tricks to Save Computing Resources

The Monte-Carlo integration, Eq. 3.7, is the most time-consuming step and needs to be calculated over and over again each time the fitter varies the floating variables. However, presuming the widths and masses of resonances are fixed, one can precalculate the amplitude matrix, $U_{\alpha,\beta}$ in Eq. 3.30, to speed up the fit dramatically. The Monte-Carlo integration can be written as

$$\frac{1}{N_{g,ph}} \sum_{j}^{N_{s,ph}} |A(a_i, p_j)|^2 = \frac{1}{N_{g,ph}} \sum_{j}^{N_{s,ph}} \sum_{\alpha} a_\alpha A_\alpha(p_j) \sum_{\beta} a_\beta^* A_\beta^*(p_j) \,. \tag{3.29}$$

By switching the order of summation,

$$\frac{1}{N_{g,ph}}\sum_{j}^{N_{s,ph}}|A(a_i,p_j)|^2 = \frac{1}{N_{g,ph}}\sum_{\alpha,\beta} a_\alpha a_\beta^* \sum_{j}^{N_{s,ph}} A_\alpha(p_j)A_\beta^*(p_j)\,,$$
$$= \frac{1}{N_{g,ph}}\sum_{\alpha,\beta} a_\alpha a_\beta^* U_{\alpha,\beta}, \tag{3.30}$$

where $U_{\alpha,\beta} \equiv \sum_j^{N_{s,ph}} A_\alpha(p_j)A_\beta^*(p_j)$. The size of the matrix $U_{\alpha,\beta}$ is i^2, where i is the number of amplitude modes, and thus the Monte-Carlo integration needs to be calculated only i^2 times. Furthermore, $U_{\alpha,\beta}$ can be precalculated once and used many times in the case fitting to many data samples without changing the parameterization, number of amplitude modes, and the phase-space MC samples, such as the study of systematics of fitter performance (Section 8.1.4).

Chapter 4

Data Set and Event Selection

4.1 Dataset and Monte-Carlo Samples

The BESIII detector collected a 2.93 fb^{-1} dataset in 2010 and 2011 at the $\psi(3770)$ resonance [30, 31]. The $\psi(3770)$ decays predominantly to $D^0\bar{D}^0$ or D^+D^-. Both data and Monte-Carlo samples are generated and reconstructed using software release BOSS 6.6.4p02. All samples used in this analysis are listed in Table 4.1. Luminosities of Monte-Carlo samples are given in multiples of data luminosity.

Table 4.1: Dataset and Monte-Carlo samples for $\sqrt{s} = 3.773$ GeV. "10.9x" means 10.9 times the data statistics, etc.

Reaction	**Luminosities (pb^{-1})**	
$e^+e^- \to X$	2010	2011
Data	932.4	1999.4
$\psi(3770) \to D^0\bar{D}^0$	21.8x	21.8x
$\psi(3770) \to D^+D^-$	10.9x	10.8x
$q\bar{q}$	7.8x	7.3x

4.2 Photon, Tracking and PID

Photons are reconstructed as energy clusters in the EMC. The shower time is required be less than 700 ns from the event start time in order to suppress fake photons due to electronic noise or e^+e^- beam noise. Photon candidates in $|\cos\theta| < 0.80$ (barrel) are required to have > 25 MeV energy deposition and those with $0.86 < |\cos\theta| < 0.92$ (endcap) must have > 50 MeV energy deposition. To suppress noise from hadronic splitoffs, the calorimeter positions of photon candidates must be at least $10°$ away from all charged tracks.

Candidate π^0s are reconstructed through $\pi^0 \to \gamma\gamma$, with at least one barrel photon. The invariant mass is required to $0.115 < M_{\gamma\gamma} < 0.150$ GeV/c^2. We further perform a constrained fit on the photons pairs to the nominal π^0 mass, and require $\chi^2 < 2500$.

The properties of charged tracks are determined based on the MDC information. Charged track candidates must satisfy $|\cos\theta| < 0.93$, where θ is the polar angle with respect to the direction of the positron beam. The closest approach to the interaction point is required to be less than 10 cm in the beam direction and less than 1 cm in the plane perpendicular to the beam.

Charged tracks are identified as pions or kaons with Particle Identification (PID), which is implemented by combining the information of the energy loss (dE/dx) in the MDC and the time-of-flight measured from the TOF system. For charged kaon candidates, the probability of the hypothesis of a kaon, $Prob(K)$, is required to be positive and larger than that for a pion, $Prob(\pi)$. For charged pion candidates, the probability for the pion hypothesis is required to be positive and larger than that for a kaon.

The requirements for photons, π^0s, charged tracks, and PID are summarized below.

- **Photons**
  - shower time < 700 ns
  - $|\cos\theta| < 0.80$ (barrel) or $0.86 < |\cos\theta| < 0.92$ (endcap)
  - Energy deposition > 25 MeV for photons in barrel
  - Energy deposition > 50 MeV for photons in endcap
  - $10°$ isolation from any charged tracks
- π^0
  - $0.115 <$ unconstrained two-photon mass < 0.150 GeV
  - Number of photons reconstructed in the end cap ≤ 1
  - Mass fit $\chi^2 < 2500$
- **Charged tracks**
  - $|\cos\theta| < 0.93$
  - Closest approach to IP in the beam direction < 10 cm
  - Closest approach to IP perpendicularly to the beam < 1 cm
- **Particle identification (PID)**
  - For K, $Prob(K) > 0$ and $Prob(K) > Prob(\pi)$
  - For π, $Prob(\pi) > 0$ and $Prob(\pi) > Prob(K)$

4.3 D Meson Reconstruction and DTag

After charged kaons, charged pions, and neutral pions are identified, hadronic D decays can be reconstructed with the DTag package. The two variables, beam constrained mass M_{BC} and energy difference ΔE, are used to identify the D meson.

$$M_{\mathrm{BC}} = \sqrt{E_{\mathrm{beam}}^2 - |\vec{p}_D|^2}\,, \tag{4.1}$$

$$\Delta E = E_D - E_{\mathrm{beam}}\,, \tag{4.2}$$

where $|\vec{p}_D|^2$ and E_D are the total reconstructed momentum and energy of the D candidate in the center-of-mass frame of the $\psi(3770)$, respectively, and E_{beam} is the calibrated beam energy. D signals will be consistent with the nominal D mass in M_{BC} and with zero in ΔE. M_{BC} is related to momentum conservation, and ΔE to energy conservation.

The DTag technique uses all combinations of the identified daughter particles to reconstruct D mesons with $|\Delta E| < 100$ MeV and $M_{\mathrm{BC}} > 1.83$ GeV/c^2. There are two types of samples used in the DTag technique: single tag (ST) and double tag (DT) samples. In the ST sample, only one D or $\bar{D}$ meson is reconstructed through a chosen hadronic decay without any requirement on the remaining measured tracks and showers. For multiple candidates, only the D candidate with smallest $|\Delta E|$ is kept. In the DT sample, both D and $\bar{D}$ are reconstructed, where one meson reconstructed through the hadronic decay of interest is called the "signal side", and the other meson is called the "tag side" (usually reconstructed through well-known and clean hadronic decays). For multiple $D\bar{D}$ candidates, the best candidate is chosen based on the smallest $|\Delta E|$ of both sides. By reconstructing both D mesons, the DT sample provides lower background levels but smaller statistics than if ST were used for the signal mode. After ST or DT candidates are reconstructed, reasonable cuts in M_{BC} and ΔE may be applied to further veto bad candidates. The loose DTag cuts stated above are chosen to include sidebands.

It is worth noting that DTag allows there to be other, unused photon candidates in DT samples. No veto on extra clusters is applied since such clusters are common due to noise or "split-offs" from messy hadronic showers. A veto on extra clusters both hurts efficiency and would be hard to simulate properly. As for tracks, DTag requires that all track candidates must be used in DT samples.

4.4 Peaking Background

A sample of ST $K^-\pi^+\pi^0\pi^0$ candidates from the public MC simulation are used to study peaking backgrounds, where the D^0 meson is reconstructed in the $K^-\pi^+\pi^0\pi^0$ mode. Those single tag candidates must satisfy $-0.05 < \Delta E < 0.03$ GeV. (The asymmetry is due to asymmetric photon resolution.) Because $K^-K_S\pi^+$ is expected to be the major peaking background, we apply a nominal K_S mass veto of $0.458 <$

$M_{\pi^0\pi^0} < 0.520$. In order to get yields, we perform a χ^2 fit to the $M_{\rm BC}$ distribution with a Crystal Ball plus an Argus background.

The results are given in Tables 4.2, 4.3. The fitting plots are shown in Figures 4.1, 4.2. Taking the advantage of Truthtag, we split single tag candidates into many subsets. "Truthtag" refers to generator-level information only; no reconstruction information is involved. In other words, we check only the number and the types of particles generated by MC. D^0 ($\bar{D}^0$) Truthtag indicates the true $D^0(\bar{D}^0)$ decays in the MC. We use "!" to indicate excluding certain decay (but including all other decays). We note that both $D^0 \to K_sK^-\pi^+$ and $\bar{D}^0 \to K_sK^-\pi^+$ occur. That is, for these singly-Cabibbo supressed decays, the sign of the $K^\pm$ does not indicate the charm of the parent. However, only the first decay will be relevant in our DT sample with a $\bar{D}^0 \to K^+\pi^-$. The table demonstrates that peaking backgrounds are dominated by these two decay modes.

Table 4.2: Mode 2 $K^-\pi^+\pi^0\pi^0$ (without K_S mass cut)

$\boldsymbol{D^0}$ Truthtag	$\boldsymbol{\bar{D}^0}$ Truthtag	**Yield** (10^4)	**Ratio**
–	–	222.17 ± 0.35	
$K^-\pi^+\pi^0\pi^0$	–	214.03 ± 0.18	100%
!$K^-\pi^+\pi^0\pi^0$	–	7.53 ± 0.12	3.52%
$K_sK^-\pi^+$	**!**$K_sK^-\pi^+$	4.75 ± 0.027	2.22%
!$K^-\pi^+\pi^0\pi^0$ **!**$K_sK^-\pi^+$	$K_sK^-\pi^+$	2.64 ± 0.02	1.23%
$K_sK^-\pi^+$	$K_sK^-\pi^+$	0.00 ± 0.00	0.00%
other	–	0.10 ± 0.05	0.05%
!$K^-\pi^+\pi^0\pi^0$	$K_sK^-\pi^+$	0.31 ± 0.01	0.15%

4.4.1 K_S Peaking Background

The decay $D^0 \to K^-K_S\pi^+$ with $K_S \to \pi^0\pi^0$ is expected to contribute the major peaking background of $D \to K^-\pi^+\pi^0\pi^0$. Figure 4.3 shows the $\pi^0\pi^0$ invariant mass, $M_{\pi^0\pi^0}$, distributions of data and generic Monte Carlo samples. The K_S peak of generic Monte-Carlo sample is sharper and larger than that of data. We further subtract the K_S peak from data, where the K_S peak is obtained by truthtagging the generic Monte-Carlo and normalized to data size based on luminosity. As expected, data appears over-subtracted in Figure 4.3(c). We will not use the MC background level prediction directly due to this.

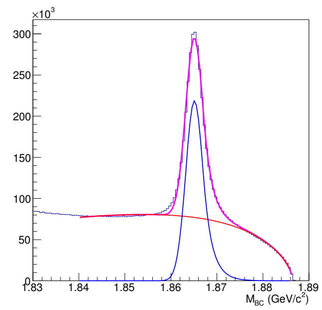

(a) – vs. –

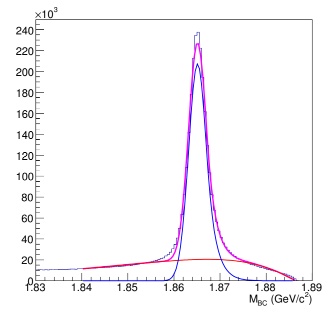

(b) $K^-\pi^+\pi^0\pi^0$ vs. –

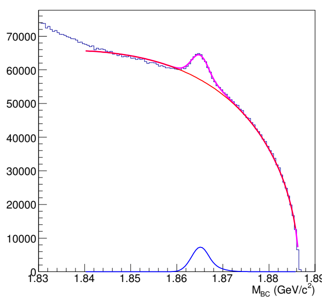

(c) **!**$K^-\pi^+\pi^0\pi^0$ vs. –

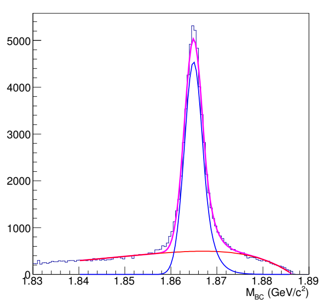

(d) $K_sK^-\pi^+$ vs. **!**$K_sK^-\pi^+$

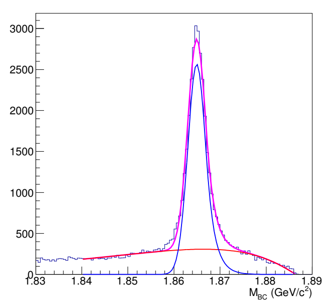

(e) **!**$K^-\pi^+\pi^0\pi^0$ or **!**$K_sK^-\pi^+$ vs. $K_sK^-\pi^+$

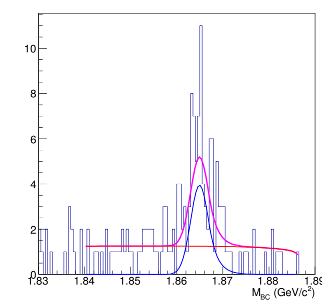

(f) $K_sK^-\pi^+$ vs. $K_sK^-\pi^+$

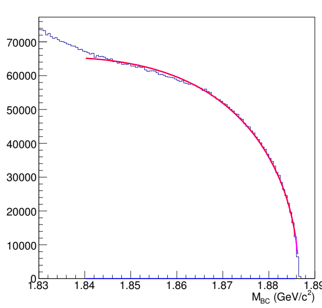

(g) **other** vs. –

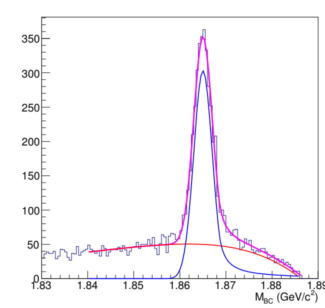

(h) $K^-\pi^+\pi^0\pi^0$ vs. $K_sK^-\pi^+$

Figure 4.1: M_{BC} single-tag yield fits without K_S mass cut.

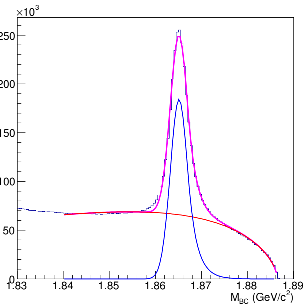

(a) – vs. –

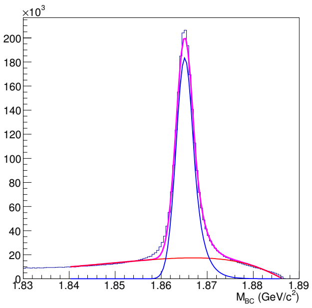

(b) $K^-\pi^+\pi^0\pi^0$ vs. –

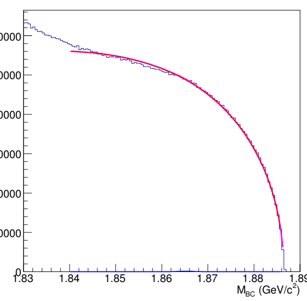

(c) **!**$K^-\pi^+\pi^0\pi^0$ vs. –

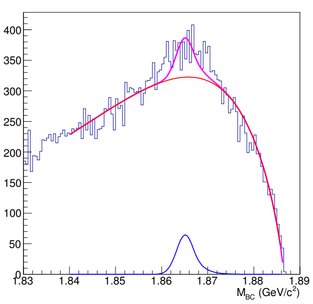

(d) $K_sK^-\pi^+$ vs. **!**$K_sK^-\pi^+$

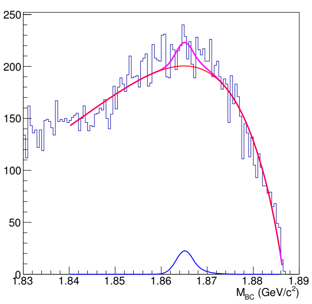

(e) **!**$K^-\pi^+\pi^0\pi^0$ or **!**$K_sK^-\pi^+$ vs. $K_sK^-\pi^+$

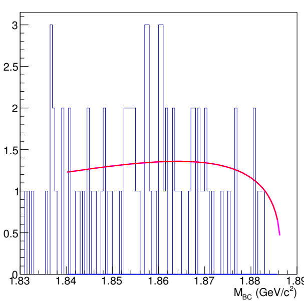

(f) $K_sK^-\pi^+$ vs. $K_sK^-\pi^+$

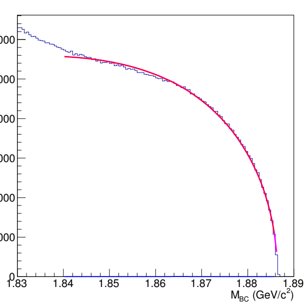

(g) **other** vs. –

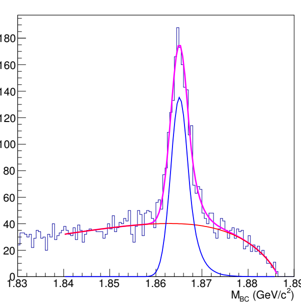

(h) $K^-\pi^+\pi^0\pi^0$ vs. $K_sK^-\pi^+$

Figure 4.2: M_{BC} single-tag yield fits with K_S mass cut.

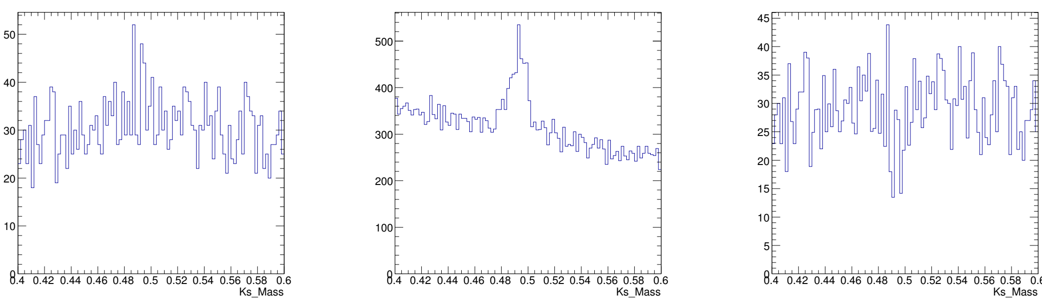

(a) data (b) generic Monte Carlo (c) data with K_S subtracted

Figure 4.3: $M_{\pi^0\pi^0}$ distributions for $K^- K_S \pi^+$ peaking background study.

Table 4.3: Mode 2 $K^-\pi^+\pi^0\pi^0$ (with K_S mass cut)

D^0 **Truthtag**	$\bar{D}^0$ **Truthtag**	**Yield** (10^4)	**Ratio**
–	–	187.62 ± 0.33	
$K^-\pi^+\pi^0\pi^0$	–	186.90 ± 0.16	100%
$!K^-\pi^+\pi^0\pi^0$	–	0.15 ± 0.05	0.08%
$K_sK^-\pi^+$	$!K_sK^-\pi^+$	0.07 ± 0.01	0.04%
$!K^-\pi^+\pi^0\pi^0$ $!K_sK^-\pi^+$	$K_sK^-\pi^+$	0.02 ± 0.01	0.01%
$K_sK^-\pi^+$	$K_sK^-\pi^+$	0.00 ± 0.00	0.00%
other	–	0.06 ± 0.10	0.03%
$!K^-\pi^+\pi^0\pi^0$	$K_sK^-\pi^+$	0.14 ± 0.01	0.07%

In addition, we study the shape, especially the tails of this K_S peak based on signal Monte-Carlo of $D^0 \to K^-K_S\pi^+$ with $K_S \to \pi^0\pi^0$. The $M_{\pi^0\pi^0}$ distribution, Figure 4.4 (a), shows a low mass tail of the K_S peak. Because the K_S decays to two π^0s, three criteria related to π^0s have been studied. First, we reconstruct a variable "dang", which measure isolation angle from charged tracks. Dang is the space angle between photon showers and charged tracks. We keep only π^0s that are reconstructed using only photons whose calorimeter position is at least 20° or at least 15° away from any charged tracks (dang > 20 or > 15), shown in Figures 4.4 (b)(c). Second, we keep only π^0s that are reconstructed using only photons whose energy is at least 50 MeV ($E_{min} > 50$ MeV), shown in Figures 4.4 (d). Third, we keep only K_S whose decay point is less than 6 or 4 cm from the interacting point (K_S IP distance < 6 or < 4 cm), shown in Figures 4.4 (e)(f). The corresponding $M_{\pi^0\pi^0}$ distributions of events excluded by these criteria options are shown in Figures 4.5.

The E_{min} option can exclude soft photons. Soft photons are more likely to be fake and are vulnerable to noise. As shown in Figure 4.5 (d), the events excluded by the E_{min} option have larger tails at both sides of $M_{\pi^0\pi^0}$ peak. The dang option can exclude hadronic splitoffs, which could create fake photons or add energy on real photons. By adding energy on real photons, hadronic splitoffs cause noise tail at the right side of $M_{\pi^0\pi^0}$ peak, shown in Figures 4.5 (b) and (c), The K_S IP distance criteria option can exclude K_Ss, which decay into two π^0s after flying a certain distance away from IP. Since π^0s are reconstructed assuming they decay at IP, the reconstructed decaying angle of those π^0s will be smaller than the real one. As a result, the events excluded by the K_S IP distance criteria option makes the $M_{\pi^0\pi^0}$ peak shifting toward lower K_S mass, shown in Figures 4.5 (e) and (f). Based on the results shown in Tables

4.2 and 4.3, we impose a $K_S \to \pi^0\pi^0$ veto in this analysis. Further, understanding these background sources are helpful when assigning a systematic uncertainty.

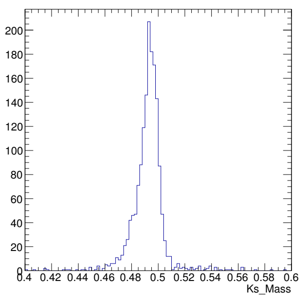

(a) $K^- K_S \pi^+$ signal MC

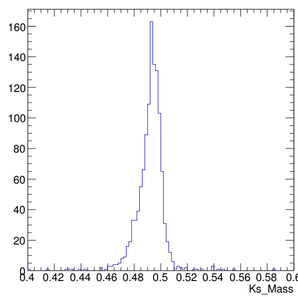

(b) dang > 20

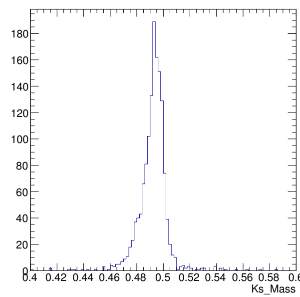

(c) dang > 15

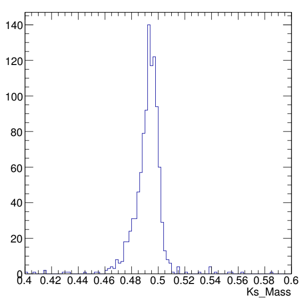

(d) $E_{min} > 50$ MeV

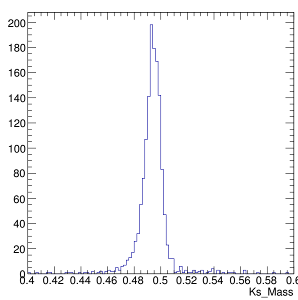

(e) K_S IP distance < 6

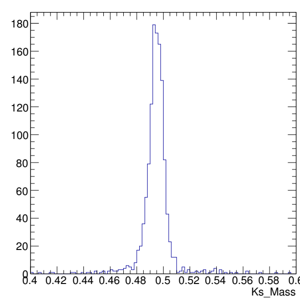

(f) K_S IP distance < 4

Figure 4.4: $M_{\pi^0\pi^0}$ plots of $K^- K_S \pi^+$, $K_S \to \pi^0\pi^0$ signal Monte-Carlo.

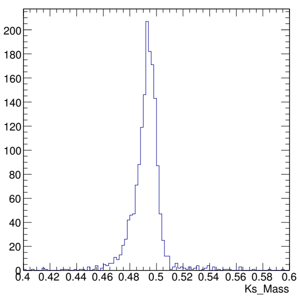

(a) $K^-K_S\pi^+$ signal MC

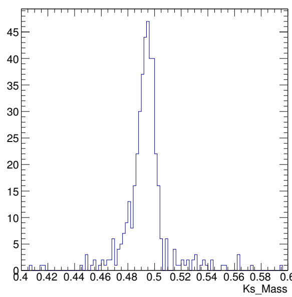

(b) dang < 20

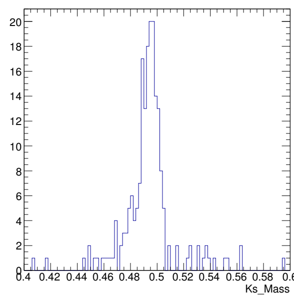

(c) dang < 15

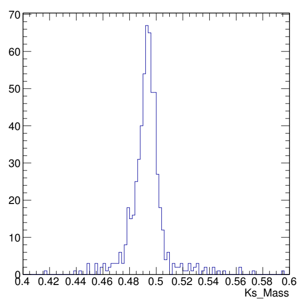

(d) $E_{min} < 50$ MeV

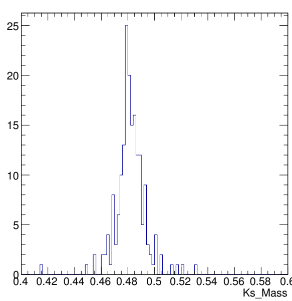

(e) K_S IP distance > 6

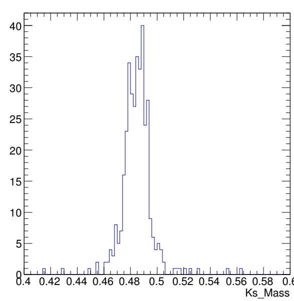

(f) K_S IP distance > 4

Figure 4.5: $M_{\pi^0\pi^0}$ plots of $K^-K_S\pi^+$, $K_S \to \pi^0\pi^0$ signal Monte-Carlo. (cuts reversed)

4.5 PWA Event Selection

The DT candidates used in this PWA analysis are required to have D^0 meson decaying to $K^-\pi^+\pi^0\pi^0$ as the signal, and the $\bar{D}^0$ meson decaying to $K^+\pi^-$ as the tag. For charged tracks of the signal side, a vertex fit is performed and the χ^2 must be less than 100. We then perform a three-constraint kinematic fit in which the invariant masses of the signal D candidate and the two π^0s are constrained to their PDG values. The events with kinematic fit $\chi^2 > 80$ are discarded. The kinematic fit χ^2 distributions of data and the public MC are shown in Figure 4.6

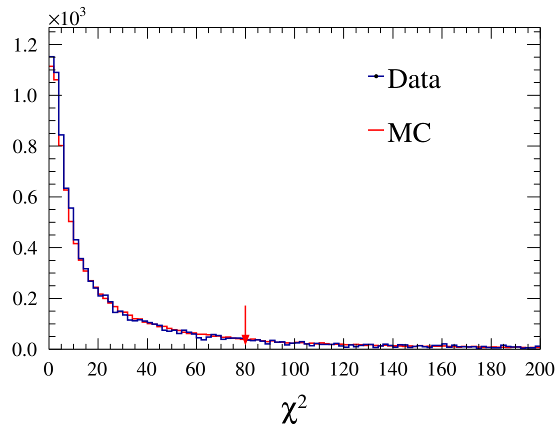

Figure 4.6: Kinematic fit χ^2 distribution.

Furthermore, the tag side is required to satisfy $1.8575 < M_{\mathrm{BC}} < 1.8775$ GeV and $-0.03 < \Delta E < 0.02$ GeV. These cuts on the tag side are relatively wide because the resolutions of M_{BC} and ΔE distributions on the tag side are well simulated and the backgrounds from fake tags are quite low. On the signal side, a $K_S \to \pi^0\pi^0$ mass veto is applied to remove the dominant peaking background, $K^-K_S\pi^+$. More details are discussed in Section 4.5.1. In order to study the effect of M_{BC} and ΔE cut on the signal side, we apply the "tight cuts", our default cut for the PWA analysis, or the "wide cut", to study systematic effects, as needed. These cuts are chosen as:

Tight Cuts

- $1.8600 < M_{\mathrm{BC}} < 1.8730$ GeV.
- $-0.04 < \Delta E < 0.02$ GeV.
- $M_{\pi^0\pi^0} < 0.458$ or $0.520 < M_{\pi^0\pi^0}$ GeV.

Wide Cuts

- $1.8575 < M_{\mathrm{BC}} < 1.8775$ GeV.

- $-0.05 < \Delta E < 0.03$ GeV.
- $M_{\pi^0\pi^0} < 0.458$ or $0.520 < M_{\pi^0\pi^0}$ GeV.

The $M_{\rm BC}$ and ΔE distributions of data and public MC are given in Figures 4.7-4.9, where public MC are normalized to the size of data. Note that we always cut on ΔE before plotting M_{BC}, and vice-versa.

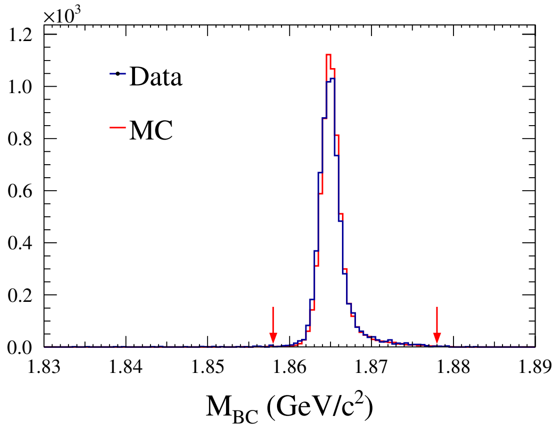

(a) $M_{\rm BC}$

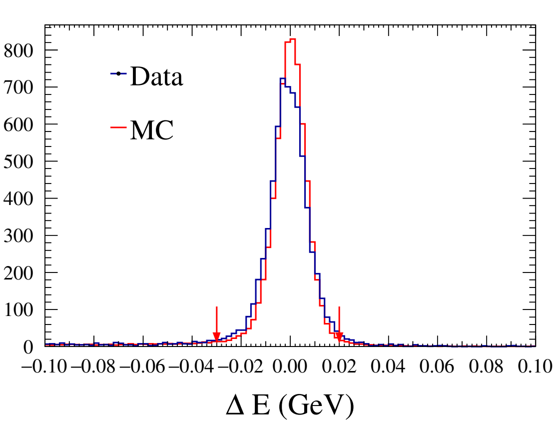

(b) ΔE

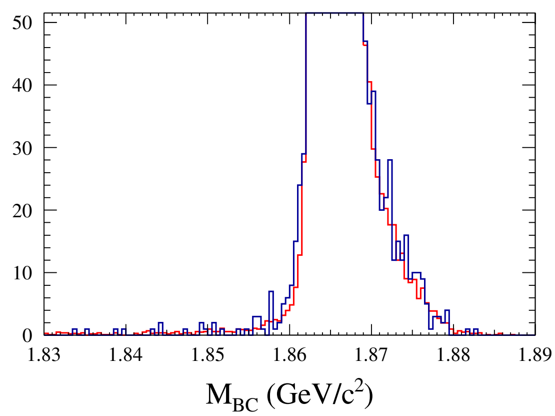

(c) $M_{\rm BC}$

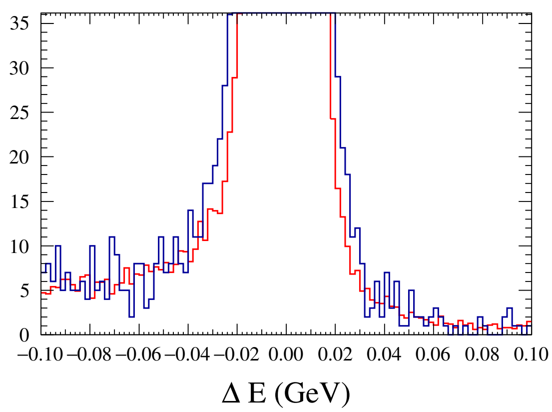

(d) ΔE

Figure 4.7: $M_{\rm BC}$ and ΔE on the tag side. Plots (c) and (d) are the same as (a) and (b), but with a zoomed-in vertical scale.

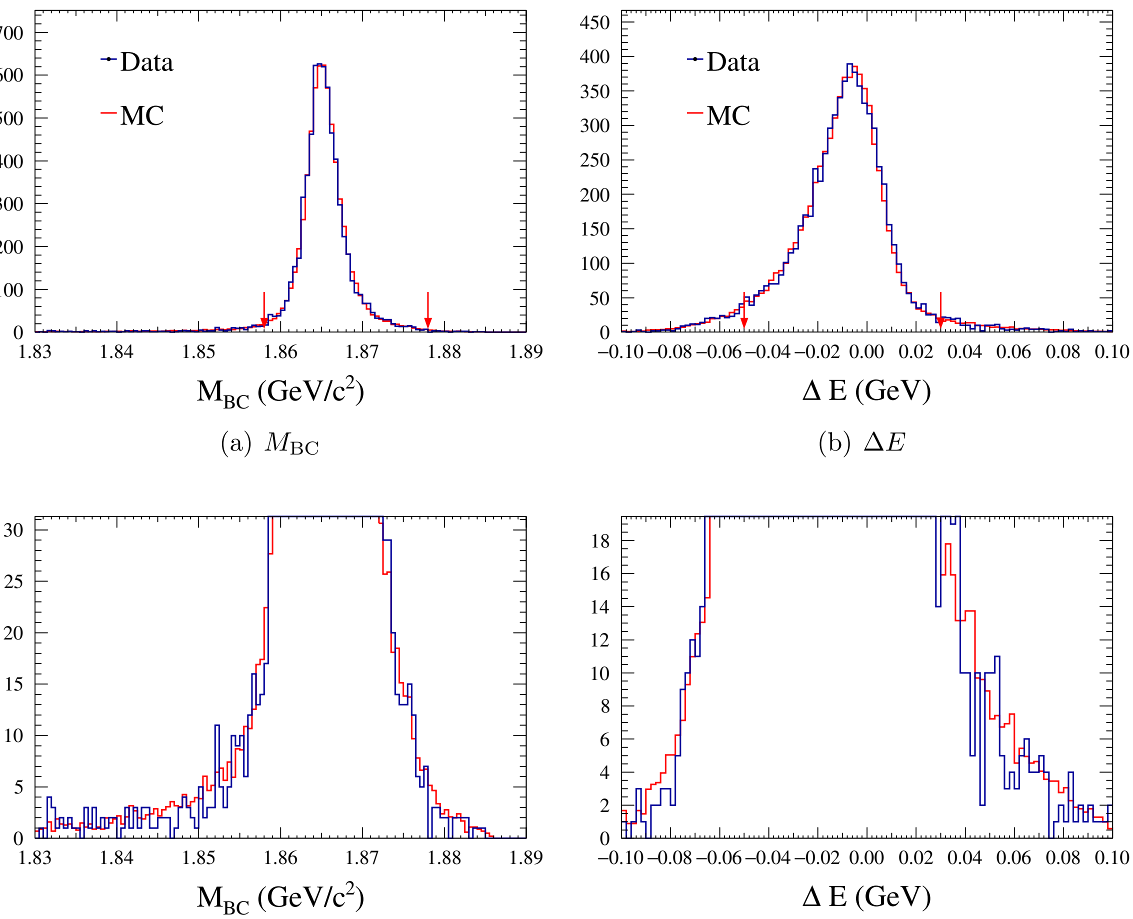

(a) $M_{\rm BC}$

(b) ΔE

(c) $M_{\rm BC}$

(d) ΔE

Figure 4.8: $M_{\rm BC}$ and ΔE on the signal side with wide cuts. Plots (c) and (d) are the same as (a) and (b), but with a zoomed-in vertical scale.

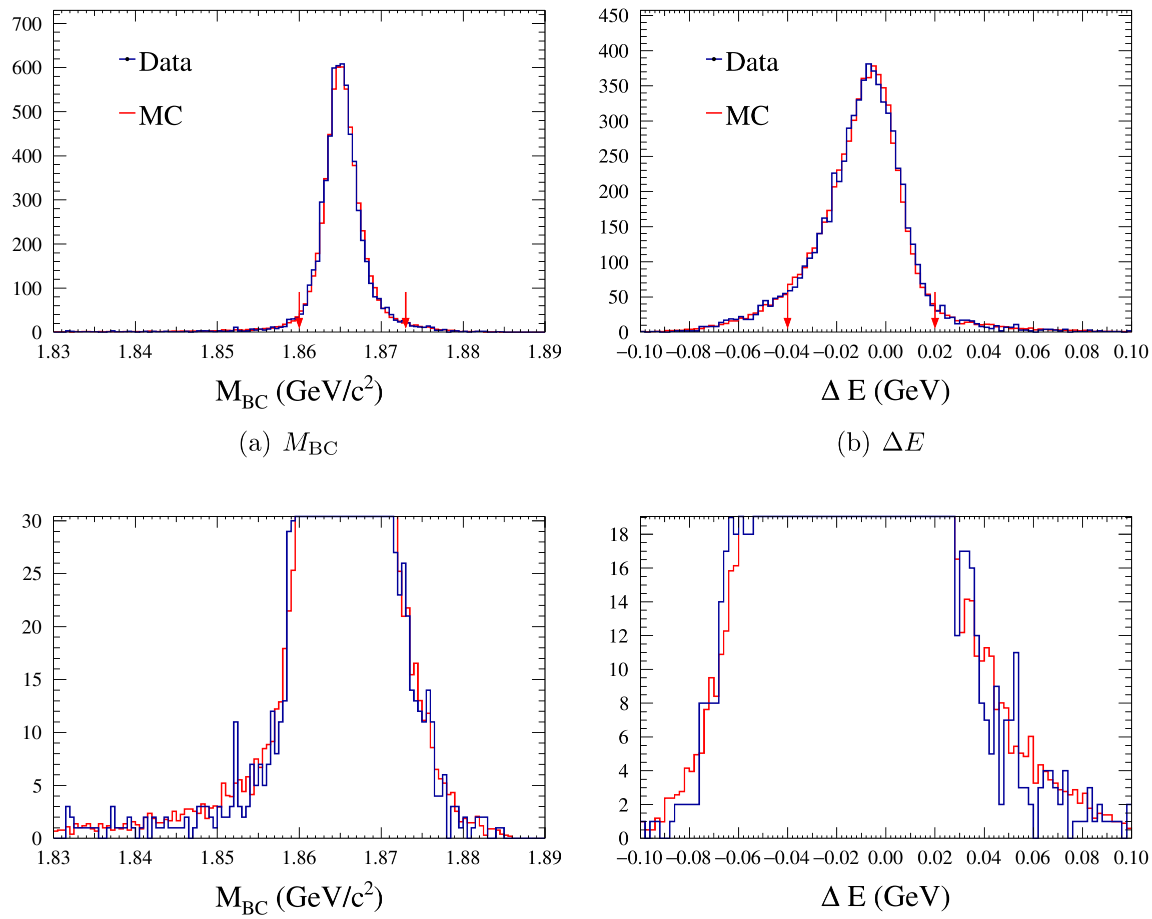

(a) M_{BC}

(b) ΔE

(c) M_{BC}

(d) ΔE

Figure 4.9: M_{BC} and ΔE on the signal side with tight cuts. Plots (c) and (d) are the same as (a) and (b), but with a zoomed-in vertical scale.

4.5.1 PWA Background Study

The background of the DT candidates should be suppressed as much as possible for the PWA analysis. However, strict requirements will sacrifice statistics. The purpose of this section is to study the background of the double tag candidates with different requirements.

Public MC is used to estimate the background of the DT candidates. With the advantage of truth tag, we split background into the peaking background ($K^- K_S \pi^0$ vs. $K^+ \pi^-$) and other background. As shown in Tables 4.4-4.7, the K_S mass veto, $0.458 < M_{\pi^0\pi^0} < 0.520$ GeV, can suppress the peaking background from more than 2.2% to 0.1%. Also, the tight $M_{\rm BC}$, ΔE cuts reduce the total background to 1.0% vs. the wide cut leaving a 1.7% background. The tight cut with the K_S mass veto will be used in the PWA fitting. The remaining 1.0% background will be treated as a source of systematic uncertainty. More details are discussed in Section 8.1.

Table 4.4: Tight cut without K_S mass veto.

	event	**ratio**
$K^-\pi^+\pi^0\pi^0$ vs. $K^+\pi^-$	66050	100%
$K^-K_S\pi^+$ vs. $K^+\pi^-$	1452	2.20%
other background	788	1.19%
Total background	2240	3.39%

Table 4.5: Tight cut with K_S mass veto.

	event	**ratio**
$K^-\pi^+\pi^0\pi^0$ vs. $K^+\pi^-$	57653	100%
$K^-K_S\pi^+$ vs. $K^+\pi^-$	45	0.07%
other background	690	1.04%
Total background	735	1.11 %

Table 4.6: Wide cut without K_S mass veto.

	event	**ratio**
$K^-\pi^+\pi^0\pi^0$ vs. $K^+\pi^-$	72248	100%
$K^-K_S\pi^+$ vs. $K^+\pi^-$	1587	2.20 %
other background	1252	1.73%
Total background	2839	3.93%

Table 4.7: Wide cut with K_S mass veto.

	event	**ratio**
$K^-\pi^+\pi^0\pi^0$ vs. $K^+\pi^-$	63131	100%
$K^-K_S\pi^+$ vs. $K^+\pi^-$	66	0.10%
other background	1101	1.74%
Total background	1167	1.85 %

Chapter 5

PWA Algorithm and Results

5.1 The Optimal Set Algorithm

We consider all possible decay channels with angular structures having $l \leq 2$. Besides intermediate resonances, we also consider non-trivial angular structures without resonances, e.g. $K^{*-}(\pi^+\pi^0)_V$ and $(K^-\pi^0)_V\rho^+$. Note that we use these non-trivial angular structures (which have no B-W peak in mass) only when there is a corresponding mass resonance. For example, $(K^-\pi^0)_V\rho^+$ is used since we also consider $K^{*-}\rho^+$ Thus, there are more than 60 possible amplitude modes, but not all of them will be significant. One method to approach the optimal set of amplitude modes is starting with all possible amplitude modes and then dropping the non-significant ones. However, this method is not practical. The computing resources required for more than 60 amplitude modes are prohibitive. Also, it is difficult to set up reasonable starting values in order to make the PWA fitting converge. Considering those constraints, we design an algorithm where we start with a smaller set, called the starting set, and then use a mechanism to approach an optimal set of amplitude modes.

Our starting set includes all the resonance amplitude modes without non-resonant angular structure except S or S-wave plus the "phase-space" amplitude modes. Since we consider the $K\pi$ S-wave effect (see Section 3.6), modes that would naively correspond to phase-space, $(K^-\pi^+)_S(\pi^0\pi^0)_S$ or $(K^-\pi^0)_S(\pi^+\pi^0)_S$, are not present. Thus, there are two modes similar to phase-space, $(K^-\pi^+)_{S\text{-wave}}(\pi^0\pi^0)_S$ and $(K^-\pi^0)_{S\text{-wave}}(\pi^+\pi^0)_S$. We later check that the $K\pi$ S-wave formfactor gives a better fit than phase-space (see Section 5.5). Our mechanism to approach the optimal set includes two phases and each phase includes three steps. The first phase is called "adding modes". We calculate the significance of every amplitude mode which does not exist in the current amplitude set in parallel. The second step is adding the most significant one (if larger than 4σ) to the current amplitude set. The third step is repeating step one and step two until the most significant amplitude mode has significance less than 4σ. The second phase is called "dropping modes". The first step is calculating the significance of every amplitude existing mode in parallel. The second step is dropping the least significant one from the current amplitude set. The third step is repeating step one and step two until the least significant amplitude mode has significance bigger than 4σ.

Our algorithm begins with the starting set and repeats both "adding modes" and then "dropping modes" until all amplitude modes included have significance larger than 4σ and all amplitude modes not included have significance less than 4σ. For this analysis, several add-drop cycles are required, but only the first three cycles involve adding and dropping more than two modes.

5.1.1 Special Cases

Ambiguity may happen when the PDFs of two modes in the amplitude set are too similar to each other. The off-diagonal elements of the correlation matrix will be close to unity, which indicates the strong correlation between those two amplitude modes.

We arbitrarily choose one mode to keep and discard the other (see Table 5.1), and try to keep consistency by choosing similar modes with similar structures. For example, the PDF of $(K^{*-}\pi^0)_V\pi^+$ is very similar with that of $(K^{*-}\pi^+)_V\pi^0$ due to the small mass difference of charged and neutral π. We arbitrarily keep the latter one and discard the other. The effects of alternate choices are discussed in Section 5.6.

Table 5.1: Ambiguous amplitudes

mode kept	**mode discarded**
$K^{*0}(\pi^0\pi^0)_S$	$(K^{*0}\pi^0)_P\pi^0$
$K^{*-}(\pi^+\pi^0)_S$	$(K^{*-}\pi^+)_P\pi^0$
$(K^-\pi^0)_{S\text{-wave}}\rho^+$	$(K^-\rho^+)_P\pi^0$
$(K^{*-}\pi^+)_V\pi^0$	$(K^{*-}\pi^0)_V\pi^+$
$(K^-\rho^+)_V\pi^0$	$K^-(\rho^+\pi^0)_V$

5.2 Nominal Fit and Result

We perform an unbinned likelihood fit using the likelihood described in Section 3.1, where only the complex a_i are floating. With the algorithm described in Sections 5.1 and 5.1.1, there are 26 amplitudes chosen as the optimal set, listed in Table 5.2. The statistical and systematic uncertainties are discussed in Sections 3.5 and 8.1, respectively. Other tested amplitudes are listed in Table J.1. Table 5.2 gives fit fractions, which are more meaningful than amplitudes, since they are free from normalization issues. For completeness, the values of the amplitudes are listed in Table K.1. The amplitude $D \to K^-a_1(1260)^+$, $a_1(1260)^+[S] \to \rho^+\pi^0$ is expected to have the largest fitting fraction. Thus, we chose this amplitude as the reference phase in the PWA fitting. Other important amplitudes are $D \to (K^-\pi^0)_S\rho^+$, $D \to K^-a_1(1260)^+$ with $a_1(1260)^+[S] \to \rho^+\pi^0$, and $D \to K^-a_1(1260)^+$ with $a_1(1260)^+[S] \to \rho^+\pi^0$. Fit projections are shown in Figure 5.1. There are clear $K^*(892)^0$ and $K^*(892)^-$ resonances around 0.796 GeV^2/c^4 in the $M^2_{K^-\pi^+}$ and $M^2_{K^-\pi^0}$ projections, respectively, and a $\rho^+(770)$ resonance around 0.593 GeV^2/c^4 in the $M^2_{\pi^+\pi^0}$ projection. The gap in the $M^2_{\pi^0\pi^0}$ projection is due to the K_S mass veto. In order to check fit quality, we also make several 2D "χ" plots, shown in Figure 5.2. The χ is defined by $(N_{\mathrm{bin}} - N_{\mathrm{res}})/\sqrt{N_{\mathrm{bin}}}$, where N_{bin} is the number of events in each bin and N_{res} is the fitting result. A more detailed goodness-of-fit study is presented in Section 5.4. The generator-level comparison of the public MC and the PWA signal MC overlays are shown in Figure 5.3. One sees that the PWA result makes an great improvement on the public MC. The PWA result, correspondingly, improves the accuracy of DT efficiency (needed to determine the branching fraction), which is discussed in more detail in Section 7.3.

Table 5.2: Amplitude modes included. Note: fit fractions are always positive. The meaning of statistic uncertainties are discussed in Section 3.5

#	**Amplitude mode**	**FF**(%)	**Phase** (ϕ)
	$D \to SS$		
1	$D \to (K^-\pi^+)_{S\text{-wave}}(\pi^0\pi^0)_S$	$6.92 \pm 1.44 \pm 2.86$	$-0.75 \pm 0.15 \pm 0.47$
2	$D \to (K^-\pi^0)_{S\text{-wave}}(\pi^+\pi^0)_S$	$4.18 \pm 1.02 \pm 1.77$	$-2.90 \pm 0.19 \pm 0.47$
	$D \to AP, A \to VP$		
8S	$D \to K^-a_1(1260)^+, \rho^+\pi^0[S]$	$28.36 \pm 2.50 \pm 3.53$	0 (fixed)
8D	$D \to K^-a_1(1260)^+, \rho^+\pi^0[D]$	$0.68 \pm 0.29 \pm 0.30$	$-2.05 \pm 0.17 \pm 0.25$
9S	$D \to K_1(1270)^-\pi^+, K^{*-}\pi^0[S]$	$0.15 \pm 0.09 \pm 0.18$	$1.84 \pm 0.34 \pm 0.43$
11S	$D \to K_1(1270)^0\pi^0, K^{*0}\pi^0[S]$	$0.39 \pm 0.18 \pm 0.30$	$-1.55 \pm 0.20 \pm 0.26$
11D	$D \to K_1(1270)^0\pi^0, K^{*0}\pi^0[D]$	$0.11 \pm 0.11 \pm 0.13$	$-1.35 \pm 0.43 \pm 0.48$
12S	$D \to K_1(1270)^0\pi^0, K^-\rho^+[S]$	$2.71 \pm 0.38 \pm 0.29$	$-2.07 \pm 0.09 \pm 0.20$
14S	$D \to (K^{*-}\pi^0)_A\pi^+, K^{*-}\pi^0[S]$	$1.85 \pm 0.62 \pm 1.11$	$1.93 \pm 0.10 \pm 0.15$
16S	$D \to (K^{*0}\pi^0)_A\pi^0, K^{*0}\pi^0[S]$	$3.13 \pm 0.45 \pm 0.58$	$0.44 \pm 0.12 \pm 0.21$
16D	$D \to (K^{*0}\pi^0)_A\pi^0, K^{*0}\pi^0[D]$	$0.46 \pm 0.17 \pm 0.29$	$-1.84 \pm 0.26 \pm 0.42$
17D	$D \to (\rho^+K^-)_A\pi^0, K^-\rho^+[D]$	$0.75 \pm 0.40 \pm 0.60$	$0.64 \pm 0.36 \pm 0.53$
	$D \to AP, A \to SP$		
21	$D \to ((K^-\pi^+)_{S\text{-wave}}\pi^0)_A\pi^0$	$1.99 \pm 1.08 \pm 1.55$	$-0.02 \pm 0.25 \pm 0.53$
	$D \to VS$		
26	$D \to (K^-\pi^0)_{S\text{-wave}}\rho^+$	$14.63 \pm 1.70 \pm 2.41$	$-2.39 \pm 0.11 \pm 0.35$
27	$D \to K^{*-}(\pi^+\pi^0)_S$	$0.80 \pm 0.38 \pm 0.26$	$1.59 \pm 0.19 \pm 0.24$
28	$D \to K^{*0}(\pi^0\pi^0)_S$	$0.12 \pm 0.27 \pm 0.27$	$1.45 \pm 0.48 \pm 0.51$
	$D \to VP, V \to VP$		
33	$D \to (K^{*-}\pi^+)_V\pi^0$	$2.25 \pm 0.43 \pm 0.45$	$0.52 \pm 0.12 \pm 0.17$
	$D \to VV$		
38S	$D[S] \to K^{*-}\rho^+$	$5.15 \pm 0.75 \pm 1.28$	$1.24 \pm 0.11 \pm 0.23$
38P	$D[P] \to K^{*-}\rho^+$	$3.25 \pm 0.55 \pm 0.41$	$-2.89 \pm 0.10 \pm 0.18$
38D	$D[D] \to K^{*-}\rho^+$	$10.90 \pm 1.53 \pm 2.36$	$2.41 \pm 0.08 \pm 0.16$
39P	$D[P] \to (K^-\pi^0)_V\rho^+$	$0.36 \pm 0.19 \pm 0.27$	$-0.94 \pm 0.19 \pm 0.28$
39D	$D[D] \to (K^-\pi^0)_V\rho^+$	$2.13 \pm 0.56 \pm 0.92$	$-1.93 \pm 0.22 \pm 0.25$
40D	$D[D] \to K^{*-}(\pi^+\pi^0)_V$	$1.66 \pm 0.52 \pm 0.61$	$-1.17 \pm 0.20 \pm 0.39$
43S	$D[S] \to (K^-\pi^0)_V(\pi^+\pi^0)_V$	$5.17 \pm 1.91 \pm 1.82$	$-1.74 \pm 0.20 \pm 0.31$
	$D \to TS$		
46	$D \to (K^-\pi^+)_{S\text{-wave}}(\pi^0\pi^0)_T$	$0.30 \pm 0.21 \pm 0.32$	$-2.93 \pm 0.31 \pm 0.82$
47	$D \to (K^-\pi^0)_{S\text{-wave}}(\pi^+\pi^0)_T$	$0.14 \pm 0.12 \pm 0.10$	$2.23 \pm 0.38 \pm 0.65$

Table 5.3: The significance checks for amplitude modes

#	**Amplitude mode**	**Significance**(σ)
	$D \to SS$	
1	$D \to (K^-\pi^+)_{S\text{-wave}}(\pi^0\pi^0)_S$	> 10
2	$D \to (K^-\pi^0)_{S\text{-wave}}(\pi^+\pi^0)_S$	5.99
	$D \to AP, A \to VP$	
8S	$D \to K^-a_1(1260)^+, \rho^+\pi^0[S]$	> 10
8D	$D \to K^-a_1(1260)^+, \rho^+\pi^0[D]$	6.12
9S	$D \to K_1(1270)^-\pi^+, K^{*-}\pi^0[S]$	4.92
11S	$D \to K_1(1270)^0\pi^0, K^{*0}\pi^0[S]$	4.81
11D	$D \to K_1(1270)^0\pi^0, K^{*0}\pi^0[D]$	4.01
12S	$D \to K_1(1270)^0\pi^0, K^-\rho^+[S]$	> 10
14S	$D \to (K^{*-}\pi^0)_A\pi^+, K^{*-}\pi^0[S]$	7.83
16S	$D \to (K^{*0}\pi^0)_A\pi^0, K^{*0}\pi^0[S]$	> 10
16D	$D \to (K^{*0}\pi^0)_A\pi^0, K^{*0}\pi^0[D]$	5.86
17D	$D \to (\rho^+K^-)_A\pi^0, K^-\rho^+[D]$	5.14
	$D \to AP, A \to SP$	
21	$D \to ((K^-\pi^+)_{S\text{-wave}}\pi^0)_A\pi^0$	6.95
	$D \to VS$	
26	$D \to (K^-\pi^0)_{S\text{-wave}}\rho^+$	> 10
27	$D \to K^{*-}(\pi^+\pi^0)_S$	4.12
28	$D \to K^{*0}(\pi^0\pi^0)_S$	4.13
	$D \to VP, V \to VP$	
33	$D \to (K^{*-}\pi^+)_V\pi^0$	> 10
	$D \to VV$	
38S	$D[S] \to K^{*-}\rho^+$	> 10
38P	$D[P] \to K^{*-}\rho^+$	> 10
38D	$D[D] \to K^{*-}\rho^+$	> 10
39P	$D[P] \to (K^-\pi^0)_V\rho^+$	5.67
39D	$D[D] \to (K^-\pi^0)_V\rho^+$	> 10
40D	$D[D] \to K^{*-}(\pi^+\pi^0)_V$	7.55
43S	$D[S] \to (K^-\pi^0)_V(\pi^+\pi^0)_V$	7.63
	$D \to TS$	
46	$D \to (K^-\pi^+)_{S\text{-wave}}(\pi^0\pi^0)_T$	5.76
47	$D \to (K^-\pi^0)_{S\text{-wave}}(\pi^+\pi^0)_T$	4.02

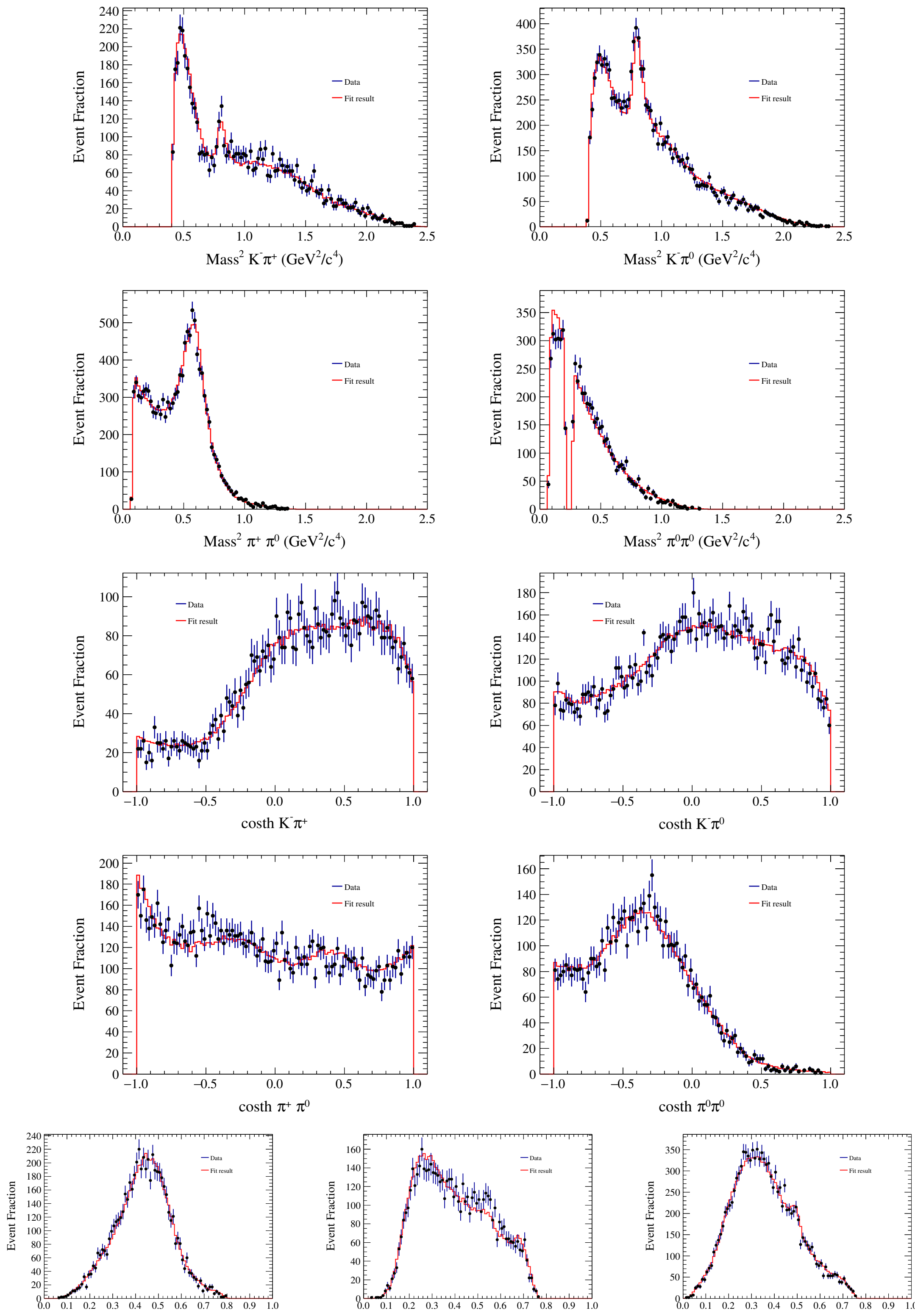

Figure 5.1: Projections of the result of the PWA fitting.

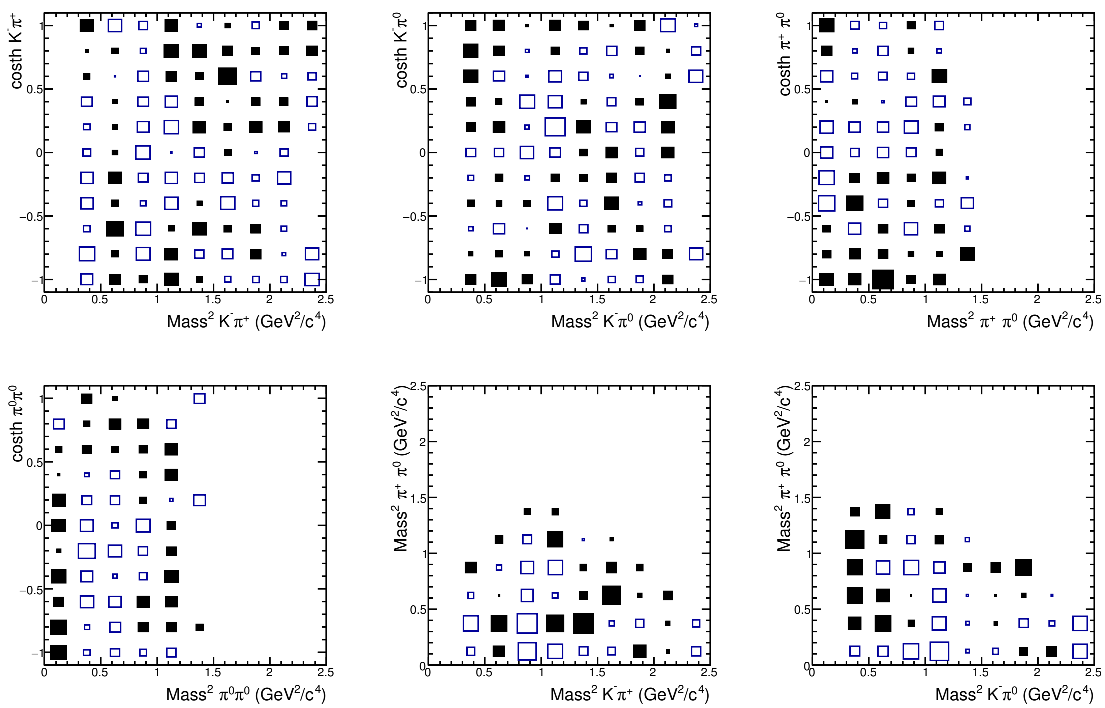

Figure 5.2: Two-dimensional projections of the result of the PWA fitting. The χ is proportional to the area of the box. Black boxes indicate positive, white ones indicate negative. Box scale is same for all projections and the largest box has $\chi = 4.57$.

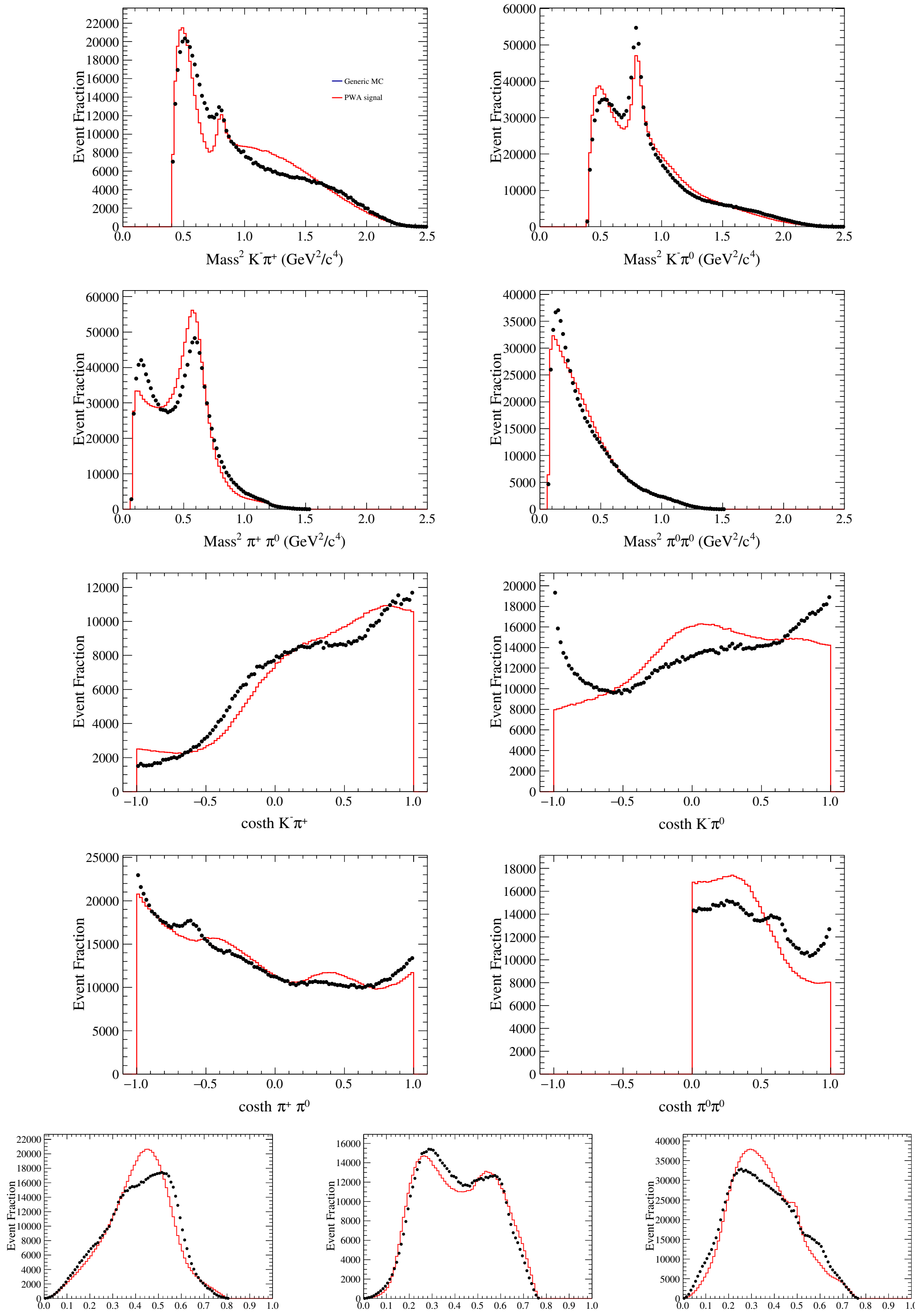

Figure 5.3: Generator-level overlays of the public MC and PWA result.

5.3 Discussion of Structures in Detection Efficiency Plots

Curves for the signal reconstruction efficiency vs. several kinematic variable are shown in Fig. 5.4. Note that in order to avoid doing dozens of complicated 2-D fits, these efficiencies are determined with "cut and count" yields of either pure PWA signal MC or truth-tagged public MC, with M_{BC} cuts added. The main effect of this simplification is a small global reduction in efficiency values due to the M_{BC} cuts cutting off tails of peaks. However, the relative efficiency *shapes* vs. the various kinematic variables (our main interest) should be largely unaffected. Likewise, the relative efficiencies of the two MC samples should be unaltered.

It is instructive to attempt to explain some of the more dramatic effects in these plots. One should keep in mind, however, that these are 1-D projections from a 5-D phase space. There are many correlations among variables induced by phase-space boundaries, intermediate resonances, angular distributions, etc. Nonetheless, many of the basic features are not wholly unexpected.

1) Efficiency decrease at low momentum for p_K, p_π.
These are both due to a tracking efficiency roll-off at low momentum (low p_T, really) due to soft tracks curling in the magnetic field. It is more dramatic for kaons since they lose more energy in the inner detector material (dE/dx).

2) Higher efficiency, then a dip, at low p_{π^0}.
This is due to the interplay of the kinematics of π^0 decay and our minimum cluster energy requirement. In particular, when $p_{\pi^0} = 0$, one gets two 70 MeV photons, which easily pass cluster energy cuts. An increasing boost (momentum) eventually results in soft backward photons that fail the cut. At larger boosts, the range of photon energies continues to increase, such that the fraction of soft photons failing this cut decreases, and the efficiency increases from the dip minimum.

Most of the rest of the effects which we discuss come from kinematic correlations with effects 1) and 2).

3) Effect 1) also leads to the roll-offs at high values of $m^2_{\pi^0\pi^0}$. A large mass leaves decreasing energy for the K^- and π^+, and those soft tracks decrease the efficiency. It is most dramatic here (of the m^2_{12} plots) since there are *two* charged tracks that become soft.

4) For $m^2_{K\pi}$, effect 2) is in play. High $m^2_{K\pi}$ values lead to two soft π^0, and we see the mirror-image of the low-momentum portion of the p_{π^0} plot.

5) Effects 1) and 2) combine for high values of $m^2_{\pi\pi^0}$ and $m^2_{K\pi^0}$. The larger decrease

when the K is not included in the x-axis variable (i.e., $m^2_{\pi\pi^0}$) is due to the tracking efficiency decrease being larger for kaons than for pions. For $m^2_{K\pi^0}$, the decrease for soft π^+ and the increase for soft π^0 end to cancel. (Remember that we are projecting out four other dimensions, with lots of correlation: these are just general trends to be expected!)

6) For $\cos\theta_{K\pi^0}$, $\cos\theta_{K\pi}$, the roll-off at high momentum corresponds to backwards going kaons being soft. (The sign convention is that $\cos\theta_{12} > 0$ is a faster, forward-boosted particle 2 and a slower, backward-boosted particle 1.)

7) For $\cos\theta_{K\pi^0}$, $\cos\theta_{\pi\pi^0}$, we see an increase at small values due to soft backwards-going π^0 (the mirror image of the p_{π^0} plot).

8) Finally, we address the dip near 0.6 GeV/c in the p_π plot. Here, we must appeal to one of the missing dimensions. In Fig. 5.5, we plot the number of generated events as function of both p_π and p_K. Imagine the loss of events with soft kaons: one might approximate the efficiency roll-off as a cut at 0.15 or 0.20 GeV/c or so. We see that there is an enhancement of events with soft kaons and pions near 0.6 Gev/c. Such momentum distributions arise from resonances inducing mass peaks and angular structures. For example, the fit fraction of $D^0 \to K^- a_1^+$ is about 30%. (There is also a dip at lower p_π, but it is a smaller fraction of the total, and there are of course more correlations in the other three independent variables not plotted which can distinguish these regions...)

In summary, most of the striking features can be related to kinematics and basic detector behaviors.

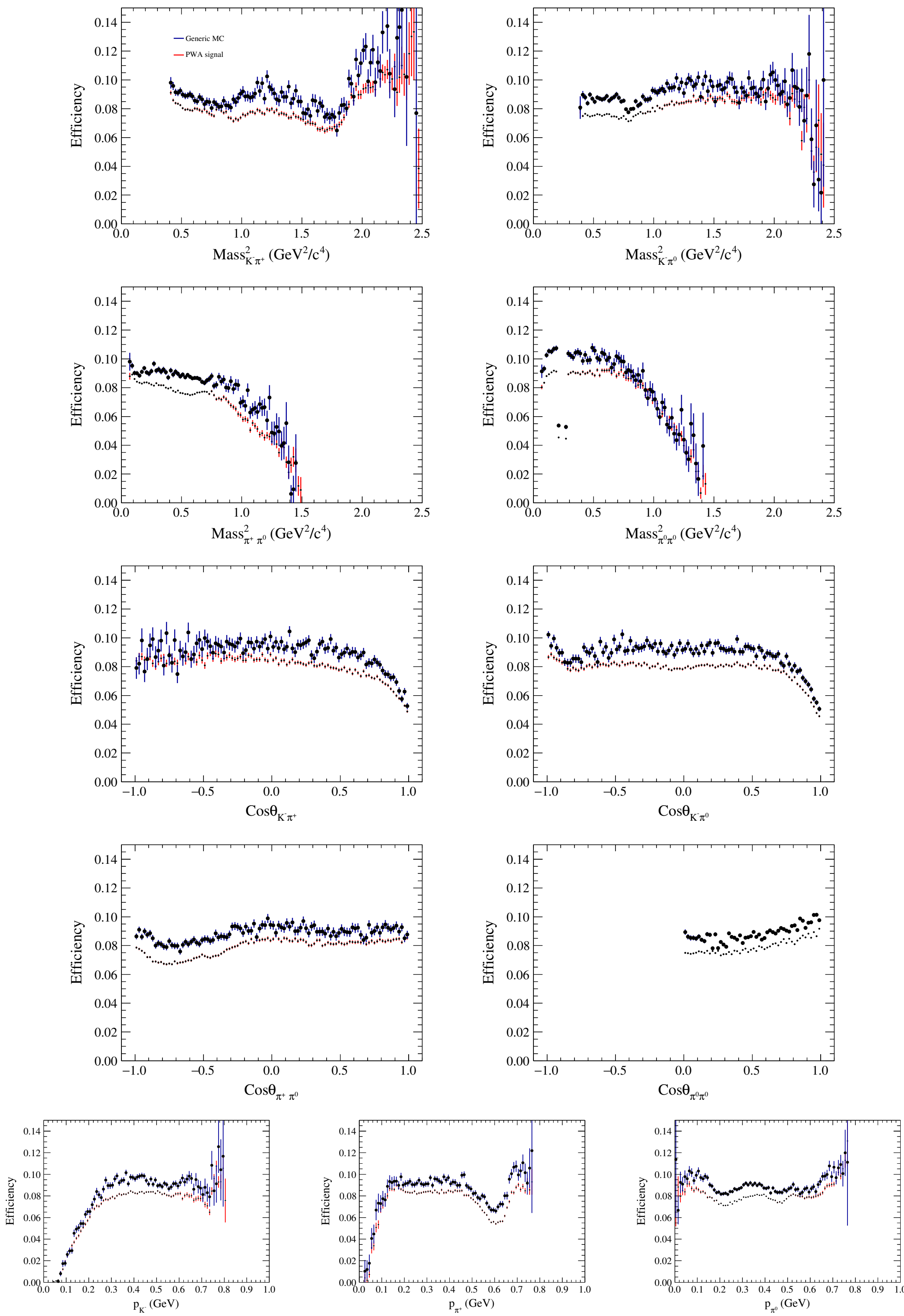

Figure 5.4: Efficiency projection overlays of the PWA signal MC and the generic MC.

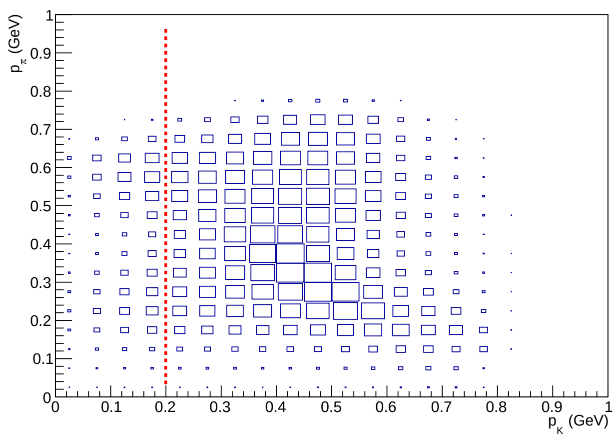

Figure 5.5: The distribution of PWA signal MC on the momentum of K vs. momentum of π plane. The red dashed line indicates where the efficiency starts decreasing toward low K momentum.

5.4 Goodness of Fit

We have programed a "mixed-sample method" for determining the goodness of an unbinned likelihood fit [32]; see Appendix C for more details. According to the method, we can calculate the "T" value of the mixing of two samples, the expectation mean, μ_{T}, and the variance, σ_{T}^2. From T, μ_{T}, and σ_{T}, we can calculate a "pull", $\frac{\mathrm{T}-\mu_{\mathrm{T}}}{\sigma_{\mathrm{T}}}$, and the pull should distribute as a normal Gaussian due to statistical fluctuations. Further, the pull is expected to center at zero if the two samples come from the same parent PDF, and be biased toward larger values otherwise. In the case of this PWA fit, the pull is expected to be a little larger than zero because some amplitudes with small significance are dropped. In other words, adding more amplitudes into the model would be expected to decrease the pull.

To check the goodness-of-fit of our PWA results, we calculate the pull of the T value of the mixing of data sample and the PWA signal MC generated based on our PWA results and it is determined to be 0.97, which is quite acceptable. We also test the mixing of data sample and the public MC. The pull of its T value is determined to be 10.12, which indicates the public MC doesn't agree with data well in terms of the $K^-\pi^+\pi^0\pi^0$ decay structures.

5.5 Significance of $K\pi$ S-wave Effect

As mentioned in Section 3.6, we consider the kinematic modifications associated with $K\pi$ S-wave scattering and use the parameterization from BABAR. In order to check the significance of this $K\pi$ S-wave effect, we switch all $(K\pi)_{S-\mathrm{wave}}$ angular structures to phase-space, $(K\pi)_S$, and then perform the PWA fit again with the optimal set. Note that one of $(K^-\pi^+)_{S\text{-wave}}(\pi^0\pi^0)_S$ and $(K^-\pi^0)_{S\text{-wave}}(\pi^+\pi^0)_S$ must be removed since $(K^-\pi^+)_S(\pi^0\pi^0)_S$ and $(K^-\pi^0)_S(\pi^+\pi^0)_S$ have exactly the same structure. The $-2\log$ likelihood value is 56 larger than that of the nominal result, which demonstrates the significantly superior fit quality when including the $K\pi$ S-wave effect.

5.6 Checks for Special Cases

In Section 5.1.1, we discuss the special cases that five amplitudes are discarded due to strong correlation. After the nominal PWA results are determined, these special cases are tested one by one by switching to the alternate amplitude. The changes in $-2\log$ likelihood are listed in Table 5.4. The amplitude $(K^-\rho^+)_V\pi^0$ is not tested because it is not included in the final amplitude set.

As a summary, we perform the switches on four special cases. One of them decreases the minimum of $-2\log$ likelihood by a small amount, while other three of them increase the minimum of $-2\log$ likelihood slightly. None of the changes are statistical significant.

Table 5.4: Checks for ambiguous amplitudes. The change in $-2\log\text{likelihood}$ is defined as the minimum of $-2\log\text{likelihood}$ of fit with mode discarded minus that of fit with mode kept.

mode kept	**mode discarded**	**changes in** $-2\log\text{likelihood}$
$\bar{K}^{*0}(\pi^0\pi^0)_S$	$(\bar{K}^{*0}\pi^0)_P\pi^0$	$+4.89$
$K^{*-}(\pi^+\pi^0)_S$	$(K^{*-}\pi^+)_P\pi^0$	-5.78
$(K^-\pi^0)_{S\text{-wave}}\rho^+$	$(K^-\rho^+)_P\pi^0$	$+2.31$
$(K^{*-}\pi^+)_V\pi^0$	$(K^{*-}\pi^0)_V\pi^+$	$+0.38$
$(K^-\rho^+)_V\pi^0$	$K^-(\rho^+\pi^0)_V$	N/A

5.7 Conclusion from PWA

In summary, the amplitude fit works well as shown in Figures 5.1 and 5.2. We find that the amplitude $D \to K^-a_1(1260)^+, a_1(1260)^+[S] \to \rho^+\pi^0$ has the largest fitting fraction, 28.36%. We also notice that amplitudes with larger significance tend to contribute larger fitting fractions. All amplitudes which are not included in the optimal set have fitting fractions smaller than 0.2% if we perform the fit with them added to the optimal set. This PWA result will be used in our $K^-\pi^+\pi^0\pi^0$ branching fraction study and specifically contributes a better efficiency determination.

Chapter 6

$K^-\pi^+\pi^0\pi^0$ PHSP MC Size Check

In order to check the quality of our fitter, we fit to a sample of the PWA signal MC with a size roughly equal to the data size. Three different sizes of PHSP samples, 1x, 20x , and 100x of data size, are tested in the phase-space Monte-Carlo integration, Eq. 3.7. Those PHSP samples are used to provide the efficiency information for the likelihood function, the first term of Eq. 3.6. The sizes of those PHSP samples must be large enough to provide stable behaviour, which we investigate here.

The normalized deviations of amplitudes (ρ) and phases (ϕ) are shown in Tables 6.1-6.6. The normalized deviation distributions are shown in Figures 6.1-6.3. According to these distributions, we conclude that the size of PHSP efficiency samples should be about 100x data size, otherwise the statistical errors from the PHSP efficiency samples will contribute to the fitting errors. Note that this study was done with a preliminary 20-amplitude PWA model. However, the conclusions about PHSP MC size should still be valid. The actual 26-amplitude fits use about 121x PHSP MC.

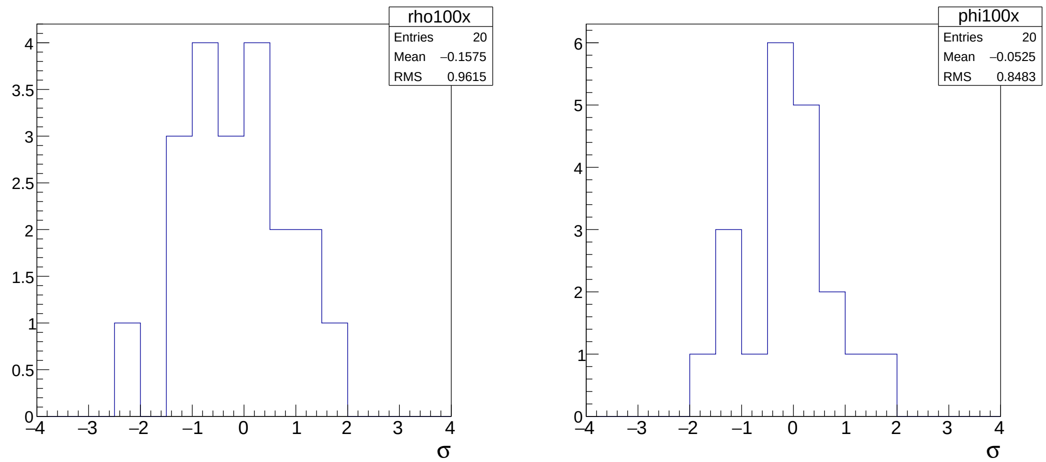

(a) The normalized deviations of ρ

(b) The normalized deviations of ϕ

Figure 6.1: The normalized deviation distributions of the set of all ρ and ϕ values for one sample of 100x phase-space MC

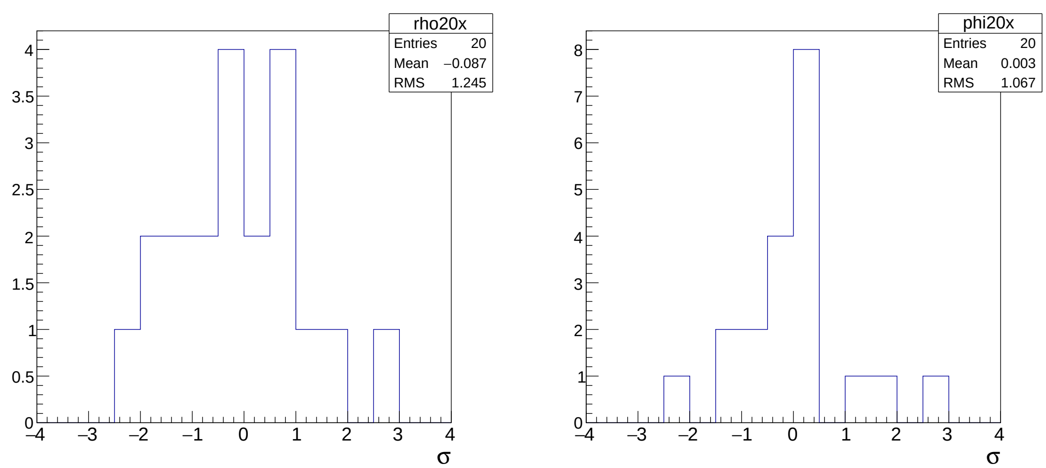

(a) The normalized deviations of ρ

(b) The normalized deviations of ϕ

Figure 6.2: The normalized deviation distributions of the set of all ρ and ϕ values for one sample of 20x phase-space MC

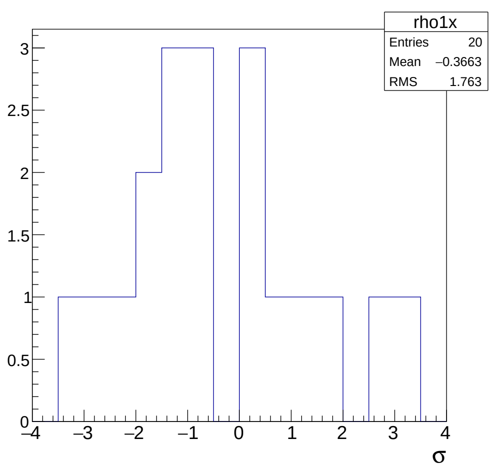

(a) The normalized deviations of ρ

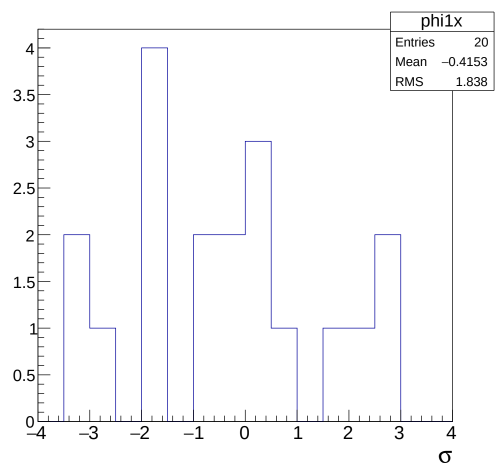

(b) The normalized deviations of ϕ

Figure 6.3: The normalized deviation distributions of the set of all ρ and ϕ values for one sample of 1x phase-space MC

Table 6.1: The normalized deviations of ρ for 100x phase-space MC

Enum	**Expectation**	**Value**	**# of σ**
rho_1	1.42	1.57 ± 0.09	1.66
rho_11S	4.28×10^{-2}	$4.37 \pm 0.60 \times 10^{-2}$	0.16
rho_12S	2.49×10^{-1}	$2.50 \pm 0.21 \times 10^{-1}$	0.56
rho_13S	1.16	0.86 ± 0.14	-2.09
rho_15S	6.37×10^{-1}	$5.73 \pm 0.58 \times 10^{-1}$	-1.12
rho_17D	1.70	1.71 ± 0.15	0.10
rho_21	1.74	2.01 ± 0.19	1.42
rho_26	8.24×10^{-1}	$7.49 \pm 0.65 \times 10^{-1}$	-1.14
rho_27	2.67×10^{-1}	$2.50 \pm 0.33 \times 10^{-1}$	-0.51
rho_28	3.02×10^{-1}	$2.91 \pm 0.22 \times 10^{-1}$	-0.49
rho_33	8.59×10^{-1}	$7.81 \pm 0.84 \times 10^{-1}$	-0.93
rho_38D	2.14×10^{-1}	$2.02 \pm 0.14 \times 10^{-1}$	-0.86
rho_38P	7.81×10^{-2}	$7.58 \pm 0.78 \times 10^{-1}$	-0.30
rho_38S	1.31×10^{-1}	$1.16 \pm 0.12 \times 10^{-1}$	-1.33
rho_39D	1.35	1.38 ± 0.15	0.21
rho_39P	9.29×10^{-1}	$8.84 \pm 0.87 \times 10^{-1}$	-0.52
rho_40D	3.69×10^{-1}	$4.29 \pm 0.47 \times 10^{-1}$	1.27
rho_47	9.03×10^{-1}	$8.43 \pm 1.47 \times 10^{-1}$	-0.41
rho_8D	2.95×10^{-1}	$3.16 \pm 0.62 \times 10^{-1}$	0.33
rho_9S	3.39×10^{-2}	$3.93 \pm 0.67 \times 10^{-2}$	0.80

Table 6.2: The normalized deviations of ϕ for 100x phase-space MC

Enum	**Expectation**	**Value**	**# of σ**
phi_1	-2.37×10^{-1}	$-3.29 \pm 0.79 \times 10^{-1}$	-1.16
phi_11S	-9.55×10^{-1}	$-9.25 \pm 1.39 \times 10^{-1}$	0.21
phi_12S	-1.29	$-1.23 \pm 0.09 \times 10^{-1}$	0.63
phi_13S	2.40	2.23 ± 0.13	-1.27
phi_15S	-1.08	-1.24 ± 0.10	-1.66
phi_17D	2.11	2.06 ± 0.09	-0.51
phi_21	-1.72	-1.77 ± 0.22	-0.23
phi_26	-1.76	-1.79 ± 0.10	-0.25
phi_27	-7.62×10^{-1}	$-5.06 \pm 1.34 \times 10^{-1}$	1.71
phi_28	-1.96	-1.96 ± 0.08	-0.01
phi_33	-2.38	-2.44 ± 0.11	-0.47
phi_38D	-3.44	-3.43 ± 0.08	0.19
phi_38P	6.75×10^{-1}	$6.78 \pm 0.98 \times 10^{-1}$	0.03
phi_38S	1.46	1.46 ± 0.094	-0.01
phi_39D	-7.13×10^{-1}	-8.34 ± 1.06	-1.14
phi_39P	2.50	2.50 ± 0.09	-0.03
phi_40D	-5.77×10^{-1}	$-4.75 \pm 1.93 \times 10^{-1}$	0.53
phi_47	-2.67	-2.63 ± 0.15	0.24
phi_8D	3.95	4.33 ± 0.26	1.46
phi_9S	2.39	2.46 ± 0.16	0.49

Table 6.3: The normalized deviations of ρ for 20x phase-space MC

Enum	**Expectation**	**Value**	**# of σ**
rho_1	1.42	1.22 ± 0.09	-2.14
rho_11S	4.28×10^{-2}	$4.31 \pm 0.59 \times 10^{-2}$	0.06
rho_12S	2.49×10^{-1}	$2.43 \pm 0.21 \times 10^{-1}$	-0.31
rho_13S	1.16	0.87 ± 0.14	-1.99
rho_15S	6.37×10^{-1}	$7.20 \pm 0.56 \times 10^{-1}$	1.48
rho_17D	1.70	1.69 ± 0.14	-0.07
rho_21	1.74	1.86 ± 0.19	0.61
rho_26	8.24×10^{-1}	$7.17 \pm 0.63 \times 10^{-1}$	-1.70
rho_27	2.67×10^{-1}	$2.92 \pm 0.32 \times 10^{-1}$	0.77
rho_28	3.02×10^{-1}	$2.85 \pm 0.22 \times 10^{-1}$	-0.79
rho_33	8.59×10^{-1}	$7.64 \pm 0.81 \times 10^{-1}$	-1.18
rho_38D	2.14×10^{-1}	1.99 ± 0.14	-1.09
rho_38P	7.81×10^{-2}	$7.47 \pm 0.76 \times 10^{-2}$	-0.44
rho_38S	1.31×10^{-1}	$1.51 \pm 0.11 \times 10^{-1}$	1.73
rho_39D	1.35	1.37 ± 0.14	0.16
rho_39P	9.29×10^{-1}	8.58 ± 0.84	-0.85
rho_40D	3.69×10^{-1}	$5.01 \pm 0.46 \times 10^{-1}$	2.87
rho_47	9.03×10^{-1}	$8.64 \pm 1.45 \times 10^{-1}$	-0.27
rho_8D	2.95×10^{-1}	$3.37 \pm 0.63 \times 10^{-1}$	0.66
rho_9S	3.39×10^{-2}	$3.89 \pm 0.66 \times 10^{-1}$	0.75

Table 6.4: The normalized deviations of ϕ for 20x phase-space MC

Enum	**Expectation**	**Value**	**# of σ**
phi_1	-2.37×10^{-1}	$-3.09 \pm 0.79 \times 10^{-1}$	-0.91
phi_11S	-9.55×10^{-1}	$-8.96 \pm 1.41 \times 10^{-1}$	0.42
phi_12S	-1.29	-1.48 ± 0.09	-2.13
phi_13S	2.40	2.25 ± 0.13	-1.19
phi_15S	-1.08	-1.23 ± 0.10	-1.48
phi_17D	2.11	2.08 ± 0.09	-0.33
phi_21	-1.72	-1.80 ± 0.22	-0.40
phi_26	-1.76	-1.49 ± 0.11	2.59
phi_27	-7.62×10^{-1}	$-5.92 \pm 1.36 \times 10^{-1}$	1.25
phi_28	-1.96	-1.96 ± 0.08	0.03
phi_33	-2.38	-2.39 ± 0.12	-0.08
phi_38D	-3.44	-3.43 ± 0.08	0.13
phi_38P	6.75×10^{-1}	$6.98 \pm 0.98 \times 10^{-1}$	0.24
phi_38S	1.46	1.48 ± 0.10	0.26
phi_39D	-7.13×10^{-1}	$-8.09 \pm 1.05 \times 10^{-1}$	-0.91
phi_39P	2.50	2.48 ± 0.09	-0.18
phi_40D	-5.77×10^{-1}	$-4.90 \pm 0.20 \times 10^{-1}$	0.44
phi_47	-2.67	-2.65 ± 0.15	0.17
phi_8D	3.95	4.41 ± 0.24	1.95
phi_9S	2.39	2.42 ± 0.16	0.19

Table 6.5: The normalized deviations of ρ for 1x phase-space MC

Enum	**Expectation**	**Value**	**# of σ**
rho_1	1.42	1.25 ± 0.09	-1.90
rho_11S	4.28×10^{-2}	$4.92 \pm 0.57 \times 10^{-2}$	1.13
rho_12S	2.49×10^{-1}	$2.55 \pm 0.22 \times 10^{-1}$	0.26
rho_13S	1.16	0.81 ± 0.14	-2.56
rho_15S	6.37×10^{-1}	$5.54 \pm 0.56 \times 10^{-1}$	-1.50
rho_17D	1.70	1.74 ± 0.14	0.33
rho_21	1.74	1.05 ± 0.20	-3.47
rho_26	8.24×10^{-1}	$6.88 \pm 0.64 \times 10^{-1}$	-2.14
rho_27	2.67×10^{-1}	$3.28 \pm 0.32 \times 10^{-1}$	1.91
rho_28	3.02×10^{-1}	$2.72 \pm 0.21 \times 10^{-1}$	-1.40
rho_33	8.59×10^{-1}	$8.08 \pm 0.84 \times 10^{-1}$	-0.61
rho_38D	2.14×10^{-1}	1.61 ± 0.13	-4.20
rho_38P	7.81×10^{-2}	$8.86 \pm 0.83 \times 10^{-2}$	1.27
rho_38S	1.31×10^{-1}	$1.11 \pm 0.11 \times 10^{-1}$	-1.86
rho_39D	1.35	1.21 ± 0.13	-1.06
rho_39P	9.29×10^{-1}	$8.56 \pm 0.86 \times 10^{-1}$	-0.85
rho_40D	3.69×10^{-1}	$5.33 \pm 0.47 \times 10^{-1}$	3.46
rho_47	9.03×10^{-1}	$6.88 \pm 1.40 \times 10^{-1}$	-1.54
rho_8D	2.95×10^{-1}	$4.78 \pm 0.65 \times 10^{-1}$	2.84
rho_9S	3.39×10^{-2}	$3.84 \pm 0.62 \times 10^{-1}$	0.73

Table 6.6: The normalized deviations of ϕ for 1x phase-space MC

Enum	**Expectation**	**Value**	**# of σ**
phi_1	-2.37×10^{-1}	$-3.65 \pm 0.77 \times 10^{-1}$	-1.66
phi_11S	-9.55×10^{-1}	$-9.77 \pm 1.59 \times 10^{-1}$	-0.14
phi_12S	-1.29	-0.92 ± 0.09	4.08
phi_13S	2.40	2.18 ± 0.14	-1.55
phi_15S	-1.08	-1.42 ± 0.10	-3.44
phi_17D	2.11	1.93 ± 0.09	-1.97
phi_21	-1.71	-1.84 ± 0.24	-0.54
phi_26	-1.76	-1.48 ± 0.11	2.60
phi_27	-7.62×10^{-1}	$-4.76 \pm 1.53 \times 10^{-1}$	-1.88
phi_28	-1.96	-1.97 ± 0.09	-0.14
phi_33	-2.38	-2.44 ± 0.11	-0.49
phi_38D	-3.44	-3.43 ± 0.08	0.09
phi_38P	6.75×10^{-1}	$6.31 \pm 0.87 \times 10^{-1}$	-0.50
phi_38S	1.46	1.25 ± 0.10	-2.15
phi_39D	-7.13×10^{-1}	-4.03 ± 1.11	2.80
phi_39P	2.50	2.56 ± 0.09	0.73
phi_40D	-5.77×10^{-1}	-1.34 ± 0.22	-3.49
phi_47	-2.67	-2.72 ± 0.18	-0.26
phi_8D	3.95	4.33 ± 0.18	2.11
phi_9S	2.39	2.80 ± 0.21	1.99

Chapter 7

Branching Fraction

7.1 Tagging Technique and Branching Fraction

To extract the absolute branching fraction of $D^0 \to K^-\pi^+\pi^0\pi^0$, we first reconstruct the $\bar{D}^0$ meson through $\bar{D}^0 \to K^+\pi^-$, which is called a single-tag (ST), as mentioned in Section 4.3. Then we fully reconstruct both D^0 and $\bar{D}^0$ through $D^0 \to K^-\pi^+\pi^0\pi^0$ and $\bar{D}^0 \to K^+\pi^-$ as the signal side and the tag side, respectively, which is called a double-tag (DT). The yield of ST is given by

$$N_{\text{tag}}^{\text{ST}} = 2N_{D^0\bar{D}^0}\mathcal{B}_{\text{tag}}\varepsilon_{\text{tag}} \,, \tag{7.1}$$

and the yield of DT is given by

$$N_{\text{tag,sig}}^{\text{DT}} = 2N_{D^0\bar{D}^0}\mathcal{B}_{\text{tag}}\mathcal{B}_{\text{sig}}\varepsilon_{\text{tag,sig}} \,, \tag{7.2}$$

where $N_{D^0\bar{D}^0}$ is the total number of produced $D^0\bar{D}^0$ pairs, $\mathcal{B}_{\text{tag(sig)}}$ is the branching fraction of the tag (signal) side, and the ε are the corresponding efficiencies.

The branching fraction of the signal side is determined by isolating $\mathcal{B}_{\text{sig}}$ such that

$$\mathcal{B}_{\text{sig}} = \frac{N_{\text{tag,sig}}^{\text{DT}}}{N_{\text{tag}}^{\text{ST}}}\frac{\varepsilon_{\text{tag}}}{\varepsilon_{\text{tag,sig}}} \,. \tag{7.3}$$

We note that the efficiency approximately factorizes: $\varepsilon_{\text{tag,sig}} \approx \varepsilon_{\text{tag}}\varepsilon_{\text{sig}}$. In this limit, ε_{tag} cancels. We do not assume this, and use the MC to obtain $\varepsilon_{\text{tag,sig}}$ and ε_{tag}. However, the near perfect cancellation will greatly reduce systematic uncertainties from the tag side efficiency.

7.2 Fitting Model

The ST yield, $N_{\text{tag}}^{\text{ST}}$, is obtained by maximum-likelihood fitting to the M_{BC} vs. M_{BC} distribution for signal and tag. A CrystalBall function, along with a Gaussian, is used to model the signal while an Argus function is used to model the background. The signal shape is

$$f \times \mathrm{CB}(x;\mu,\sigma,\alpha,n) + (1-f) \times \mathrm{Gaussian}(\mu_G,\sigma_G), \tag{7.4}$$

where f is a fraction ranging from 0 to 1, μ_G and σ_G are the mean and the width of the Gaussian function, respectively. The CrystalBall function, CB, is a Gaussian core but transitioning to a power-law tail at certain point, given by

$$\mathrm{CB}(x;\mu,\sigma,\alpha,n) = N \begin{cases} \exp\left(-\frac{(x-\mu)^2}{2\sigma^2}\right), & \text{if } \frac{x-\mu}{\sigma} > \alpha \\ \left(\frac{n}{|\alpha|}\right)^n \exp\left(-\frac{|\alpha|^2}{2}\right)\left(\frac{n}{|\alpha|} - |\alpha| - \frac{x-\mu}{\sigma}\right)^{-n}, & \text{otherwise} \end{cases} \tag{7.5}$$

where N is the normalization and α controls the start of the tail.

The DT yield, $N^{\mathrm{DT}}_{\mathrm{tag,sig}}$, is obtained by maximum-likelihood fitting to the 2-D M_{BC} vs. M_{BC} distribution with a 2-D fitting technique introduced by CLEO [33]. This technique analytically models the signal peak, and considers the initial state radiation and mispartition effects, which are non-factorizable in the 2-D plane. In this fitting, the mass of $\Psi(3770)$ is fixed to be 3.774 GeV and the beam energy (end point of Argus background) is fixed to be 1.8868 GeV. More details can be found in Appendix B.

To avoid local maxima, both ST and DT fitting are performed repeatedly with the initial values of the fit function parameters are randomly generated within reasonable ranges.

7.3 Efficiency and Data Yields

The four-body decay $K^-\pi^+\pi^0\pi^0$ involves many substructures, such as Ka_1, $K_1\pi$, $K^*\rho$, etc. Different substructures have different angular distributions and momentum distributions, which results in different efficiency. Unfortunately, they are not well-measured yet and are simulated in the current public MC only based on educated guesses. Hence, a updated MC sample based on the result of our PWA result, called "replaced MC" is used to determine the efficiency. The replaced MC is the public MC with the $K^-\pi^+\pi^0\pi^0$ vs. $K^+\pi^-$ events replaced by PWA signal MC. Note that the decay $D^0 \to K^-K_S\pi^+$ with $K_S \to \pi^0\pi^0$ is considered as background, so $K^-K_S\pi^+$ is not replaced in the public MC.

All event selection criteria mentioned in Chapter 4 are applied except the M_{BC} cuts. The nominal ΔE cut used here is $-0.03 < \Delta E < 0.02$ GeV on the tag side and $-0.04 < \Delta E < 0.02$ GeV on the signal side. A "wide ΔE" cut is also tested for systematic purposes, used in Section 8.2, which is $-0.04 < \Delta E < 0.03$ GeV on the tag side and $-0.05 < \Delta E < 0.03$ GeV on the signal side.

The DT and ST fits of the replaced MC are shown in Figures 7.1 and 7.2, respectively. The fit plots of data is shown in Figures 7.3 and 7.4. A finer binning, due to the high statistics, is used in the MC fits in order to obtain better fitting performance. As for χ^2, the expected error, i.e. square root of the PDF value in the bin, is used instead of square root of the bin content because the clean DT samples cause many zero bins in the 2-D M_{BC} vs. M_{BC} histograms.

We also include the log scale and the pull plots to show the goodness-of-fit. In the case of DT, Figures 7.1 and 7.3, the log scale plots along with the χ^2 values indicate the good fitting performance. In the case of ST, Figures 7.2 and 7.4, the plots look fine although the χ^2 values are larger than expected.

As a cross check, we calculate ST yields by an alternative method which is very insensitive to the signal shape. We sum the total bin contents across the peak region, $1.855-1.887$ GeV, and then subtract the integral of the background function. For this method, the only "purpose" of the signal function is to provide an adequate enough description of the signal that the background fit is not significantly biased high or low. We obtain a shift in the net signal yields of 871 (118) for MC (data), which is only 0.015% (0.022%) of the yield itself. These fractions are small since the residuals, Figures 7.2(c) and 7.4(c), tend to cancel (some > 0, some < 0). Therefore, we believe the assumption that the signal shape is good enough not to bias background fit is valid, and we have shown that the effect on signal yields is of order 0.02%.

The efficiencies are summarized in Table 7.1, where we also include the efficiencies of the public MC to show the improvement. The data yields are summarized in Table 7.3.

7.4 Results of Branching Fraction

Inserting the values of $N^{\rm DT}_{\rm tag,sig}$, $N^{\rm ST}_{\rm tag}$, $\varepsilon_{\rm tag,sig}$, and $\varepsilon_{\rm tag}$ into Eq. 7.3, We determine the branching fraction of $K^-\pi^+\pi^0\pi^0$, $\mathcal{B}(D^0 \to K^-\pi^+\pi^0\pi^0) = (8.98 \pm 0.13({\rm stat}) \pm 0.40({\rm syst}))\%$. The systematics are discussed in Section 8.2.

Table 7.1: ST and DT efficiency (nominal ΔE cut). The uncertainty of efficiency is calculated by the uncertainty of yield dividing the size generated.

ST Sample	**yield (10^4)**	**size generated**	**ST efficiency(%)**
Public MC	599.20 ± 0.27	9039268	66.29 ± 0.03
Replaced MC	596.71 ± 0.27	9039268	66.01 ± 0.03

DT Sample	**yield (10^3)**	**size generated**	**DT efficiency(%)**
Public MC	62.24 ± 0.27	660749	9.42 ± 0.04
Replaced MC	55.43 ± 0.25	660749	8.39 ± 0.04

Table 7.2: ST and DT efficiency (wide ΔE cut). The uncertainty of efficiency is calculated by the uncertainty of yield dividing the size generated.

ST Sample	**yield** (10^4)	**size generated**	**ST efficiency**(%)
Public MC	605.42 ± 0.30	9039268	66.98 ± 0.03
Replaced MC	602.32 ± 0.30	9039268	66.63 ± 0.03

DT Sample	**yield** (10^3)	**size generated**	**DT efficiency**(%)
Public MC	67.29 ± 0.29	660749	10.18 ± 0.04
Replaced MC	59.84 ± 0.27	660749	9.06 ± 0.04

Table 7.3: ST and DT data yields.

	yield (tight ΔE cut)	**yield (wide ΔE cut)**
$N^{\mathrm{ST}}_{\mathrm{tag}}$	534581 ± 769	544497 ± 866
$N^{\mathrm{DT}}_{\mathrm{tag,sig}}$	6101 ± 83	6691 ± 84

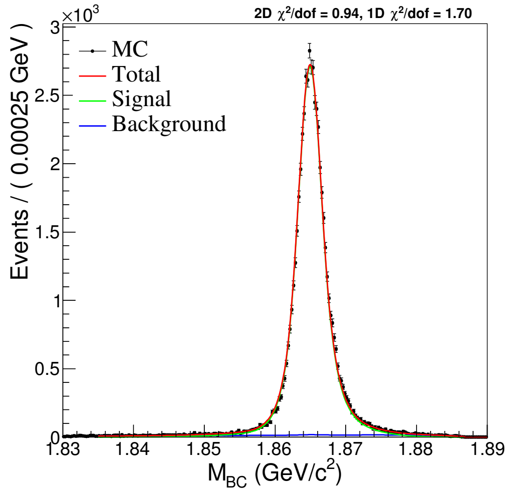

(a) Projection on M_{BC} of $K^-\pi^+\pi^0\pi^0$

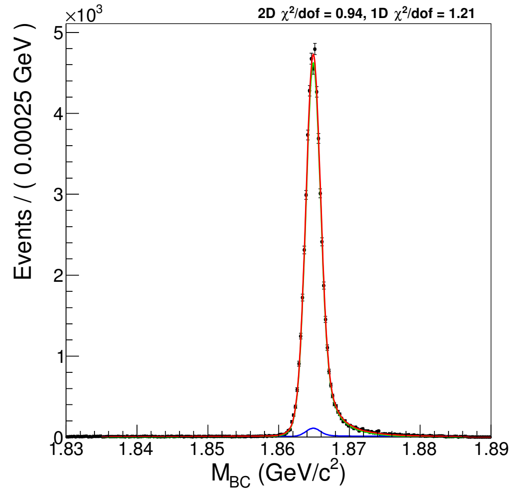

(b) Projection on M_{BC} of $K^+\pi^-$

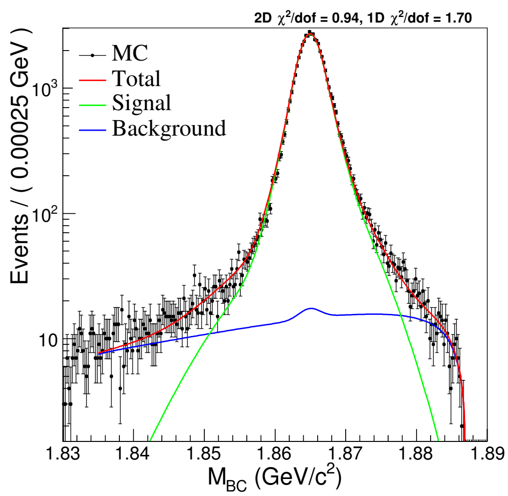

(c) Log scale ($K^-\pi^+\pi^0\pi^0$)

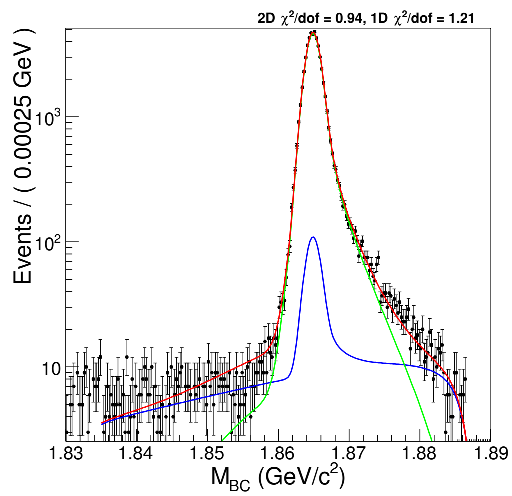

(d) Log scale ($K^+\pi^-$)

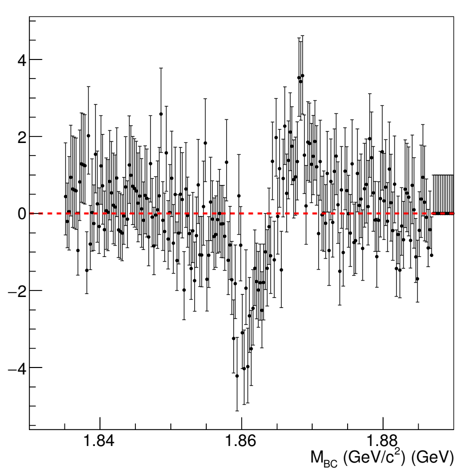

(e) Pull ($K^-\pi^+\pi^0\pi^0$)

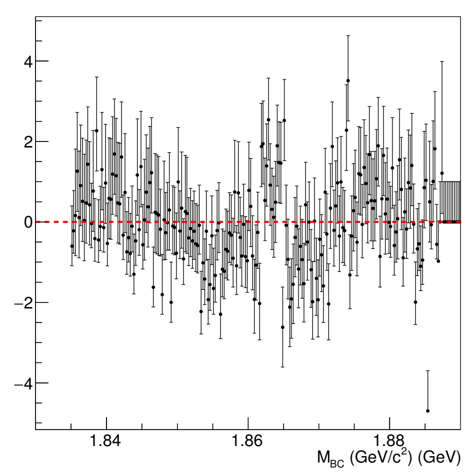

(f) Pull ($K^+\pi^-$)

Figure 7.1: M_{BC} vs. M_{BC} 2-D fit to DT of the replaced MC.

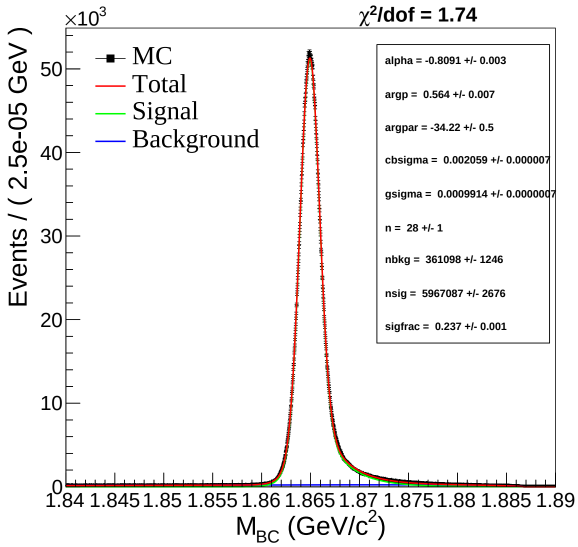

(a) Linear scale

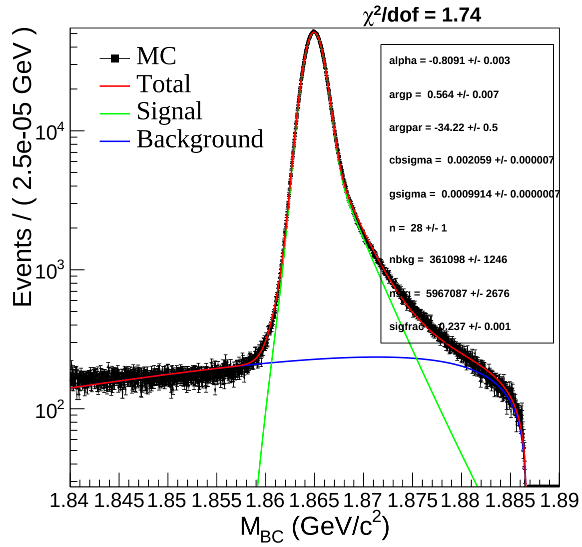

(b) Log scale

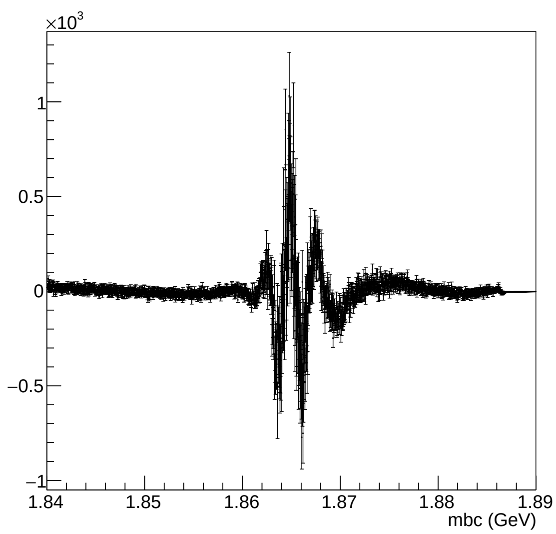

(c) Residual

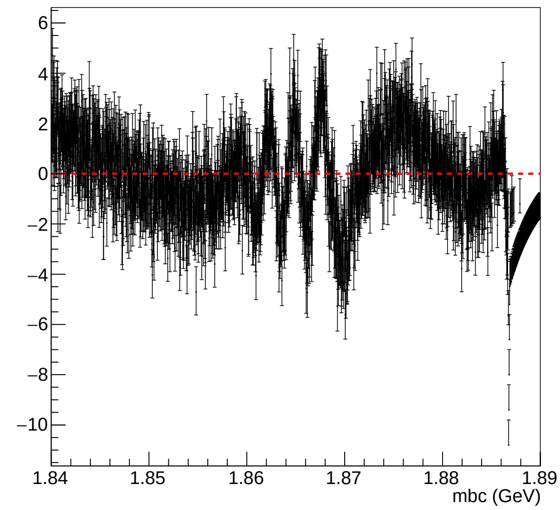

(d) Pull

Figure 7.2: M_{BC} Fit to ST of the replaced MC.

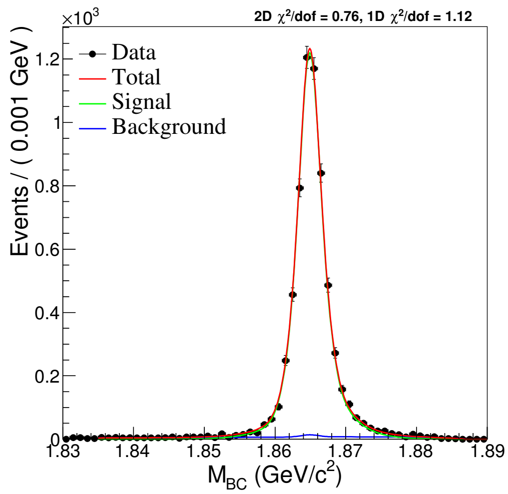

(a) Projection on M_{BC} of $K^-\pi^+\pi^0\pi^0$

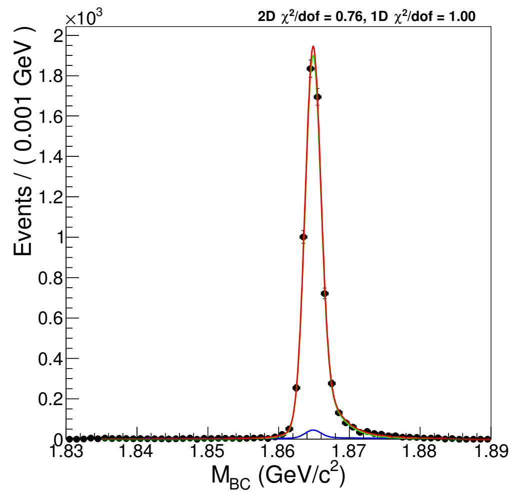

(b) Projection on M_{BC} of $K^+\pi^-$

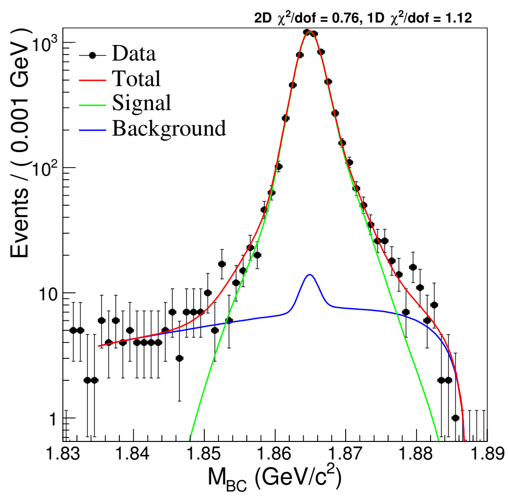

(c) Log scale ($K^-\pi^+\pi^0\pi^0$)

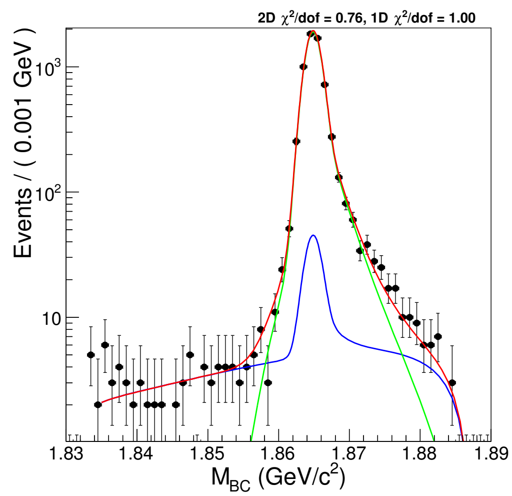

(d) Log scale ($K^+\pi^-$)

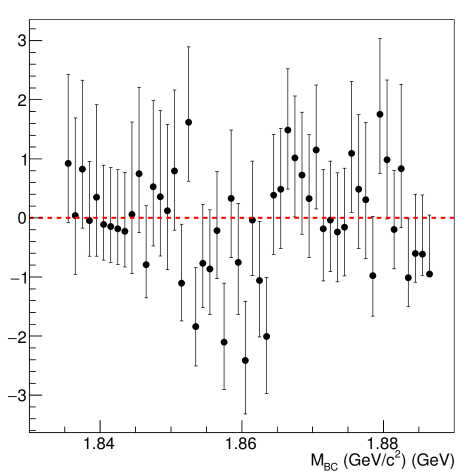

(e) Pull ($K^-\pi^+\pi^0\pi^0$)

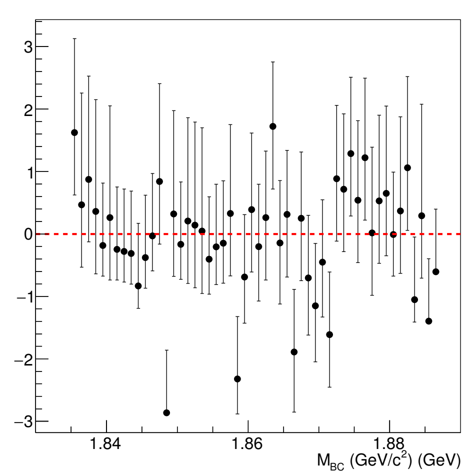

(f) Pull ($K^+\pi^-$)

Figure 7.3: M_{BC} vs. M_{BC} 2-D fit of the data sample.

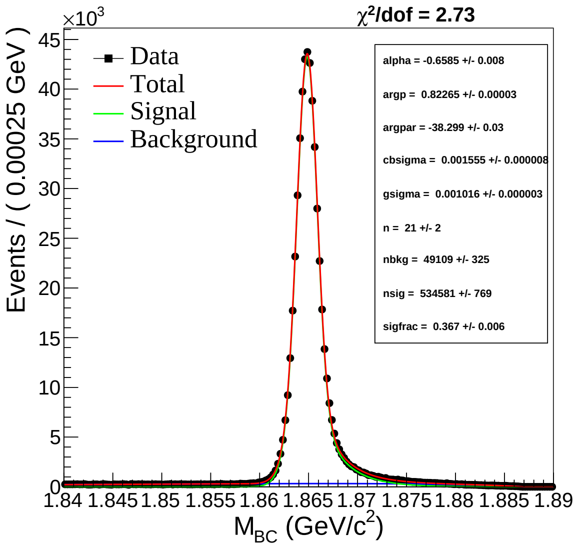

(a) Linear scale

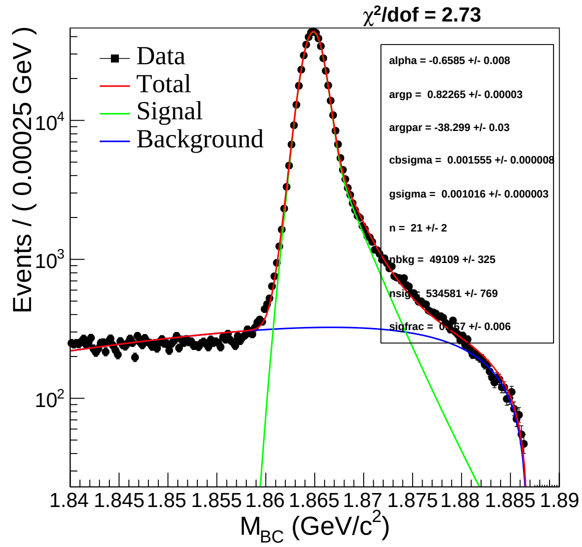

(b) Log scale

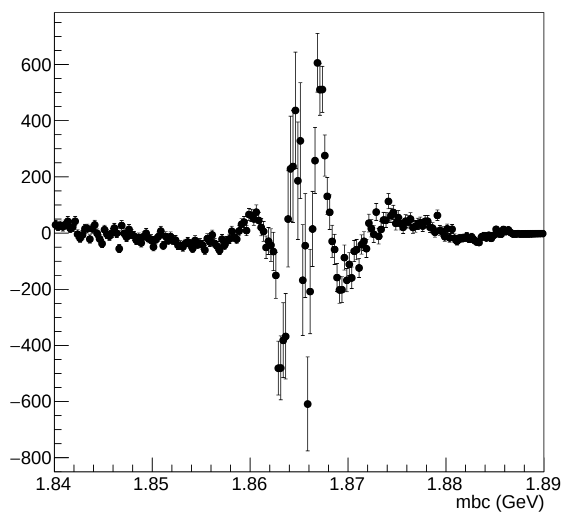

(c) Residual

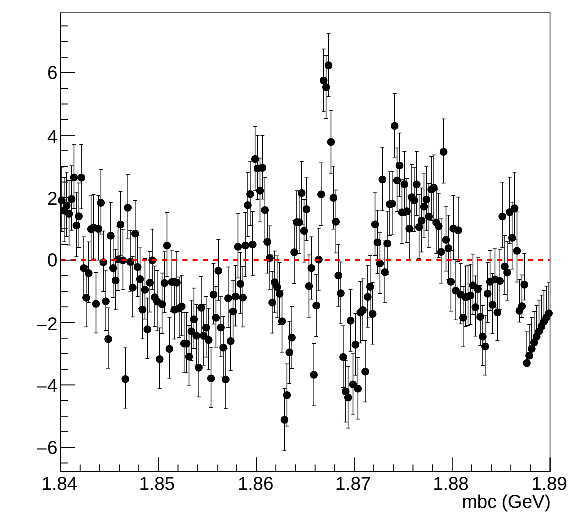

(d) Pull

Figure 7.4: M_{BC} Fit to ST of the data sample.

Chapter 8

Systematic Uncertainties

The systematic uncertainties of PWA and branching fraction measurement are discussed in Sections 8.1 and 8.2, respectively.

8.1 PWA

The systematic uncertainties for our PWA are studied in four categories:

- Amplitude model
- Background
- Experimental effects
- Fitter performance

The systematic uncertainties for fit fractions and phases contributed by different categories are given in Tables 8.1 and 8.2. The uncertainties of these categories are added in quadrature to obtain the total systematic uncertainties.

8.1.1 Amplitude Model

The effects of amplitude model arise from three possible sources: $K\pi$ S-wave model, the effective barrier radius, and the mass and width of intermediate particles. To determine the systematic uncertainties due to $K\pi$ S-wave model, the fixed parameters of the model are varied according to the BABAR measurement uncertainties [17, 29], listed in Table 3.3. The effective barrier radius R is varied from 1.5 to 4.5 GeV^{-1} for intermediate resonances, and 3.0 to 7.0 GeV^{-1} for the D^0. The mass and width of intermediate particles are perturbed according to their published uncertainties in the PDG. The consequent changes of fitting results are considered as the systematic uncertainties inherent in the amplitude model. More specifically, the fit is performed with each parameter separately varied by $+1$ or -1 uncertainty. The uncertainty caused by a given parameter is defined as the larger of the two changes (from the

$\pm 1\sigma$ variations) in the fit result. The summary of these systematic uncertainties are given in Tables L.1 and L.2 of Appendix L and more details are given in Tables L.3−L.10.

8.1.2 Background

The effects of background estimation are separated into non-peaking background, and peaking background. According to the truth information of the MC, there is still 1.04% non-peaking background in the data sample for the PWA fitting. The uncertainties associated with non-peaking background are studied by increasing this background. Thus, we shift the M_{BC} and ΔE cuts on signal side from "the tight cut" to "the wide cut" mentioned in Section 4.5, which increase the non-peaking background from 1.04% to 1.74%. The peaking background can be mostly removed by the $K_S \to \pi^0\pi^0$ veto. However, this veto is also a source of uncertainties. The result of the PWA is determined by the complex structure of data sample in the five-dimension phase space. It is necessary to study how the K_S veto influences the structure while keeping peaking background negligible. This is studied by widening the veto from the nominal $0.458 < M_{\pi^0\pi^0} < 0.520$ GeV/c^2 to $0.418 < M_{\pi^0\pi^0} < 0.542$ GeV/c^2. There is 0.07% peaking background with the nominal veto applied and 0.04% peaking background with the studied veto applied. The details are given in Tables L.11 and L.12 of Appendix L.

8.1.3 Experimental Effects

The experimental effects are related to the acceptance difference between MC and data caused by π^0 reconstruction, tracking, and PID efficiencies, which weight the normalization of the signal PDF. To estimate the uncertainties associated with the experimental effects, the amplitude fit is performed varying π^0 reconstruction, tracking and PID efficiencies according to their uncertainties, as listed in Appendix I. The details of the uncertainties due to π^0 reconstruction, tracking, and PID efficiencies are given in Tables L.13 and L.14 of Appendix L.

8.1.4 Fitter Performance

The fitter performance has been tested with 200 toy MC samples generated based on the PWA model. The distribution of each fit fraction or phase is fitted with a Gaussian function, shown in Appendix M. The difference of the mean and the nominal value is considered as the uncertainty associated with fitter performance.

Table 8.1: FF systematics (in units of statistical standard deviations). (I) Amplitude model, (II) Background, (III) Experimental effects, (IV) Fitter performance.

num	**Amplitude mode**	**I**	**II**	**III**	**IV**	**Total**
	$D \to SS$					
1	$D \to (K^-\pi^+)_S(\pi^0\pi^0)_S$	1.518	1.258	0.072	0.235	1.987
2	$D \to (K^-\pi^0)_S(\pi^+\pi^0)_S$	1.524	0.835	0.078	0.004	1.740
	$D \to AP, A \to VP$					
8S	$D \to K^-a_1(1260)^+, \rho^+\pi^0[S]$	1.293	0.436	0.030	0.363	1.412
8D	$D \to K^-a_1(1260)^+, \rho^+\pi^0[D]$	0.938	0.368	0.024	0.284	1.046
9S	$D \to K_1(1270)^-\pi^+, K^{*-}\pi^0[S]$	1.643	1.175	0.160	0.182	2.035
11S	$D \to K_1(1270)^0\pi^0, K^{*0}\pi^0[S]$	1.562	0.567	0.034	0.036	1.662
11D	$D \to K_1(1270)^0\pi^0, K^{*0}\pi^0[D]$	0.989	0.541	0.035	0.068	1.201
12S	$D \to K_1(1270)^0\pi^0, K^-\rho^+[S]$	0.713	0.221	0.098	0.172	0.772
14S	$D \to (K^{*-}\pi^0)_A\pi^+, K^{*-}\pi^0[S]$	1.253	1.254	0.076	0.237	1.790
16S	$D \to (K^{*0}\pi^0)_A\pi^0, K^{*0}\pi^0[S]$	1.145	0.524	0.022	0.162	1.278
16D	$D \to (K^{*0}\pi^0)_A\pi^0, K^{*0}\pi^0[D]$	0.865	1.468	0.052	0.106	1.708
17D	$D \to (\rho^+K^-)_A\pi^0, K^-\rho^+[D]$	1.249	0.812	0.084	0.186	1.504
	$D \to AP, A \to SP$					
21	$D \to ((K^-\pi^+)_S\pi^0)_A\pi^0$	1.377	0.372	0.102	0.164	1.439
	$D \to VS$					
26	$D \to (K^-\pi^0)_S\rho^+$	1.308	0.252	0.070	0.476	1.416
27	$D \to K^{*-}(\pi^+\pi^0)_S$	0.381	0.549	0.023	0.166	0.689
28	$D \to K^{*0}(\pi^0\pi^0)_S$	0.880	0.417	0.078	0.232	1.005
	$D \to VP, V \to VP$					
33	$D \to (K^{*-}\pi^+)_V\pi^0$	0.688	0.752	0.033	0.273	1.056
	$D \to VV$					
38S	$D[S] \to K^{*-}\rho^+$	0.980	1.354	0.059	0.371	1.713
38P	$D[P] \to K^{*-}\rho^+$	0.425	0.506	0.031	0.348	0.747
38D	$D[D] \to K^{*-}\rho^+$	1.365	0.598	0.049	0.398	1.543
39P	$D[P] \to (K^-\pi^0)_V\rho^+$	0.695	1.223	0.027	0.140	1.414
39D	$D[D] \to (K^-\pi^0)_V\rho^+$	1.335	0.848	0.237	0.401	1.649
40D	$D[D] \to K^{*-}(\pi^+\pi^0)_V$	0.751	0.894	0.049	0.074	1.171
43S	$D[S] \to (K^-\pi^0)_V(\pi^+\pi^0)_V$	0.818	0.443	0.046	0.211	0.955
	$D \to TS$					
46	$D \to (K^-\pi^+)_S(\pi^0\pi^0)_T$	1.171	0.936	0.084	0.273	1.528
47	$D \to (K^-\pi^0)_S(\pi^+\pi^0)_T$	0.803	0.188	0.068	0.018	0.828

Table 8.2: Phase, ϕ, systematics (in units of statistical standard deviations). (I) Amplitude model, (II) Background, (III) Experimental effects, (IV) Fitter performance.

num	**Amplitude mode**	**I**	**II**	**III**	**IV**	**Total**
	$D \to SS$					
1	$D \to (K^-\pi^+)_S(\pi^0\pi^0)_S$	3.137	0.093	0.043	0.030	3.139
2	$D \to (K^-\pi^0)_S(\pi^+\pi^0)_S$	2.330	0.850	0.044	0.109	2.483
	$D \to AP, A \to VP$					
8S	$D \to K^-a_1(1260)^+, \rho^+\pi^0[S]$	0.000	0.000	0.000	0.000	0.000
8D	$D \to K^-a_1(1260)^+, \rho^+\pi^0[D]$	1.194	0.761	0.081	0.479	1.497
9S	$D \to K_1(1270)^-\pi^+, K^{*-}\pi^0[S]$	0.953	0.820	0.054	0.124	1.264
11S	$D \to K_1(1270)^0\pi^0, K^{*0}\pi^0[S]$	1.051	0.556	0.029	0.565	1.316
11D	$D \to K_1(1270)^0\pi^0, K^{*0}\pi^0[D]$	1.002	0.483	0.045	0.121	1.120
12S	$D \to K_1(1270)^0\pi^0, K^-\rho^+[S]$	2.007	0.188	0.079	0.847	2.188
14S	$D \to (K^{*-}\pi^0)_A\pi^+, K^{*-}\pi^0[S]$	1.208	0.706	0.048	0.455	1.472
16S	$D \to (K^{*0}\pi^0)_A\pi^0, K^{*0}\pi^0[S]$	1.711	0.365	0.053	0.214	1.750
16D	$D \to (K^{*0}\pi^0)_A\pi^0, K^{*0}\pi^0[D]$	1.501	0.605	0.051	0.187	1.630
17D	$D \to (\rho^+K^-)_A\pi^0, K^-\rho^+[D]$	1.195	0.613	0.133	0.611	1.482
	$D \to AP, A \to SP$					
21	$D \to ((K^-\pi^+)_S\pi^0)_A\pi^0$	2.039	0.410	0.045	0.446	2.127
	$D \to VS$					
26	$D \to (K^-\pi^0)_S\rho^+$	3.159	0.471	0.053	0.216	3.201
27	$D \to K^{*-}(\pi^+\pi^0)_S$	1.207	0.258	0.045	0.156	1.245
28	$D \to K^{*0}(\pi^0\pi^0)_S$	0.938	0.476	0.062	0.116	1.060
	$D \to VP, V \to VP$					
33	$D \to (K^{*-}\pi^+)_V\pi^0$	1.260	0.471	0.032	0.490	1.432
	$D \to VV$					
38S	$D[S] \to K^{*-}\rho^+$	1.995	0.154	0.070	0.712	2.125
38P	$D[P] \to K^{*-}\rho^+$	1.612	0.214	0.035	0.864	1.842
38D	$D[D] \to K^{*-}\rho^+$	1.586	1.108	0.051	0.588	2.022
39P	$D[P] \to (K^-\pi^0)_V\rho^+$	1.429	0.324	0.023	0.128	1.471
39D	$D[D] \to (K^-\pi^0)_V\rho^+$	0.401	0.832	0.133	0.666	1.146
40D	$D[D] \to K^{*-}(\pi^+\pi^0)_V$	1.445	1.313	0.040	0.190	1.962
43S	$D[S] \to (K^-\pi^0)_V(\pi^+\pi^0)_V$	1.354	0.213	0.041	0.726	1.551
	$D \to TS$					
46	$D \to (K^-\pi^+)_S(\pi^0\pi^0)_T$	2.544	0.724	0.057	0.189	2.653
47	$D \to (K^-\pi^0)_S(\pi^+\pi^0)_T$	1.533	0.718	0.050	0.135	1.699

8.2 Branching Fraction

We examine the systematic uncertainties for the branching fraction from the following sources:

- Tag-side efficiency
- Tracking, particle ID, and π^0 efficiencies for signal
- $K^-\pi^+\pi^0\pi^0$ decay (PWA) model
- Yield fits
- K_S peaking backgrounds and the K_S mass veto
- Doubly Cabibbo-Suppressed Decays (DCSD)

A summary is given in Section 8.2.8.

8.2.1 Tag-Side Efficiency Systematic Uncertainties

The efficiency for reconstructing the tag-side, $\bar{D}^0 \to K^+\pi^-$, should almost cancel, and any residual effects caused by the tag-side are expected to be negligible.

Those residual effects might occur when the factorization of $\varepsilon_{\text{tag,sig}} \approx \varepsilon_{\text{tag}}\varepsilon_{\text{sig}}$ is violated. In other words, the DT efficiency is not completely the product of both sides ST efficiencies, since ST candidates are measured with the opposite D meson decaying generically, while the tag side of DT candidates are measured versus a specific decay mode. The multiplicity of the opposite D decay matters due to the decay products' overlapping. The worst case is missing signal photons due to photon isolation from charged tracks. This effect, however, is believed to be small due to the fine-grained BESIII detector. The violations of factorization are not negligible, but the data-MC difference due to imperfect MC should be. We note that most BESIII analyses do not even discuss this issue.

8.2.2 Tracking, Particle ID, and π^0 Systematics

Unlike the case of the tag-side, the reconstruction efficiency of the signal-side does not cancel in the double-tag to single-tag ratio. This efficiency of the signal-side is determined with the PWA signal MC. The mismatches of tracking, particle ID, and π^0 reconstruction between data and MC simulation, therefore, bring in systematic uncertainties.

One possible source of those uncertainties is that the momentum spectra simulated in MC do not match those in data, which will cause incorrect momentum-weighted average of the efficiencies, if there are any variations in efficiency vs. momentum. This effect, however, is expected to be small due to the PWA signal MC's successfully-modeling the momentum spectra in data, as shown in Figure 5.1. The major possible source of the tracking, particle ID, and π^0 systematic uncertainties is that, although the momentum spectra in MC and data follow each other well, the efficiency of MC disagrees with that of data as the function of momentum. This disagreement results in taking a correctly weighted average of incorrect efficiencies.

Detailed studies of the tracking, particle ID, and π^0 systematic uncertainties have been performed by the BESIII Collaboration:

- Charged-particle tracking for $K^{\pm}$ and $\pi^{\pm}$ [34]: 1.0% per track
- Charged-particle identification of $K^{\pm}$ and $\pi^{\pm}$ [34]: 1.0% per track
- π^0 reconstruction [35]: 1.5% per π^0

The study of and tracking systematics is done with the double-tag technique; missing mass is used to obtain yields. The tag modes are $K\pi$, $K\pi\pi\pi$, and $K\pi\pi^0$. For K tracking, the signal modes are $K\pi$, and $K\pi\pi\pi$. For π tracking, the signal modes are $K\pi$, $K\pi\pi\pi$, and $K\pi\pi^0$.

The study of charged-particle identification is done with the D^0 and D^+ samples. For D^0 decays, for K PID, $K\pi\pi^0$ is used in the single-tag samples, and $K\pi$, $K\pi\pi\pi$ and KK are used as signal in the double-tag samples. For π PID, $K\pi\pi^0$ and $K_S\pi\pi$ are used in the single-tag samples, and $K\pi$ and $K\pi\pi\pi$ are used as signal in the double-tag samples. For D^+ decays, for K PID, $K\pi\pi\pi^0$ and K_SK are used in the single-tag samples, and $K\pi\pi$ and K_SK are used as signal in the double-tag samples. For π PID, $K_S\pi$ is used in the single-tag samples, and $K\pi\pi$ and $K_S\pi$ are used as signal in the double-tag samples.

The systematics of π^0 reconstruction are done in our own separate memo with a double-tag technique, Appendix A. Missing-mass squared peaks provide the normalization. The mode $K\pi\pi^0$ is chosen as the signal, and $K\pi$ and $K\pi\pi\pi$ are chosen as the tag.

8.2.3 $K^-\pi^+\pi^0\pi^0$ Decay Model

To estimate the systematic uncertainty caused by the imperfections of the decay model, one can compare the efficiency difference of a good and a bad model. We will then use some fraction of this difference as the systematic uncertainty. The fraction to use is somewhat of an arbitrary judgement, but it clearly should depend on how good or bad the two models are.

We saw that our PWA model makes a 10% relative shift on efficiency (compared to public MC), shown in Table 7.1. We also proved the consistency of data and our PWA model is excellent, while the public MC poorly represents the data, as discussed in Sections 5.2 and 5.4. We therefore believe that one tenth of the 10% relative shift of efficiency, that is 1%, is conservative as a systematic for the effect of any remaining decay modeling imperfections on the efficiency.

8.2.4 Yield Fits

To get the the systematics of yield fits, we change the nominal ΔE cut to a wider one, as mentioned in Section 7.3, and the changes of the branching fraction are considered as the systematics of yield fits. The branching fraction with the wide ΔE cut is calculated according to the numbers in Table 7.2 while the nominal branching fraction is calculated according to the numbers in Table 7.1. The systematics associated with ST and DT are determined separately.

8.2.5 K_S Peaking Backgrounds and the K_S Mass Veto

According to the truth information of the MC, the K_S mass cut can veto most K_S peaking backgrounds and reduce it to only 0.07%. However, the peaking background simulation is not perfect and the K_S mass cut also vetos about 13% signal events. Thus, we estimate the uncertainty by narrowing the veto from $0.458 < M_{\pi^0\pi^0} < 0.520$ to $0.470 < M_{\pi^0\pi^0} < 0.510$, while the K_S peaking background increases from 0.07% to 0.15% and the branching fraction change is 0.18% of itself. We take this full shift as the uncertainty due to the K_S mass veto on the peaking background.

8.2.6 Other Backgrounds

The smooth Argus background level is about 1% in the signal region. In addition, the 2-D $M_{\rm BC}$ vs. $M_{\rm BC}$ fit works well for background determination. Thus, we believe the uncertainties of the 1% background will be very small and we neglect them.

8.2.7 DCSD Correction Systematics

Our tag and signal are required to have opposite-sign kaons. This means that our double-tags decays are either both Cabibbo-favored or both doubly-Cabibbo-suppressed. These contributions can interfere with each other, with amplitude ratios that are approximately known, but with a priori unknown phase. The fractional size of the interference term varies between approximately $\pm 2|A_{DCSD}/A_{CF}|^2 \simeq \pm 2\tan^4\theta_C$ (the square in the first term arises as one power from each decay mode in the cross-term). The two amplitude ratios are not exactly equal to $\tan^2\theta_C$, due to differing structure in the CF and DCSD modes, but nonetheless we believe $2\tan^4\theta_C$ is a conservative uncertainty to set as an approximate "1 σ" scale to combine with other uncertainties.

8.2.8 Summary of Branching Fraction Uncertainties

Systematic uncertainties on the branching fraction are summarized in Table 8.3, where the total uncertainty is calculated by quadrature sum of individual contributions.

Table 8.3: $K\pi\pi^0\pi^0$ Branching Fraction Systematics

Source	Systematic (%)	Comment
Tracking effic.	2.0	1.0% per track
Particle ID	2.0	1.0% per track
π^0 effic.	3.0	1.5% per π^0
Decay Model	1.0	1/10 of decay.dec vs. PWA model
Yield fits (ST)	0.6	vary ΔE cut
Yield fits (DT)	1.2	vary ΔE cut
Peaking Background	0.2	BF of modes, K_S veto
DCSD Correction	0.6	from $2\tan^4\theta_C$
TOTAL	4.5	in quad.; all correl's are within lines

Chapter 9

Conclusion

Soon after the J/ψ meson was identified in 1974 by Ting and Richter and their collaborators, the D mesons were discovered in 1976 by Mark I. The D mesons are a perfect place to study the weak decay of the charm quark. All $D \to \bar{K}\pi$ and $D \to \bar{K}\pi\pi$ decays have been well studied, but $D \to \bar{K}3\pi$ decays with at least two π^0s are unmeasured. The main reason is the efficiency and resolution of π^0s are worse than that of charged particles. However, the BESIII detector has a sophisticated Electro-Magnetic Calorimeter consisting of CsI(TI) crystals, which provide a good opportunity to study $D \to \bar{K}3\pi$ decays with at lease two π^0s.

Based on the 2.93 fb^{-1} sample of e^+e^- annihilation data near $D\bar{D}$ threshold collected by BESIII detectors, we report the first amplitude analysis of $D^0 \to K^-\pi^+\pi^0\pi^0$ and the first measurement of the branching fraction for this four-body decay mode. In our analysis, we perform a unbinned likelihood fit on a double-tag sample with a detailed probability density function including intermediate resonances. The probability density function includes an optimal set of 26 amplitudes. We also test more than 40 other amplitudes, all of which have small significance. In order to check the goodness-of-fit of our amplitude analysis result, we make many 1-D and 2-D projections; we also apply the mixed-sample method to obtain a quantitative measure of quality. With the result of the amplitude analysis in hand, we are able to obtain an accurate efficiency for the $K^-\pi^+\pi^0\pi^0$ data sample. To extract the absolute branching fraction for $D^0 \to K^-\pi^+\pi^0\pi^0$, we use the tagging technique on our $D\bar{D}$ threshold data.

The results of the amplitude analysis is given in Table 5.2 and we obtain $\mathcal{B}(D^0 \to K^-\pi^+\pi^0\pi^0) = (8.98 \pm 0.13(\text{stat}) \pm 0.40(\text{syst}))\%$.

Appendix A

Systematic Uncertainty from π^0 Reconstruction Efficiency

The π^0 reconstruction efficiency and its systematic error in $\psi(3770)$ data are investigated. Data and Monte-Carlo from 2010 and 2011 are used under BOSS version 6.6.4p2. We study $D^0 \to K^-\pi^+\pi^0$ vs. a fully reconstructed $D \to K^-\pi^+$ or $D \to K^-\pi^+\pi^+\pi^-$ tag. We also consider the sensitivity of data-MC efficiency differences to π^0 quality requirements. Results are presented in five π^0 momentum bins between 0.0 - 1.0 GeV and with different π^0 quality requirements.

A.1 Introduction

DTagTool is used to tag a D^0 decay to $K^-\pi^+$ and $K^-\pi^+\pi^+\pi^-$; on the signal side $\bar{D}^0 \to K^-\pi^+\pi^0$ is either fully reconstructed or partially reconstructed from only $K^-\pi^+$ (charge conjugation is implied throughout in this note). Missing-mass squared is used to count the π^0 yield. The details are given in the following sections.

This study for the BOSS 6.6.4p2 is an update of CMU group's "π^0 Reconstruction Efficiency"[1]. The technique is the same, but some small changes are made. Many technical improvement were made and bugs were fixed. Accordingly, the stability and quality of fitting are improved. Finally as discussed below in Section A.2, the selection of the best π^0 candidate is also changed.

For completeness, we include some content from the previous study. Readers who are familiar with that study can jump to "Difference from Previous Study" section, where the updates are listed.

[1] π^0 Reconstruction Efficiency at BES III - BESIII Doc. 165 by O. Albayrak *et al.*

A.2 Event Selection

In this study, BOSS 6.6.4p2 is used for the analysis of the $\psi(3770)$ data samples from 2010 and 2011 and all of the $D^0\bar{D}^0$ and D^+D^- Monte-Carlo available for 2010 and 2011 samples. The packages used are as follows:

- `DTagAlg` version 56
- `DTagTool` version 11
- `SimplePIDSvc` version 11
- `Pi0EtaToGGRecAlg` version 10

On the tag side, DTagTool single tag $K\pi$ and $K\pi\pi\pi$ decays are used. For the single tag candidates the requirements in Table A.1 are used.

Table A.1: Requirements for tag side ($K\pi$ and $K\pi\pi\pi$.).

Requirements	m_{BC} [GeV]	ΔE [GeV]
	$1.8605 < m_{BC} < 1.8685$	$\lvert\Delta E\rvert < 0.03$

For the signal side, two tracks are identified as a kaon and a pion by `SimplePIDSvc` and must have opposite charges. The details of the kaon and pion selection are given elsewhere[2]. If the event has π^0(s) in addition to these tracks, unconstrained mass and χ^2 requirements are applied to the π^0 candidates. These requirements are:

- $0.115 <$ unconstrained π^0 mass < 0.150 GeV
- $\chi^2 < 2500$
- Number of endcap photons per $\pi^0 \leq 1$

A π^0 candidate that satisfies these requirements is called good π^0 candidate. If there is more than one good π^0 candidate, then the π^0 with the smallest $|\Delta E|$ of the $K\pi\pi^0$ candidate is chosen.

To further suppress the background, two additional requirements are applied. First, events are required to have opposite kaon charge for the signal and the tag side decays. Secondly, to suppress the electron background for the signal side pion, this track is required to have a probability of being a pion larger than that for being an electron, provided by the `SimplePIDSvc` package. The package uses combined dE/dx and TOF information. Details are given elsewhere[2].

[2] DTag Event Selection at BES III - BESIII Doc. 105 by Chunlei Liu

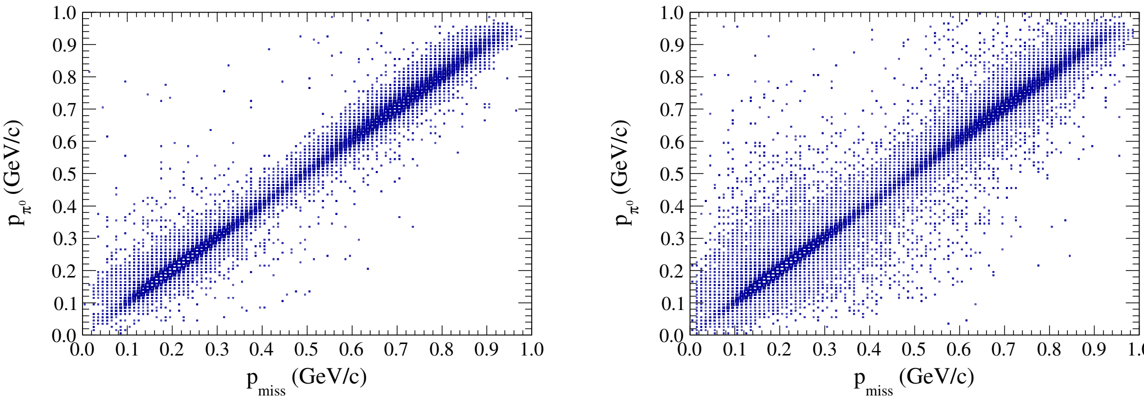

(a) 2011 and 2010 Data (b) 2011 and 2010 MC

Figure A.1: p_{miss} vs p_{π^0} for $K\pi\pi^0$ events.

After reconstructing all the tracks, the missing momentum and missing energy can be calculated as follows:

$$\vec{p}_{miss} = -\vec{p'}_{tag} - \vec{p}_K - \vec{p}_\pi \tag{A.1}$$
$$E_{miss} = E_{beam} - E_K - E_\pi \tag{A.2}$$

where $\vec{p'}_{tag}$ is obtained by using the direction of the measured momentum of the tag side, $\vec{p}_{tag}$ but with the magnitude constrained such that $p'_{tag} = [E^2_{beam} - m^2_{PDG}]^{1/2}\hat{p}_{tag}$. If the event has a π^0 that is reconstructed correctly, p_{miss} should be equal the π^0 momentum. This can be seen in Figure A.1, with signal π^0 in the diagonal band.

Our final requirement for selecting signal events applies to the mass of $K\pi\pi^0$ system. Events with a π^0 should satisfy this requirement, a "classification criterion", to be classified as "π^0 found". There is more than one way to define such classification criteria. One example is $1.78 < M_{K\pi\pi^0} < 1.92$ GeV (Figure A.2). Studies have been carried out using different classification criteria; the final results are sensitive to these changes as shown later.

Figure A.3a shows the statistics in each of our five p_{miss} bins; Figure A.3b shows the data-MC agreement of the p_{π^0} spectra.

A.3 Missing-Mass Squared (MM^2)

The key variable used to calculate the π^0 reconstruction efficiency is the missing-mass squared (MM^2) of the signal-side D^0. This MM^2 is given as:

$$MM^2 = (E_{beam} - E_K - E_\pi)^2 - p^2_{miss}$$

If the signal event has a π^0 missing, the variable is expected to peak around 0.019 GeV^2. Events will be plotted in two different categories; "π^0 found" and "π^0 not

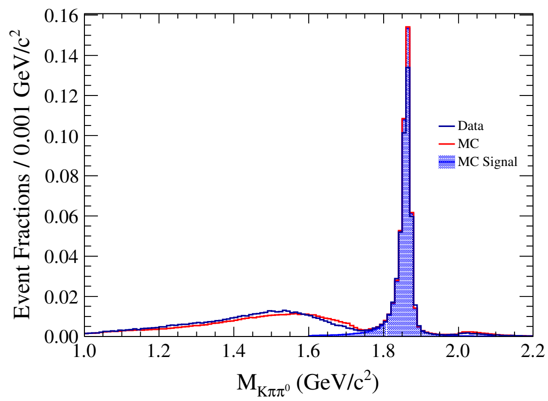

Figure A.2: Mass of the $K\pi\pi^0$ system.

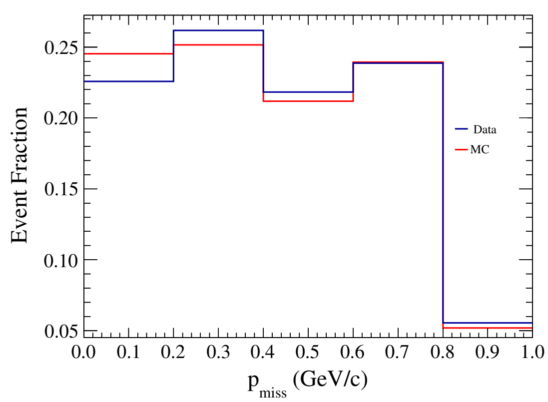

(a) p_{miss} spectrum

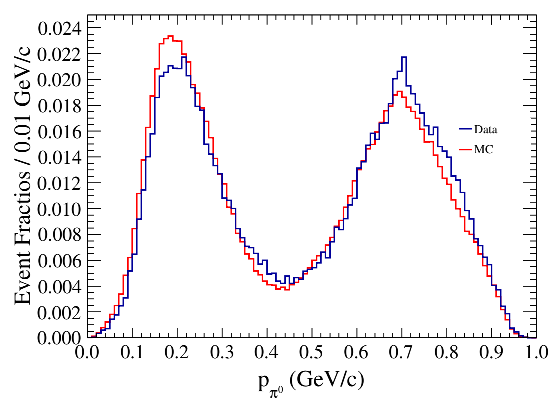

(b) p_{π^0} spectrum

Figure A.3: p_{miss} and p_{π^0} for $K\pi\pi^0$ events.

found".

The "found" case occurs when a signal event has the required tracks identified as a kaon and a pion of opposite charge and a π^0 candidate which satisfies all of the requirements given in the Section A.2.

The "not found" case occurs when a signal event has the required tracks identified as a kaon and a pion of opposite charge, but the event does not have any good π^0 candidate, or has a good π^0 candidate but the $K\pi\pi^0$ system fails the found/not-found classification criteria.

All these events also satisfy the conditions given in Table A.1 for the tag side.

The MM^2 distributions in each bin are given in Figures A.4, A.5, A.6, A.7, A.8, using the default classification criterion $1.78 < M_{K\pi\pi^0} < 1.92$ GeV as an example.

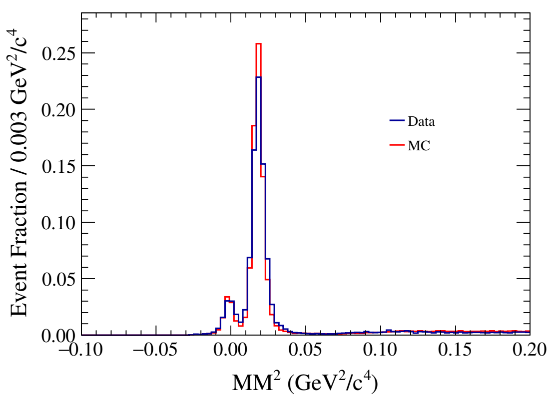

(a) The not found case.

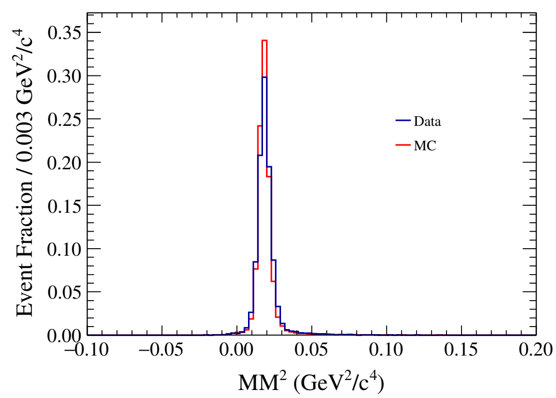

(b) The found case.

Figure A.4: MM^2 distribution for the not found and the found cases in $0 < p_{miss} <$ 200 MeV bin.

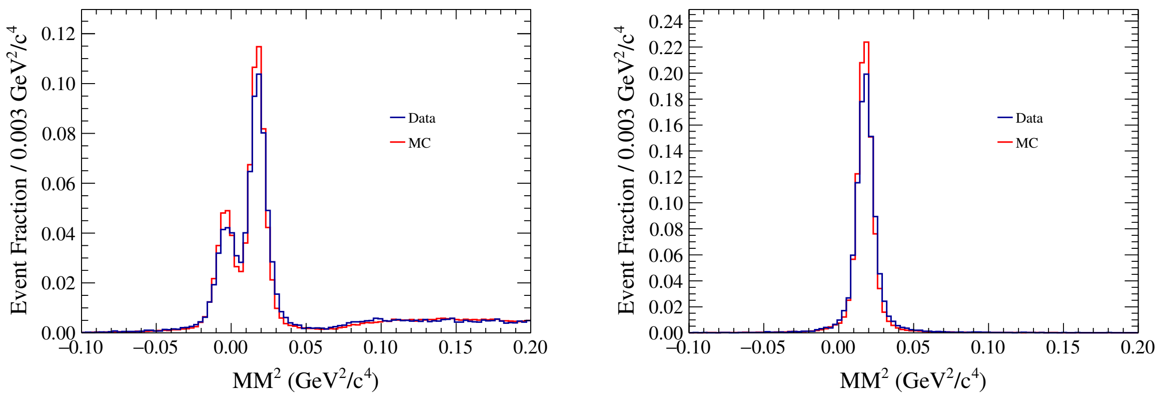

(a) The not found case.

(b) The found case.

Figure A.5: MM^2 distribution for the not found and the found cases in $200 < p_{miss} <$ 400 MeV bin.

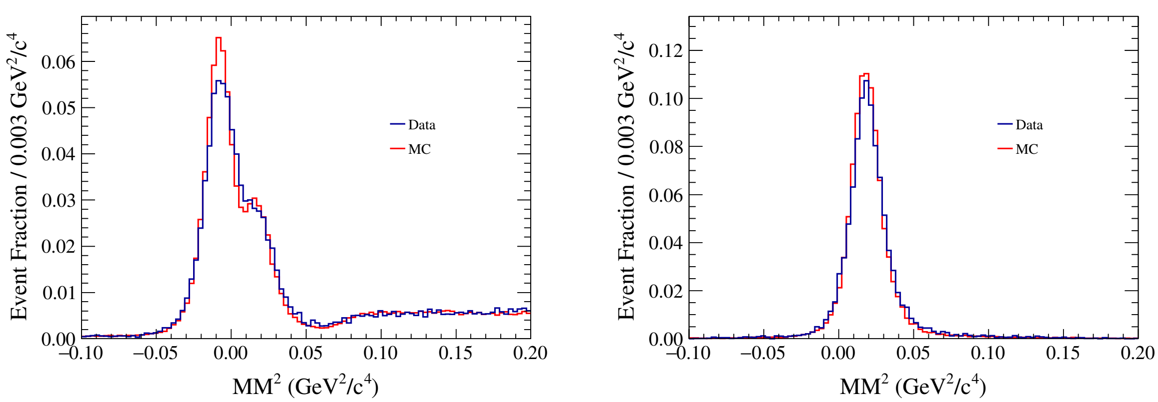

(a) The not found case.

(b) The found case.

Figure A.6: MM^2 distribution for the not found and the found cases in $400 < p_{miss} <$ 600 MeV bin.

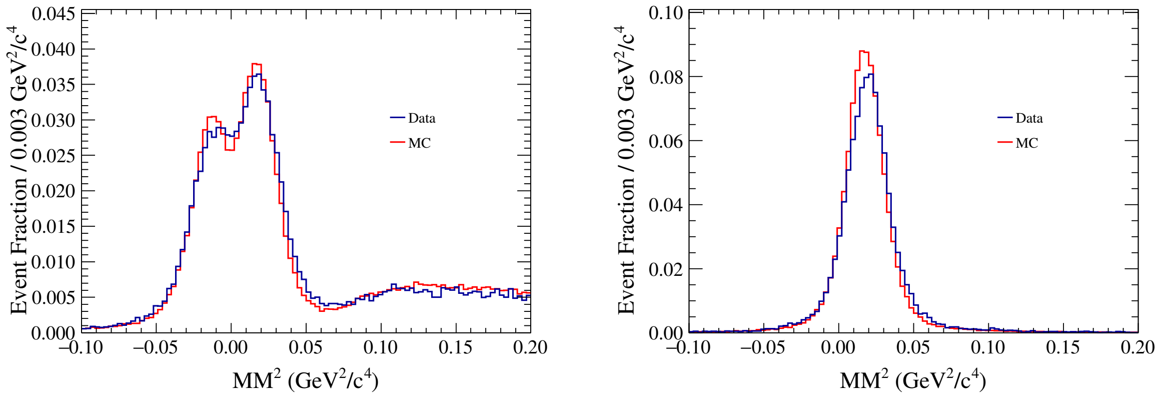

(a) The not found case.

(b) The found case.

Figure A.7: MM^2 distribution for the not found and the found cases in $600 < p_{miss} < 800$ MeV bin.

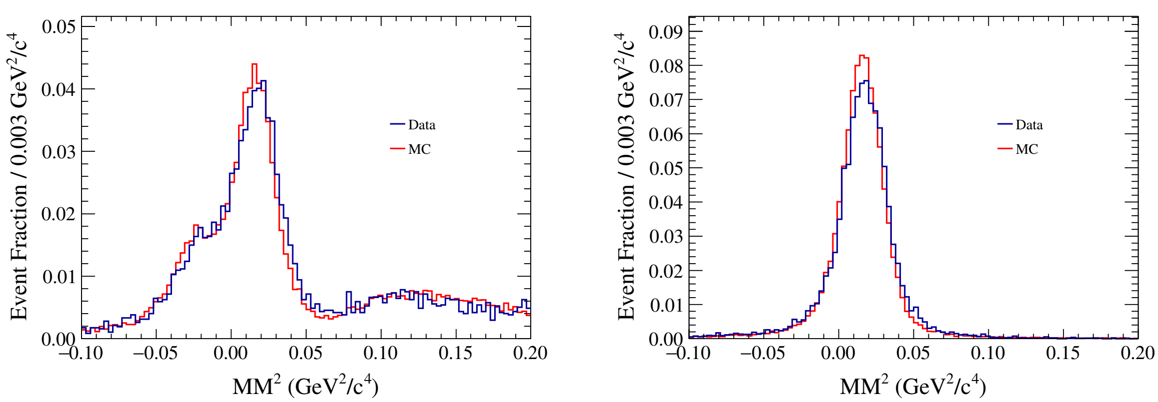

(a) The not found case.

(b) The found case.

Figure A.8: MM^2 distribution for the not found and the found cases in $800 < p_{miss} < 1000$ MeV bin.

A.4 Backgrounds

Backgrounds are identified using a generator-level truth-matching tool where the final state for the D mesons are determined. Backgrounds are examined separately for the π^0 found and π^0 not-found cases.

Background and signal events are classified using the scheme given in Table A.2.

Table A.2: Classification of events as signal and different background components.

	Real Signal	$K\mu\nu$	$K\pi\pi^0\pi^0$	other modes
Real Tag	signal	$K\mu\nu$ bkg	$K\pi\pi^0\pi^0$ bkg	other bkg
Fake Tag	other bkg	other bkg	other bkg	other bkg

Two of the largest contributions to background come from $D^0 \to K\mu\nu$ and $D^0 \to K\pi\pi^0\pi^0$ decays. The MM^2 distribution for $D^0 \to K\mu\nu$ decay is centered at 0, below the signal peak, since the ν mistaken for the π^0 is massless. The MM^2 distribution for $K\pi\pi^0\pi^0$ background forms a plateau beginning near $MM^2 \sim (2m_{\pi^0})^2 \sim 0.08$ GeV^2 due to the kinematics of this decay. Potential $Ke\nu$ decay backgrounds are suppressed with our particle identification (PID) requirements on the signal side pion.

Another contribution to the not-found case in the first missing momentum bin comes from $D^0 \to K\pi$ decays. The MM^2 values for these decays are centered about 0 as there is no missing mass in the event. This background is mostly removed using the mass of the $K\pi$ system (in the lowest bin only). Events with $M_{K\pi} > 1.75$ GeV are removed.

Background fractions for different momentum bins are given in the Sections A.15, Figures A.31, A.33, A.35 , A.37 and A.39. MM^2 values for these specific backgrounds can be found in two dimensional Figures A.32, A.34, A.36, A.38 and A.40.

A.5 Fitting Procedure

The RooFit package is used to fit the missing-mass squared distributions. Signal and background templates are created using the Monte-Carlo truth information.

The signal is defined as having the correct tag mode ($K\pi$ or $K\pi\pi\pi$) opposite a $K\pi\pi^0$ decay. Background templates are separated in three different histograms. First is $K\mu\nu$ background for the signal. This contribution to the background is saved to a separate background template due to the high fraction within background in most of the bins. Second, the same is done for $K\pi\pi^0\pi^0$ background due to its size and the poorly known branching fraction in the MC. Third, all the other background contributions are collected in the third background template.

For not-found cases, each background has a floating normalization. All the background components and the signal are smeared with the same floating Gaussian to compensate the difference of the resolutions between Monte-Carlo and the data. For found cases, due to the small size background the fitting procedure is changed to use one summed background template.

Fits for different missing momentum bins are given in the Figures A.9, A.10, A.11, A.12 and A.13 (using the classification $1.78 < M_{K\pi\pi^0} < 1.92$ GeV as an example).

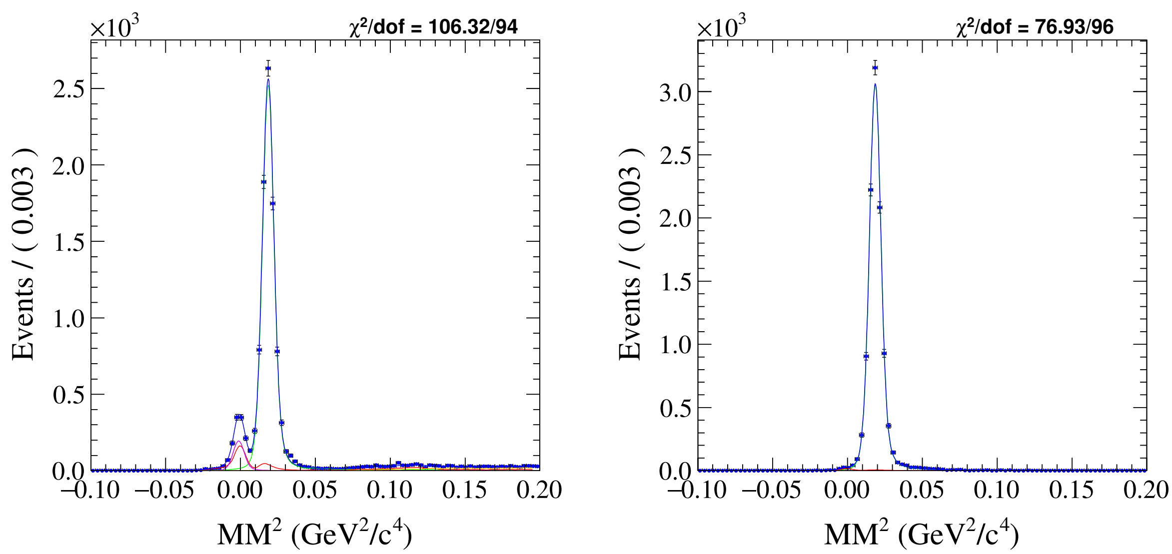

(a) MM^2 fit of the not found case

(b) MM^2 fit of the found case

Figure A.9: MM^2 fit in $0 < p_{miss} < 200$ MeV bin. Green curve represents the signal; violet, $K\mu\nu$ background; orange $K\pi\pi^0\pi^0$ background; and red curve for all the other background.

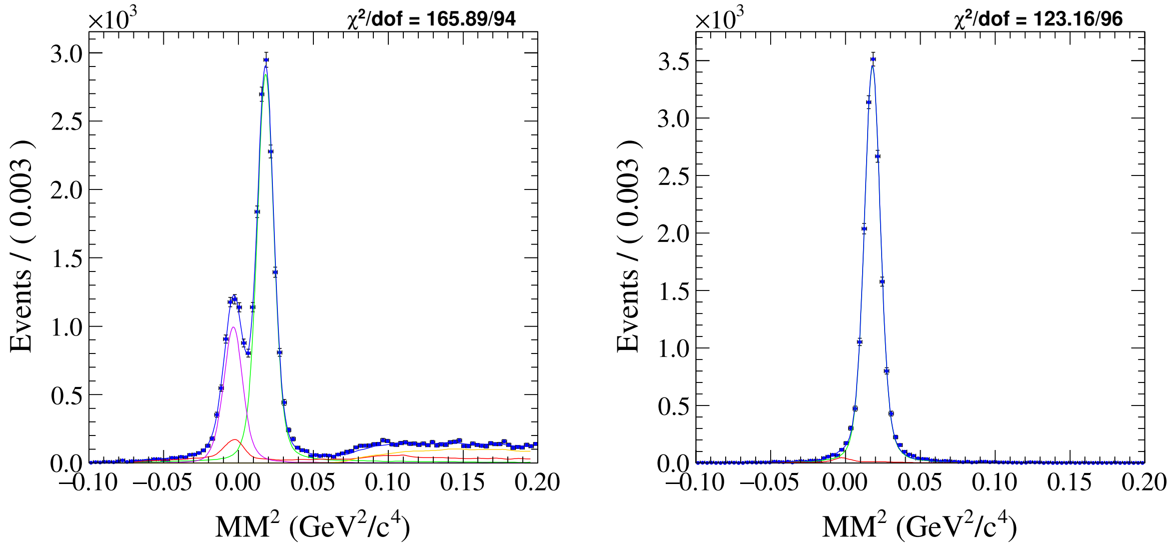

(a) MM^2 fit of the not found case

(b) MM^2 fit of the found case

Figure A.10: MM^2 fit in $200 < p_{miss} < 400$ MeV bin. Green curve represents the signal; violet, $K\mu\nu$ background; orange $K\pi\pi^0\pi^0$ background; and red curve for all the other background.

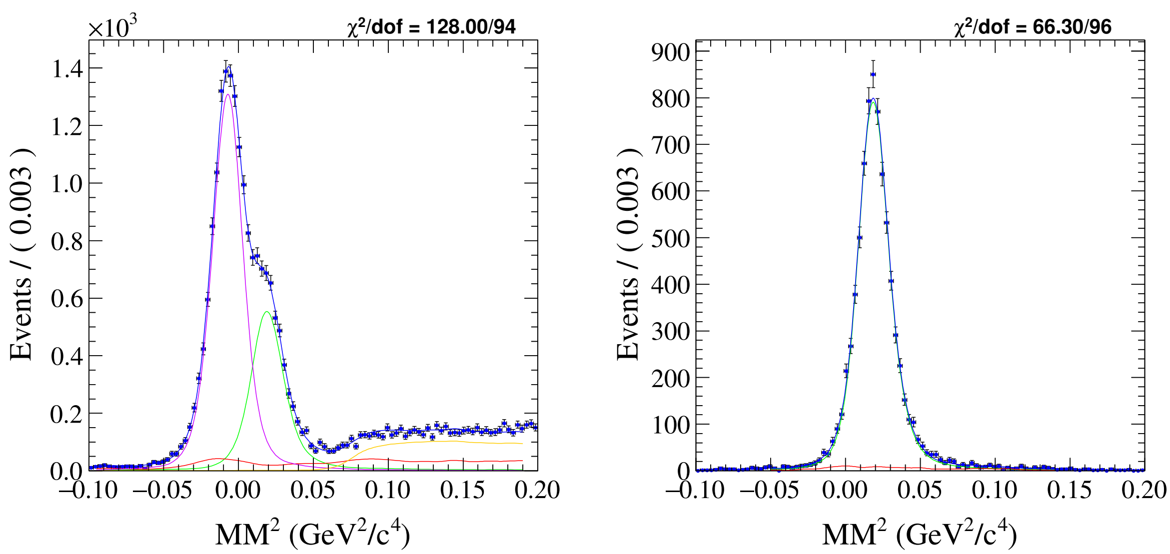

(a) MM^2 fit of the not found case

(b) MM^2 fit of the found case

Figure A.11: MM^2 fit in $400 < p_{miss} < 600$ MeV bin. Green curve represents the signal; violet, $K\mu\nu$ background; orange $K\pi\pi^0\pi^0$ background; and red curve for all the other background.

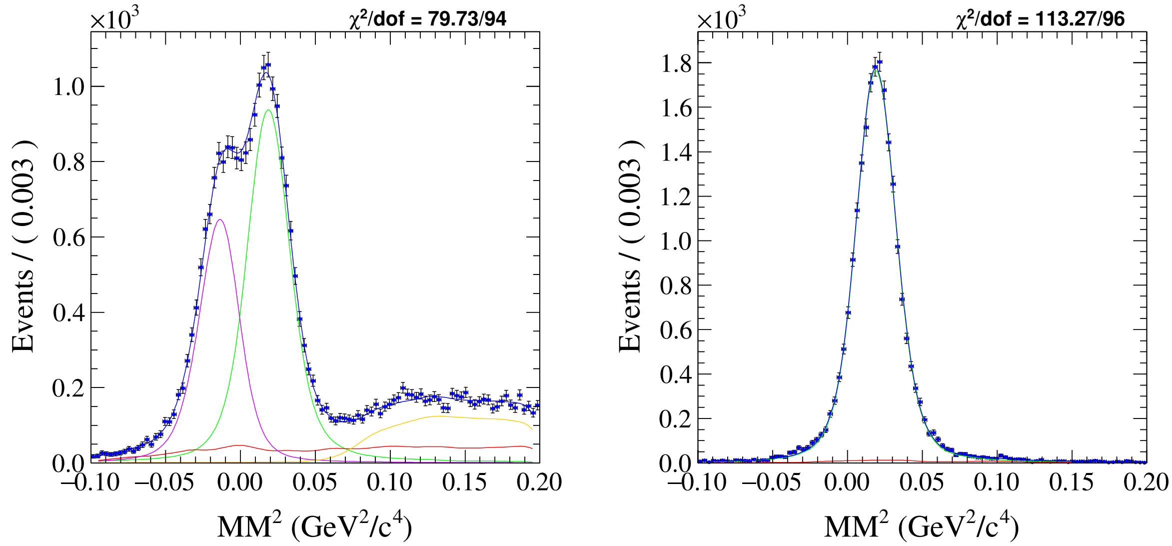

(a) MM^2 fit of the not found case

(b) MM^2 fit of the found case

Figure A.12: MM^2 fit in $600 < p_{miss} < 800$ MeV bin. Green curve represents the signal; violet, $K\mu\nu$ background; orange $K\pi\pi^0\pi^0$ background; and red curve for all the other background.

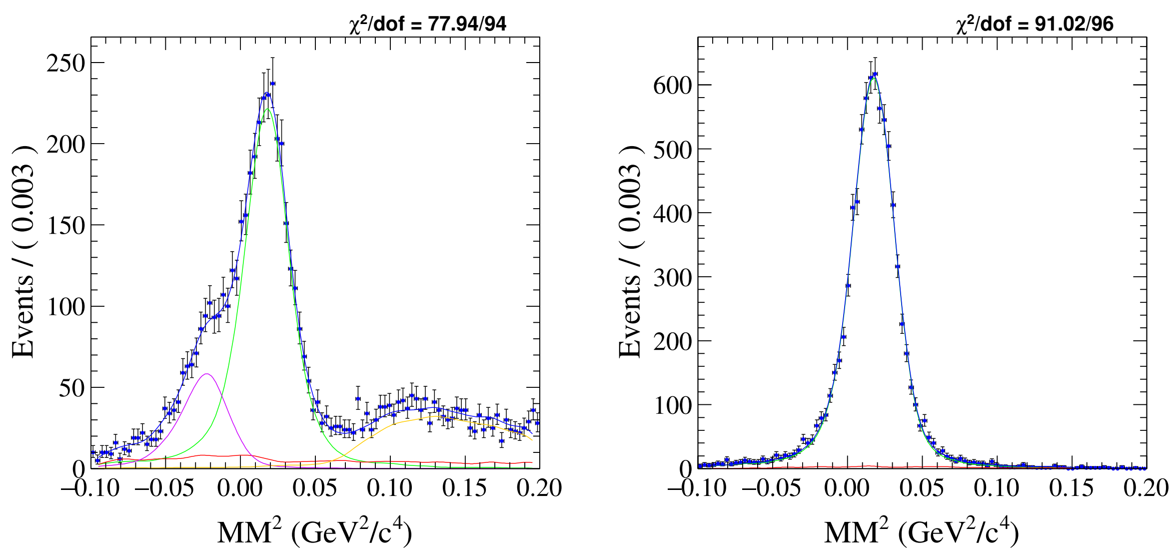

(a) MM^2 fit of the not found case

(b) MM^2 fit of the found case

Figure A.13: MM^2 fit in $800 < p_{miss} < 1000$ MeV bin. Green curve represents the signal; violet, $K\mu\nu$ background; orange $K\pi\pi^0\pi^0$ background; and red curve for all the other background.

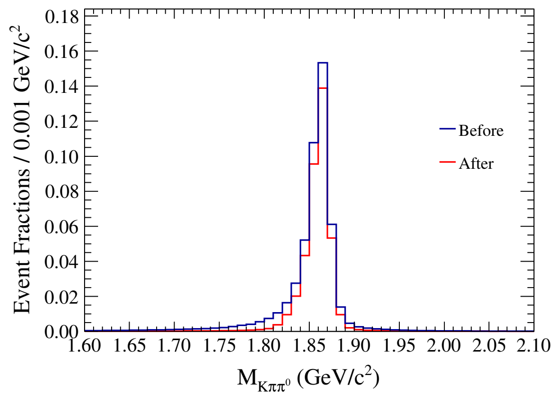

Figure A.14: Mass of the $K\pi\pi^0$ system. MC Signal before and after removing π^0 with poor truth match

A.6 Comments on Multiple Candidates and π^0 Quality

We have "events cuts", critera on the tag and the signal-side K^-, π^+, to remove uninteresting events that cause backgrounds in the MM^2 plots; inevitably, some events that look similar to our intended sample survive. But after fitting, the MM^2 peak area identifies the number of the events where the tag is correct and the signal side $K^- \pi^+$ came from a real $K^-\pi^+\pi^0$ event. We also have the classification to check the quality of π^0. Events in which no π^0 passes this classification cut will be moved to not found case. Even for "true" events, some π^0s are not reconstructible due to minimum energy and geometry (beam hole, gap, etc...). In some fraction of those events, some fake π^0s can be still found in the $M_{\gamma\gamma}$ window. Users may worry that the classification cuts out sizable real π^0s. As shown in Figure A.14, one can see that our $M_{K\pi\pi^0}$ classification, $1.78 < M_{K\pi\pi^0} < 1.92$ GeV, is generous enough, only cutting out a tiny fraction of the MC signal $M_{K\pi\pi^0}$ with π^0 passing the truth match. That is, truth-matching indicates almost all of the far low-side tail are not good π^0 candidates. There is some small innefiency of truth matching, as seen the signal peak. But this does not alter the basic conclusion about the nature of the tail.

In events with multiple π^0 candidates, we select the best candidate using the π^0 mass resulting smallest $|\Delta E|$ of $K\pi\pi^0$. Most analyses use some sort of best candidate selection, and any criteria will have some inefficiency. However, analyses may use a different criteria, such as choosing the best candidates based on π^0 mass or m_{BC}. This small difference affects the π^0 systematics. We have a comparison between the smallest $|\Delta E|$ selection and the best π^0 mass selection in Sections A.12.

A.7 Efficiency

After fitting the MM^2 distributions in different momentum bins for found and not found cases, efficiency for π^0 reconstruction is calculated. The efficiency and the fractional efficiency difference is given by:

$$\epsilon = \frac{N_{Found}}{N_{Found} + N_{NotFound}} \tag{A.3}$$

$$\delta\epsilon = \frac{\epsilon_{MC} - \epsilon_{Data}}{\epsilon_{MC}} \tag{A.4}$$

These momentum-dependent efficiency differences can be weighted depending on the momentum distribution of the analysis of interest.

A.8 Difference from Previous Study

Generally, we use the same method as that of the previous study while some modifications and improvements are made. In addition, we find the sensitivity of final result to found/not-found classification criteria and investigate the sensitivity. The following are the modifications and improvements we made.

- The selection of the best π^0 candidate in events with multiple π^0 candidates is changed from the best π^0 mass to the smallest $|\Delta E|$. The comparison is shown in Sections A.12.
- The EMC endcap region changes in BOSS 6.6.4; $|\cos\theta| : 0.84 \sim 0.92 \rightarrow 0.86 \sim 0.92$. The effect is to remove a small tail of photons just below 0.86.
- The $K\pi$ mass cut to veto $D^0 \rightarrow K\pi$ is moved from 1.81 to 1.75 GeV.
- In this study, the $K\pi\pi^0$ decay background templates are separated into three pieces: $K\mu\nu$, $K\pi\pi^0\pi^0$ and "other"; in the old study, these three pieces are $K\mu\nu$, $Ke\nu$ and "other".
- In this study, each of the three background templates has a floating normalization for not-found cases and one summed background template is used for found cases; in the old study, three floated background templates, partly summed background templates, or one summed background template is used for both not-found and found cases depending on the size of background and the quality of fitting.
- We made technical improvements and fixed bugs.
- We made fitting input/output tests, monitor fit parameters in detail, and tried different random number seeds to insure quality, stability, and consistency of fitting results (see Sections A.13).

- We studied different found/not-found classification criteria to understand the sensitivity.

A.9 Sensitivity to Classification Criteria

We start by comparing two different types of found/not-found classification requirements. The first one is four-vector mass window $1.78 < M_{K\pi\pi^0} < 1.92$ GeV ($M_{K\pi\pi^0}$) requirement, already used in the previous study. The second one is ΔE and m_{BC} windows $-0.06 < \Delta E < 0.04$ GeV and $1.856 < m_{BC} < 1.874$ GeV (dEmBC) requirement. The absolute efficiency is given in Figure A.15 and efficiency difference is given in figure A.16. Obviously, different classification requirements change absolute efficiency. The problem is that efficiency difference changes as well. There is a roughly 2% shift between $M_{K\pi\pi^0}$ and dEmBC requirements at the lowest p_{miss} bin ($0.0 - 0.2$ GeV/c). Note that the error bars mostly come from statistics. At the lowest p_{miss} bin, data sets are highly correlated in different classification requirement, switching which is used moves less than 10% events between found and not found cases. Therefore, even a "one sigma" shift is actually very signigicant. The Figures also show results for an m_{BC} cut only: this demonstrates that the shift in the lowest bin is due to m_{BC} alone, and not ΔE.

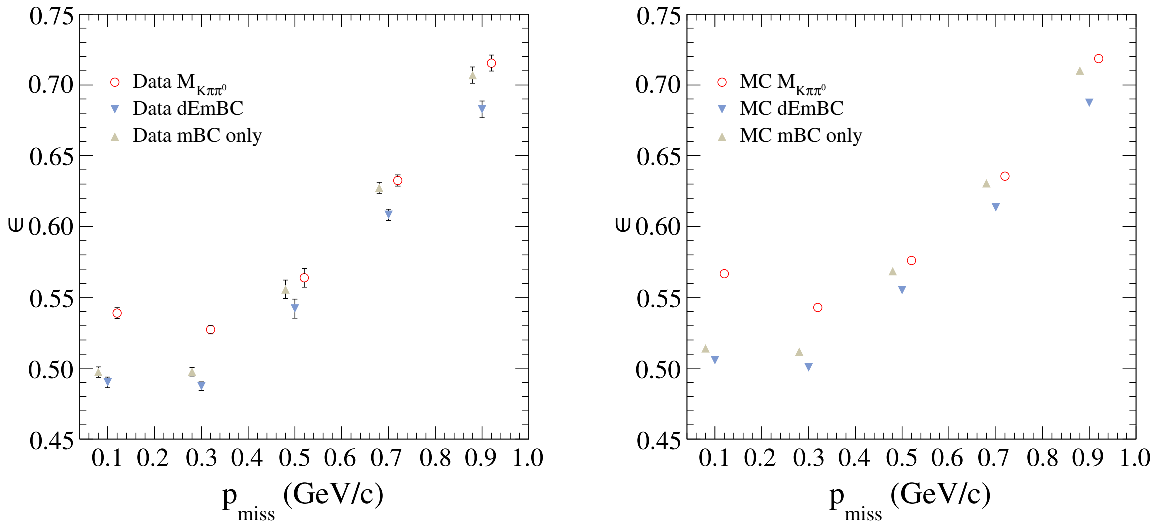

(a) π^0 Reconstruction efficiency for data.

(b) π^0 Reconstruction efficiency for MC

Figure A.15: 2011 and 2010 samples for different studies

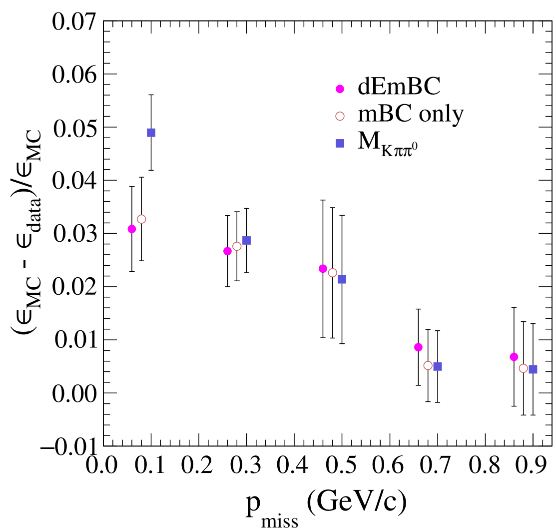

Figure A.16: Difference in π^0 reconstruction efficiency.

In order to understand this sensitivity to m_{BC}, the relation between $M_{K\pi\pi^0}$ and dEmBC requirements is shown in Figure A.17, ΔE vs. m_{BC} plots with $M_{K\pi\pi^0}$ requirement applied. An $M_{K\pi\pi^0}$ cut is looser than our dEmBC requirement and the small slope of the $M_{K\pi\pi^0}$ requirement shows that it is very similar to using a wide ΔE cut only. In addition, the projections of m_{BC}, given in Figure A.18, show big tails of m_{BC} in the lowest two p_{miss} bins, which will be moved from the found to the not-found case when $1.856 < m_{BC} < 1.874$ GeV is applied. So, it can be concluded that the sensitivity is caused by mismatch of this m_{BC} tails. Note that this issue is not that these tails happen, but if data and MC agree about their size.

Furthermore, the m_{BC} tails have been proved to be due to bad photons, which could be junk photons or corruption of a true photon. First, a truth match is performed by pairing the two reconstructed π^0 photons with the two generated π^0 photons. Then, the reconstructed-generated daughter photon energies and their cosine differences are used to determinate if the truth match is good or not. Figure A.19 shows the tails can be removed by removing π^0 with poor truth match.

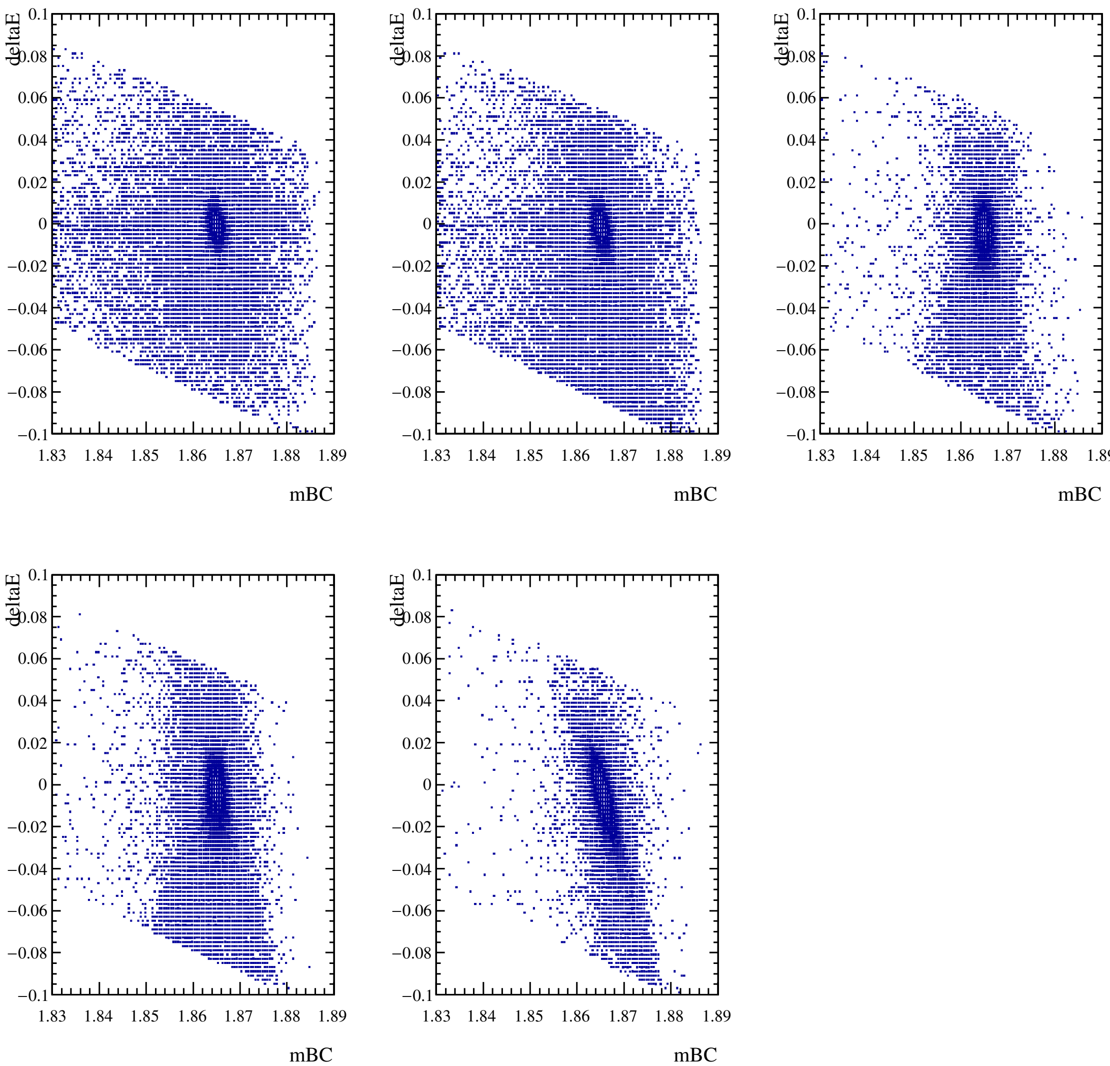

Figure A.17: ΔE vs m_{BC} for each p_{miss} bin with $M_{K\pi\pi^0}$ requirement applied

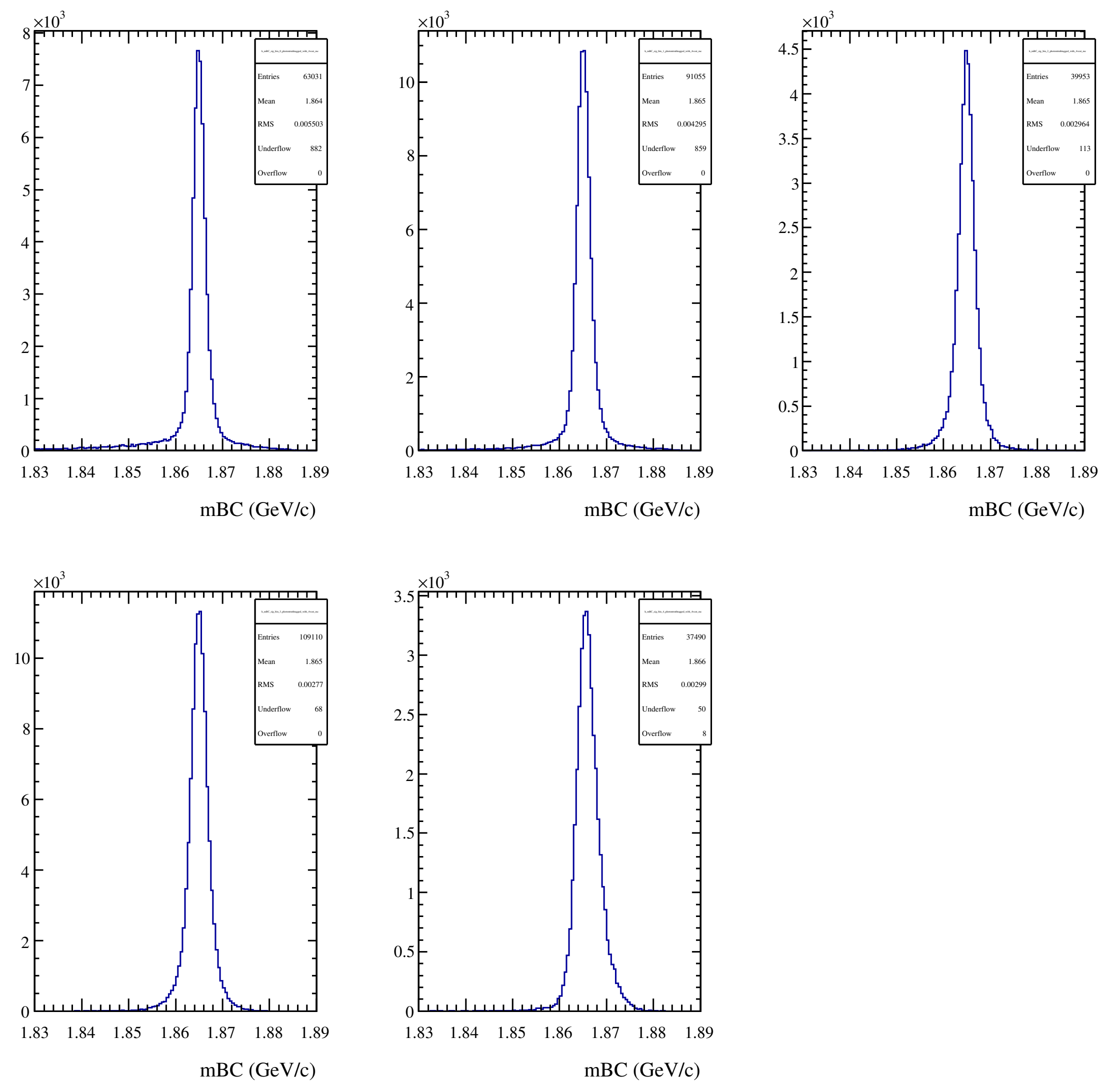

Figure A.18: m_{BC} for each p_{miss} bin

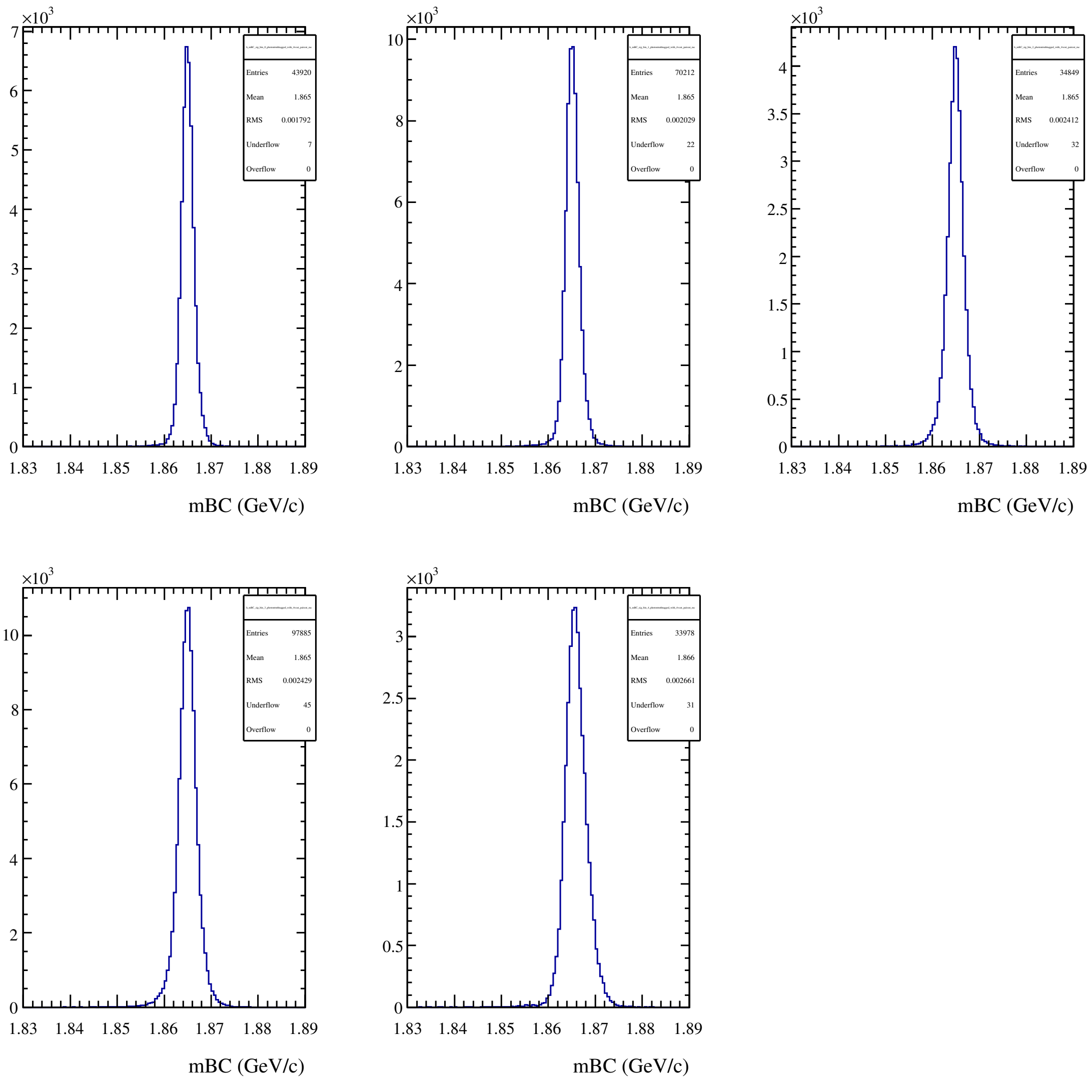

Figure A.19: m_{BC} for each p_{miss} bin (removing π^0 with poor truth match)

A.10 Further Investigation to the Sensitivity

Because the sensitivity is caused by photons, three classification criteria options (defining "found" π^0) related to photons have been studied (listed below). First, we use π^0s that are reconstructed using only photons coming from the CsI barrel. Second, we use π^0s that are reconstructed using only photons whose calorimeter position is at least 20°(or 10°) away from every charged track. Third, we use π^0s that are reconstructed using only photons whose energy is at least 50 MeV.

- Use barrel photons only (barrel)
- All track-photon angles $> 20°$ (dang 20) or $> 10°$ (dang 10)
- Require photon energy > 50 MeV (Emin)

The barrel option should exclude noise near the beam directions. In Figure A.20, closed points are the data-MC efficiency difference of $M_{K\pi\pi^0}$ v.s. dEmBC classifications and open points are with barrel option applied. There is not much change, indicating that noise near the beams is not important for the sensitivity.

The dang options are intended to exclude hadronic splitoffs, which create fake photons or alter real ones. In Figure A.21 (a), open points are with dang 20 option applied. Dang 20 option reduces the sensitivity to $M_{K\pi\pi^0}$ vs. dEmBC classifications. So, hadronic splitoffs are part of the effect. One can compare dang 20 with dang 10 option given in Figure A.21 (b). Dang 10 option doesn't reduce the sensitivity as obviouly as dang 20 does, especially at the second lowest p_{miss} bin.

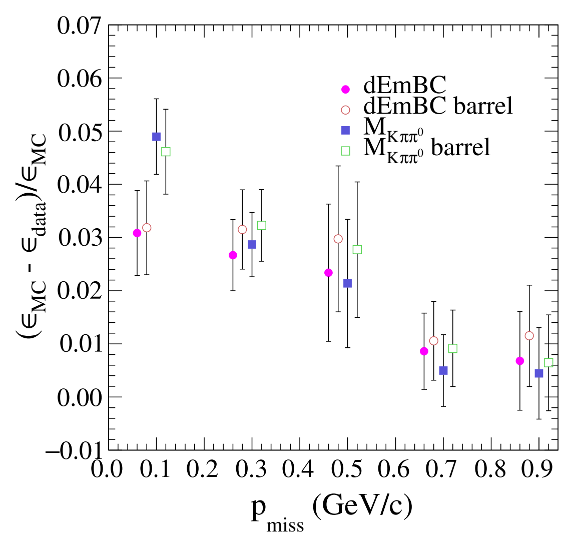

Figure A.20: Difference in π^0 reconstruction efficiency.

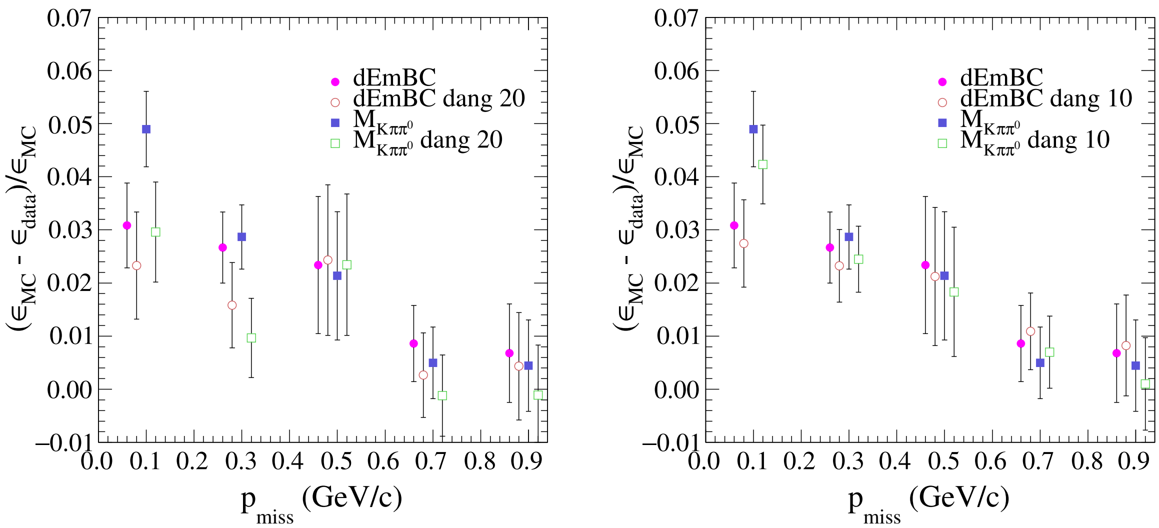

(a) dang 20

(b) dang 10

Figure A.21: Difference in π^0 reconstruction efficiency.

Raising the Emin cut excludes soft photons. In Figure A.22, open points are with Emin option applied. The Emin change also reduces the sensitivity to $M_{K\pi\pi^0}$ vs. dEmBC classifications. Soft photons are responsible to part of the effect. Both noise and hadronic splitoffs would be expected to cause larger changes for π^0s with soft photons. Based on results from the previous two (barrel-only and dang photon isolation) studies, we believe the effect is mostly splitoffs, and not noise, though either would suffice to give the Emin effect observed.

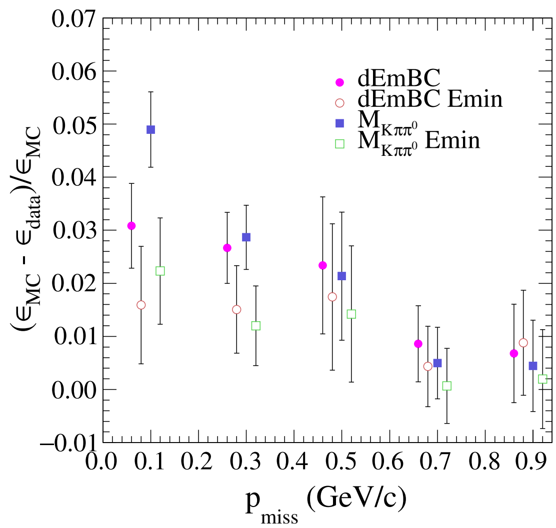

Figure A.22: Difference in π^0 reconstruction efficiency.

Overall, we see evidence that much of the sensitivity is due to hadronic splitoffs creating bad photons or altering real ones. In particular, improper simulation of these splitoff effects appear to be root cause of data-MC disagreement.

A.11 Suggested Usage

Since we observe the π^0 reconstruction efficiency difference is sensitive to π^0 quality requirements, we provide multiple result sets in order to match analyses more precisely. Users have to decide which set is most compatible with user's kinematic cut. In Table A.3, we provide results for two kinematic cuts:

- $-0.06 < \Delta E < 0.04$ GeV and $1.856 < m_{BC} < 1.874$ GeV (dEmBC)
- $1.78 < M_{K\pi\pi^0} < 1.92$ GeV ($M_{K\pi\pi^0}$)

Since hadronic splitoffs influence π^0 efficiency difference, we also provide values with photon isolation cuts: dang 20 and dang 10.

If it is not obvious which kinematic cut is more compatible, users could check whether or not the long m_{BC} tail is cut out. The presence (absence) of a long m_{BC} tail indicates more consistent with our $M_{K\pi\pi^0}$ (dEmBC) cuts.

Table A.3: Suggested difference in π^0 reconstruction efficiency, $(\epsilon_{MC} - \epsilon_{data})/\epsilon_{MC}$.

class'n criteria	$0.0 - 0.2$ GeV	$0.2 - 0.4$ GeV	$0.4 - 0.6$ GeV	$0.6 - 0.8$ GeV	$0.8 - 1$ Ge
dEmBC	0.031 ± 0.008	0.027 ± 0.007	0.023 ± 0.013	0.008 ± 0.007	0.007 ± 0.0
$M_{K\pi\pi^0}$	0.049 ± 0.007	0.029 ± 0.006	0.021 ± 0.012	0.005 ± 0.007	0.004 ± 0.0
dEmBC, dang 20	0.023 ± 0.010	0.016 ± 0.008	0.024 ± 0.014	0.003 ± 0.009	0.004 ± 0.0
$M_{K\pi\pi^0}$, dang 20	0.029 ± 0.009	0.010 ± 0.008	0.023 ± 0.015	-0.001 ± 0.008	-0.001 ± 0
dEmBC, dang 10	0.027 ± 0.008	0.023 ± 0.007	0.021 ± 0.013	0.011 ± 0.007	0.008 ± 0.0
$M_{K\pi\pi^0}$, dang 10	0.042 ± 0.007	0.025 ± 0.006	0.018 ± 0.012	0.007 ± 0.007	0.001 ± 0.0

A.12 An Alternative Selection of the Best π^0 Candidate: the Best π^0 Mass

Our results are sensitive to the method used to select the best π^0 candidate. The default selection of this memo is choosing the π^0 candidate resulting the smallest $|\Delta E|$ of $K\pi\pi^0$ (the smallest $|\Delta E|$ selection). However, we present the comparison with choosing the π^0 with the closet π^0 mass to the PDG value (the best mass selection). The absolute efficiencies of the smallest $|\Delta E|$ selection are larger than that of the best mass selection, shown in Figure A.23, because smallest $|\Delta E|$ selection tends to narrow the ΔE and four-vector mass distributions, which help events pass the classification criteria. We saw $2\% - 4\%$ absolute differences betweend two selections.

Figure A.24 shows that the efficiency differences of the smallest $|\Delta E|$ selection are systematically larger than that of the best mass selection, especially at $0.4-0.6$ GeV p_{miss} bin. We also notice the efficiency differences of the smallest $|\Delta E|$ selection for difference classification criteria are smaller in the two lowest momentum bins than those of the best mass selection. Numerical results for the best mass selection are provided in Table A.4

Table A.4: Suggested difference in π^0 reconstruction efficiency, $(\epsilon_{MC} - \epsilon_{data})/\epsilon_{MC}$.

class'n criteria	$0.0-0.2$ GeV	$0.2-0.4$ GeV	$0.4-0.6$ GeV	$0.6-0.8$ GeV	$0.8-1$ G
dEmBC	0.024 ± 0.007	0.013 ± 0.007	0.004 ± 0.014	-0.001 ± 0.008	$-0.005 \pm$
$M_{K\pi\pi^0}$	0.049 ± 0.007	0.021 ± 0.006	0.001 ± 0.013	-0.003 ± 0.007	$-0.003 \pm$
dEmBC, dang 20	0.012 ± 0.010	-0.002 ± 0.009	-0.002 ± 0.015	-0.005 ± 0.008	$-0.014 \pm$
$M_{K\pi\pi^0}$, dang 20	0.026 ± 0.009	-0.004 ± 0.008	-0.005 ± 0.014	-0.011 ± 0.008	$-0.012 \pm$
dEmBC, dang 10	0.019 ± 0.009	0.009 ± 0.007	0.000 ± 0.014	-0.001 ± 0.008	$-0.006 \pm$
$M_{K\pi\pi^0}$, dang 10	0.041 ± 0.008	0.015 ± 0.006	-0.004 ± 0.014	-0.002 ± 0.007	$-0.005 \pm$

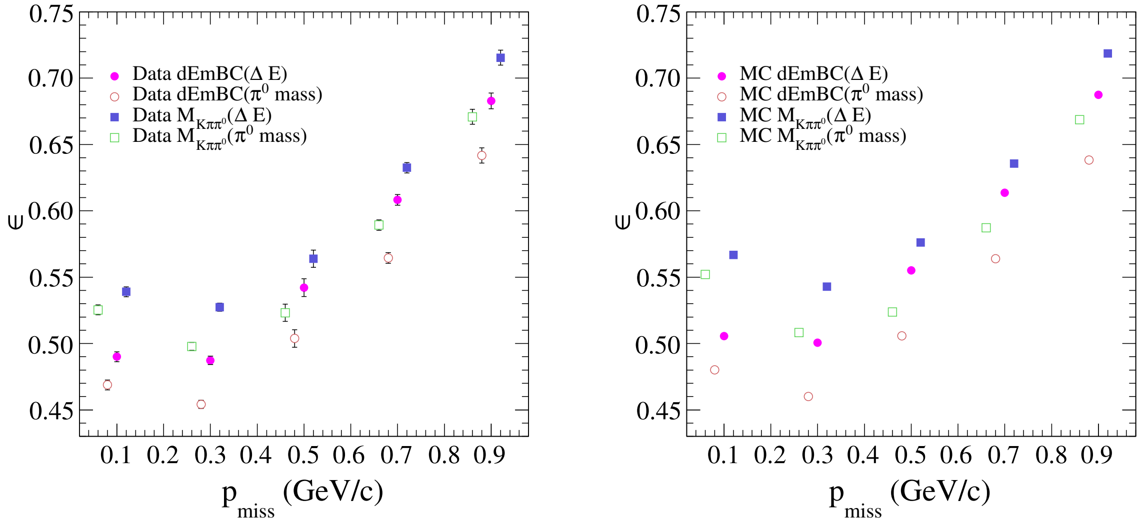

(a) π^0 Reconstruction efficiency for data.

(b) π^0 Reconstruction efficiency for MC

Figure A.23: 2011 and 2010 samples for different studies

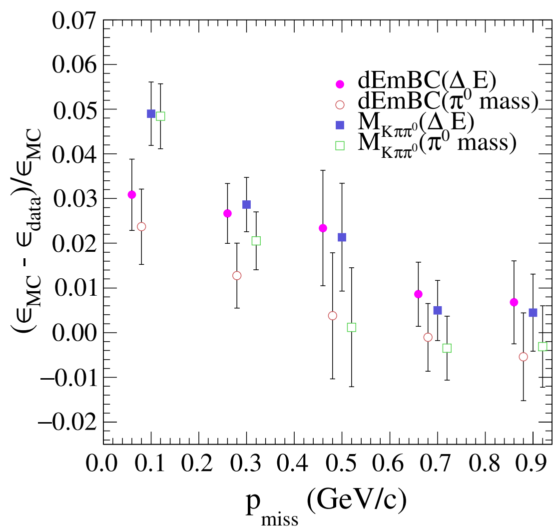

Figure A.24: Difference in π^0 reconstruction efficiency.

A.13 Input-Output Tests and Parameter Monitor

The standard template fitting procedure is to split MC samples into two equal parts and then use the second part to create templates used to fit the first part and the data samples. In order to ensure the fitting quality, there is the need to provide for input-output tests. The absolute efficiency input-output tests presented in five p_{miss} bins are given in Fig. A.25 (a). The red open-circles represent the fit results of the MC samples. The green closed-circles represent the truth information of the MC samples including the statistcal errors. The truth information means the $N_{\rm found}$ and the $N_{\rm not-found}$ in Eq. A.4 are determinated by sepatating each found and not-found cases into signal and background pieces according to the truth information and reading out the total number of events of the signal pieces. This procedure is the same procedure as creating the fitting templates. Details are given in Section A.5. Figure A.25 (a) shows our fitting results track the truth information very well considering the big jumps between different p_{miss} bins. In addition, the difference of the fit results and the truth informaion (red open-circles minus green closed-circles of Fig. A.25 (a)) are given in Fig. A.25 (b). The blue line is the expectation of zero if fit results match the truth information perfectly. The signal and background input-output tests are given in Fig. A.26, where the red circles represent the found cases and the blue triangles represent not-found cases, and the red horizontal line represents the expectation value, yield/truth = 1. Overall signal and background yields agree with truth information well. Although the background yields for found tend to be small in higher p_{miss} bins, the backgound size is $< 0.5\%$ of the signal size in signal

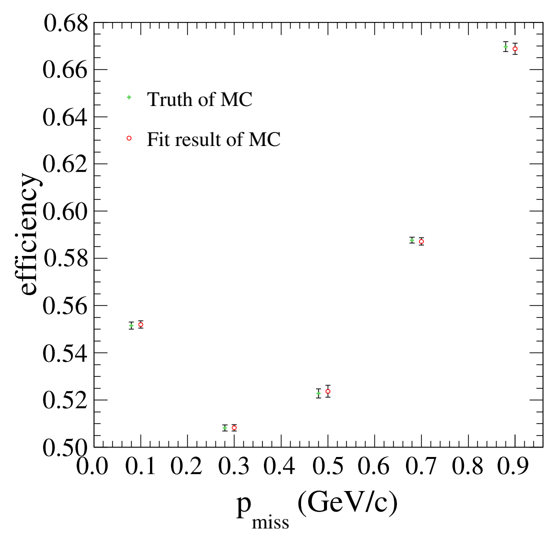

(a) The absolute efficiencies from the fit results and the truth information

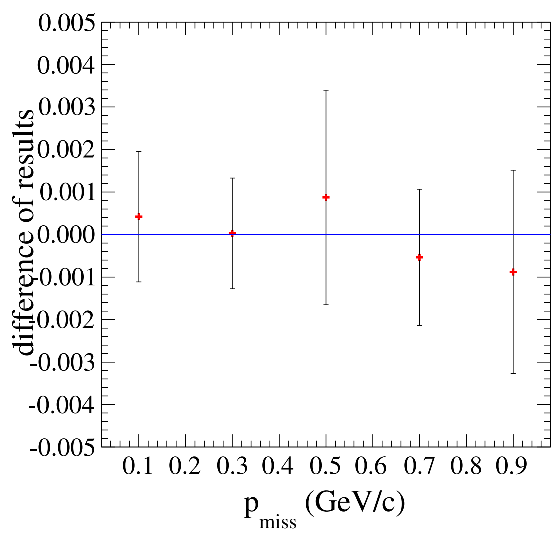

(b) The difference of the fit results and the truth information

Figure A.25: The absolute efficiency input-output tests

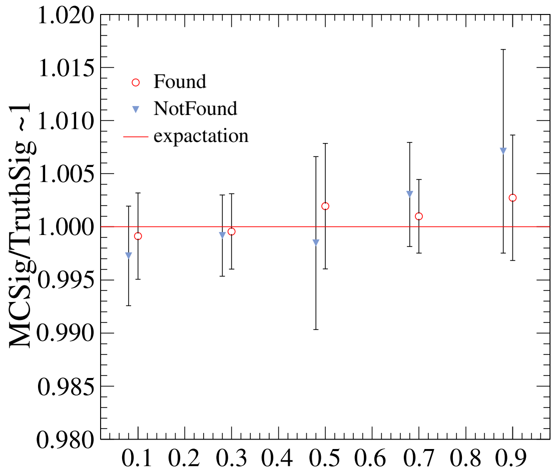

(a) Fitting signal yields divided by truth information

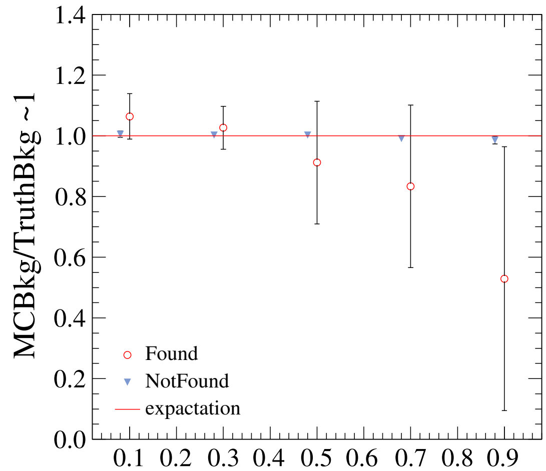

(b) Fitting background yields divided by truth information

Figure A.26: Fitting signal and background yields divided by truth information

region according to truth information. Note that the deviations in Fig. A.25 (b) are related as expected to the found and not-found differences in Fig. A.26 (a).

We also monitor the parameters of the smearing Gaussian functions. The means of the smearing Gaussian functions are given in Figure A.27. The means for MC fitting cluster around zero. The means for data fitting tend to be larger, up to 0.0025 GeV in higher p_{miss} bins, but 0.0025 GeV is just half of our MM^2 binning width.

The sigmas of the smearing Gaussians are shown vs. p_{miss} bin in Fig. A.28. Naively, the MC sigma values are expected to be zero. But since they must be ≥ 0, it is perhaps not surprising to see non-zero values. The values are always less than our bin width (0.003 GeV), and even for large p_{miss} are much smaller than the peak width. It is curious that the values are sometimes inconsistent with zero, but given their small absolute size, we are not too concerned. The values of the smearing sigmas for data are larger. We expect non-zero values for data since the MC templates have somewhat over-optimistic resolutions: a well-known feature of BESIII MC. Since the peak width increases with increasing p_{miss}, increasing all peak resolutions by a constant fraction (if that is indeed what is needed) would require increasing values of the smearing sigmas, as we observe.

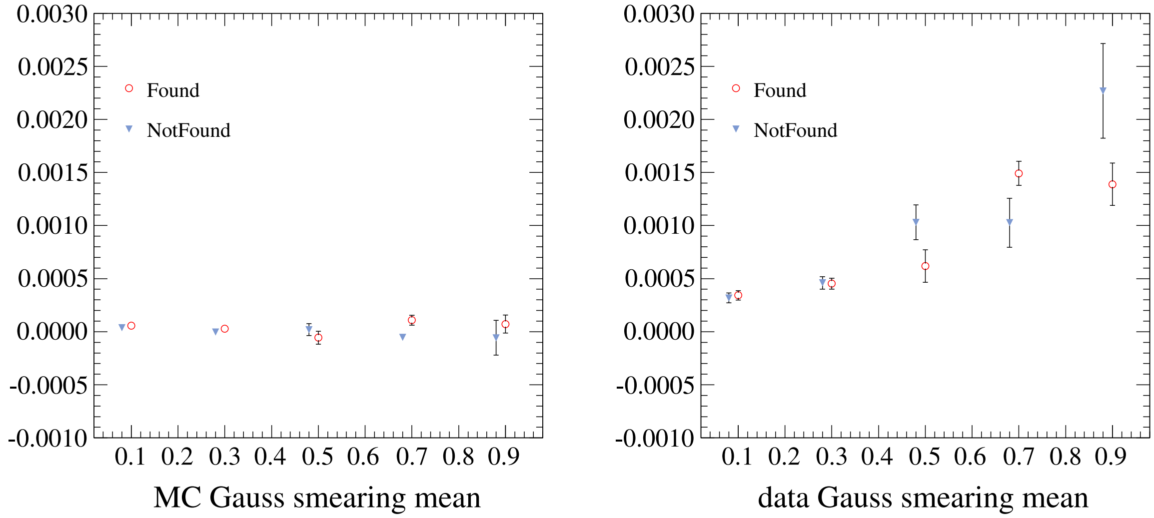

(a) MC fitting (b) Data fitting

Figure A.27: The means of the smearing Gaussian functions

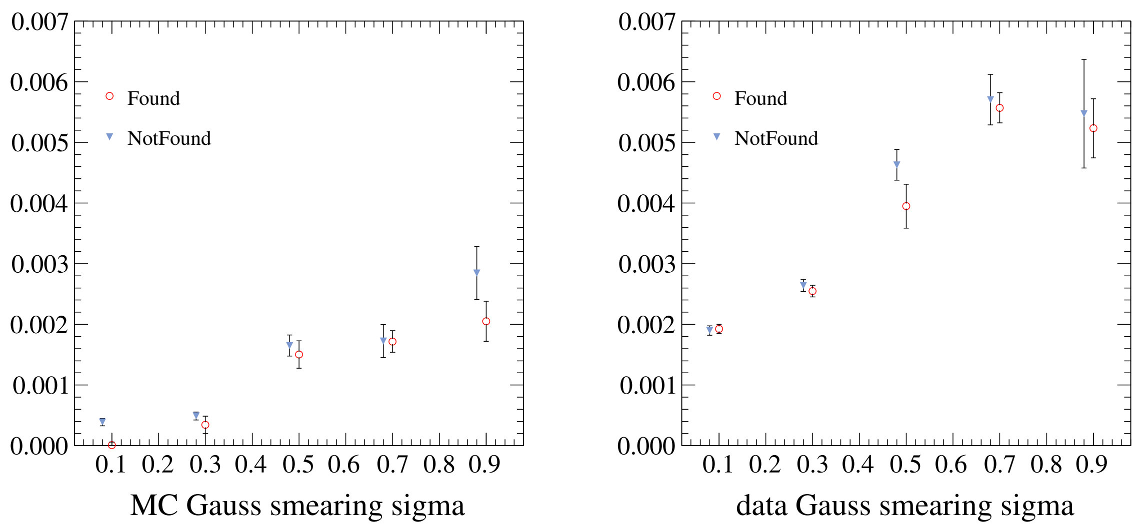

(a) MC fitting (b) Data fitting

Figure A.28: The sigmas of the smearing Gaussian functions

A.14 A Wide π^0 Classification Study

In this section, we study a wide classification criterion, $1.60 < M_{K\pi\pi^0} < 2.0$ GeV, and compare it to the standard $M_{K\pi\pi^0}$ and dEmBC classification criteria. The absolute efficiencies and the efficiency differences are shown in Figures A.29 and A.30, respectively. All absolute efficiencies increase as expected, because a wider classification allows more π^0 candidates to be classified as good candidates.

The effciency differences of the wide classification have significant shifts from that of the standard $M_{K\pi\pi^0}$ and dEmBC classification criteria. However, this very wide cut is unlike any criteria used in a real physics analysis, and hence it is both an overly stringent test of data-MC agreement and not relevant as a guide to systematics in actual analyses. But we have left it in for completeness.

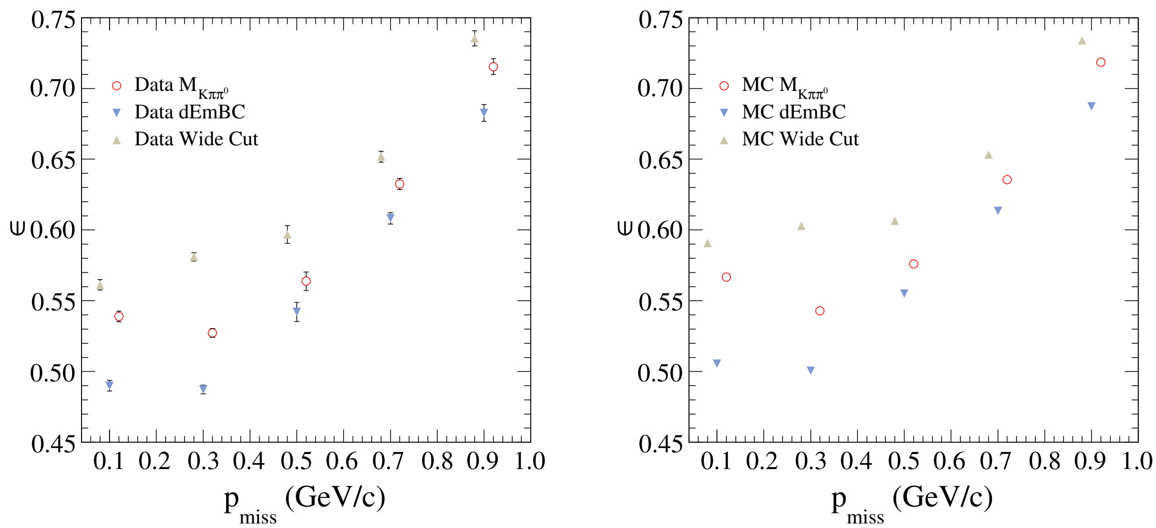

(a) π^0 Reconstruction efficiency for data.

(b) π^0 Reconstruction efficiency for MC

Figure A.29: 2011 and 2010 samples for different studies

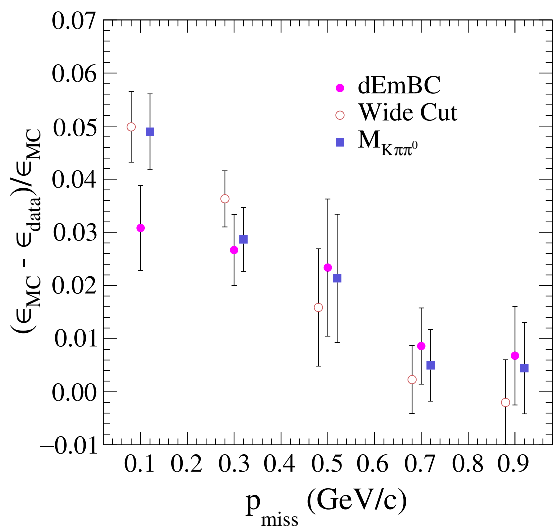

Figure A.30: Difference in π^0 reconstruction efficiency.

A.15 Background Fractions

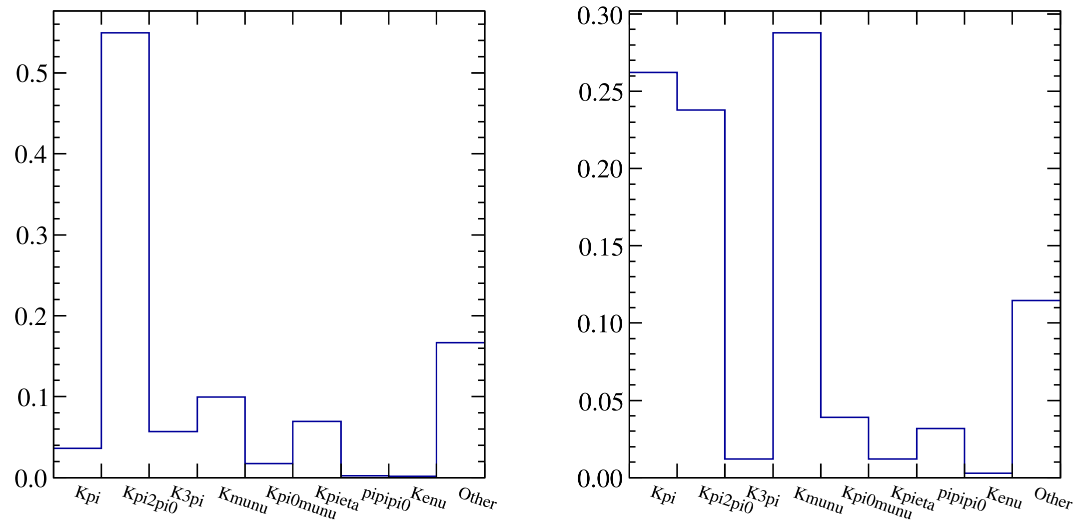

Figure A.31: Background mode fractions in MM^2 distribution for the not found (left) and the found (right) cases in $0 < p_{miss} < 200$ MeV bin.

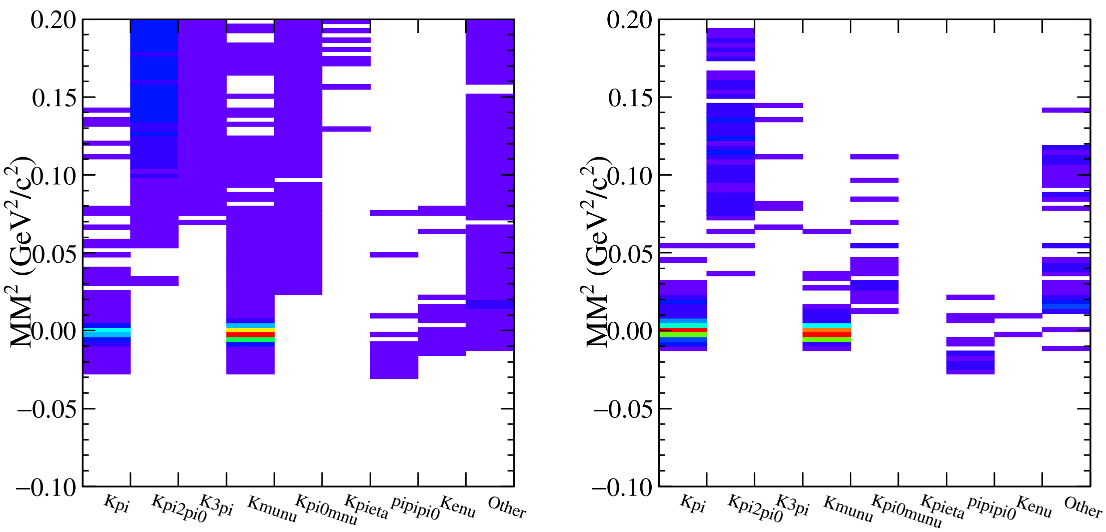

Figure A.32: MM^2 vs background modes distribution for the not found (left) and the found (right) cases in $0 < p_{miss} < 200$ MeV bin.

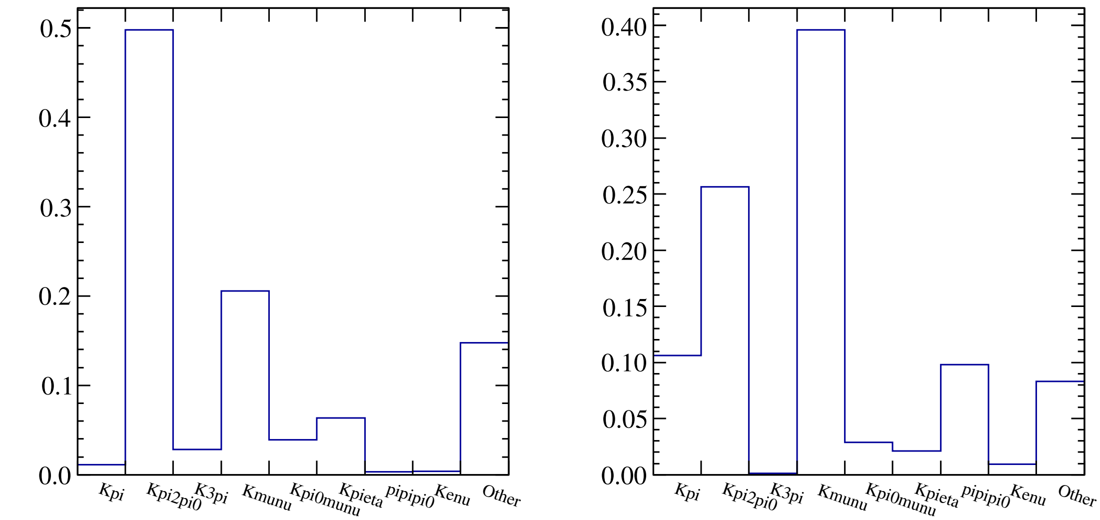

Figure A.33: Background mode fractions in MM^2 distribution for the not found (left) and the found (right) cases in $200 < p_{miss} < 400$ MeV bin.

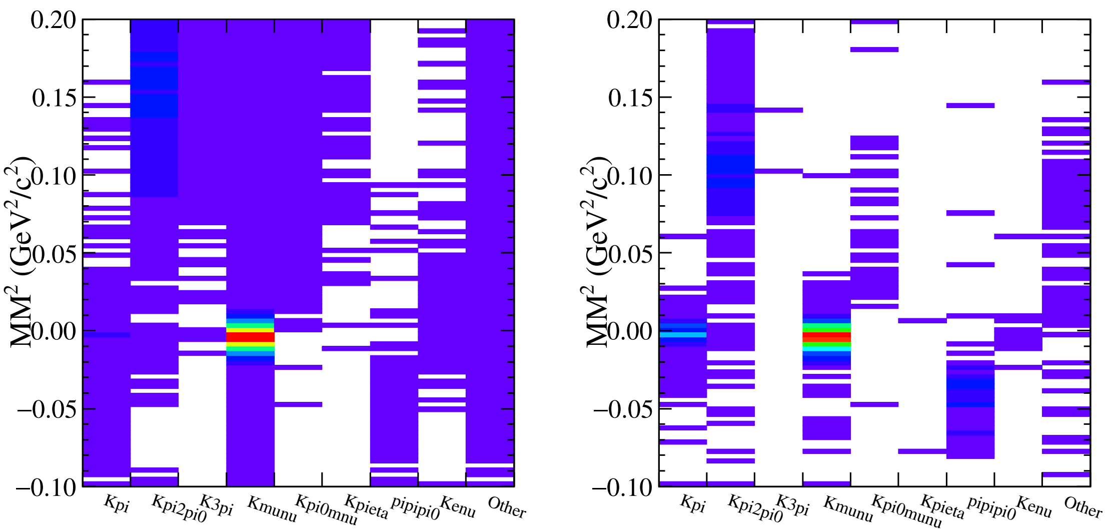

Figure A.34: MM^2 vs background modes distribution for the not found (left) and the found (right) not cases in $200 < p_{miss} < 400$ MeV bin.

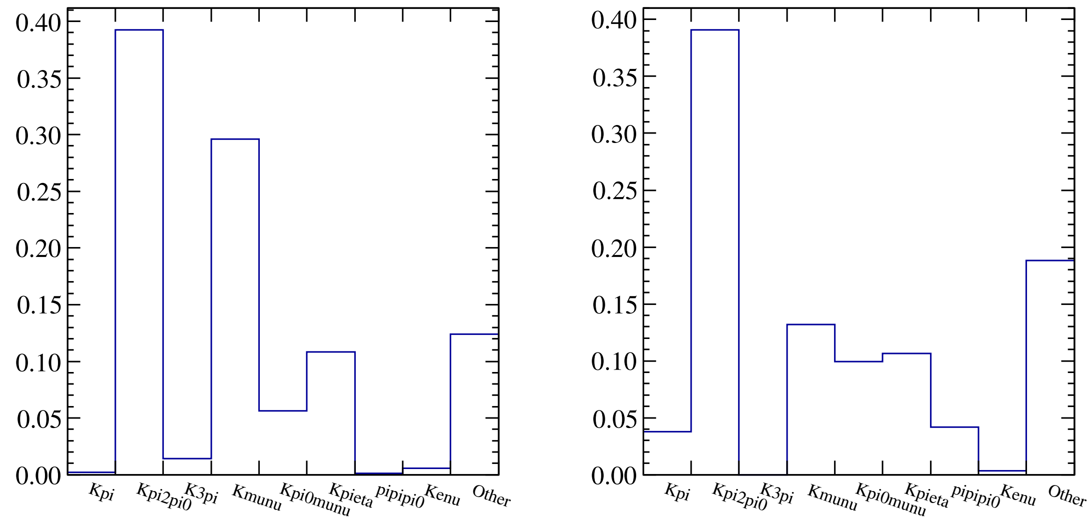

Figure A.35: Background mode fractions in MM^2 distribution for the not found (left) and the found (right) cases in $400 < p_{miss} < 600$ MeV bin.

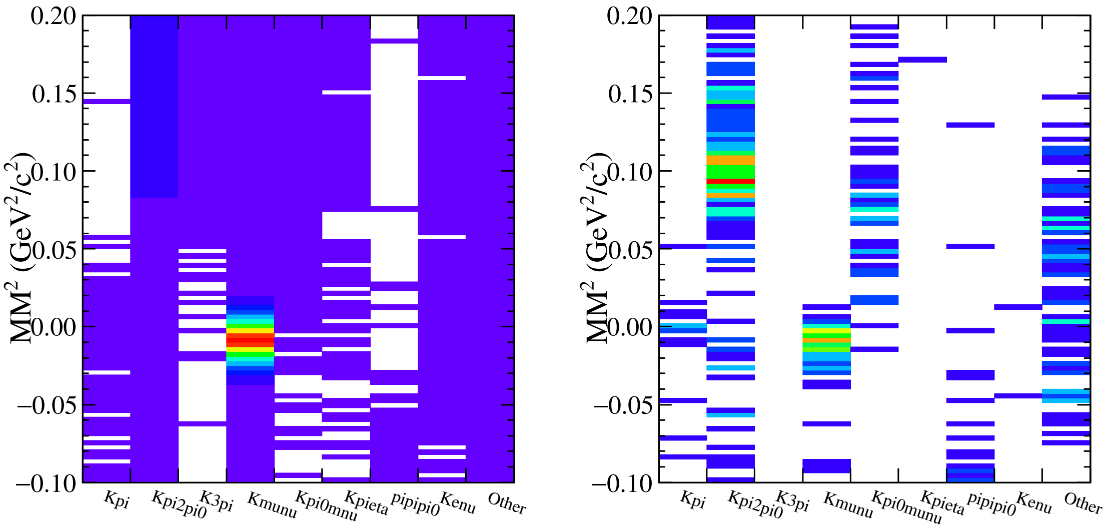

Figure A.36: MM^2 vs background modes distribution for the not found (left) and the found (right) cases in $400 < p_{miss} < 600$ MeV bin.

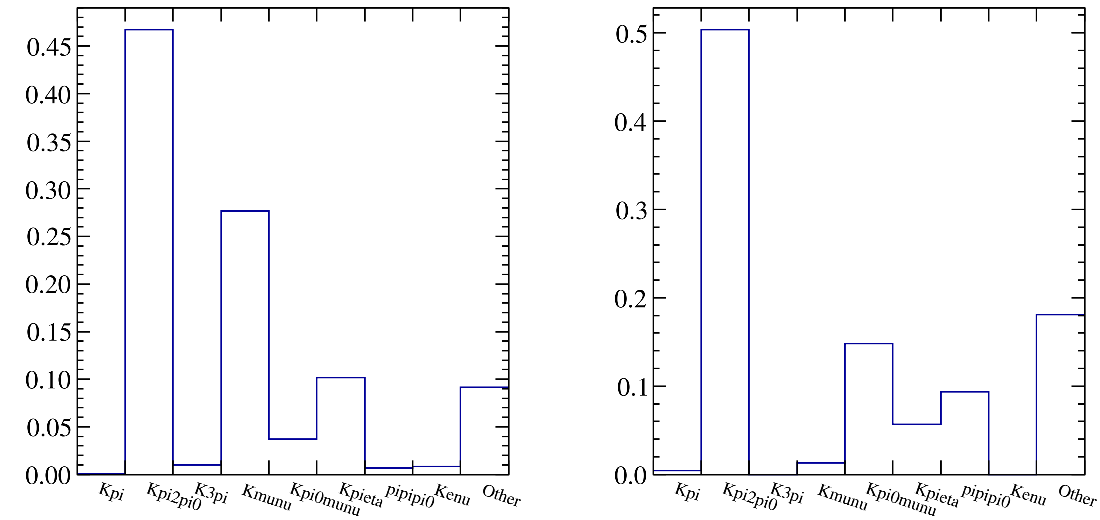

Figure A.37: Background mode fractions in MM^2 distribution for the not found (left) and the found (right) cases in $600 < p_{miss} < 800$ MeV bin.

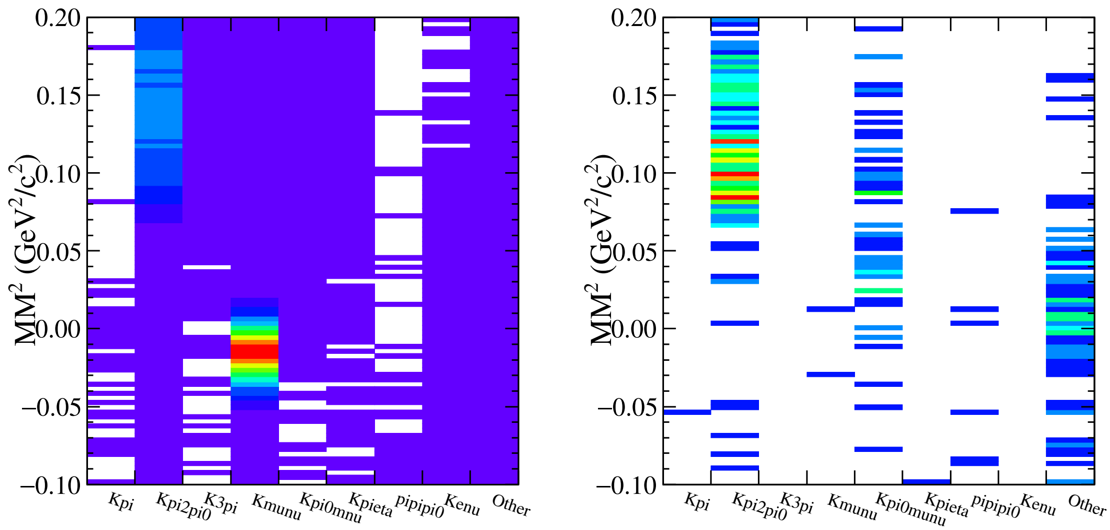

Figure A.38: MM^2 vs background modes distribution for the not found (left) and the found (right) cases in $600 < p_{miss} < 800$ MeV bin.

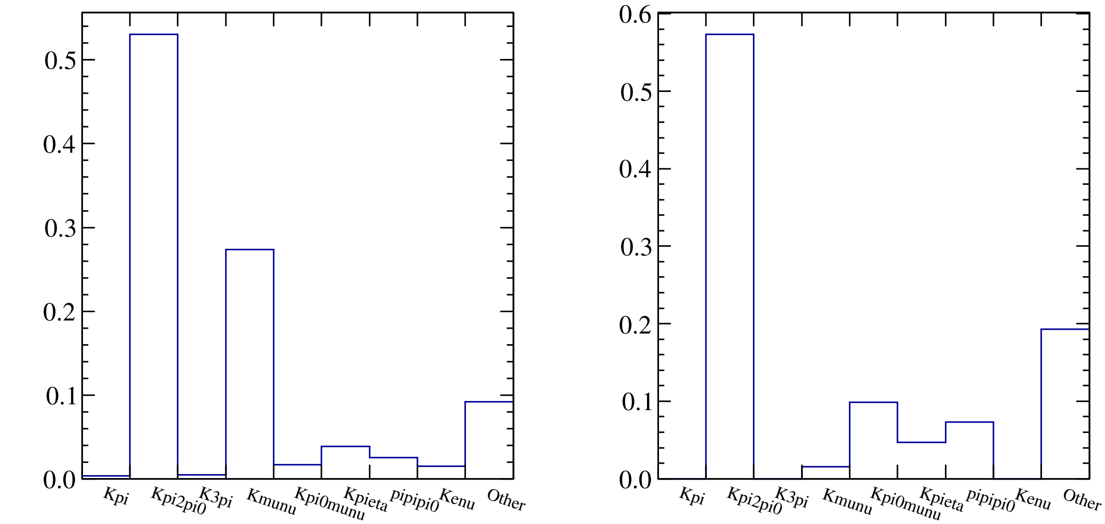

Figure A.39: Background mode fractions in MM^2 distribution for the not found (left) and the found (right) cases in $800 < p_{miss} < 1000$ MeV bin.

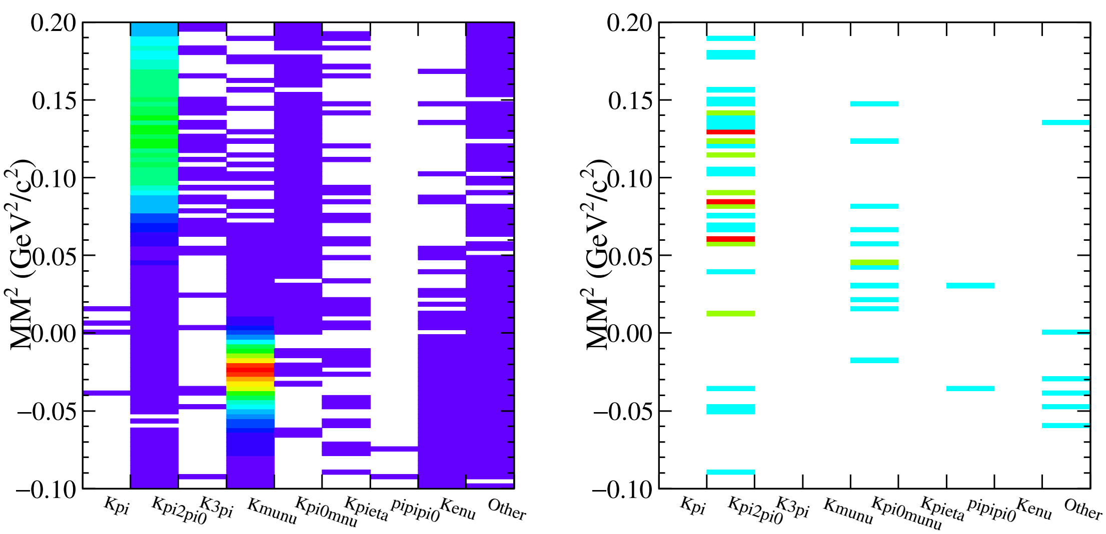

Figure A.40: MM^2 vs background modes distribution for the not found (left) and the found (right) cases in $800 < p_{miss} < 1000$ MeV bin.

A.16 Monte-Carlo MM^2 fits

A.16.1 2011 and 2010 MC samples

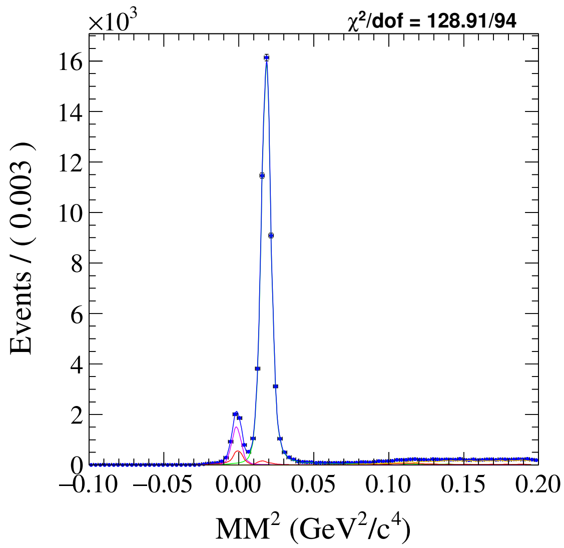

(a) MM^2 fit when a π^0 is not found.

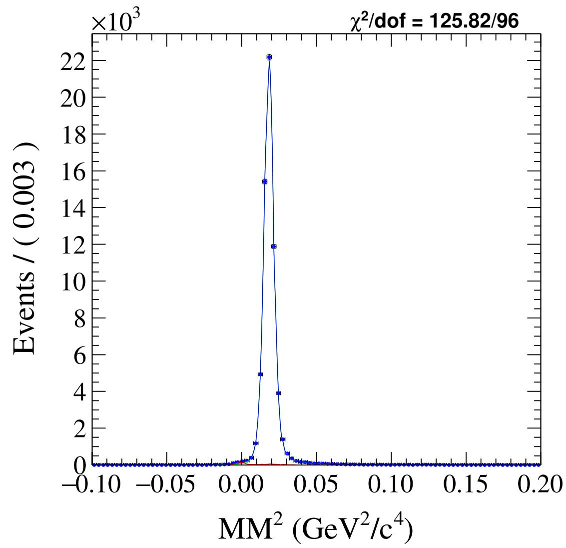

(b) MM^2 fit when a π^0 is found.

Figure A.41: MM^2 fit in $0 < p_{miss} < 200$ MeV bin for 2011 and 2010 MC samples. Green curve represents the signal; violet, $K\mu\nu$ background; orange $K\pi\pi^0\pi^0$ background; and red curve for all the other background.

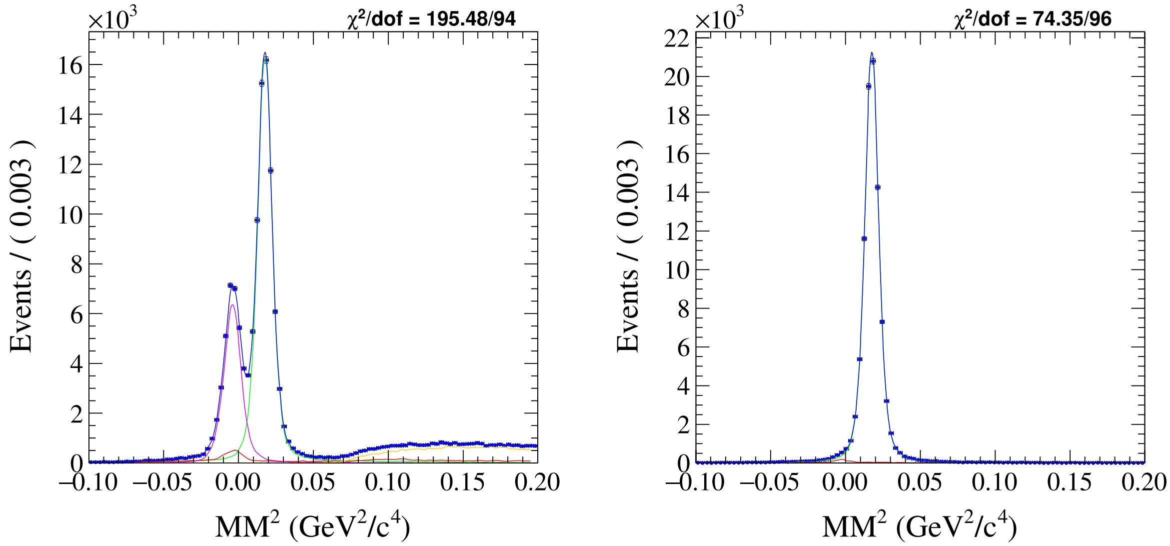

(a) MM^2 fit when a π^0 is not found.

(b) MM^2 fit when a π^0 is found.

Figure A.42: MM^2 fit in $200 < p_{miss} < 400$ MeV bin for 2011 and 2010 MC samples. Green curve represents the signal; violet, $K\mu\nu$ background; orange $K\pi\pi^0\pi^0$ background; and red curve for all the other background.

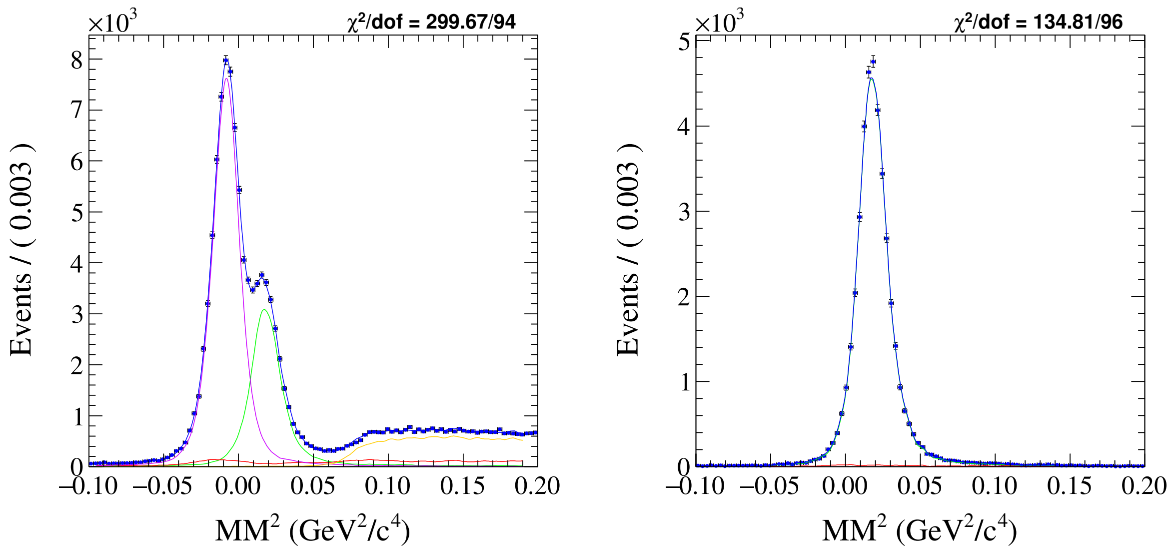

(a) MM^2 fit when a π^0 is not found.

(b) MM^2 fit when a π^0 is found.

Figure A.43: MM^2 fit in $400 < p_{miss} < 600$ MeV bin for 2011 and 2010 MC samples. Green curve represents the signal; violet, $K\mu\nu$ background; orange $K\pi\pi^0\pi^0$ background; and red curve for all the other background.

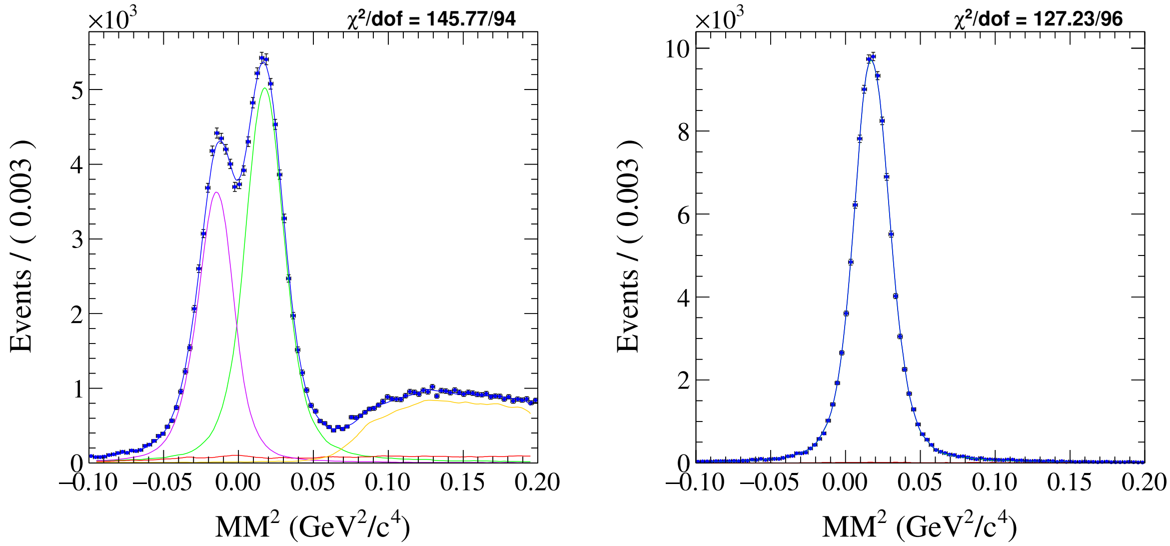

(a) MM^2 fit when a π^0 is not found. (b) MM^2 fit when a π^0 is found.

Figure A.44: MM^2 fit in $600 < p_{miss} < 800$ MeV bin for 2011 and 2010 MC samples. Green curve represents the signal; violet, $K\mu\nu$ background; orange $K\pi\pi^0\pi^0$ background; and red curve for all the other background.

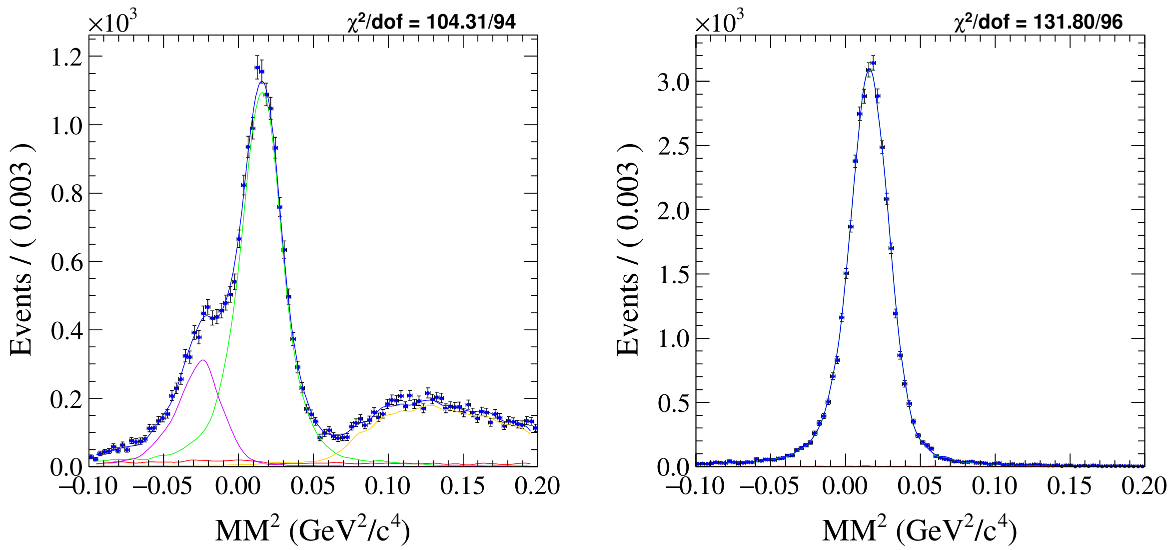

(a) MM^2 fit when a π^0 is not found. (b) MM^2 fit when a π^0 is found.

Figure A.45: MM^2 fit in $800 < p_{miss} < 1000$ MeV bin for 2011 and 2010 MC samples. Green curve represents the signal; violet, $K\mu\nu$ background; orange $K\pi\pi^0\pi^0$ background; and red curve for all the other background.

A.17 Unconstrained π^0 mass

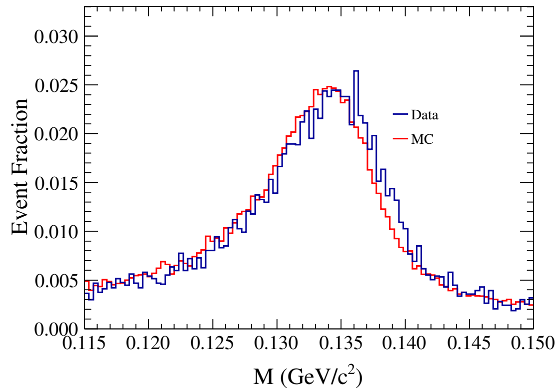

Figure A.46: π^0 mass in $0 - 200$ MeV bin.

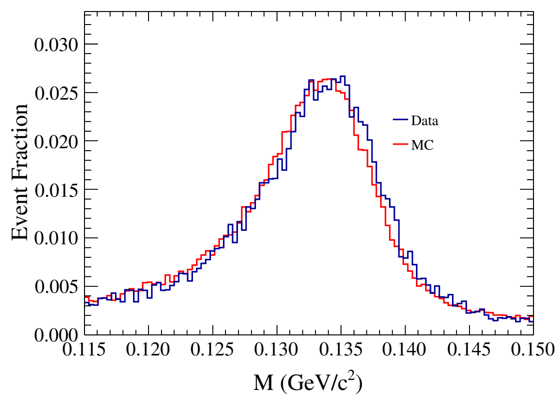

Figure A.47: π^0 mass in $200 - 400$ MeV bin.

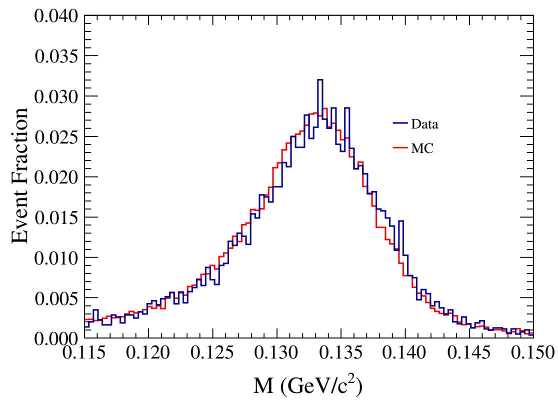

Figure A.48: π^0 mass in $400 - 600$ MeV bin.

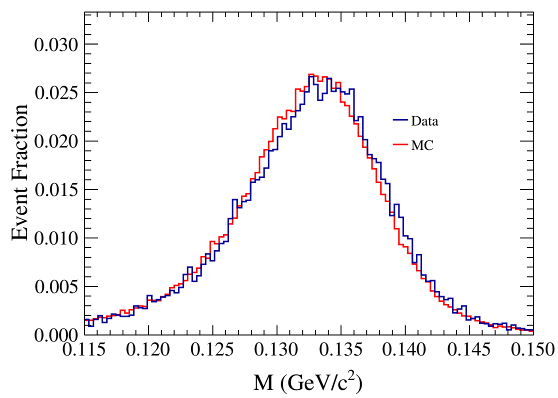

Figure A.49: π^0 mass in $600 - 800$ MeV bin.

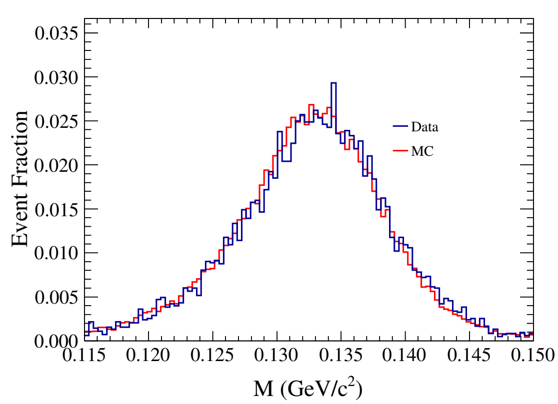

Figure A.50: π^0 mass in $800 - 1000$ MeV bin.

Appendix B

An Analytic Method of M_{BC} vs. M_{BC} Two-Dimensional Fit

Signal yields of double tag candidates can be determined by fitting to the two-dimensional M_{BC} vs. M_{BC} distribution, Figure B.1. Due to non-factorizable initial state radiation (ISR) and mispartition effects, the two-dimensional M_{BC} vs. M_{BC} distribution is not a product of two one-dimensional M_{BC} distributions. In this chapter, we discuss an M_{BC} vs. M_{BC} fitting technique introduced by CLEO [33].

According to the procedure, the distribution for double-tag candidates in the $M_{\mathrm{BC}} - M_{\mathrm{BC}}$ plane can be separated into four components: signal peak, diagonal mispartition background, horizontal and vertical background bands, and (nearly) flat background. The features of each component are discussed in the following.

B.1 Signal Peak

If event candidates are tagged correctly on both sides, they form a peak around $M_{\mathrm{BC}}(D) = M_{\mathrm{BC}}(\bar{D}) = M_D$. (In the following, we use M_{BC} and $\bar{M}_{\mathrm{BC}}$ to represent $M_{\mathrm{BC}}(D)$ and $M_{\mathrm{BC}}(\bar{D})$, respectively.) The resolution is mainly due to the beam energy spread, $\psi(3770)$ width, and momentum resolution of the detector. This signal peak also includes a diagonal ISR tail oriented toward high M_{BC}. The two-dimensional signal peak line-shape is given by

$$\begin{aligned} w_{D\bar{D}}(M_{\mathrm{BC}}, \bar{M}_{\mathrm{BC}}) \quad = \quad & \frac{M_{\mathrm{BC}}}{p}\frac{\bar{M}_{\mathrm{BC}}}{\bar{p}}\int_{2m_D}^{\infty} r(p; q(E), \sigma_p) \\ & r(\bar{p}; q(E), \bar{\sigma}_p) f_\psi(E) dE\,, \end{aligned} \tag{B.1}$$

where q is the nominal magnitude of the D meson momentum, p ($\bar{p}$) is the magnitude of the reconstructed D ($\bar{D}$) momentum, σ_p ($\bar{\sigma}_p$) is momentum resolution. $f_\psi(E)$ is the energy distribution of the produced $\psi(3770)$ mesons considering the beam energy spread, the width of the $\psi(3770)$, and ISR effects. In addition, $r(p; q(E), \sigma_p)$ and

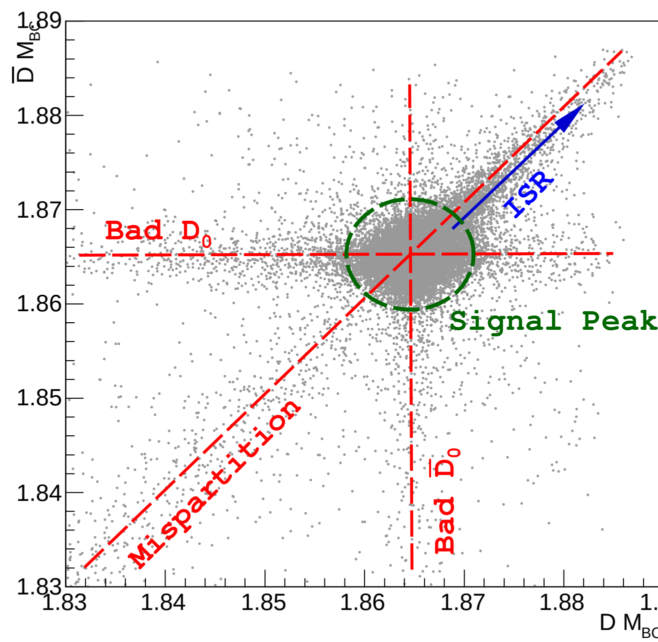

Figure B.1: example plots of M_{BC} vs. M_{BC} two-dimensional distribution.

$r(\bar{p}; q(E), \bar{\sigma}_p)$ are functions used to describe the momentum resolution of the detector. In this analysis, $r(p; q(E), \sigma_p)$ is derived from a sum of three Gaussian functions:

$$
\begin{aligned}
G(\mathbf{p}; \mathbf{q}, \sigma_p, f_a, s_a, f_b, s_b) &= \frac{1}{(2\pi)^{3/2}\sigma_p^3}\Bigg[(1 - f_a - f_b)e^{-(\mathbf{p}-\mathbf{q})^2/(2\sigma_p^2)} \\
&+ \frac{f_a}{s_a^3}e^{(\mathbf{p}-\mathbf{q})^2/(2(s_a\sigma_p)^2)} + \frac{f_b}{(s_a s_b)^3}e^{(\mathbf{p}-\mathbf{q})^2/(2(s_a s_b \sigma_p)^2)}\Bigg] ,
\end{aligned} \tag{B.2}
$$

where f_a, f_b determine the fractional sizes, and s_a, s_b determine the width ratios of these three Gaussian functions. Since $M_{\rm BC}$, $\bar{M}_{\rm BC}$, and E in Eq. B.1 are independent of the polar and the azimuth angles, $G(\mathbf{p}; \mathbf{q}, \sigma_p, f_a, s_a, f_b, s_b)$ can be reduced to $r(p; q(E), \sigma_p)$ by intergraling over the polar and the azimuth angles:

$$
\begin{aligned}
r(p; q(E), \sigma_p) &= \int G(\mathbf{p}; \mathbf{q}, \sigma_p, f_a, s_a, f_b, s_b)p^2 d\Omega \\
&= \frac{p}{q}\frac{1}{\sqrt{2\pi}\sigma_p}\Bigg[(1 - f_a - f_b)(e^{-(p-q)^2/(2\sigma_p^2)} - e^{-(p+q)^2/(2\sigma_p^2)}) \\
&+ \frac{f_a}{s_a^3}(e^{-(p-q)^2/(2(s_a\sigma_p)^2)} - e^{-(p+q)^2/(2(s_a\sigma_p)^2)}) \\
&+ \frac{f_a}{(s_a s_b)^3}(e^{-(p-q)^2/(2(s_a s_b\sigma_p)^2)} - e^{-(p+q)^2/(2(s_a s_b\sigma_p)^2)})\Bigg] .
\end{aligned} \tag{B.3}
$$

The function $r(\bar{p}; q(E), \bar{\sigma}_p)$ is derived in the same way, and shares f_a, f_b, s_a, and s_b with $r(p; q(E), \sigma_p)$.

B.2 Horizontal and Vertical Background Bands

If candidates are reconstructed correctly on one side but not the other side, they form a peak in the corresponding correctly-reconstructed axis and spread out on the other axis, which visually forms a horizontal or vertical band centered at $M_{\rm BC} = M_D$ or $\bar{M}_{\rm BC} = M_D$, respectively. To represent this background, a D meson line-shape, w_D, for the correctly reconstructed side is multiplied by an ARGUS background for the incorrectly reconstructed side. Assuming the D is correctly reconstructed and $\bar{D}$ is not, this background is given by

$$
\begin{aligned}
w_D(M_{\rm BC}) \times ARGUS(\bar{M}_{\rm BC}) &= \frac{M_{\rm BC}}{p}\int_{2m_D}^{\infty} r(p; q(E), \sigma_p) f_\psi(E) dE \\
&\times \; ARGUS(\bar{M}_{\rm BC}) ,
\end{aligned} \tag{B.4}
$$

where $r(p; q(E), \sigma_p)$ is given by Eq. B.3. Comparing to Eq. B.1, $w_D(M_{\rm BC})$ includes only one $r(p; q(E), \sigma_p)$ instead of both.

B.3 Diagonal Mispartition Background

Double tag modes sharing the same final state particle combination form a diagonal mispartition band, in which one or more particles are moved between the D daughtors and the $\bar{D}$ daughtors. Thus, the momentum of each side is misreconstructed by the same amount. Correspondingly, $M_{\rm BC}$ of each side shifts the same amount. In other words, the $M_{\rm BC}$ of both sides are equal since the momenta of both D candidates are equal in magnitude after any particle movement between candidates, due to the sum of momenta being zero (assuming all daughter particles are well-reconstructed). For example, $K^-\pi^+\pi^0$ vs. $K^-\pi^+\pi^0$ could fake $K^-\pi^+\pi^0\pi^0$ vs. $K^-\pi^+$ by "mispartitioning" via moving a π^0. Note that the correct candidates should contribute little to the mispartition band due to choosing among multiple candidates based on the best ΔE values.

To represent this background, an ARGUS background shape in the diagonal axis, $(\bar{M}_{\rm BC}+M_{\rm BC})/2$, is multiplied by a Gaussian in the anti-diagonal axis, $(\bar{M}_{\rm BC}-M_{\rm BC})/2$.

B.4 Flat Background

There is a nearly flat and small background which comes from candidates reconstructed incorrectly on both sides. To describe this background, an ARGUS background in $M_{\rm BC}$ is multiplied by an ARGUS background in $\bar{M}_{\rm BC}$.

B.5 Example

A sample fitting result is shown in Figure B.2. The sample used is a $K^-\pi^+\pi^0\pi^0$ vs. $K^+\pi^-$ double-tag sample. In the projections, the small Argus background in $K^-\pi^+\pi^0\pi^0$ leads to a background peak in the $K^+\pi^-$ $M_{\rm BC}$ on events with a correct tag and fake signal (the horizontal band). The corresponding vertical band is very small, yielding a negligible background peak for $K^-\pi^+\pi^0\pi^0$.

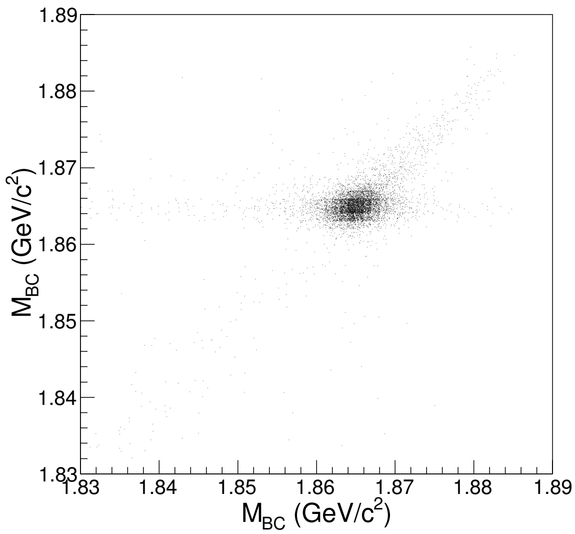

(a) The distribution for $K^-\pi^+\pi^0\pi^0$ vs. $K^-\pi^+$ candidates in the $M_{\rm BC} - M_{\rm BC}$ plane

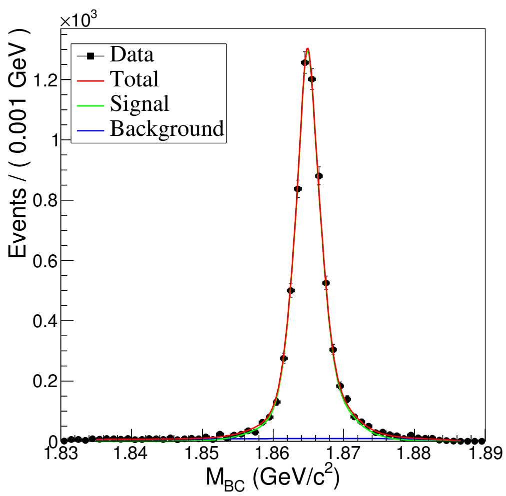

(b) Projection on $M_{\rm BC}$ of $K^-\pi^+\pi^0\pi^0$

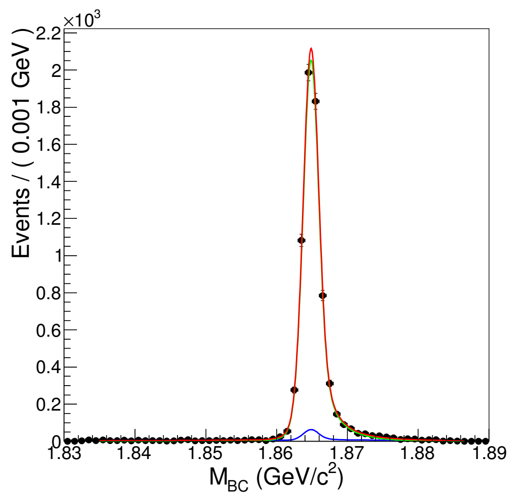

(c) Projection on $M_{\rm BC}$ of $K^+\pi^-$

Figure B.2: Example fitting of $K^-\pi^+\pi^0\pi^0$ vs. $K^+\pi^-$. The red lines are the total fits and the blue lines are the total background.

Appendix C

Goodness-of-Fit in Unbinned Maximum-Likelihood Fits

A maximum-likelihood fit to unbinned data, which is not limited by small statistics, is generally more powerful than a χ^2 fit to binned data, and frequently utilized by high energy physicists to extract information about parameters of interest in multi-dimensional analyses. However, the measurement of goodness-of-fit is not available in a unbinned maximum-likelihood fit itself, where the comparison of likelihood values tells only which hypothesis is better, instead of how good a hypothesis is. In order to obtain the goodness-of-fit, a common method is to bin the data and calculate the χ^2 after an unbinned maximum-likelihood fit. However, binning the data always loses detailed information, especially in case of low statistics. Actually, there are many existing methods for obtaining a goodness-of-fit measure after performing an unbinned maximum-likelihood fit [32].

The "point-to-point dissimilarity method" is a very powerful tool even for low data statistics, but the drawback is requiring sizable amount of computing resource. The concept of this method is to compare every two points, one from data and one from MC, with a weight function. This weight function could be changed in different cases to optimize the power of this method. The "distance to nearest neighbor method" has a poor rejection power, but its needing very few processing time makes it a good tool for quick check. The concept is that the multi-dimensional hyper-spherical volume around any given data event to its nearest neighbor is inversely proportional to density, in other words, the fit PDF, if the hypothesis is correct. Another method is called as the "local-density method", which has a good rejection power requiring non-trivial amount of computing resource. One downside worth being aware is that it takes some efforts to determine the p-value, which may need generating MC samples. Its concept is that in a region centered at a certain event with a certain (multi-dimensional) radius, the number of events dividing the (multi-dimensional) area, called local-density, should be comparable to the expectation from PDF. In the following, I will discuss the "mixed-sample method" in detail, which is the goodness-of-fit method used in the

PWA.

The concept of the mixed-sample method is that the mixing of two samples will be complete if the hypothesis is valid: the parent distributions of the two samples are identical. In other words, in a combination of two samples, any given event from one sample will be well surrounded by events from another sample if the distributions of the two samples match, while events tend to be surrounded by events from the same sample otherwise. Before one quantitatively describes the concept of the mixed-sample method, the "distance" in multi-dimensional space must be defined. Here, we use the normalized Euclidean distance as the distance between event i and event j,

$$|\vec{x}_i - \vec{x}_j|^2 = \sum_{\nu=1}^{D} \left(\frac{x_i^\nu - x_j^\nu}{w_\nu} \right)^2 , \tag{C.1}$$

where D is the number of dimensions, $x^\nu_{i(j)}$ is the position of event $i(j)$ in the multi-dimensional space, and w_ν is the weight. There is no unique choice of w_ν. One choice is the root mean square of x^ν and another one is $x_\nu^{\max} - x_\nu^{\min}$. However, any reasonable choice of w_ν should result in the same final conclusion of this goodness-of-fit test.

After the multi-dimensional distance is defined, one can define a statistic to quantitatively describe the neighbors of events in the combined sample. For convenience, we use "a" to denote one of the two samples and "b" the other one. The statistic, T, is given by

$$T = \frac{1}{n_k(n_a + n_b)} \sum_{i=1}^{n_a+n_b} \sum_{k=1}^{n_k} I(i,k) , \tag{C.2}$$

where $I(i,k) = 1$ if event i and its k^{th} nearest neighbor are components of the same sample and $I(i,k) = 0$ otherwise, $n_{a(b)}$ indicates the number of events in sample $a(b)$,and n_k denotes the number of nearest neighbors considered. If the parent distributions of the two samples are not identical, the statistic T will achieve a larger than expected value toward 1 because the neighbors of a given event tends to be from the same sample. If the parent distributions are identical, $(T - \mu_T)/\sigma_T$ will be a standard normal distribution. The expectation mean μ_T is given by

$$\mu_T = \frac{n_a(n_a - 1) + n_b(n_b - 1)}{n(n-1)} , \tag{C.3}$$

where $n = n_a + n_b$. The limiting value of the variance σ_T is given by

$$\lim_{n, n_k, D \to \infty} \sigma_T^2 = \frac{1}{n n_k} \left(\frac{n_a n_b}{n^2} + 4 \frac{n_a^2 n_b^2}{n^4} \right) . \tag{C.4}$$

This limitation converges very fast and achieves a good approximation even if for $D = 2$.

Here is a test to justify the argument that the pull of T will be a standard distribution. We split our $D^0 \to K^-\pi^+\pi^0\pi^0$ MC sample by the ratio 1:9 randomly multiple times with different different random seeds. This special sample and ratio 1:9 should not cause the loss of generality. Since coming from the same sample, the two parts of each split satisfy the hypothesis that the parent distributions are the same. The statistic T of each split is then calculated. Figure C.1 shows the pull distribution fitted by a Gaussian, whose mean and sigma is consistent to zero and one, respectively.

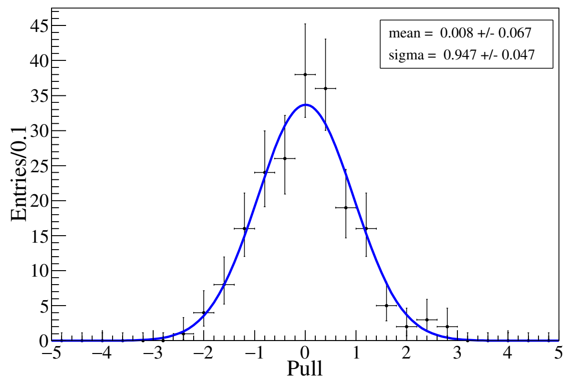

Figure C.1: The pull, $(T - \mu_T)/\sigma_T$, distribution fitted by a Gaussian.

In real cases of high energy physics, one can obtain the goodness-of-fit in a unbinned maximum-likelihood fit using the mixed-sample method on the data sample and the toy MC sample generated according to the fitted probability distribution function. The values T, μ_T, and σ_T can be easily computed by Eqs. C.2, C.3, and C.4, respectively. The value $(T - \mu_T)/\sigma_T$ will indicate the goodness-of-fit.

In conclusion, the mixed-sample method is an easy but powerful tool to obtain the goodness-of-fit in unbinned maximum-likelihood fits. The procedure is performed directly on the unbinned data. Computing χ^2 by binning the data can't sufficiently reveal the goodness-of-fit. Furthermore, the mixed-sample method is performed without knowing the parent probability distribution function, which is a great advantage when the parent probability distribution function is difficult to obtain, for example, the public MC. We use w_ν values to be the root mean square of x^ν of the data sample and take $k = 10$, when applying this method to our analysis.

Appendix D

Branching Fractions in BESIII Monte-Carlo

The $K^-\pi^+\pi^0\pi^0$ events in the MC are created via an incoherent sum of many different resonant decays. We try to list all decay channels of $K^-\pi^+\pi^0\pi^0$ in DECAY.DEC, which controls generic MC generator in BESIII. The branching fraction of each channel is calculated and listed in Table D.1, where VVS PWAVE means VVS PWAVE 1.0 0.0 0.0 0.0 0.0 0.0, SVV HELAMP 1 0 1 means SVV HELAMP 1.0 0.0 0.0 0.0 1.0 0.0 etc., and an extra factor of 0.5 is included for K^0 or $\bar{K}^0$ detected as a K_S. The numbers after VVS PWAVE and SVV HELAMP are parameters to control angular structures. In Table D.2, we proof that the BF calculated based on truthtag is consistent with what we obtained from DECAY.DEC. The truth tag branching fraction ($\mathcal{B}$) is calculated based on both sides of 1345311 total $D^0\bar{D}^0$ events. The absolute uncertainty of truth tag branching fraction is calculated by $\sqrt{\mathcal{B}(1-\mathcal{B})/\text{total events}}$.

Table D.1: $D^0 \to K^-\pi^+\pi^0\pi^0$

DECAY.DEC		**BF DEC**
K- pi+ pi0 pi0	0.0036 PHSP	3.6×10^{-3}
a_1+ K-	0.0780 SVS	
a_1+ →rho+ pi0	0.5080 VVS PWAVE	3.962%
K_1- pi+	0.0160 SVS	
K_1- →K- pi0 pi0	0.0412 PHSP	6.592×10^{-4}
K_1- →K*- pi0	0.0533 VVS PWAVE	
K*-→K- pi0	0.3330 VSS	2.840×10^{-4}
K*- rho+	0.0640 SVV HELAMP .5 1 .5	
K*-→K- pi0	0.3330 VSS	2.131%
$anti - K_1 0$ pi0	0.0056 SVS	
$anti - K_1 0$ →rho+ K-	0.2800 VVS PWAVE	1.568×10^{-3}
$anti - K_1 0$ →K*- pi+	0.1067 VVS PWAVE	
K*-→K- pi0	0.3330 VSS	1.990×10^{-4}
$anti - K_1 0$ →anti-K*0 pi0	0.0533 VVS PWAVE	
anti-K*0→K- pi+	0.6657 VSS	1.987×10^{-4}
$anti - K_1 0$ →K- pi+ pi0	0.1244 PHSP	6.966×10^{-4}
K*- pi+ pi0	0.0062 PHSP	
K*-→K- pi0	0.3330 VSS	2.065×10^{-3}
K- rho+ pi0	0.0008 PHSP	8.000×10^{-4}
anti-K*0 pi0 pi0	0.0035 PHSP	
anti-K*0→K- pi+	0.6657 VSS	2.330×10^{-3}
	TOTAL	7.333%

Table D.2: Branching Fraction Summary. Truth tag branching fraction ($\mathcal{B}$) is calculated based on both sides of 1345311 total $D^0\bar{D}^0$ events. The absolute uncertainty of truth tag branching fraction is calculated by $\sqrt{\mathcal{B}(1-\mathcal{B})/\text{total events}}$.

Mode	**BF PDG**	**BF DEC**	**BF Truth Tag**	**$\#\sigma$ off**
$\boldsymbol{K^-\pi^+\pi^0\pi^0}$	none	7.333%	$7.349 \pm 0.016\%$	1.000

Appendix E

Frequency of Multiple Candidates in DTag

There could be multiple D candidates satisfying the requirements of DTag. Although we only chose the candidate with the smallest ΔE, understanding the multiplicity of DTag is necessary to determine its systematic uncertainty. Figure E.1 shows the multiplicity of DT $K^-\pi^+\pi^0\pi^0$ vs. $K^-\pi^+$. DTag has wide ΔE and M_{BC} requirements in order to retain sidebands. If there are no extra cuts applied besides the default requirements in DTag, there is more than 20% events with multiplicity more than one. However, proper M_{BC} and ΔE cuts are usually applied around the signal region. After either wider or tighter signal region cuts are added, only about $(9-11)\%$ of events has multiplicity more than one.

Figure E.2 shows the multiplicity of ST $K^-\pi^+$. The tag $K^-\pi^+$ has a very tiny portion ($< 0.3\%$) of events with multiplicity more than one. Figures E.3 and E.4 show the multiplicity of $K^-\pi^+\pi^0\pi^0$ and $K^-\pi^+$ in DT, respectively. Allmost none events of $K^-\pi^+$ in DT has multiplicity more than one. Comparing to Figure E.1, we conlude that most of the multiplicity of DT $K^-\pi^+\pi^0\pi^0$ vs. $K^-\pi^+$ are caused by the multiplicity of $K^-\pi^+\pi^0\pi^0$.

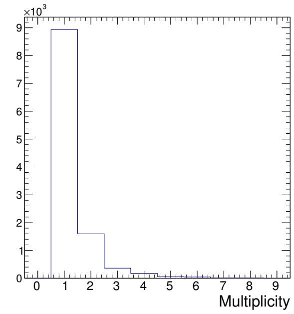

(a) Data without extra cuts

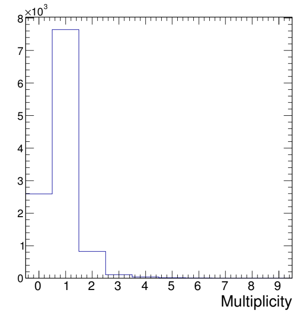

(b) Data with the wider cuts

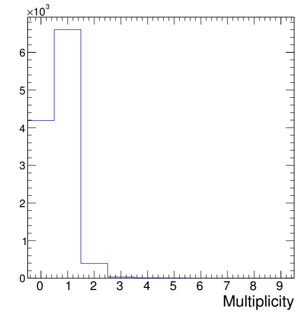

(c) Data with the tighter cuts

Figure E.1: The multiplicity of DT $K^-\pi^+\pi^0\pi^0$ vs. $K^-\pi^+$.

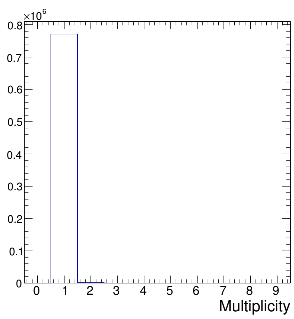

(a) Data without extra cuts

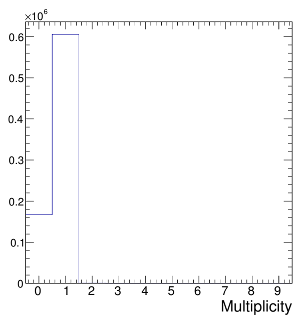

(b) Data with the wide cut

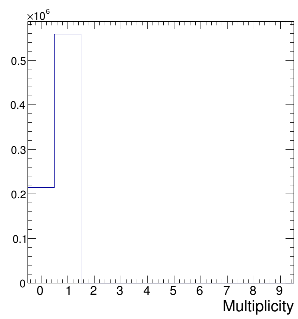

(c) Data with the tight cut

Figure E.2: The multiplicity of ST $K^-\pi^+$.

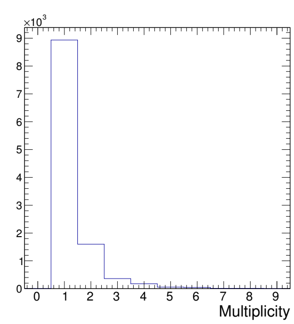

(a) Data without extra cuts

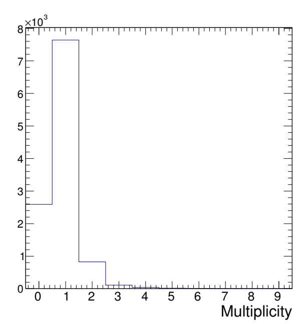

(b) Data with the wide cut

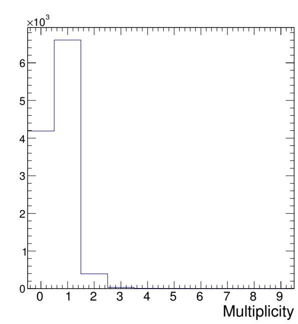

(c) Data with the tight cut

Figure E.3: The multiplicity of $K^-\pi^+\pi^0\pi^0$ in DT.

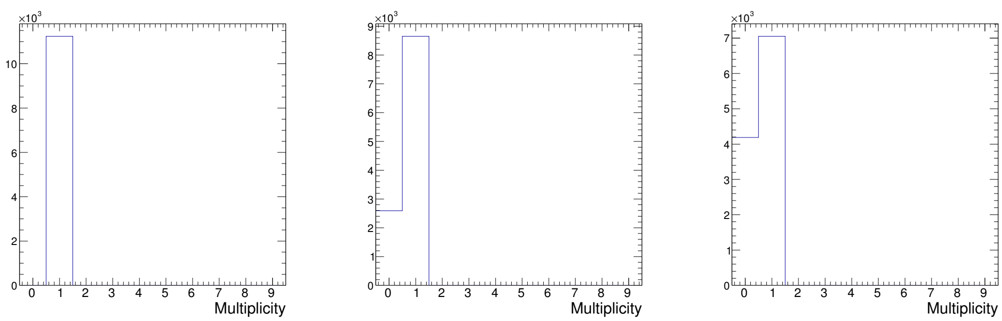

(a) Data without extra cuts (b) Data with the wide cut (c) Data with the tight cut

Figure E.4: The multiplicity of $K^-\pi^+$ in DT.

Appendix F

Shower Isolation Cut from Tracks

Photons are reconstructed from the energy deposit in EMC, called showers, which are produced due to secondary interactions of particle impacting EMC. One problem of identifying photons is the recognition of hadronic splitoffs, which create fake photons or alter real ones. Hadronic splitoffs are showers produced in distance of where charged particle colliding EMC. These hadronic splitoffs can be excluded by the shower isolation cut from charged tracks. The shower isolation cut is a cut on the space angle between charged tracks and photon candidates, called “dang”.

There are four photon showers and four charged tracks included in $D^0 \to K^-\pi^+\pi^0\pi^0$ vs. $\bar{D}^0 \to K^-\pi^+$. Thus, 16 dang are examined in each event. The distribution of the smallest dang with the default dang cut of BOSS is shown in Figure F.1. The dang > 10 cut will be applied in our next update. This dang cut removes 2.05% of data and 2.73% in public MC.

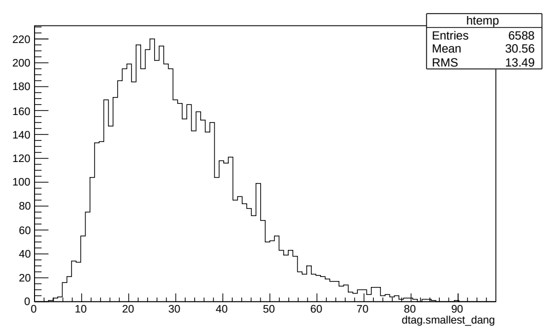

Figure F.1: The distribution of the smallest dang.

Appendix G

An Alternative Method to Access K_S Mass: the Recoil Mass of $\pi^0\pi^0$

The mass of the $\pi^0\pi^0$ system is used to identify K_S background in this study. To calculate the mass of $\pi^0\pi^0$ system, the default method is calculating the invariant mass of $\pi^0\pi^0$ based on the information of the two reconstructed π^0s. As a result, the resolution of the π^0s propagates to the $\pi^0\pi^0$ system. In addition, the π^0 vetos is assumed to be at the beam spot. While accurate for prompt π^0, this is not valid for π^0 daughtors from K_S decay. Considering that the resolution of charged tracks is excellent, we also test the recoil mass of the $\pi^0\pi^0$, which is the invariant mass of the four-momentum of the initial e^+e^- beam minus that of the two charged kaons and the two charged pions. However, we find the resolution of the recoil mass is obviously poorer; see Figure G.1

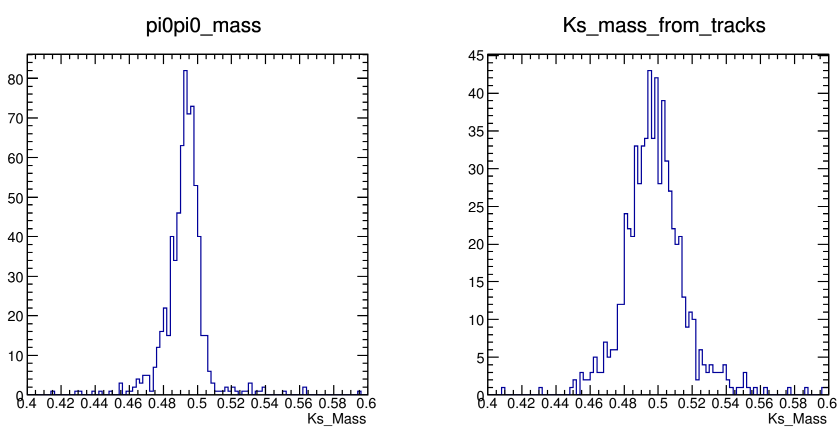

Figure G.1: The distributions of the invariant mass and the recoil mass of $\pi^0\pi^0$, where a signal $K^-\pi^+K_S$ vs. $K^+\pi^-$, $K_S \to \pi^0\pi^0$, MC sample is used.

Appendix H

$K\pi$ S-Wave Formfactor

The $K\pi$ S-wave formfactor is modeled by a parameterization from scattering data, Eq. 3.28. For the parameters, the results of $D^0 \to K_S\pi\pi$ by BaBar [17] are used in this analysis. Figure H.1 shows the effects of $K\pi$ S-wave on the two-body mass of $K\pi$. Note that the small upturn at large $K\pi$ mass is heavily suppressed by phase space.

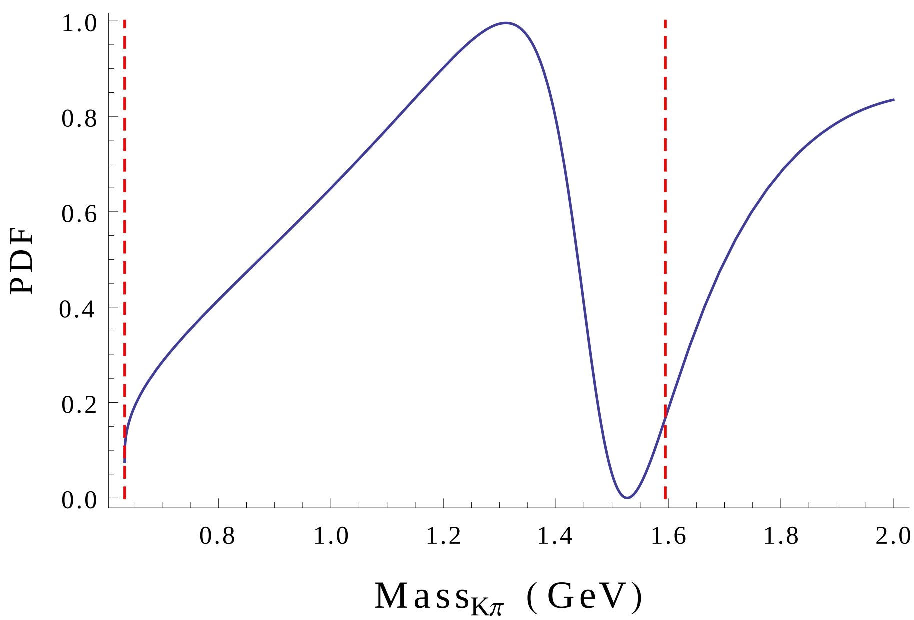

Figure H.1: The $K\pi$ S-wave formfactor with parameters fixed to the results by BaBar [17]. The red lines indicate the kinematic limits.

Appendix I

Efficiency Correction

In section 3.1, an efficiency correction is applied on the phase-space Monte-Carlo integration to correct the efficiency differences between data and MC, Eq. 3.9. There are several types of efficiency corrections considered in this analysis:

- π^0 reconstruction
- $K^{\pm}$ and $\pi^{\pm}$ PID efficiency
- $K^{\pm}$ and $\pi^{\pm}$ tracking efficiency

The π^0 reconstruction efficiency study is discussed in Appendix A (or see [35]). The efficiency correction of π^0 reconstruction is listed in Table I.1. The PID and tracking efficiency are done in separate BESIII studies [36], [34]. The efficiency correction of PID is listed in Table I.2, and that of tracking in Table I.3.

Table I.1: π^0 reconstruction efficiency, $\epsilon_{data}/\epsilon_{MC}$ [35].

class'n critetia	$0.0 - 0.2$ GeV	$0.2 - 0.4$ GeV	$0.4 - 0.6$ GeV
dEmBC, dang 10	0.981 ± 0.009	0.991 ± 0.007	1.000 ± 0.014

	$0.6 - 0.8$ GeV	$0.8 - 1$ GeV
dEmBC, dang 10	1.001 ± 0.008	1.006 ± 0.010

Table I.2: $K^{\pm}$ and $\pi^{\pm}$ PID efficiency, $\epsilon_{data}/\epsilon_{MC}$ [36].

	$0.0-0.2$ GeV	$0.2-0.3$ GeV	$0.3-0.4$ GeV	$0.4-0.5$ GeV
π^-	0.9982 ± 0.0019	0.9990 ± 0.0009	1.0005 ± 0.0009	1.0014 ± 0.0014
π^+	1.0012 ± 0.0004	0.9997 ± 0.0007	1.0001 ± 0.0007	1.0011 ± 0.0010

	$0.5-0.6$ GeV	$0.6-0.7$ GeV	>0.7 GeV
π^-	0.9975 ± 0.0030	0.9963 ± 0.0051	0.9901 ± 0.0108
π^+	0.9970 ± 0.0030	1.0033 ± 0.0038	0.9650 ± 0.0125

	$0.0-0.3$ GeV	$0.3-0.4$ GeV	$0.4-0.5$ GeV
K^-	1.0167 ± 0.0039	0.9912 ± 0.0032	0.9998 ± 0.0022
K^+	0.9981 ± 0.0050	0.9873 ± 0.0037	0.9841 ± 0.0031

	$0.5-0.6$ GeV	$0.6-0.7$ GeV	>0.7 GeV
K^-	1.0005 ± 0.0027	0.9955 ± 0.0044	1.0096 ± 0.0070
K^+	0.9938 ± 0.0032	1.0052 ± 0.0036	0.9967 ± 0.0073

Table I.3: $K^{\pm}$ and $\pi^{\pm}$ tracking efficiency, $\epsilon_{data}/\epsilon_{MC}$ [34].

	$0.0-0.2$ GeV	$0.2-0.3$ GeV	$0.3-0.4$ GeV	$0.4-0.5$ GeV
π^-	1.0354 ± 0.0102	1.0082 ± 0.0052	1.0029 ± 0.0040	0.9969 ± 0.0043
π^+	1.0325 ± 0.0103	0.9992 ± 0.0053	0.9931 ± 0.0041	0.9954 ± 0.0043

	$0.5-0.6$ GeV	$0.6-0.7$ GeV	>0.7 GeV
π^-	0.9931 ± 0.0059	1.0057 ± 0.0085	1.0178 ± 0.0103
π^+	0.9955 ± 0.0060	1.0053 ± 0.0093	0.9912 ± 0.0130

	$0.00-0.17$ GeV	$0.17-0.21$ GeV	$0.21-0.25$ GeV	$0.25-0.35$ GeV
K^-	1.1196 ± 0.0623	1.0694 ± 0.0261	1.0536 ± 0.0235	1.0037 ± 0.0086
K^+	0.7869 ± 0.0925	0.9655 ± 0.0795	0.9880 ± 0.0389	1.0341 ± 0.0087

	$0.35-0.45$ GeV	$0.45-0.55$ GeV	$0.55-0.65$ GeV	>0.65 GeV
K^-	1.0285 ± 0.0059	1.0073 ± 0.0057	1.0139 ± 0.0072	0.9847 ± 0.0118
K^+	1.0061 ± 0.0059	1.0123 ± 0.0055	1.0131 ± 0.0077	0.9974 ± 0.0141

Appendix J

Tested PWA Modes

Table J.1 lists all amplitude modes tested during the optimal set algorithm, Section 5.1, but not included in the final fit set.

Table J.1: Amplitudes not included in the final fit set.

Amplitude mode
$D \to SS$
$D \to PP, P \to VP$
$D \to (K^{*-}\pi^0)_P\pi^+$
$D \to K^-(\rho^+\pi^0)_P$
$D \to AP, A \to VP$
$D \to K_1(1270)^-\pi^+, K^{*-}\pi^0[D]$
$D \to K_1(1270)^0\pi^0, K^{*-}\pi^+[S]$
$D \to K_1(1270)^0\pi^0, K^{*-}\pi^+[D]$
$D \to K_1(1270)^0\pi^0, K^-\rho^+[D]$
$D \to K^-(\rho^+\pi^0)_A, \rho^+\pi^0[D]$
$D \to K^-(\rho^+\pi^0)_A[S]$
$D \to (K^{*-}\pi^+)_A\pi^0, K^{*-}\pi^+[S]$
$D \to (K^{*-}\pi^0)_A\pi^+, K^{*-}\pi^0[D]$
$D \to (K^{*-}\pi^+)_A\pi^0, K^{*-}\pi^+[D]$
$D \to (\rho^+K^-)_A\pi^0, K^-\rho^+[S]$
$D \to AP, A \to SP$
$D \to K^-((\pi^+\pi^0)_S\pi^0)_A$
$D \to K^-((\pi^0\pi^0)_S\pi^+)_A$
$D \to ((K^-\pi^0)_S\pi^+)_A\pi^0$
$D \to ((K^-\pi^0)_S\pi^0)_A\pi^+$
$D \to (K^-(\pi^+\pi^0)_S)_A\pi^0$
$D \to (K^-(\pi^0\pi^0)_S)_A\pi^+$

Continued on next page

Table J.1 Amplitudes not included in the final fit set–continued.

Amplitude mode
$D \to VS$
$D \to (K^-\pi^0)_S(\pi^+\pi^0)_V$
$D \to (K^-\pi^+)_V(\pi^0\pi^0)_S$
$D \to (K^-\pi^0)_V(\pi^+\pi^0)_S$
$D \to VP, V \to VP$
$D \to (K^{*0}\pi^0)_V\pi^0$
$D \to (K^-\rho^+)_V\pi^0$
$D \to VV$
$D[S] \to (K^-\pi^0)_V\rho^+$
$D[S] \to K^{*-}(\pi^+\pi^0)_V$
$D[P] \to K^{*-}(\pi^+\pi^0)_V$
$D[P] \to (K^-\pi^0)_V(\pi^+\pi^0)_V$
$D[D] \to (K^-\pi^0)_V(\pi^+\pi^0)_V$
$D \to TS$
$D \to (K^-\pi^+)_T(\pi^0\pi^0)_S$
$D \to (K^-\pi^0)_T(\pi^+\pi^0)_S$
Other
$D \to TV$ amplitudes
$K^{*-}(1410)\pi^+$, $K^{*0}(1410)\pi^0$, $K^{*-}(1680)\pi^+$, $K^{*0}(1680)\pi^0$
$K_2^{*-}(1430)\pi^+$, $K_2^{*0}(1430)\pi^+$, $K_2^{*-}(1770)\pi^+$, $K_2^{*0}(1770)\pi^+$
$K^-a_2^+(1320)$
$K^-\pi^+(1300)$
$K^-\omega^+(1420)$
$K^-a_1^+(1260)$
$K^{*0}f_0(980)$
$K_2^{*0}(1430)(\pi^+\pi^-)_S$, $K_2^{*-}(1430)(\pi^+\pi^0)_S$
$K_2^{*-}(1430)\rho^+$
$K_2^{*0}(1430)f_2(1270)$
$(K^-\pi^+)_{S\text{-wave}}f_2(1270)$
$(K^{*-}\pi^+)_T\pi^0$, $(K^{*-}\pi^0)_T\pi^+$, $(K^{*0}\pi^0)_T\pi^0$
$(K^-\rho^+)_T\pi^0$

Appendix K

The Values of PWA Amplitudes

In Section 5.2, we only report fit fractions since they are more physically meaningful than amplitude and free from normalization issues. For completeness, we give the values of PWA amplitudes in Table K.1. Note that amplitude modes don't share the same normalization. Thus, the relative size between two amplitudes can't reflect the relative size of their corresponding fit fractions.

Table K.1: The values of Amplitudes.

num	Amplitude mode	Amplitude (ρ)
	$D \to SS$	
1	$D \to (K^-\pi^+)_S(\pi^0\pi^0)_S$	2.02 ± 0.24
2	$D \to (K^-\pi^0)_S(\pi^+\pi^0)_S$	1.66 ± 0.23
	$D \to AP, A \to VP$	
8S	$D \to K^-a_1(1260)^+, \rho^+\pi^0[S]$	1 (fixed)
8D	$D \to K^-a_1(1260)^+, \rho^+\pi^0[D]$	$8.42 \pm 1.70 \times 10^{-1}$
9S	$D \to K_1(1270)^-\pi^+, K^{*-}\pi^0[S]$	$2.18 \pm 0.70 \times 10^{-2}$
11S	$D \to K_1(1270)^0\pi^0, K^{*0}\pi^0[S]$	$3.36 \pm 0.72 \times 10^{-2}$
11D	$D \to K_1(1270)^0\pi^0, K^{*0}\pi^0[D]$	$1.09 \pm 0.47 \times 10^{-1}$
12S	$D \to K_1(1270)^0\pi^0, K^-\rho^+[S]$	$1.96 \pm 0.14 \times 10^{-1}$
14S	$D \to (K^{*-}\pi^0)_A\pi^+, K^{*-}\pi^0[S]$	$3.63 \pm 0.61 \times 10^{-1}$
16S	$D \to (K^{*0}\pi^0)_A\pi^0, K^{*0}\pi^0[S]$	$5.55 \pm 0.46 \times 10^{-1}$
16D	$D \to (K^{*0}\pi^0)_A\pi^0, K^{*0}\pi^0[D]$	$5.26 \pm 1.08 \times 10^{-1}$
17D	$D \to (\rho^+K^-)_A\pi^0, K^-\rho^+[D]$	1.00 ± 0.23
	$D \to AP, A \to SP$	
21	$D \to ((K^-\pi^+)_S\pi^0)_A\pi^0$	3.34 ± 0.85
	$D \to VS$	
26	$D \to (K^-\pi^0)_S\rho^+$	1.76 ± 0.14
27	$D \to K^{*-}(\pi^+\pi^0)_S$	$1.75 \pm 0.38 \times 10^{-1}$
28	$D \to K^{*0}(\pi^0\pi^0)_S$	$3.97 \pm 2.35 \times 10^{-1}$
	$D \to VP, V \to VP$	
33	$D \to (K^{*-}\pi^+)_V\pi^0$	1.02 ± 0.11
	$D \to VV$	
38S	$D[S] \to K^{*-}\rho^+$	$1.46 \pm 0.14 \times 10^{-1}$
38P	$D[P] \to K^{*-}\rho^+$	$9.78 \pm 0.89 \times 10^{-2}$
38D	$D[D] \to K^{*-}\rho^+$	$2.33 \pm 0.17 \times 10^{-1}$
39P	$D[P] \to (K^-\pi^0)_V\rho^+$	$4.24 \pm 0.98 \times 10^{-1}$
39D	$D[D] \to (K^-\pi^0)_V\rho^+$	1.03 ± 0.12
40D	$D[D] \to K^{*-}(\pi^+\pi^0)_V$	$4.74 \pm 0.77 \times 10^{-1}$
43S	$D[S] \to (K^-\pi^0)_V(\pi^+\pi^0)_V$	6.74 ± 1.26
	$D \to TS$	
46	$D \to (K^-\pi^+)_S(\pi^0\pi^0)_T$	1.54 ± 0.48
47	$D \to (K^-\pi^0)_S(\pi^+\pi^0)_T$	1.36 ± 0.50

Appendix L

Systematic Uncertainties

The systematics due to the amplitude model, which includes $K\pi$ S-wave, effective barrier radius, and the mass and width of intermediate resonances, are summarized in Tables L.1 and L.2. Tables L.3 and L.4 show the details of the systematics due to $K\pi$ S-wave parameters. The values of these parameters and their uncertainties are listed in Table 3.3. Tables L.5 and L.6 show the details of the systematics due to effective barrier radius. The effective barrier radius is varied from 1.5 to 4.5 GeV^{-1} for intermediate resonances and from 3.0 to 7.0 GeV^{-1} for the D meson. Tables L.7 and L.8 show the details of the systematics due to the mass and width of K_1 and a_1. Tables L.9 and L.10 show the details of the systematics due to the mass and width of K^{*0}, K^{*-}, and ρ. The mass and width of intermediate resonances are varied within their uncertainties according to the PDG.

Tables L.11 and L.12 show the systematics due to background. The uncertainties caused by the effect of M_{BC} and ΔE cuts on the signal side are studied by shifting the cuts from the "tight cut" to the "wide cut" mentioned in Section 4.5. The uncertainties caused by the $K_S \to \pi^0\pi^0$ veto are studied by shifting the veto from the nominal $0.458 < M_{\pi^0\pi^0} < 0.520$ to $0.418 < M_{\pi^0\pi^0} < 0.542$.

The systematics due to experimental effects, including π^0 reconstruction, PID, and track reconstruction, are summarized in Tables L.13 and L.14. Tables L.15-L.16 show the details of systematics due to π^0 reconstruction. Tables L.17-L.20 show the details of systematics due to PID. Tables L.21-L.24 show the details of systematics due to track reconstruction.

Table L.1: FF systematics due to amplitude model (in units of statistical standard deviations). (I) $K\pi$ S wave, (II) barrier effective radius, (III) mass and width of K_1 and a_1, (IV) mass and width of K^{*0}, K^{*-} and ρ.

num	**Amplitude mode**	**I**	**II**	**III**	**IV**	**Total**
	$D \to SS$					
1	$D \to (K^-\pi^+)_S(\pi^0\pi^0)_S$	0.935	0.747	0.933	0.051	1.518
2	$D \to (K^-\pi^0)_S(\pi^+\pi^0)_S$	1.107	0.495	0.922	0.032	1.524
	$D \to AP, A \to VP$					
8S	$D \to K^-a_1(1260)^+, \rho^+\pi^0[S]$	0.186	0.812	0.986	0.077	1.293
8D	$D \to K^-a_1(1260)^+, \rho^+\pi^0[D]$	0.179	0.374	0.840	0.049	0.938
9S	$D \to K_1(1270)^-\pi^+, K^{*-}\pi^0[S]$	0.162	1.033	1.263	0.105	1.643
11S	$D \to K_1(1270)^0\pi^0, K^{*0}\pi^0[S]$	0.202	0.931	1.232	0.112	1.562
11D	$D \to K_1(1270)^0\pi^0, K^{*0}\pi^0[D]$	0.198	0.727	0.628	0.111	0.989
12S	$D \to K_1(1270)^0\pi^0, K^-\rho^+[S]$	0.053	0.292	0.648	0.026	0.713
14S	$D \to (K^{*-}\pi^0)_A\pi^+, K^{*-}\pi^0[S]$	0.112	0.814	0.941	0.097	1.253
16S	$D \to (K^{*0}\pi^0)_A\pi^0, K^{*0}\pi^0[S]$	0.038	0.633	0.951	0.076	1.145
16D	$D \to (K^{*0}\pi^0)_A\pi^0, K^{*0}\pi^0[D]$	0.161	0.674	0.511	0.084	0.865
17D	$D \to (\rho^+K^-)_A\pi^0, K^-\rho^+[D]$	0.562	0.789	0.786	0.058	1.249
	$D \to AP, A \to SP$					
21	$D \to ((K^-\pi^+)_S\pi^0)_A\pi^0$	0.135	1.029	0.904	0.040	1.377
	$D \to VS$					
26	$D \to (K^-\pi^0)_S\rho^+$	0.252	0.378	1.238	0.014	1.308
27	$D \to K^{*-}(\pi^+\pi^0)_S$	0.118	0.096	0.343	0.065	0.381
28	$D \to K^{*0}(\pi^0\pi^0)_S$	0.261	0.730	0.417	0.039	0.880
	$D \to VP, V \to VP$					
33	$D \to (K^{*-}\pi^+)_V\pi^0$	0.075	0.530	0.430	0.028	0.688
	$D \to VV$					
38S	$D[S] \to K^{*-}\rho^+$	0.083	0.666	0.706	0.101	0.980
38P	$D[P] \to K^{*-}\rho^+$	0.114	0.311	0.261	0.049	0.425
38D	$D[D] \to K^{*-}\rho^+$	0.071	1.277	0.463	0.111	1.365
39P	$D[P] \to (K^-\pi^0)_V\rho^+$	0.123	0.553	0.398	0.059	0.395
39D	$D[D] \to (K^-\pi^0)_V\rho^+$	0.538	1.211	0.119	0.110	1.335
40D	$D[D] \to K^{*-}(\pi^+\pi^0)_V$	0.155	0.307	0.667	0.039	0.751
43S	$D[S] \to (K^-\pi^0)_V(\pi^+\pi^0)_V$	0.658	0.114	0.469	0.063	0.818
	$D \to TS$					
46	$D \to (K^-\pi^+)_S(\pi^0\pi^0)_T$	0.879	0.695	0.350	0.028	1.171
47	$D \to (K^-\pi^0)_S(\pi^+\pi^0)_T$	0.182	0.549	0.556	0.027	0.803

Table L.2: Phase, ϕ, systematics due to barrier effective radius (in units of statistical standard deviations). (I) $K\pi$ S-wave, (II) barrier effective radius, (III) mass and width of K_1 and a_1, (IV) mass and width of K^{*0}, K^{*-} and ρ.

num	Amplitude mode	I	II	III	IV	Total
	$D \to SS$					
1	$D \to (K^-\pi^+)_S(\pi^0\pi^0)_S$	2.372	0.792	1.894	0.028	3.137
2	$D \to (K^-\pi^0)_S(\pi^+\pi^0)_S$	1.990	0.682	1.001	0.025	2.330
	$D \to AP, A \to VP$					
8S	$D \to K^-a_1(1260)^+, \rho^+\pi^0[S]$	0.000	0.000	0.000	0.000	0.000
8D	$D \to K^-a_1(1260)^+, \rho^+\pi^0[D]$	0.274	0.841	0.800	0.058	1.194
9S	$D \to K_1(1270)^-\pi^+, K^{*-}\pi^0[S]$	0.156	0.285	0.894	0.062	0.953
11S	$D \to K_1(1270)^0\pi^0, K^{*0}\pi^0[S]$	0.061	0.513	0.915	0.038	1.051
11D	$D \to K_1(1270)^0\pi^0, K^{*0}\pi^0[D]$	0.195	0.699	0.690	0.035	1.002
12S	$D \to K_1(1270)^0\pi^0, K^-\rho^+[S]$	0.116	0.257	1.987	0.039	2.007
14S	$D \to (K^{*-}\pi^0)_A\pi^+, K^{*-}\pi^0[S]$	0.091	0.921	0.774	0.060	1.208
16S	$D \to (K^{*0}\pi^0)_A\pi^0, K^{*0}\pi^0[S]$	0.243	0.409	1.641	0.084	1.711
16D	$D \to (K^{*0}\pi^0)_A\pi^0, K^{*0}\pi^0[D]$	0.181	1.249	0.810	0.055	1.501
17D	$D \to (\rho^+K^-)_A\pi^0, K^-\rho^+[D]$	0.370	0.945	0.629	0.037	1.195
	$D \to AP, A \to SP$					
21	$D \to ((K^-\pi^+)_S\pi^0)_A\pi^0$	1.686	0.376	1.082	0.038	2.039
	$D \to VS$					
26	$D \to (K^-\pi^0)_S\rho^+$	1.673	1.660	2.102	0.063	3.159
27	$D \to K^{*-}(\pi^+\pi^0)_S$	0.074	0.865	0.837	0.049	1.207
28	$D \to K^{*0}(\pi^0\pi^0)_S$	0.623	0.507	0.480	0.063	0.938
	$D \to VP, V \to VP$					
33	$D \to (K^{*-}\pi^+)_V\pi^0$	0.070	0.165	1.244	0.094	1.260
	$D \to VV$					
38S	$D[S] \to K^{*-}\rho^+$	0.101	1.049	1.692	0.068	1.995
38P	$D[P] \to K^{*-}\rho^+$	0.083	0.403	1.554	0.126	1.612
38D	$D[D] \to K^{*-}\rho^+$	0.137	0.705	1.408	0.127	1.586
39P	$D[P] \to (K^-\pi^0)_V\rho^+$	0.072	1.095	0.912	0.078	1.429
39D	$D[D] \to (K^-\pi^0)_V\rho^+$	0.218	0.147	0.298	0.057	0.401
40D	$D[D] \to K^{*-}(\pi^+\pi^0)_V$	0.144	1.347	0.496	0.088	1.445
43S	$D[S] \to (K^-\pi^0)_V(\pi^+\pi^0)_V$	0.562	0.557	1.099	0.017	1.354
	$D \to TS$					
46	$D \to (K^-\pi^+)_S(\pi^0\pi^0)_T$	1.045	1.023	2.081	0.048	2.544
47	$D \to (K^-\pi^0)_S(\pi^+\pi^0)_T$	0.437	0.646	1.320	0.029	1.533

Table L.3: FF systematics due to $K\pi$ S-wave (in units of statistical standard deviations). (I) M, (II) Γ, (III) F, (IV) ϕ_F, (V) ϕ_R, (VI) a, (VII) r.

num	**I**	**II**	**III**	**IV**	**V**	**VI**	**VII**	**Total**
1	0.030	0.016	0.618	0.657	0.169	0.092	0.153	0.935
2	0.047	0.026	0.955	0.287	0.148	0.377	0.254	1.107
8S	0.015	0.006	0.019	0.146	0.031	0.107	0.006	0.186
8D	0.004	0.008	0.151	0.073	0.020	0.047	0.035	0.179
9S	0.012	0.022	0.088	0.125	0.038	0.010	0.018	0.162
11S	0.001	0.021	0.073	0.056	0.044	0.152	0.082	0.202
11D	0.000	0.017	0.081	0.128	0.058	0.105	0.041	0.198
12S	0.011	0.007	0.010	0.001	0.004	0.036	0.035	0.053
14S	0.004	0.020	0.046	0.034	0.021	0.081	0.044	0.112
16S	0.004	0.005	0.001	0.032	0.017	0.001	0.012	0.038
16D	0.002	0.000	0.096	0.089	0.040	0.067	0.049	0.161
17D	0.013	0.004	0.189	0.501	0.163	0.032	0.037	0.562
21	0.025	0.004	0.101	0.031	0.013	0.031	0.072	0.135
26	0.004	0.006	0.205	0.096	0.029	0.105	0.014	0.252
27	0.004	0.003	0.030	0.017	0.002	0.101	0.050	0.118
28	0.013	0.001	0.098	0.215	0.095	0.020	0.059	0.261
33	0.000	0.004	0.022	0.067	0.018	0.015	0.003	0.075
38S	0.018	0.013	0.043	0.044	0.033	0.040	0.003	0.083
38P	0.004	0.009	0.035	0.090	0.037	0.035	0.028	0.114
38D	0.004	0.002	0.007	0.064	0.019	0.012	0.019	0.071
39P	0.001	0.010	0.033	0.067	0.030	0.076	0.053	0.123
39D	0.036	0.001	0.360	0.351	0.122	0.092	0.109	0.538
40D	0.010	0.010	0.045	0.070	0.003	0.120	0.048	0.155
43S	0.023	0.009	0.523	0.338	0.123	0.134	0.105	0.658
46	0.002	0.016	0.441	0.712	0.243	0.077	0.028	0.875
47	0.010	0.005	0.106	0.111	0.036	0.065	0.065	0.182

Table L.4: Phase,ϕ, systematics due to $K\pi$ S-wave (in units of statistical standard deviations). (I) M, (II) Γ, (III) F, (IV) ϕ_F, (V) ϕ_R, (VI) a, (VII) r.

num	**I**	**II**	**III**	**IV**	**V**	**VI**	**VII**	**Total**
1	0.045	0.053	0.146	2.109	0.593	0.845	0.300	2.372
2	0.022	0.028	0.067	1.837	0.510	0.548	0.145	1.990
8S	0.000	0.000	0.000	0.000	0.000	0.000	0.000	0.000
8D	0.003	0.011	0.187	0.172	0.075	0.068	0.010	0.274
9S	0.001	0.010	0.082	0.121	0.048	0.023	0.005	0.156
11S	0.008	0.010	0.006	0.048	0.003	0.017	0.031	0.061
11D	0.002	0.006	0.109	0.101	0.039	0.100	0.066	0.195
12S	0.014	0.000	0.005	0.063	0.025	0.077	0.052	0.116
14S	0.013	0.016	0.013	0.083	0.011	0.024	0.011	0.091
16S	0.003	0.009	0.022	0.106	0.027	0.195	0.093	0.243
16D	0.004	0.007	0.037	0.140	0.060	0.075	0.051	0.181
17D	0.014	0.013	0.345	0.098	0.058	0.067	0.019	0.370
21	0.015	0.005	0.205	1.540	0.435	0.470	0.141	1.686
26	0.011	0.016	0.555	1.481	0.331	0.418	0.118	1.673
27	0.006	0.008	0.072	0.001	0.009	0.003	0.007	0.074
28	0.015	0.012	0.443	0.368	0.144	0.172	0.074	0.623
33	0.002	0.005	0.027	0.056	0.002	0.006	0.031	0.070
38S	0.000	0.014	0.076	0.047	0.035	0.020	0.020	0.101
38P	0.005	0.008	0.049	0.061	0.002	0.018	0.019	0.083
38D	0.005	0.016	0.039	0.027	0.044	0.111	0.044	0.137
39P	0.000	0.011	0.037	0.027	0.001	0.047	0.027	0.072
39D	0.020	0.004	0.155	0.020	0.008	0.131	0.075	0.218
40D	0.003	0.010	0.114	0.001	0.024	0.082	0.016	0.144
43S	0.006	0.017	0.314	0.407	0.149	0.170	0.027	0.562
46	0.004	0.022	0.550	0.783	0.176	0.360	0.120	1.045
47	0.010	0.015	0.305	0.207	0.030	0.223	0.065	0.437

Table L.5: FF systematics of barrier effective radius (in units of statistical standard deviations). (I) for intermediate resonance, (II) for D meson.

num	**Amplitude mode**	**I**	**II**	**Total**
	$D \to SS$			
1	$D \to (K^-\pi^+)_S(\pi^0\pi^0)_S$	0.744	0.069	0.747
2	$D \to (K^-\pi^0)_S(\pi^+\pi^0)_S$	0.356	0.344	0.495
	$D \to AP, A \to VP$			
8S	$D \to K^-a_1(1260)^+, \rho^+\pi^0[S]$	0.802	0.123	0.812
8D	$D \to K^-a_1(1260)^+, \rho^+\pi^0[D]$	0.342	0.153	0.374
9S	$D \to K_1(1270)^-\pi^+, K^{*-}\pi^0[S]$	0.743	0.717	1.033
11S	$D \to K_1(1270)^0\pi^0, K^{*0}\pi^0[S]$	0.253	0.896	0.931
11D	$D \to K_1(1270)^0\pi^0, K^{*0}\pi^0[D]$	0.541	0.489	0.727
12S	$D \to K_1(1270)^0\pi^0, K^-\rho^+[S]$	0.246	0.157	0.292
14S	$D \to (K^{*-}\pi^0)_A\pi^+, K^{*-}\pi^0[S]$	0.363	0.728	0.814
16S	$D \to (K^{*0}\pi^0)_A\pi^0, K^{*0}\pi^0[S]$	0.007	0.633	0.633
16D	$D \to (K^{*0}\pi^0)_A\pi^0, K^{*0}\pi^0[D]$	0.455	0.497	0.674
17D	$D \to (\rho^+K^-)_A\pi^0, K^-\rho^+[D]$	0.780	0.116	0.789
	$D \to AP, A \to SP$			
21	$D \to ((K^-\pi^+)_S\pi^0)_A\pi^0$	0.892	0.512	1.029
	$D \to VS$			
26	$D \to (K^-\pi^0)_S\rho^+$	0.063	0.333	0.338
27	$D \to K^{*-}(\pi^+\pi^0)_S$	0.014	0.095	0.096
28	$D \to K^{*0}(\pi^0\pi^0)_S$	0.697	0.222	0.930
	$D \to VP, V \to VP$			
33	$D \to (K^{*-}\pi^+)_V\pi^0$	0.528	0.054	0.530
	$D \to VV$			
38S	$D[S] \to K^{*-}\rho^+$	0.519	0.417	0.666
38P	$D[P] \to K^{*-}\rho^+$	0.036	0.309	0.311
38D	$D[D] \to K^{*-}\rho^+$	0.966	0.836	1.277
39P	$D[P] \to (K^-\pi^0)_V\rho^+$	0.327	0.446	0.553
39D	$D[D] \to (K^-\pi^0)_V\rho^+$	0.999	0.684	1.211
40D	$D[D] \to K^{*-}(\pi^+\pi^0)_V$	0.200	0.233	0.307
43S	$D[S] \to (K^-\pi^0)_V(\pi^+\pi^0)_V$	0.028	0.111	0.114
	$D \to TS$			
46	$D \to (K^-\pi^+)_S(\pi^0\pi^0)_T$	0.210	0.663	0.695
47	$D \to (K^-\pi^0)_S(\pi^+\pi^0)_T$	0.505	0.217	0.549

Table L.6: Phase, ϕ, systematics of barrier effective radius (in units of statistical standard deviations). (I) for intermediate resonance (II) for D meson.

num	Amplitude mode	I	II	Total
	$D \to SS$			
1	$D \to (K^-\pi^+)_S(\pi^0\pi^0)_S$	0.088	0.787	0.792
2	$D \to (K^-\pi^0)_S(\pi^+\pi^0)_S$	0.226	0.643	0.682
	$D \to AP, A \to VP$			
8S	$D \to K^-a_1(1260)^+, \rho^+\pi^0[S]$	0.000	0.000	0.000
8D	$D \to K^-a_1(1260)^+, \rho^+\pi^0[D]$	0.007	0.841	0.841
9S	$D \to K_1(1270)^-\pi^+, K^{*-}\pi^0[S]$	0.007	0.285	0.285
11S	$D \to K_1(1270)^0\pi^0, K^{*0}\pi^0[S]$	0.507	0.080	0.513
11D	$D \to K_1(1270)^0\pi^0, K^{*0}\pi^0[D]$	0.624	0.314	0.699
12S	$D \to K_1(1270)^0\pi^0, K^-\rho^+[S]$	0.257	0.003	0.257
14S	$D \to (K^{*-}\pi^0)_A\pi^+, K^{*-}\pi^0[S]$	0.309	0.868	0.921
16S	$D \to (K^{*0}\pi^0)_A\pi^0, K^{*0}\pi^0[S]$	0.303	0.275	0.409
16D	$D \to (K^{*0}\pi^0)_A\pi^0, K^{*0}\pi^0[D]$	0.888	0.879	1.249
17D	$D \to (\rho^+K^-)_A\pi^0, K^-\rho^+[D]$	0.339	0.882	0.945
	$D \to AP, A \to SP$			
21	$D \to ((K^-\pi^+)_S\pi^0)_A\pi^0$	0.101	0.362	0.376
	$D \to VS$			
26	$D \to (K^-\pi^0)_S\rho^+$	0.859	1.421	1.660
27	$D \to K^{*-}(\pi^+\pi^0)_S$	0.154	0.851	0.865
28	$D \to K^{*0}(\pi^0\pi^0)_S$	0.193	0.469	0.507
	$D \to VP, V \to VP$			
33	$D \to (K^{*-}\pi^+)_V\pi^0$	0.012	0.165	0.165
	$D \to VV$			
38S	$D[S] \to K^{*-}\rho^+$	0.330	0.996	1.049
38P	$D[P] \to K^{*-}\rho^+$	0.383	0.124	0.403
38D	$D[D] \to K^{*-}\rho^+$	0.317	0.630	0.705
39P	$D[P] \to (K^-\pi^0)_V\rho^+$	0.842	0.700	1.095
39D	$D[D] \to (K^-\pi^0)_V\rho^+$	0.143	0.034	0.147
40D	$D[D] \to K^{*-}(\pi^+\pi^0)_V$	0.918	0.986	1.347
43S	$D[S] \to (K^-\pi^0)_V(\pi^+\pi^0)_V$	0.429	0.355	0.557
	$D \to TS$			
46	$D \to (K^-\pi^+)_S(\pi^0\pi^0)_T$	1.023	0.001	1.023
47	$D \to (K^-\pi^0)_S(\pi^+\pi^0)_T$	0.216	0.609	0.646

Table L.7: FF systematics due to mass and width of K_1 and a_1 (in units of statistical standard deviations). (I) mass of K_1, (II) width of K_1, (III) mass of a_1, (IV) width of a_1.

num	**Amplitude mode**	**I**	**II**	**III**	**IV**	**Total**
	$D \to SS$					
1	$D \to (K^-\pi^+)_S(\pi^0\pi^0)_S$	0.046	0.320	0.823	0.288	0.933
2	$D \to (K^-\pi^0)_S(\pi^+\pi^0)_S$	0.004	0.416	0.787	0.218	0.922
	$D \to AP, A \to VP$					
8S	$D \to K^-a_1(1260)^+, \rho^+\pi^0[S]$	0.184	0.090	0.955	0.125	0.986
8D	$D \to K^-a_1(1260)^+, \rho^+\pi^0[D]$	0.083	0.069	0.828	0.039	0.840
9S	$D \to K_1(1270)^-\pi^+, K^{*-}\pi^0[S]$	0.222	1.150	0.472	0.038	1.263
11S	$D \to K_1(1270)^0\pi^0, K^{*0}\pi^0[S]$	0.250	1.191	0.142	0.121	1.232
11D	$D \to K_1(1270)^0\pi^0, K^{*0}\pi^0[D]$	0.233	0.465	0.349	0.023	0.628
12S	$D \to K_1(1270)^0\pi^0, K^-\rho^+[S]$	0.386	0.481	0.194	0.009	0.648
14S	$D \to (K^{*-}\pi^0)_A\pi^+, K^{*-}\pi^0[S]$	0.197	0.568	0.660	0.295	0.941
16S	$D \to (K^{*0}\pi^0)_A\pi^0, K^{*0}\pi^0[S]$	0.095	0.779	0.534	0.027	0.951
16D	$D \to (K^{*0}\pi^0)_A\pi^0, K^{*0}\pi^0[D]$	0.109	0.363	0.343	0.017	0.511
17D	$D \to (\rho^+K^-)_A\pi^0, K^-\rho^+[D]$	0.171	0.021	0.756	0.105	0.786
	$D \to AP, A \to SP$					
21	$D \to ((K^-\pi^+)_S\pi^0)_A\pi^0$	0.075	0.217	0.832	0.268	0.904
	$D \to VS$					
26	$D \to (K^-\pi^0)_S\rho^+$	0.225	0.243	1.176	0.186	1.238
27	$D \to K^{*-}(\pi^+\pi^0)_S$	0.084	0.055	0.318	0.080	0.343
28	$D \to K^{*0}(\pi^0\pi^0)_S$	0.072	0.111	0.391	0.130	0.417
	$D \to VP, V \to VP$					
33	$D \to (K^{*-}\pi^+)_V\pi^0$	0.236	0.165	0.314	0.036	0.430
	$D \to VV$					
38S	$D[S] \to K^{*-}\rho^+$	0.074	0.256	0.638	0.147	0.706
38P	$D[P] \to K^{*-}\rho^+$	0.023	0.219	0.138	0.012	0.261
38D	$D[D] \to K^{*-}\rho^+$	0.378	0.018	0.260	0.063	0.463
39P	$D[P] \to (K^-\pi^0)_V\rho^+$	0.057	0.291	0.263	0.006	0.398
39D	$D[D] \to (K^-\pi^0)_V\rho^+$	0.107	0.042	0.024	0.003	0.119
40D	$D[D] \to K^{*-}(\pi^+\pi^0)_V$	0.050	0.499	0.441	0.018	0.667
43S	$D[S] \to (K^-\pi^0)_V(\pi^+\pi^0)_V$	0.028	0.108	0.447	0.086	0.469
	$D \to TS$					
46	$D \to (K^-\pi^+)_S(\pi^0\pi^0)_T$	0.140	0.089	0.306	0.044	0.350
47	$D \to (K^-\pi^0)_S(\pi^+\pi^0)_T$	0.005	0.068	0.527	0.149	0.556

Table L.8: Phase, ϕ, systematics due to mass and width of K_1 and a_1 (in units of statistical standard deviations). (I) mass of K_1, (II) width of K_1, (III) mass of a_1, (IV) width of a_1.

num	**Amplitude mode**	**I**	**II**	**III**	**IV**	**Total**
	$D \to SS$					
1	$D \to (K^-\pi^+)_S(\pi^0\pi^0)_S$	0.036	0.290	1.841	0.316	1.894
2	$D \to (K^-\pi^0)_S(\pi^+\pi^0)_S$	0.069	0.160	0.979	0.118	1.001
	$D \to AP, A \to VP$					
8S	$D \to K^-a_1(1260)^+, \rho^+\pi^0[S]$	0.000	0.000	0.000	0.000	0.000
8D	$D \to K^-a_1(1260)^+, \rho^+\pi^0[D]$	0.124	0.044	0.766	0.166	0.800
9S	$D \to K_1(1270)^-\pi^+, K^{*-}\pi^0[S]$	0.343	0.081	0.815	0.099	0.894
11S	$D \to K_1(1270)^0\pi^0, K^{*0}\pi^0[S]$	0.178	0.220	0.845	0.207	0.915
11D	$D \to K_1(1270)^0\pi^0, K^{*0}\pi^0[D]$	0.097	0.537	0.417	0.058	0.690
12S	$D \to K_1(1270)^0\pi^0, K^-\rho^+[S]$	1.503	0.082	1.294	0.095	1.987
14S	$D \to (K^{*-}\pi^0)_A\pi^+, K^{*-}\pi^0[S]$	0.239	0.542	0.483	0.119	0.774
16S	$D \to (K^{*0}\pi^0)_A\pi^0, K^{*0}\pi^0[S]$	0.080	0.578	1.514	0.227	1.641
16D	$D \to (K^{*0}\pi^0)_A\pi^0, K^{*0}\pi^0[D]$	0.272	0.338	0.654	0.199	0.810
17D	$D \to (\rho^+K^-)_A\pi^0, K^-\rho^+[D]$	0.139	0.095	0.575	0.191	0.629
	$D \to AP, A \to SP$					
21	$D \to ((K^-\pi^+)_S\pi^0)_A\pi^0$	0.081	0.021	1.047	0.261	1.082
	$D \to VS$					
26	$D \to (K^-\pi^0)_S\rho^+$	0.180	0.160	2.031	0.487	2.102
27	$D \to K^{*-}(\pi^+\pi^0)_S$	0.089	0.270	0.775	0.114	0.837
28	$D \to K^{*0}(\pi^0\pi^0)_S$	0.093	0.256	0.362	0.160	0.480
	$D \to VP, V \to VP$					
33	$D \to (K^{*-}\pi^+)_V\pi^0$	0.072	0.106	1.210	0.248	1.244
	$D \to VV$					
38S	$D[S] \to K^{*-}\rho^+$	0.254	0.291	1.616	0.321	1.692
38P	$D[P] \to K^{*-}\rho^+$	0.039	0.183	1.519	0.248	1.554
38D	$D[D] \to K^{*-}\rho^+$	0.069	0.445	1.292	0.333	1.408
39P	$D[P] \to (K^-\pi^0)_V\rho^+$	0.097	0.069	0.877	0.221	0.912
39D	$D[D] \to (K^-\pi^0)_V\rho^+$	0.277	0.076	0.057	0.051	0.298
40D	$D[D] \to K^{*-}(\pi^+\pi^0)_V$	0.341	0.331	0.106	0.092	0.496
43S	$D[S] \to (K^-\pi^0)_V(\pi^+\pi^0)_V$	0.095	0.248	1.047	0.205	1.099
	$D \to TS$					
46	$D \to (K^-\pi^+)_S(\pi^0\pi^0)_T$	0.097	0.139	2.043	0.338	2.081
47	$D \to (K^-\pi^0)_S(\pi^+\pi^0)_T$	0.177	0.043	1.297	0.164	1.320

Table L.9: FF systematics due to amplitude model on mass and width of K^{*0}, K^{*-} and ρ (in units of statistical standard deviations). (I) mass of K^{*0}, (II) width of K^{*0}, (III) mass of K^{*-}, (IV) width of K^{*-}, (V) mass of ρ, (VI) width of ρ.

num	**I**	**II**	**III**	**IV**	**V**	**VI**	**Total**
1	0.003	0.009	0.011	0.012	0.047	0.006	0.051
2	0.011	0.066	0.002	0.004	0.026	0.013	0.032
8S	0.002	0.016	0.010	0.057	0.006	0.048	0.077
8D	0.002	0.012	0.018	0.022	0.004	0.037	0.049
9S	0.007	0.027	0.010	0.095	0.023	0.027	0.105
11S	0.024	0.067	0.032	0.079	0.008	0.018	0.112
11D	0.012	0.070	0.041	0.076	0.006	0.017	0.111
12S	0.009	0.007	0.007	0.015	0.003	0.015	0.026
14S	0.001	0.037	0.009	0.074	0.034	0.034	0.097
16S	0.015	0.048	0.015	0.044	0.011	0.015	0.071
16D	0.015	0.037	0.022	0.069	0.002	0.002	0.084
17D	0.000	0.013	0.006	0.052	0.000	0.019	0.058
21	0.006	0.007	0.016	0.014	0.023	0.023	0.040
26	0.003	0.012	0.005	0.005	0.002	0.002	0.014
27	0.005	0.030	0.024	0.051	0.008	0.002	0.065
28	0.013	0.013	0.013	0.026	0.013	0.007	0.039
33	0.008	0.015	0.010	0.008	0.013	0.013	0.028
38S	0.000	0.037	0.004	0.093	0.010	0.004	0.101
38P	0.014	0.014	0.021	0.032	0.000	0.023	0.049
38D	0.002	0.013	0.007	0.090	0.002	0.063	0.111
39P	0.011	0.025	0.004	0.052	0.004	0.001	0.059
39D	0.001	0.015	0.027	0.097	0.037	0.017	0.110
40D	0.000	0.021	0.012	0.030	0.008	0.005	0.039
43S	0.006	0.009	0.005	0.011	0.031	0.053	0.063
46	0.002	0.003	0.007	0.023	0.014	0.005	0.028
47	0.001	0.002	0.014	0.0010	0.006	0.021	0.027

Table L.10: Phase, ϕ, systematics due to mass and width of K^{*0}, K^{*-} and ρ (in units of statistical standard deviations). (I) mass of K^{*0}, (II) width of K^{*0}, (III) mass of K^{*-}, (IV) width of K^{*-}, (V) mass of ρ, (VI) width of ρ.

num	**I**	**II**	**III**	**IV**	**V**	**VI**	**Total**
1	0.002	0.001	0.006	0.024	0.006	0.011	0.028
2	0.001	0.002	0.008	0.019	0.012	0.006	0.025
8S	0.000	0.000	0.000	0.000	0.000	0.000	0.000
8D	0.009	0.021	0.008	0.035	0.005	0.039	0.058
9S	0.002	0.027	0.020	0.044	0.026	0.010	0.062
11S	0.032	0.004	0.001	0.019	0.006	0.001	0.038
11D	0.006	0.026	0.008	0.015	0.001	0.014	0.035
12S	0.016	0.019	0.018	0.023	0.009	0.002	0.039
14S	0.002	0.001	0.047	0.020	0.015	0.028	0.060
16S	0.045	0.061	0.014	0.028	0.007	0.017	0.084
16D	0.019	0.024	0.022	0.040	0.005	0.001	0.055
17D	0.012	0.003	0.027	0.018	0.009	0.009	0.037
21	0.005	0.000	0.003	0.031	0.008	0.019	0.038
26	0.009	0.016	0.002	0.057	0.006	0.018	0.063
27	0.009	0.010	0.035	0.031	0.006	0.002	0.049
28	0.010	0.053	0.014	0.012	0.005	0.026	0.063
33	0.013	0.007	0.062	0.059	0.017	0.033	0.094
38S	0.003	0.005	0.057	0.001	0.013	0.034	0.068
38P	0.005	0.003	0.086	0.092	0.004	0.009	0.126
38D	0.006	0.041	0.082	0.082	0.008	0.032	0.127
39P	0.010	0.024	0.045	0.054	0.012	0.019	0.078
39D	0.009	0.008	0.011	0.052	0.003	0.017	0.057
40D	0.003	0.022	0.030	0.025	0.006	0.075	0.088
43S	0.001	0.003	0.007	0.004	0.010	0.011	0.017
46	0.001	0.025	0.021	0.025	0.007	0.024	0.048
47	0.012	0.014	0.000	0.018	0.004	0.013	0.029

Table L.11: FF systematics due to background (in units of statistical standard deviations). (I) δE and M_{BC} cuts, (II) K_S veto.

num	Amplitude mode	I	II	Total
	$D \to SS$			
1	$D \to (K^-\pi^+)_S(\pi^0\pi^0)_S$	0.173	1.246	1.258
2	$D \to (K^-\pi^0)_S(\pi^+\pi^0)_S$	0.240	0.800	0.835
	$D \to AP, A \to VP$			
8S	$D \to K^-a_1(1260)^+, \rho^+\pi^0[S]$	0.353	0.257	0.436
8D	$D \to K^-a_1(1260)^+, \rho^+\pi^0[D]$	0.346	0.126	0.368
9S	$D \to K_1(1270)^-\pi^+, K^{*-}\pi^0[S]$	0.685	0.955	1.175
11S	$D \to K_1(1270)^0\pi^0, K^{*0}\pi^0[S]$	0.444	0.351	0.567
11D	$D \to K_1(1270)^0\pi^0, K^{*0}\pi^0[D]$	0.221	0.495	0.541
12S	$D \to K_1(1270)^0\pi^0, K^-\rho^+[S]$	0.117	0.187	0.221
14S	$D \to (K^{*-}\pi^0)_A\pi^+, K^{*-}\pi^0[S]$	0.711	1.033	0.125
16S	$D \to (K^{*0}\pi^0)_A\pi^0, K^{*0}\pi^0[S]$	0.068	0.520	0.524
16D	$D \to (K^{*0}\pi^0)_A\pi^0, K^{*0}\pi^0[D]$	1.455	0.190	1.468
17D	$D \to (\rho^+K^-)_A\pi^0, K^-\rho^+[D]$	0.671	0.457	0.812
	$D \to AP, A \to SP$			
21	$D \to ((K^-\pi^+)_S\pi^0)_A\pi^0$	0.186	0.323	0.372
	$D \to VS$			
26	$D \to (K^-\pi^0)_S\rho^+$	0.224	0.115	0.252
27	$D \to K^{*-}(\pi^+\pi^0)_S$	0.392	0.385	0.549
28	$D \to K^{*0}(\pi^0\pi^0)_S$	0.078	0.411	0.417
	$D \to VP, V \to VP$			
33	$D \to (K^{*-}\pi^+)_V\pi^0$	0.478	0.582	0.752
	$D \to VV$			
38S	$D[S] \to K^{*-}\rho^+$	0.049	1.353	1.354
38P	$D[P] \to K^{*-}\rho^+$	0.444	0.241	0.506
38D	$D[D] \to K^{*-}\rho^+$	0.085	0.592	0.598
39P	$D[P] \to (K^-\pi^0)_V\rho^+$	1.223	0.008	1.223
39D	$D[D] \to (K^-\pi^0)_V\rho^+$	0.833	0.158	0.848
40D	$D[D] \to K^{*-}(\pi^+\pi^0)_V$	0.323	0.834	0.894
43S	$D[S] \to (K^-\pi^0)_V(\pi^+\pi^0)_V$	0.089	0.434	0.443
	$D \to TS$			
46	$D \to (K^-\pi^+)_S(\pi^0\pi^0)_T$	0.770	0.530	0.936
47	$D \to (K^-\pi^0)_S(\pi^+\pi^0)_T$	0.179	0.060	0.188

Table L.12: Phase, ϕ, systematics due to background (in units of statistical standard deviations). (I) δE and M_{BC} cuts, (II) K_S veto.

num	**Amplitude mode**	**I**	**II**	**Total**
	$D \to SS$			
1	$D \to (K^-\pi^+)_S(\pi^0\pi^0)_S$	0.025	0.090	0.093
2	$D \to (K^-\pi^0)_S(\pi^+\pi^0)_S$	0.092	0.845	0.850
	$D \to AP, A \to VP$			
8S	$D \to K^-a_1(1260)^+, \rho^+\pi^0[S]$	0.000	0.000	0.000
8D	$D \to K^-a_1(1260)^+, \rho^+\pi^0[D]$	0.105	0.754	0.761
9S	$D \to K_1(1270)^-\pi^+, K^{*-}\pi^0[S]$	0.258	0.778	0.820
11S	$D \to K_1(1270)^0\pi^0, K^{*0}\pi^0[S]$	0.466	0.303	0.556
11D	$D \to K_1(1270)^0\pi^0, K^{*0}\pi^0[D]$	0.241	0.419	0.483
12S	$D \to K_1(1270)^0\pi^0, K^-\rho^+[S]$	0.061	0.178	0.188
14S	$D \to (K^{*-}\pi^0)_A\pi^+, K^{*-}\pi^0[S]$	0.398	0.583	0.706
16S	$D \to (K^{*0}\pi^0)_A\pi^0, K^{*0}\pi^0[S]$	0.264	0.252	0.365
16D	$D \to (K^{*0}\pi^0)_A\pi^0, K^{*0}\pi^0[D]$	0.436	0.420	0.605
17D	$D \to (\rho^+K^-)_A\pi^0, K^-\rho^+[D]$	0.550	0.271	0.613
	$D \to AP, A \to SP$			
21	$D \to ((K^-\pi^+)_S\pi^0)_A\pi^0$	0.115	0.394	0.410
	$D \to VS$			
26	$D \to (K^-\pi^0)_S\rho^+$	0.126	0.454	0.471
27	$D \to K^{*-}(\pi^+\pi^0)_S$	0.086	0.243	0.258
28	$D \to K^{*0}(\pi^0\pi^0)_S$	0.142	0.454	0.476
	$D \to VP, V \to VP$			
33	$D \to (K^{*-}\pi^+)_V\pi^0$	0.454	0.126	0.471
	$D \to VV$			
38S	$D[S] \to K^{*-}\rho^+$	0.151	0.032	0.154
38P	$D[P] \to K^{*-}\rho^+$	0.112	0.182	0.214
38D	$D[D] \to K^{*-}\rho^+$	0.121	1.101	1.108
39P	$D[P] \to (K^-\pi^0)_V\rho^+$	0.322	0.034	0.324
39D	$D[D] \to (K^-\pi^0)_V\rho^+$	0.730	0.400	0.832
40D	$D[D] \to K^{*-}(\pi^+\pi^0)_V$	0.275	1.284	1.313
43S	$D[S] \to (K^-\pi^0)_V(\pi^+\pi^0)_V$	0.209	0.043	0.213
	$D \to TS$			
46	$D \to (K^-\pi^+)_S(\pi^0\pi^0)_T$	0.475	0.547	0.724
47	$D \to (K^-\pi^0)_S(\pi^+\pi^0)_T$	0.616	0.369	0.718

Table L.13: FF systematics due to experimental effects (in units of statistical standard deviations). (I) π^0 reconstruction, (II) π PID, (III) K PID, (IV) π tracking, (IV) K tracking.

num	**Amplitude mode**	**I**	**II**	**III**	**IV**	**V**	**Total**
	$D \to SS$						
1	$D \to (K^-\pi^+)_S(\pi^0\pi^0)_S$	0.064	0.007	0.010	0.010	0.028	0.072
2	$D \to (K^-\pi^0)_S(\pi^+\pi^0)_S$	0.074	0.004	0.006	0.009	0.022	0.078
	$D \to AP, A \to VP$						
8S	$D \to K^-a_1(1260)^+, \rho^+\pi^0[S]$	0.018	0.007	0.008	0.006	0.021	0.030
8D	$D \to K^-a_1(1260)^+, \rho^+\pi^0[D]$	0.014	0.004	0.002	0.008	0.016	0.024
9S	$D \to K_1(1270)^-\pi^+, K^{*-}\pi^0[S]$	0.150	0.028	0.012	0.038	0.027	0.160
11S	$D \to K_1(1270)^0\pi^0, K^{*0}\pi^0[S]$	0.020	0.007	0.004	0.014	0.023	0.034
11D	$D \to K_1(1270)^0\pi^0, K^{*0}\pi^0[D]$	0.029	0.017	0.006	0.006	0.012	0.035
12S	$D \to K_1(1270)^0\pi^0, K^-\rho^+[S]$	0.082	0.006	0.018	0.024	0.042	0.098
14S	$D \to (K^{*-}\pi^0)_A\pi^+, K^{*-}\pi^0[S]$	0.067	0.005	0.013	0.007	0.033	0.076
16S	$D \to (K^{*0}\pi^0)_A\pi^0, K^{*0}\pi^0[S]$	0.011	0.007	0.004	0.013	0.012	0.022
16D	$D \to (K^{*0}\pi^0)_A\pi^0, K^{*0}\pi^0[D]$	0.022	0.007	0.007	0.015	0.044	0.052
17D	$D \to (\rho^+K^-)_A\pi^0, K^-\rho^+[D]$	0.071	0.011	0.006	0.019	0.037	0.084
	$D \to AP, A \to SP$						
21	$D \to ((K^-\pi^+)_S\pi^0)_A\pi^0$	0.100	0.008	0.007	0.012	0.014	0.102
	$D \to VS$						
26	$D \to (K^-\pi^0)_S\rho^+$	0.047	0.009	0.012	0.017	0.046	0.070
27	$D \to K^{*-}(\pi^+\pi^0)_S$	0.010	0.006	0.007	0.009	0.017	0.023
28	$D \to K^{*0}(\pi^0\pi^0)_S$	0.072	0.007	0.001	0.007	0.020	0.078
	$D \to VP, V \to VP$						
33	$D \to (K^{*-}\pi^+)_V\pi^0$	0.029	0.007	0.004	0.010	0.010	0.033
	$D \to VV$						
38S	$D[S] \to K^{*-}\rho^+$	0.055	0.012	0.004	0.015	0.012	0.059
38P	$D[P] \to K^{*-}\rho^+$	0.028	0.005	0.003	0.008	0.009	0.031
38D	$D[D] \to K^{*-}\rho^+$	0.024	0.005	0.006	0.006	0.042	0.049
39P	$D[P] \to (K^-\pi^0)_V\rho^+$	0.019	0.006	0.004	0.010	0.013	0.027
39D	$D[D] \to (K^-\pi^0)_V\rho^+$	0.221	0.024	0.020	0.024	0.078	0.237
40D	$D[D] \to K^{*-}(\pi^+\pi^0)_V$	0.026	0.005	0.008	0.014	0.039	0.049
43S	$D[S] \to (K^-\pi^0)_V(\pi^+\pi^0)_V$	0.043	0.004	0.006	0.006	0.014	0.046
	$D \to TS$						
46	$D \to (K^-\pi^+)_S(\pi^0\pi^0)_T$	0.082	0.014	0.009	0.009	0.012	0.084
47	$D \to (K^-\pi^0)_S(\pi^+\pi^0)_T$	0.044	0.021	0.006	0.046	0.014	0.068

Table L.14: Phase, ϕ, systematics due to experimental effects (in units of statistical standard deviations). (I) π^0 reconstruction, (II) π PID, (III) K PID, (IV) π tracking, (IV) K tracking.

num	Amplitude mode	I	II	III	IV	V	Total
	$D \to SS$						
1	$D \to (K^-\pi^+)_S(\pi^0\pi^0)_S$	0.037	0.004	0.005	0.008	0.019	0.043
2	$D \to (K^-\pi^0)_S(\pi^+\pi^0)_S$	0.037	0.005	0.006	0.014	0.018	0.044
	$D \to AP, A \to VP$						
8S	$D \to K^-a_1(1260)^+, \rho^+\pi^0[S]$	0.000	0.000	0.000	0.000	0.000	0.000
8D	$D \to K^-a_1(1260)^+, \rho^+\pi^0[D]$	0.071	0.013	0.004	0.022	0.030	0.081
9S	$D \to K_1(1270)^-\pi^+, K^{*-}\pi^0[S]$	0.029	0.012	0.008	0.034	0.026	0.054
11S	$D \to K_1(1270)^0\pi^0, K^{*0}\pi^0[S]$	0.019	0.010	0.006	0.011	0.014	0.029
11D	$D \to K_1(1270)^0\pi^0, K^{*0}\pi^0[D]$	0.031	0.009	0.011	0.024	0.017	0.045
12S	$D \to K_1(1270)^0\pi^0, K^-\rho^+[S]$	0.066	0.009	0.008	0.027	0.032	0.079
14S	$D \to (K^{*-}\pi^0)_A\pi^+, K^{*-}\pi^0[S]$	0.038	0.005	0.007	0.009	0.026	0.048
16S	$D \to (K^{*0}\pi^0)_A\pi^0, K^{*0}\pi^0[S]$	0.028	0.009	0.007	0.018	0.040	0.053
16D	$D \to (K^{*0}\pi^0)_A\pi^0, K^{*0}\pi^0[D]$	0.040	0.012	0.010	0.018	0.021	0.051
17D	$D \to (\rho^+K^-)_A\pi^0, K^-\rho^+[D]$	0.130	0.013	0.004	0.007	0.026	0.133
	$D \to AP, A \to SP$						
21	$D \to ((K^-\pi^+)_S\pi^0)_A\pi^0$	0.020	0.007	0.008	0.016	0.035	0.045
	$D \to VS$						
26	$D \to (K^-\pi^0)_S\rho^+$	0.041	0.010	0.010	0.007	0.029	0.053
27	$D \to K^{*-}(\pi^+\pi^0)_S$	0.038	0.008	0.003	0.018	0.013	0.045
28	$D \to K^{*0}(\pi^0\pi^0)_S$	0.011	0.014	0.016	0.044	0.037	0.062
	$D \to VP, V \to VP$						
33	$D \to (K^{*-}\pi^+)_V\pi^0$	0.026	0.003	0.003	0.009	0.016	0.032
	$D \to VV$						
38S	$D[S] \to K^{*-}\rho^+$	0.059	0.006	0.006	0.010	0.035	0.070
38P	$D[P] \to K^{*-}\rho^+$	0.030	0.005	0.003	0.009	0.015	0.035
38D	$D[D] \to K^{*-}\rho^+$	0.042	0.006	0.007	0.011	0.026	0.051
39P	$D[P] \to (K^-\pi^0)_V\rho^+$	0.013	0.010	0.004	0.012	0.010	0.023
39D	$D[D] \to (K^-\pi^0)_V\rho^+$	0.130	0.014	0.007	0.005	0.023	0.133
40D	$D[D] \to K^{*-}(\pi^+\pi^0)_V$	0.024	0.002	0.011	0.006	0.029	0.040
43S	$D[S] \to (K^-\pi^0)_V(\pi^+\pi^0)_V$	0.025	0.003	0.006	0.019	0.025	0.041
	$D \to TS$						
46	$D \to (K^-\pi^+)_S(\pi^0\pi^0)_T$	0.020	0.010	0.011	0.007	0.051	0.057
47	$D \to (K^-\pi^0)_S(\pi^+\pi^0)_T$	0.033	0.012	0.005	0.029	0.021	0.050

Table L.15: FF systematics due to π^0 reconstruction (in units of statistical standard deviations). (I) $0.0-0.2$, (II) $0.2-0.4$, (III) $0.4-0.6$, (IV) $0.6-0.8$, (V) > 0.8 GeV.

num	**I**	**II**	**III**	**IV**	**V**	**Total**
1	0.0002	0.0215	0.0562	0.0219	0.0001	0.0640
2	0.0040	0.0264	0.0651	0.0233	0.0001	0.0741
8S	0.0048	0.0170	0.0017	0.0004	0.0004	0.0178
8D	0.0037	0.0112	0.0073	0.0024	0.0008	0.0140
9S	0.0052	0.0800	0.1267	0.0155	0.0005	0.1507
11S	0.0003	0.0129	0.0147	0.0029	0.0006	0.0200
11D	0.0256	0.0134	0.0023	0.0099	0.0017	0.0308
12S	0.0016	0.0521	0.0633	0.0005	0.0004	0.0819
14S	0.0111	0.0387	0.0523	0.0082	0.0009	0.0665
16S	0.0023	0.0016	0.0100	0.0026	0.0003	0.0108
16D	0.0175	0.0052	0.0025	0.0114	0.0007	0.0217
17D	0.0171	0.0256	0.0602	0.0036	0.0007	0.0720
21	0.0009	0.0608	0.0787	0.0065	0.0007	0.997
26	0.0191	0.0350	0.0217	0.0115	0.0002	0.0468
27	0.0049	0.0069	0.0051	0.0028	0.0002	0.0103
28	0.0065	0.0443	0.0535	0.0072	0.0001	0.0704
33	0.0035	0.0088	0.0268	0.0001	0.0002	0.0285
38S	0.0090	0.0485	0.0203	0.0080	0.0015	0.0540
38P	0.0058	0.0058	0.0276	0.0027	0.0005	0.0289
38D	0.0012	0.0222	0.0010	0.0073	0.0002	0.0235
39P	0.0028	0.0045	0.0183	0.0038	0.0013	0.0195
39D	0.0689	0.0657	0.1973	0.0261	0.0008	0.2205
40D	0.0035	0.0027	0.0247	0.0036	0.0000	0.0254
43S	0.0102	0.0182	0.0351	0.0130	0.0004	0.0428
46	0.0383	0.0637	0.0119	0.0294	0.0051	0.0810
47	0.0375	0.0029	0.0135	0.0207	0.0011	0.0450

Table L.16: Phase, ϕ, systematics due to π^0 reconstruction (in units of statistical standard deviations). (I) $0.0-0.2$, (II) $0.2-0.4$, (III) $0.4-0.6$, (IV) $0.6-0.8$, (V) >0.8 GeV.

num	**I**	**II**	**III**	**IV**	**V**	**Total**
1	0.0331	0.0173	0.0001	0.0026	0.0004	0.0374
2	0.0215	0.0243	0.0014	0.0169	0.0005	0.0366
8S	0.0000	0.0000	0.0000	0.0000	0.0000	0.0000
8D	0.0043	0.0311	0.0633	0.0029	0.0011	0.0707
9S	0.0018	0.0218	0.0192	0.0034	0.0003	0.0293
11S	0.0013	0.0093	0.0161	0.0008	0.0009	0.0187
11D	0.0004	0.0235	0.0185	0.0068	0.0002	0.0307
12S	0.0301	0.0142	0.0559	0.0101	0.0001	0.0658
14S	0.0174	0.0012	0.0334	0.0011	0.0003	0.0377
16S	0.0047	0.0007	0.0257	0.0102	0.0009	0.0281
16D	0.0341	0.0122	0.0115	0.0111	0.0024	0.0397
17D	0.0862	0.0939	0.0214	0.0109	0.0000	0.1300
21	0.0001	0.0030	0.0160	0.0118	0.0006	0.0201
26	0.0321	0.0157	0.0199	0.0013	0.0013	0.0409
27	0.0070	0.0160	0.0318	0.0120	0.0003	0.0382
28	0.0109	0.0003	0.0008	0.0028	0.0005	0.0113
33	0.0017	0.0172	0.0189	0.0025	0.0003	0.0257
38S	0.0030	0.0318	0.0493	0.0044	0.0004	0.0589
38P	0.0016	0.0283	0.0080	0.0072	0.0016	0.0304
38D	0.0109	0.0064	0.0382	0.0124	0.0005	0.0421
39P	0.0024	0.0004	0.0122	0.0017	0.0006	0.0126
39D	0.0843	0.0973	0.0182	0.0047	0.0014	0.1301
40D	0.0030	0.0046	0.0225	0.0046	0.0000	0.0236
43S	0.0039	0.0116	0.0220	0.0019	0.0000	0.0252
46	0.0022	0.0187	0.0015	0.0048	0.0009	0.0195
47	0.0308	0.0059	0.0028	0.0081	0.0018	0.0326

Table L.17: FF systematics due to π PID (in units of statistical standard deviations). (I) $0.0-0.2$, (II) $0.2-0.3$, (III) $0.3-0.4$, (IV) $0.4-0.5$, (V) $0.5-0.6$, (VI) $0.6-0.7$, (VII) > 0.7 GeV.

num	**I**	**II**	**III**	**IV**	**V**	**VI**	**VII**	**Total**
1	0.0019	0.0003	0.0000	0.0003	0.0005	0.0018	0.0064	0.0070
2	0.0026	0.0005	0.0004	0.0009	0.0030	0.0002	0.0016	0.0044
8S	0.0006	0.0005	0.0004	0.0001	0.0061	0.0018	0.0028	0.0070
8D	0.0010	0.0004	0.0012	0.0002	0.0000	0.0010	0.0028	0.0035
9S	0.0010	0.0025	0.0085	0.0025	0.0207	0.0030	0.0152	0.0275
11S	0.0000	0.0016	0.0020	0.0012	0.0001	0.0001	0.0063	0.0069
11D	0.0023	0.0017	0.0012	0.0012	0.0035	0.0006	0.0140	0.0145
12S	0.0016	0.0029	0.0010	0.0014	0.0009	0.0015	0.0036	0.0055
14S	0.0012	0.0005	0.0008	0.0010	0.0035	0.0025	0.0013	0.0048
16S	0.0002	0.0011	0.0011	0.0021	0.0008	0.0025	0.0014	0.0070
16D	0.0010	0.0002	0.0025	0.0012	0.0049	0.0000	0.0047	0.0074
17D	0.0011	0.0004	0.0009	0.0000	0.0034	0.0039	0.0099	0.0113
21	0.0004	0.0005	0.0003	0.0000	0.0079	0.0010	0.0030	0.0085
26	0.0010	0.0005	0.0013	0.0013	0.0041	0.0041	0.0069	0.0093
27	0.0002	0.0005	0.0001	0.0014	0.0038	0.0007	0.0036	0.0054
28	0.0026	0.0001	0.0013	0.0007	0.0091	0.0007	0.0065	0.0117
33	0.0000	0.0012	0.0017	0.0013	0.0047	0.0025	0.0022	0.0063
38S	0.0016	0.0009	0.0013	0.0001	0.0099	0.0003	0.0073	0.0124
38P	0.0009	0.0003	0.0004	0.0005	0.0019	0.0001	0.0041	0.0046
38D	0.0002	0.0002	0.0002	0.0001	0.0004	0.0011	0.0052	0.0053
39P	0.0016	0.0004	0.0014	0.0013	0.0001	0.0021	0.0047	0.0057
39D	0.0007	0.0010	0.0003	0.0008	0.0165	0.0056	0.0166	0.0241
40D	0.0005	0.0003	0.0000	0.0017	0.0049	0.0013	0.0013	0.0055
43S	0.0004	0.0005	0.0011	0.0001	0.0031	0.0009	0.0018	0.0039
46	0.0014	0.0019	0.0002	0.0005	0.0131	0.0026	0.0023	0.0138
47	0.0035	0.0021	0.0003	0.0027	0.0027	0.0158	0.0122	0.0207

Table L.18: Phase, ϕ, systematics due to π PID (in units of statistical standard deviations). (I) $0.0-0.2$, (II) $0.2-0.3$, (III) $0.3-0.4$, (IV) $0.4-0.5$, (V) $0.5-0.6$, (VI) $0.6-0.7$, (VII) >0.7 GeV.

num	**I**	**II**	**III**	**IV**	**V**	**VI**	**VII**	**Total**
1	0.0024	0.0015	0.0020	0.0007	0.0013	0.0011	0.0012	0.0041
2	0.0003	0.0014	0.0000	0.0002	0.0035	0.0024	0.0019	0.0049
8S	0.0000	0.0000	0.0000	0.0000	0.0000	0.0000	0.0000	0.0000
8D	0.0078	0.0018	0.0026	0.0032	0.0011	0.0040	0.0084	0.0130
9S	0.0002	0.0014	0.0020	0.0005	0.0066	0.0067	0.0072	0.0121
11S	0.0070	0.0008	0.0066	0.0012	0.0025	0.0003	0.0004	0.0101
11D	0.0032	0.0008	0.0007	0.0012	0.0070	0.0008	0.0036	0.0087
12S	0.0024	0.0011	0.0042	0.0013	0.0028	0.0058	0.0036	0.0090
14S	0.0016	0.0002	0.0002	0.0013	0.0030	0.0001	0.0031	0.0048
16S	0.0037	0.0019	0.0011	0.0002	0.0001	0.0019	0.0073	0.0087
16D	0.0012	0.0002	0.0027	0.0017	0.0085	0.0016	0.0067	0.0115
17D	0.0008	0.0000	0.0014	0.0001	0.0080	0.0013	0.0103	0.0132
21	0.0044	0.0006	0.0043	0.0004	0.0031	0.0010	0.0005	0.0070
26	0.0069	0.0002	0.0064	0.0006	0.0019	0.0005	0.0015	0.0098
27	0.0046	0.0002	0.0049	0.0015	0.0030	0.0016	0.0028	0.0082
28	0.0036	0.0022	0.0029	0.0026	0.0038	0.0099	0.0076	0.0143
33	0.0019	0.0004	0.0019	0.0009	0.0017	0.0003	0.0004	0.0034
38S	0.0032	0.0016	0.0022	0.0009	0.0034	0.0009	0.0013	0.0057
38P	0.0028	0.0003	0.0038	0.0002	0.0003	0.0010	0.0022	0.0053
38D	0.0014	0.0002	0.0033	0.0014	0.0019	0.0011	0.0044	0.0062
39P	0.0082	0.0003	0.0025	0.0007	0.0029	0.0038	0.0000	0.0098
39D	0.0024	0.0003	0.0082	0.0002	0.0076	0.0003	0.0084	0.0142
40D	0.0007	0.0002	0.0019	0.0008	0.0004	0.0001	0.0000	0.0022
43S	0.0022	0.0000	0.0007	0.0006	0.0006	0.0009	0.0014	0.0030
46	0.0024	0.0001	0.0031	0.0010	0.0000	0.0014	0.0092	0.0101
47	0.0071	0.0016	0.0031	0.0009	0.0061	0.0054	0.0030	0.0118

Table L.19: FF systematics due to K PID (in units of statistical standard deviations). (I) $0.0 - 0.3$, (II) $0.3 - 0.4$, (III) $0.4 - 0.5$, (IV) $0.5 - 0.6$, (V) $0.6 - 0.7$, (VI) > 0.7.

num	**I**	**II**	**III**	**IV**	**V**	**VI**	**Total**
1	0.0021	0.0032	0.0024	0.0026	0.0014	0.0087	0.0103
2	0.0008	0.0008	0.0014	0.0023	0.0030	0.0041	0.0059
8S	0.0071	0.0008	0.0000	0.0008	0.0005	0.0027	0.0077
8D	0.0004	0.0002	0.0004	0.0000	0.0018	0.0020	0.0028
9S	0.0082	0.0022	0.0015	0.0068	0.0027	0.0037	0.0118
11S	0.0004	0.0016	0.0001	0.0023	0.0012	0.0028	0.0041
11D	0.0012	0.0006	0.0000	0.0017	0.0006	0.0023	0.0035
12S	0.0112	0.0037	0.0099	0.0095	0.0030	0.0012	0.0184
14S	0.0123	0.0003	0.0035	0.0025	0.0022	0.0031	0.0136
16S	0.0016	0.0020	0.0019	0.0006	0.0001	0.0025	0.0041
16D	0.0042	0.0010	0.0002	0.0007	0.0007	0.0054	0.0069
17D	0.0058	0.0002	0.0011	0.0015	0.0008	0.0013	0.0064
21	0.0041	0.0022	0.0007	0.0021	0.0002	0.0033	0.0061
26	0.0116	0.0016	0.0016	0.0000	0.0004	0.0007	0.0118
27	0.0057	0.0028	0.0013	0.0025	0.0017	0.0002	0.0072
28	0.0012	0.0006	0.0013	0.0014	0.0008	0.0011	0.0026
33	0.0029	0.0022	0.0002	0.0022	0.0008	0.0007	0.0045
38S	0.0000	0.0003	0.0000	0.0037	0.0006	0.0006	0.0038
38P	0.0028	0.0004	0.0004	0.0000	0.0008	0.0008	0.0031
38D	0.0042	0.0012	0.0000	0.0008	0.0008	0.0043	0.0063
39P	0.0023	0.0009	0.0009	0.0013	0.0011	0.0005	0.0032
39D	0.0156	0.0059	0.0022	0.0090	0.0053	0.0025	0.0200
40D	0.0061	0.0043	0.0022	0.0014	0.0024	0.0004	0.0082
43S	0.0042	0.0031	0.0018	0.0000	0.0025	0.0025	0.0065
46	0.0051	0.0028	0.0061	0.0021	0.0026	0.0026	0.0093
47	0.0033	0.0043	0.0019	0.0003	0.0001	0.0005	0.0057

Table L.20: Phase, ϕ, systematics due to K PID (in units of statistical standard deviations). (I) $0.0-0.3$, (II) $0.3-0.4$, (III) $0.4-0.5$, (IV) $0.5-0.6$, (V) $0.6-0.7$, (VI) >0.7.

num	I	II	III	IV	V	VI	Total
1	0.0026	0.0009	0.0006	0.0012	0.0006	0.0032	0.0045
2	0.0041	0.0010	0.0026	0.0009	0.0023	0.0003	0.0055
8S	0.0000	0.0000	0.0000	0.0000	0.0000	0.0000	0.0000
8D	0.0003	0.0025	0.0005	0.0007	0.0021	0.0011	0.0036
9S	0.0061	0.0025	0.0007	0.0017	0.0003	0.0035	0.0077
11S	0.0017	0.0035	0.0030	0.0003	0.0005	0.0026	0.0056
11D	0.0084	0.0023	0.0003	0.0048	0.0024	0.0051	0.0114
12S	0.0003	0.0061	0.0033	0.0009	0.0021	0.0022	0.0076
14S	0.0050	0.0015	0.0013	0.0022	0.0019	0.0025	0.0066
16S	0.0053	0.0039	0.0012	0.0006	0.0007	0.0004	0.0068
16D	0.0058	0.0022	0.0003	0.0014	0.0016	0.0079	0.0103
17D	0.0032	0.0001	0.0000	0.0014	0.0024	0.0007	0.0043
21	0.0065	0.0011	0.0024	0.0021	0.0023	0.0011	0.0078
26	0.0037	0.0052	0.0021	0.0049	0.0045	0.0022	0.0097
27	0.0000	0.0021	0.0008	0.0015	0.0015	0.0009	0.0032
28	0.0055	0.0054	0.0000	0.0018	0.0066	0.0128	0.0164
33	0.0008	0.0017	0.0000	0.0012	0.0015	0.0009	0.0028
38S	0.0047	0.0025	0.0008	0.0005	0.0005	0.0008	0.0055
38P	0.0005	0.0018	0.0009	0.0012	0.0012	0.0000	0.0027
38D	0.0068	0.0003	0.0014	0.0008	0.0001	0.0023	0.0074
39P	0.0031	0.0024	0.0002	0.0016	0.0005	0.0012	0.0044
39D	0.0070	0.0001	0.0007	0.0003	0.0012	0.0012	0.0072
40D	0.0099	0.0017	0.0004	0.0010	0.0001	0.0046	0.0111
43S	0.0022	0.0001	0.0009	0.0001	0.0010	0.0052	0.0058
46	0.0029	0.0085	0.0021	0.0003	0.0010	0.0051	0.0106
47	0.0033	0.0016	0.0022	0.0028	0.0000	0.0006	0.0051

Table L.21: FF systematics due to π tracking (in units of statistical standard deviations). (I) $0.0-0.2$, (II) $0.2-0.3$, (III) $0.3-0.4$, (IV) $0.4-0.5$, (V) $0.5-0.6$, (VI) $0.6-0.7$, (VII) > 0.7 GeV.

num	I	II	III	IV	V	VI	VII	Total
1	0.0016	0.0078	0.0022	0.0040	0.0017	0.0033	0.0037	0.0106
2	0.0061	0.0045	0.0031	0.0022	0.0006	0.0001	0.0012	0.0086
8S	0.0014	0.0017	0.0014	0.0004	0.0015	0.0047	0.0013	0.0058
8D	0.0008	0.0031	0.0047	0.0006	0.0055	0.0031	0.0012	0.0085
9S	0.0100	0.0057	0.0328	0.0108	0.0102	0.0062	0.0053	0.0387
11S	0.0109	0.0079	0.0002	0.0030	0.0003	0.0002	0.0017	0.0139
11D	0.0029	0.0023	0.0000	0.0006	0.0006	0.0023	0.0023	0.0052
12S	0.0024	0.0188	0.0063	0.0117	0.0023	0.0028	0.0004	0.0234
14S	0.0007	0.0009	0.0008	0.0014	0.0033	0.0051	0.0020	0.0067
16S	0.0039	0.0039	0.0070	0.0060	0.0001	0.0063	0.0044	0.0132
16D	0.0116	0.0032	0.0091	0.0035	0.0020	0.0007	0.0017	0.0158
17D	0.0009	0.0086	0.0011	0.0024	0.0026	0.0101	0.0133	0.0191
21	0.0112	0.0042	0.0010	0.0003	0.0003	0.0020	0.0029	0.0125
26	0.0113	0.0031	0.0018	0.0052	0.0023	0.0097	0.0058	0.0174
27	0.0039	0.0026	0.0006	0.0047	0.0050	0.0002	0.0018	0.0085
28	0.0009	0.0033	0.0052	0.0003	0.0032	0.0008	0.0013	0.0072
33	0.0004	0.0001	0.0017	0.0027	0.0052	0.0070	0.0015	0.0085
38S	0.0126	0.0027	0.0013	0.0040	0.0015	0.0046	0.0043	0.0149
38P	0.0049	0.0017	0.0004	0.0010	0.0032	0.0001	0.0035	0.0071
38D	0.0017	0.0028	0.0019	0.0037	0.0002	0.0016	0.0028	0.0061
39P	0.0067	0.0024	0.0008	0.0015	0.0034	0.0057	0.0027	0.0102
39D	0.0066	0.0051	0.0126	0.0031	0.0064	0.0137	0.0092	0.0234
40D	0.0067	0.0086	0.0070	0.0059	0.0014	0.0032	0.0006	0.0147
43S	0.0034	0.0028	0.0012	0.0028	0.0009	0.0010	0.0011	0.0057
46	0.0044	0.0040	0.0019	0.0002	0.0047	0.0056	0.0005	0.0096
47	0.0255	0.0112	0.0011	0.0114	0.0033	0.0307	0.0149	0.0456

Table L.22: Phase, ϕ, systematics due to π tracking (in units of statistical standard deviations). (I) $0.0 - 0.2$, (II) $0.2 - 0.3$, (III) $0.3 - 0.4$, (IV) $0.4 - 0.5$, (V) $0.5 - 0.6$, (VI) $0.6 - 0.7$, (VII) > 0.7 GeV.

num	**I**	**II**	**III**	**IV**	**V**	**VI**	**VII**	**Total**
1	0.0029	0.0039	0.0006	0.0030	0.0048	0.0030	0.0005	0.0081
2	0.0053	0.0107	0.0014	0.0025	0.0043	0.0053	0.0033	0.0144
8S	0.0000	0.0000	0.0000	0.0000	0.0000	0.0000	0.0000	0.0000
8D	0.0113	0.0092	0.0028	0.0056	0.0030	0.0098	0.0111	0.0219
9S	0.0111	0.0013	0.0064	0.0108	0.0240	0.0157	0.0063	0.0338
11S	0.0029	0.0059	0.0027	0.0061	0.0041	0.0016	0.0027	0.0107
11D	0.0144	0.0158	0.0027	0.0089	0.0051	0.0000	0.0010	0.0239
12S	0.0134	0.0002	0.0160	0.0022	0.0134	0.0111	0.0029	0.0274
14S	0.0073	0.0024	0.0025	0.0012	0.0011	0.0014	0.0026	0.0088
16S	0.0126	0.0037	0.0086	0.0009	0.0049	0.0064	0.0026	0.0179
16D	0.0030	0.0172	0.0000	0.0031	0.0029	0.0031	0.0020	0.0183
17D	0.0025	0.0037	0.0026	0.0006	0.0005	0.0029	0.0030	0.0067
21	0.0158	0.0031	0.0000	0.0005	0.0025	0.0018	0.0006	0.0164
26	0.0059	0.0029	0.0024	0.0001	0.0015	0.0015	0.0003	0.0073
27	0.0162	0.0023	0.0044	0.0005	0.0014	0.0046	0.0035	0.0180
28	0.0251	0.0228	0.0012	0.0063	0.0214	0.0168	0.0030	0.0440
33	0.0003	0.0089	0.0008	0.0018	0.0011	0.0008	0.0009	0.0093
38S	0.0011	0.0045	0.0032	0.0065	0.0035	0.0014	0.0029	0.0098
38P	0.0043	0.0075	0.0024	0.0008	0.0013	0.0022	0.0010	0.0094
38D	0.0079	0.0044	0.0019	0.0019	0.0033	0.0034	0.0006	0.0106
39P	0.0044	0.0066	0.0011	0.0005	0.0032	0.0059	0.0051	0.0116
39D	0.0004	0.0014	0.0003	0.0016	0.0034	0.0012	0.0034	0.0054
40D	0.0049	0.0025	0.0016	0.0005	0.0013	0.0000	0.0016	0.0061
43S	0.0188	0.0030	0.0020	0.0006	0.0014	0.0014	0.0013	0.0193
46	0.0002	0.0004	0.0004	0.0000	0.0052	0.0014	0.0038	0.0066
47	0.0211	0.0122	0.0012	0.0042	0.0091	0.0117	0.0012	0.0289

Table L.23: FF systematics due to K tracking (in units of statistical standard deviations). (I) $0.00-0.17$, (II) $0.17-0.21$, (III) $0.21-0.25$, (IV) $0.25-0.35$, (V) $0.35-0.45$, (VI) $0.45-0.55$, (VII)$0.55-0.65$, (VIII)>0.65 GeV.

num	**I**	**II**	**III**	**IV**	**V**	**VI**	**VII**	**VIII**	**Total**
1	0.0146	0.0169	0.0128	0.0017	0.0061	0.0011	0.0093	0.0002	0.0282
2	0.0105	0.0113	0.0054	0.0047	0.0004	0.0093	0.0066	0.0085	0.0221
8S	0.0011	0.0115	0.0112	0.0123	0.0008	0.0019	0.0011	0.0072	0.0216
8D	0.0055	0.0079	0.0033	0.0041	0.0010	0.0049	0.0008	0.0104	0.0159
9S	0.0088	0.0075	0.0098	0.0102	0.0025	0.0060	0.0143	0.0130	0.0273
11S	0.0093	0.0140	0.0096	0.0066	0.0014	0.0044	0.0077	0.0064	0.0232
11D	0.0064	0.0076	0.0035	0.0000	0.0017	0.0006	0.0006	0.0070	0.0128
12S	0.0164	0.0250	0.0222	0.0103	0.0050	0.0115	0.0063	0.0044	0.0413
14S	0.0176	0.0209	0.0149	0.0072	0.0013	0.0059	0.0016	0.0021	0.0327
16S	0.0027	0.0022	0.0028	0.0079	0.0020	0.0050	0.0028	0.0031	0.0114
16D	0.0250	0.0299	0.0173	0.0012	0.0032	0.0017	0.0025	0.0106	0.0442
17D	0.0206	0.0234	0.0150	0.0064	0.0019	0.0066	0.0062	0.0022	0.0366
21	0.0036	0.0036	0.0016	0.0105	0.0037	0.0034	0.0058	0.0005	0.0140
26	0.0136	0.0277	0.0228	0.0243	0.0009	0.0069	0.0070	0.0000	0.0465
27	0.0027	0.0074	0.0089	0.0097	0.0021	0.0038	0.0048	0.0013	0.0167
28	0.0063	0.0066	0.0052	0.0033	0.0014	0.0021	0.0059	0.0130	0.0183
33	0.0009	0.0021	0.0022	0.0039	0.0023	0.0039	0.0066	0.0011	0.0096
38S	0.0013	0.0024	0.0043	0.0036	0.0009	0.0049	0.0062	0.0067	0.0121
38P	0.0021	0.0023	0.0045	0.0052	0.0006	0.0005	0.0001	0.0041	0.0086
38D	0.0220	0.0272	0.0160	0.0044	0.0017	0.0024	0.0024	0.0159	0.0420
39P	0.0044	0.0068	0.0075	0.0045	0.0040	0.0025	0.0006	0.0016	0.0130
39D	0.0321	0.0470	0.0385	0.0258	0.0049	0.0154	0.0142	0.0134	0.0777
40D	0.0222	0.0246	0.0119	0.0053	0.0076	0.0009	0.0120	0.0055	0.0387
43S	0.0053	0.0076	0.0058	0.0055	0.0039	0.0012	0.0033	0.0028	0.0137
46	0.0014	0.0009	0.0019	0.0005	0.0058	0.0023	0.0023	0.0084	0.0110
47	0.0052	0.0109	0.0041	0.0030	0.0035	0.0019	0.0027	0.0016	0.0141

Table L.24: Phase, ϕ, systematics due to K tracking (in units of statistical standard deviations). (I) $0.00 - 0.17$, (II) $0.17 - 0.21$, (III) $0.21 - 0.25$, (IV) $0.25 - 0.35$, (V) $0.35 - 0.45$, (VI) $0.45 - 0.55$, (VII)$0.55 - 0.65$, (VIII)> 0.65 GeV.

num	**I**	**II**	**III**	**IV**	**V**	**VI**	**VII**	**VIII**	**Total**
1	0.0004	0.0027	0.0046	0.0115	0.0008	0.0085	0.0036	0.0106	0.0189
2	0.0061	0.0094	0.0084	0.0080	0.0033	0.0040	0.0022	0.0043	0.0176
8S	0.0000	0.0000	0.0000	0.0000	0.0000	0.0000	0.0000	0.0000	0.0000
8D	0.0179	0.0145	0.0126	0.0042	0.0101	0.0050	0.0081	0.0046	0.0303
9S	0.0060	0.0128	0.0031	0.0174	0.0051	0.0084	0.0085	0.0032	0.0263
11S	0.0041	0.0014	0.0022	0.0055	0.0052	0.0002	0.0075	0.0078	0.0141
11D	0.0043	0.0017	0.0017	0.0056	0.0024	0.0082	0.0069	0.0098	0.0165
12S	0.0174	0.0131	0.0140	0.0030	0.0132	0.0052	0.0031	0.0101	0.0315
14S	0.0099	0.0122	0.0090	0.0029	0.0010	0.0074	0.0090	0.0149	0.0264
16S	0.0259	0.0251	0.0063	0.0150	0.0046	0.0040	0.0040	0.0013	0.0403
16D	0.0038	0.0007	0.0035	0.0024	0.0004	0.0100	0.0074	0.0161	0.0211
17D	0.0084	0.0173	0.0147	0.0064	0.0022	0.0046	0.0017	0.0047	0.0260
21	0.0168	0.0159	0.0205	0.0167	0.0001	0.0024	0.0032	0.0008	0.0354
26	0.0091	0.0072	0.0025	0.0179	0.0071	0.0045	0.0139	0.0103	0.0288
27	0.0023	0.0000	0.0042	0.0101	0.0002	0.0016	0.0040	0.0037	0.0125
28	0.0217	0.0172	0.0130	0.0050	0.0079	0.0052	0.0059	0.0178	0.0374
33	0.0014	0.0008	0.0050	0.0113	0.0016	0.0014	0.0053	0.0081	0.0159
38S	0.0226	0.0221	0.0072	0.0104	0.0041	0.0011	0.0029	0.0014	0.0345
38P	0.0080	0.0085	0.0003	0.0091	0.0021	0.0011	0.0005	0.0012	0.0150
38D	0.0142	0.0117	0.0150	0.0097	0.0027	0.0020	0.0005	0.0046	0.0263
39P	0.0058	0.0007	0.0020	0.0029	0.0042	0.0004	0.0008	0.0054	0.0097
39D	0.0161	0.0077	0.0028	0.0072	0.0030	0.0084	0.0022	0.0083	0.0231
40D	0.0221	0.0199	0.0195	0.0099	0.0014	0.0020	0.0010	0.0108	0.0386
43S	0.0101	0.0113	0.0086	0.0054	0.0031	0.0049	0.0006	0.0159	0.0249
46	0.0353	0.0162	0.0216	0.0092	0.0057	0.0079	0.0064	0.0204	0.0511
47	0.0104	0.0129	0.0100	0.0034	0.0051	0.0015	0.0040	0.0041	0.0211

Appendix M

Plots for the Systematic Uncertainties Due to Fitter Performance

Two-hundred toy MC samples based on the PWA model are generated to test the uncertainty associated with fitter performance (see Section 8.1.4). This appendix shows the pull distributions of each fit fraction or phase fitted with a Gaussian function, where the pull is defined as the difference between the fit results of toy MC samples and the nominal values normalized to the corresponding statistical uncertainties. The Gaussian mean is considered as the uncertainty associated with fitter performance in units of statistical standard deviations, as listed in “Fitter performance” column of Tables 8.1 and 8.2. Fits to the fit fraction and phase pull distributions are shown in Sections M.1 and M.2, respectively. For completeness, fits to the fit fraction and phase distributions (absolute, not pull) are shown in Sections M.3 and M.4, respectively. Note that the fit fraction is non-negative; for some distributions, the limit at zero truncates the Gaussian shape. When tranlated to a pull, this cut-off will be mapped to a value which varies from case to case.

M.1 Fits to the Fit Fraction Pull Distributions

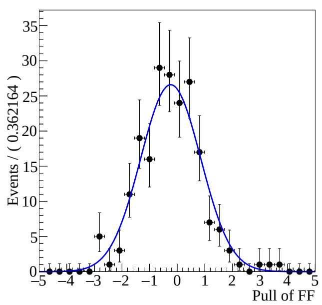

(a) $(K^-\pi^+)_S(\pi^0\pi^0)_S$

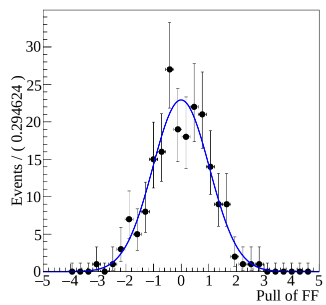

(b) $(K^-\pi^0)_S(\pi^+\pi^0)_S$

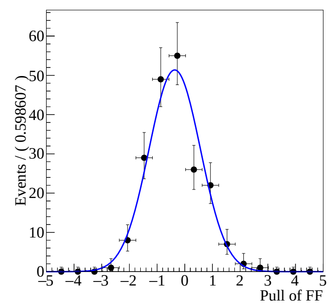

(c) $K^-a_1(1260)^+, \rho^+\pi^0[S]$

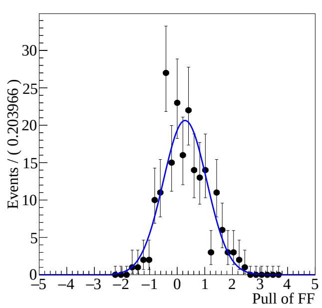

(d) $K^-a_1(1260)^+, \rho^+\pi^0[D]$

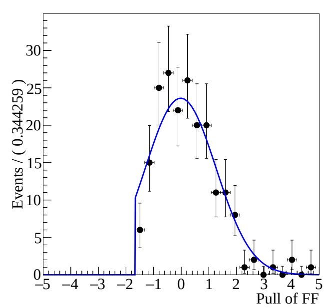

(e) $K_1(1270)^-\pi^+, K^{*-}\pi^0[S]$

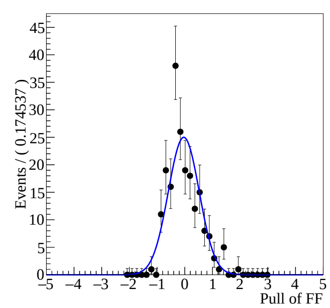

(f) $K_1(1270)^0\pi^0, K^{*0}\pi^0[S]$

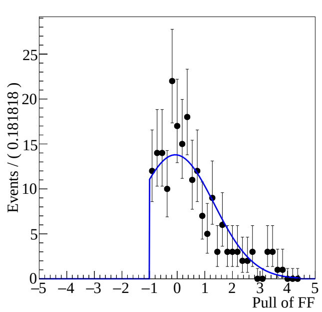

(g) $K_1(1270)^0\pi^0, K^{*0}\pi^0[D]$

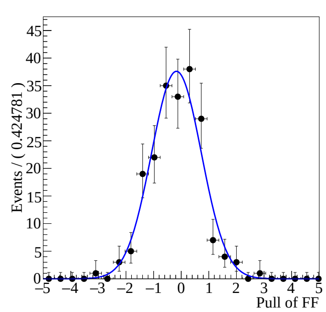

(h) $K_1(1270)^0\pi^0, K^-\rho^+[S]$

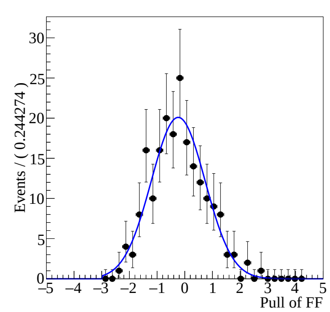

(i) $(K^{*-}\pi^0)_A\pi^+, K^{*-}\pi^0[S]$

Figure M.1: Fits to the fit fraction pull distributions (part 1).

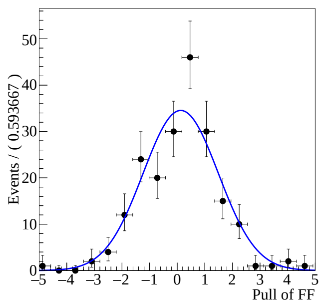

(a) $(K^{*0}\pi^0)_A\pi^0, K^{*0}\pi^0[S]$

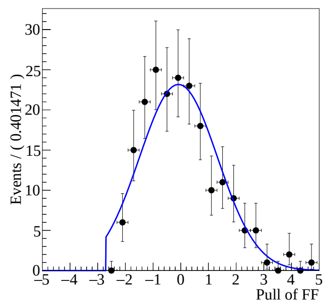

(b) $(K^{*0}\pi^0)_A\pi^0, K^{*0}\pi^0[D]$

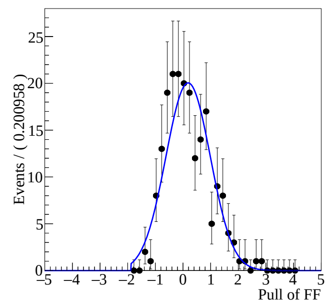

(c) $(\rho^+K^-)_A\pi^0, K^-\rho^+[D]$

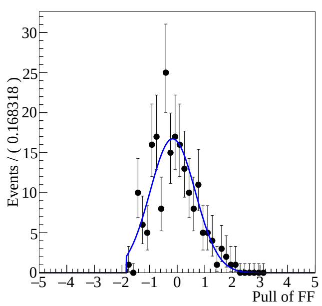

(d) $((K^-\pi^+)_S\pi^0)_A\pi^0$

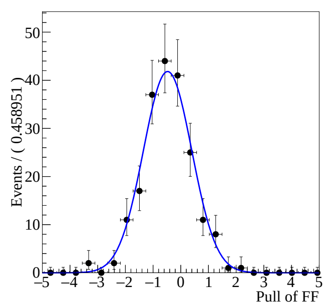

(e) $(K^-\pi^0)_S\rho^+$

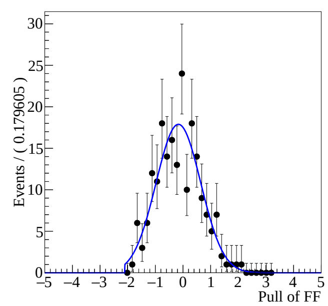

(f) $K^{*-}(\pi^+\pi^0)_S$

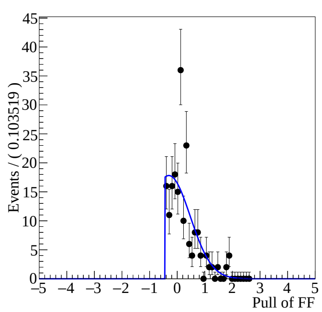

(g) $K^{*0}(\pi^0\pi^0)_S$

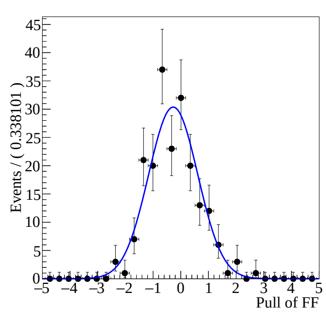

(h) $(K^{*-}\pi^+)_V\pi^0$

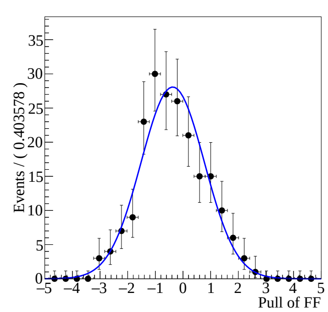

(i) $K^{*-}\rho^+[S]$

Figure M.2: Fits to the fit fraction pull distributions (part 2).

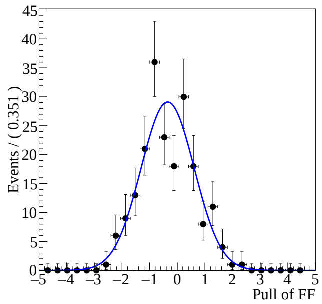

(a) $K^{*-}\rho^{+}[P]$

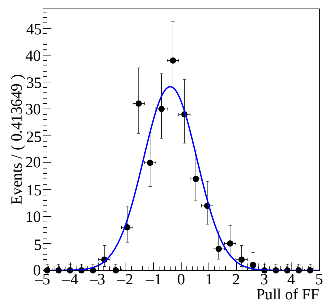

(b) $K^{*-}\rho^{+}[D]$

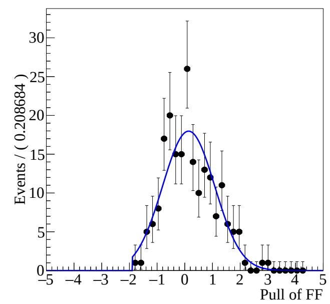

(c) $(K^{-}\pi^{0})_{V}\rho^{+}[P]$

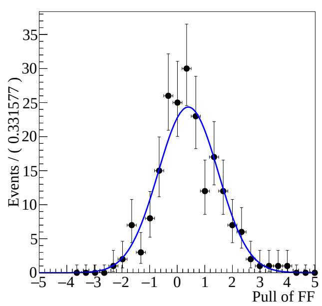

(d) $(K^{-}\pi^{0})_{V}\rho^{+}[D]$

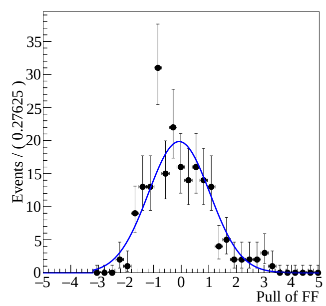

(e) $K^{*-}(\pi^{+}\pi^{0})_{V}[D]$

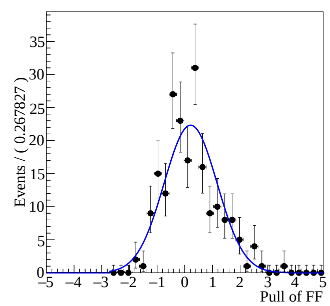

(f) $(K^{-}\pi^{0})_{V}(\pi^{+}\pi^{0})_{V}[S]$

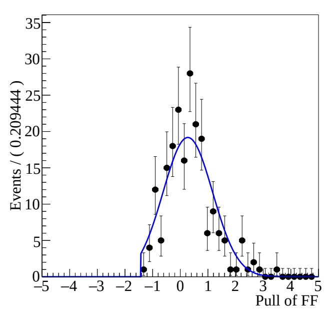

(g) $(K^{-}\pi^{+})_{S}(\pi^{0}\pi^{0})_{T}$

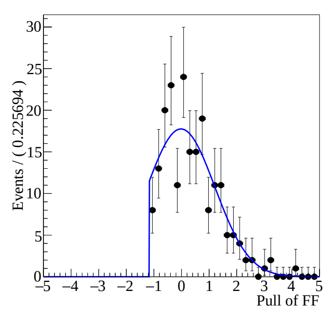

(h) $(K^{-}\pi^{0})_{S}(\pi^{+}\pi^{0})_{T}$

Figure M.3: Fits to the fit fraction pull distributions (part 3).

M.2 Fits to the Phase Pull Distributions

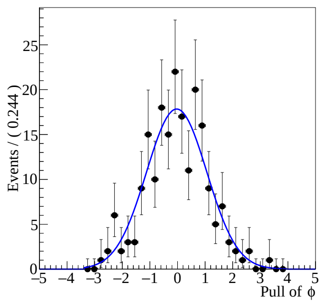

(a) $(K^-\pi^+)_S(\pi^0\pi^0)_S$

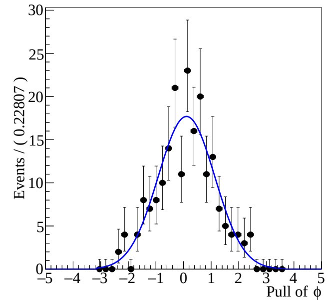

(b) $(K^-\pi^0)_S(\pi^+\pi^0)_S$

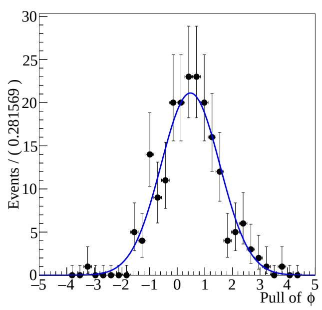

(c) $K^-a_1(1260)^+, \rho^+\pi^0[D]$

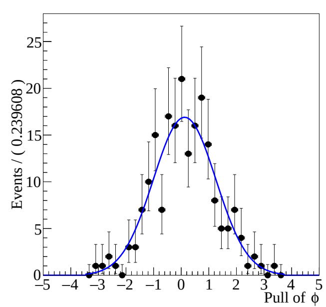

(d) $K_1(1270)^-\pi^+, K^{*-}\pi^0[S]$

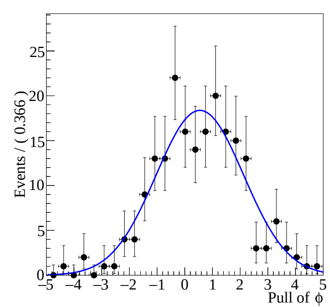

(e) $K_1(1270)^0\pi^0, K^{*0}\pi^0[S]$

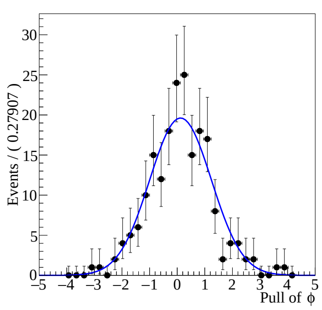

(f) $K_1(1270)^0\pi^0, K^{*0}\pi^0[D]$

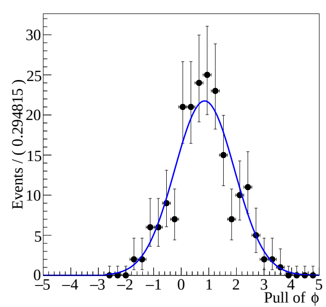

(g) $K_1(1270)^0\pi^0, K^-\rho^+[S]$

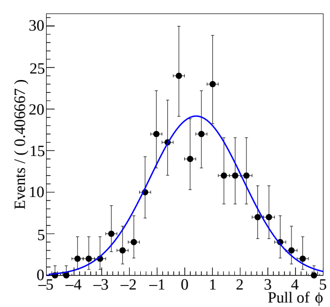

(h) $(K^{*-}\pi^0)_A\pi^+, K^{*-}\pi^0[S]$

Figure M.4: Fits to the phase pull distributions (part 1).

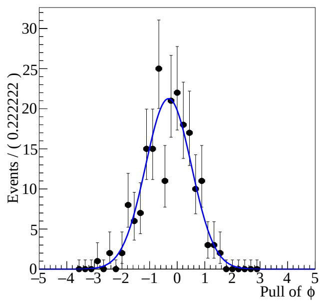

(a) $(K^{*0}\pi^0)_A\pi^0, K^{*0}\pi^0[S]$

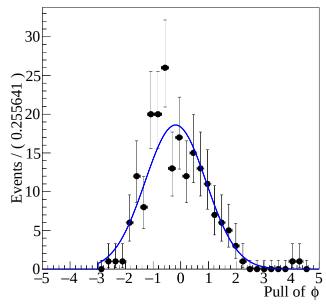

(b) $(K^{*0}\pi^0)_A\pi^0, K^{*0}\pi^0[D]$

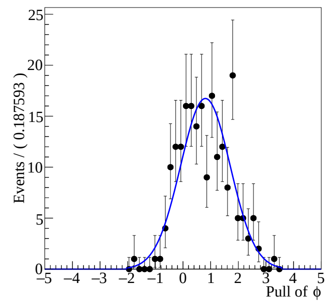

(c) $(\rho^+K^-)_A\pi^0, K^-\rho^+[D]$

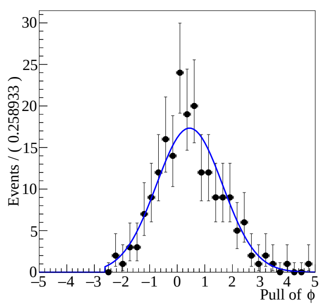

(d) $((K^-\pi^+)_S\pi^0)_A\pi^0$

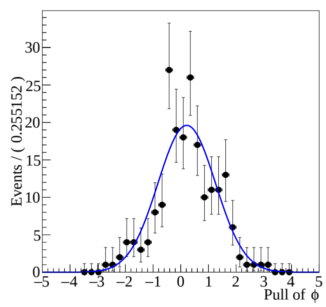

(e) $(K^-\pi^0)_S\rho^+$

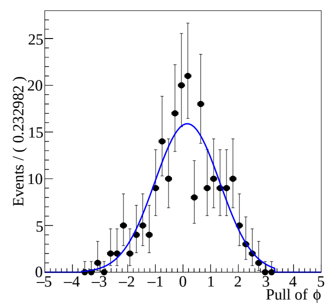

(f) $K^{*-}(\pi^+\pi^0)_S$

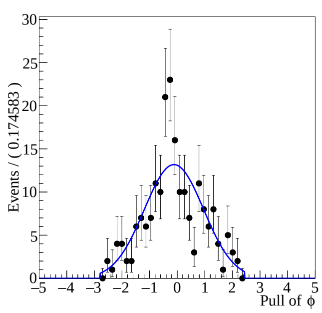

(g) $K^{*0}(\pi^0\pi^0)_S$

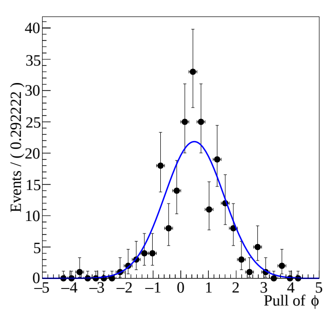

(h) $(K^{*-}\pi^+)_V\pi^0$

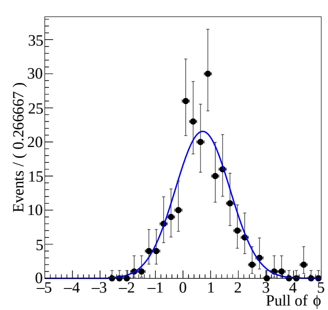

(i) $K^{*-}\rho^+[S]$

Figure M.5: Fits to the phase pull distributions (part 2).

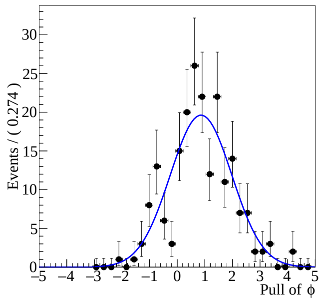

(a) $K^{*-}\rho^{+}[P]$

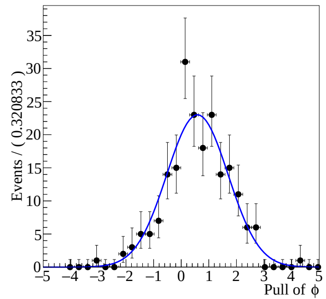

(b) $K^{*-}\rho^{+}[D]$

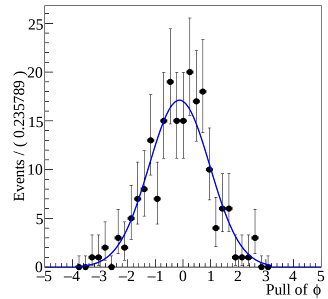

(c) $(K^{-}\pi^{0})_{V}\rho^{+}[P]$

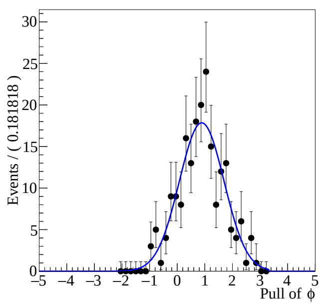

(d) $(K^{-}\pi^{0})_{V}\rho^{+}[D]$

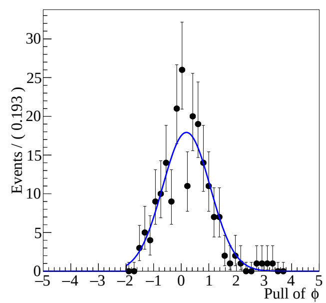

(e) $K^{*-}(\pi^{+}\pi^{0})_{V}[D]$

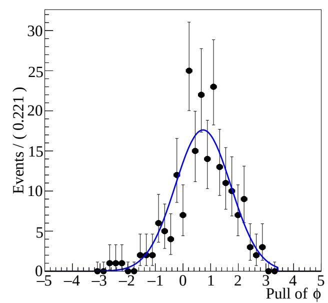

(f) $(K^{-}\pi^{0})_{V}(\pi^{+}\pi^{0})_{V}[S]$

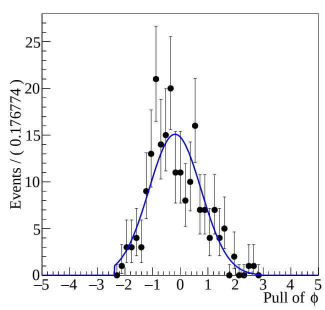

(g) $(K^{-}\pi^{+})_{S}(\pi^{0}\pi^{0})_{T}$

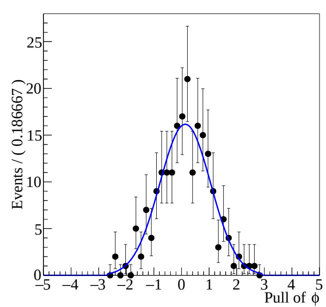

(h) $(K^{-}\pi^{0})_{S}(\pi^{+}\pi^{0})_{T}$

Figure M.6: Fits to the phase pull distributions (part 3).

M.3 Fits to the Fit Fraction Distributions

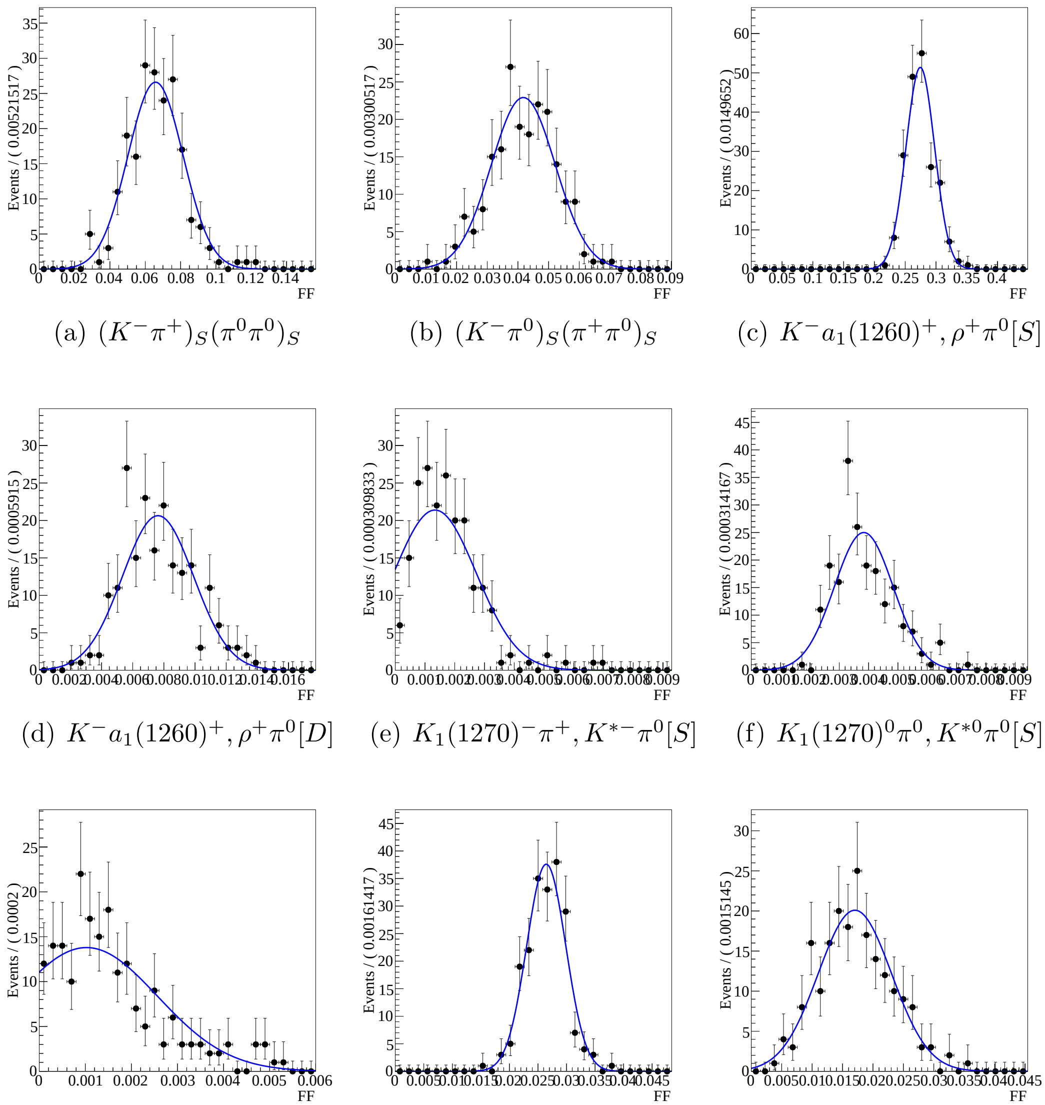

(a) $(K^-\pi^+)_S(\pi^0\pi^0)_S$ (b) $(K^-\pi^0)_S(\pi^+\pi^0)_S$ (c) $K^-a_1(1260)^+, \rho^+\pi^0[S]$

(d) $K^-a_1(1260)^+, \rho^+\pi^0[D]$ (e) $K_1(1270)^-\pi^+, K^{*-}\pi^0[S]$ (f) $K_1(1270)^0\pi^0, K^{*0}\pi^0[S]$

(g) $K_1(1270)^0\pi^0, K^{*0}\pi^0[D]$ (h) $K_1(1270)^0\pi^0, K^-\rho^+[S]$ (i) $(K^{*-}\pi^0)_A\pi^+, K^{*-}\pi^0[S]$

Figure M.7: Fits to the fit fraction distributions (part 1).

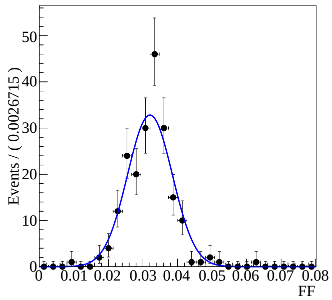

(a) $(K^{*0}\pi^0)_A\pi^0, K^{*0}\pi^0[S]$

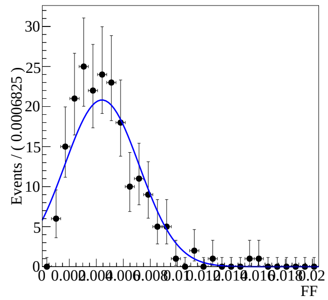

(b) $(K^{*0}\pi^0)_A\pi^0, K^{*0}\pi^0[D]$

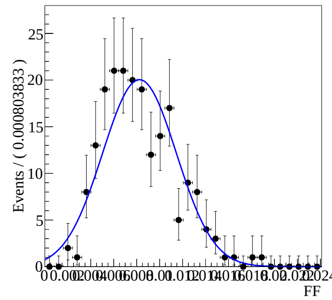

(c) $(\rho^+K^-)_A\pi^0, K^-\rho^+[D]$

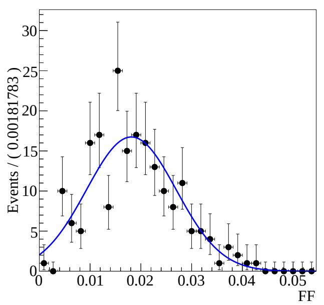

(d) $((K^-\pi^+)_S\pi^0)_A\pi^0$

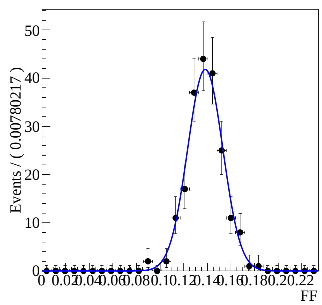

(e) $(K^-\pi^0)_S\rho^+$

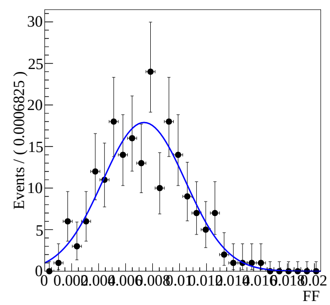

(f) $K^{*-}(\pi^+\pi^0)_S$

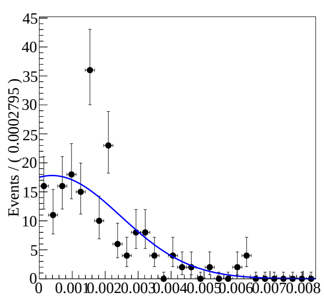

(g) $K^{*0}(\pi^0\pi^0)_S$

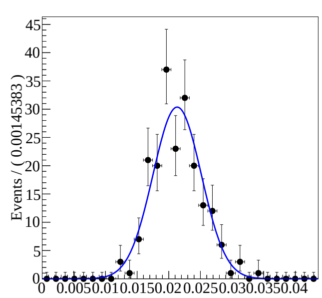

(h) $(K^{*-}\pi^+)_V\pi^0$

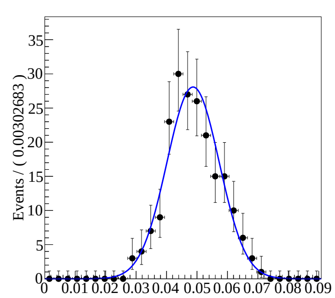

(i) $K^{*-}\rho^+[S]$

Figure M.8: Fits to the fit fraction distributions (part 2).

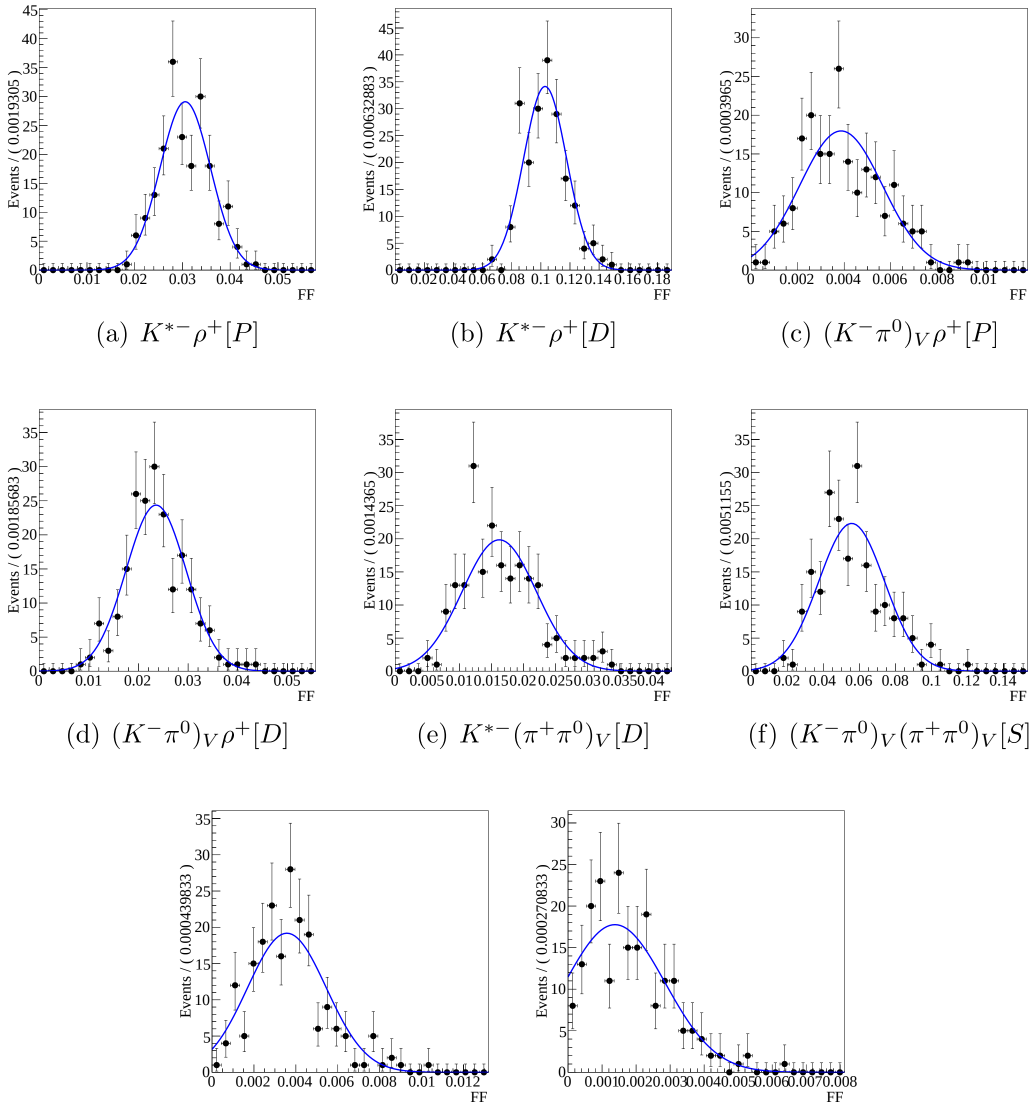

(a) $K^{*-}\rho^{+}[P]$ (b) $K^{*-}\rho^{+}[D]$ (c) $(K^{-}\pi^{0})_{V}\rho^{+}[P]$

(d) $(K^{-}\pi^{0})_{V}\rho^{+}[D]$ (e) $K^{*-}(\pi^{+}\pi^{0})_{V}[D]$ (f) $(K^{-}\pi^{0})_{V}(\pi^{+}\pi^{0})_{V}[S]$

(g) $(K^{-}\pi^{+})_{S}(\pi^{0}\pi^{0})_{T}$ (h) $(K^{-}\pi^{0})_{S}(\pi^{+}\pi^{0})_{T}$

Figure M.9: Fits to the fit fraction distributions (part 3).

M.4 Fits to the Phase Distributions

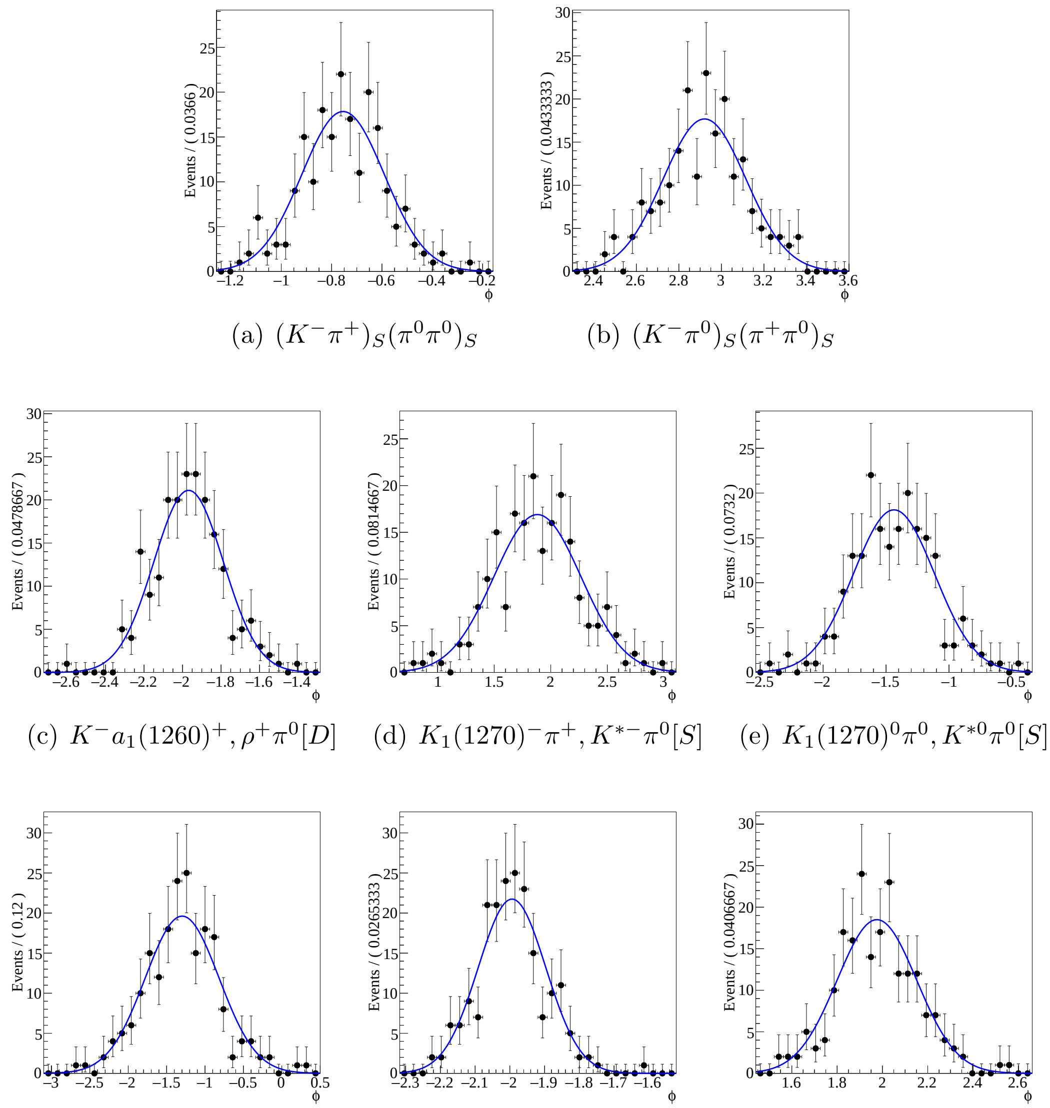

(a) $(K^-\pi^+)_S(\pi^0\pi^0)_S$ (b) $(K^-\pi^0)_S(\pi^+\pi^0)_S$

(c) $K^-a_1(1260)^+, \rho^+\pi^0[D]$ (d) $K_1(1270)^-\pi^+, K^{*-}\pi^0[S]$ (e) $K_1(1270)^0\pi^0, K^{*0}\pi^0[S]$

(f) $K_1(1270)^0\pi^0, K^{*0}\pi^0[D]$ (g) $K_1(1270)^0\pi^0, K^-\rho^+[S]$ (h) $(K^{*-}\pi^0)_A\pi^+, K^{*-}\pi^0[S]$

Figure M.10: Fits to the phase distributions (part 1).

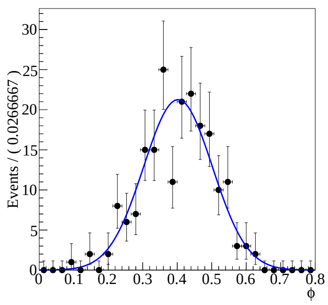

(a) $(K^{*0}\pi^0)_A\pi^0, K^{*0}\pi^0[S]$

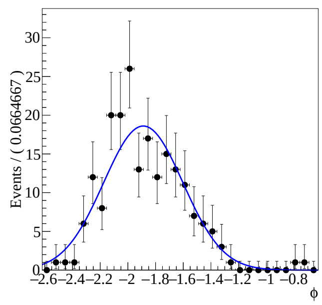

(b) $(K^{*0}\pi^0)_A\pi^0, K^{*0}\pi^0[D]$

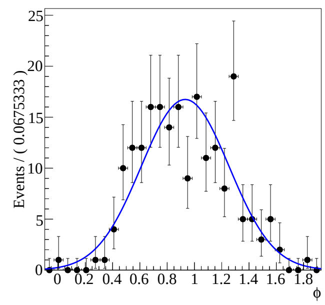

(c) $(\rho^+K^-)_A\pi^0, K^-\rho^+[D]$

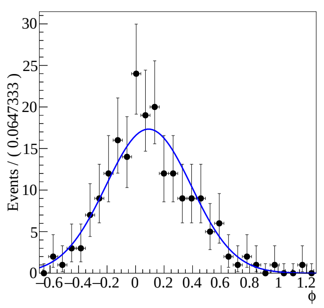

(d) $((K^-\pi^+)_S\pi^0)_A\pi^0$

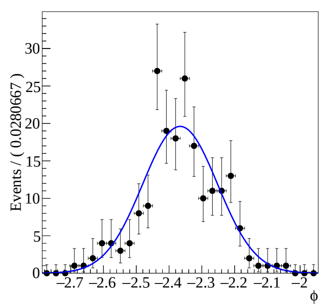

(e) $(K^-\pi^0)_S\rho^+$

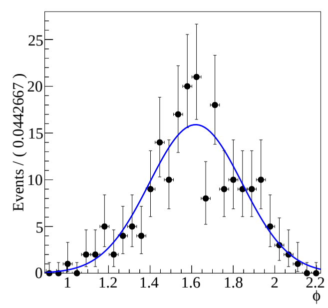

(f) $K^{*-}(\pi^+\pi^0)_S$

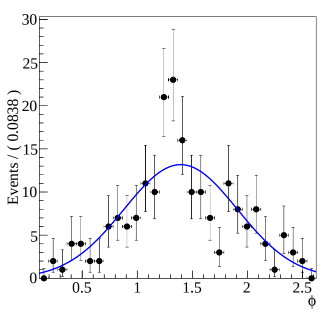

(g) $K^{*0}(\pi^0\pi^0)_S$

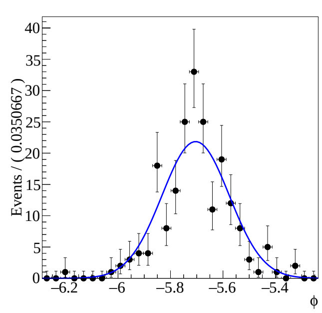

(h) $(K^{*-}\pi^+)_V\pi^0$

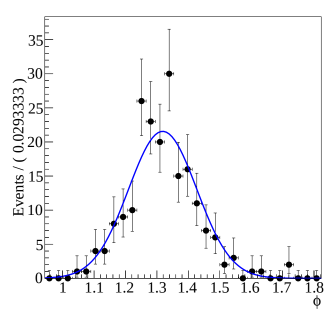

(i) $K^{*-}\rho^+[S]$

Figure M.11: Fits to the phase distributions (part 2).

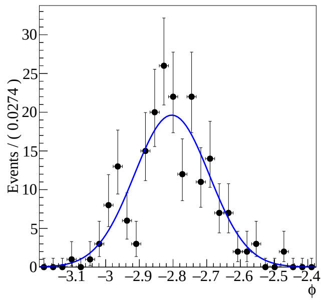

(a) $K^{*-}\rho^{+}[P]$

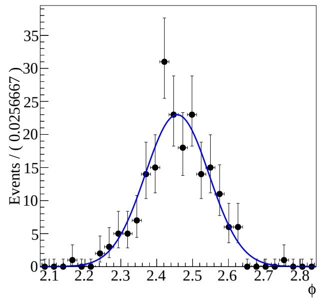

(b) $K^{*-}\rho^{+}[D]$

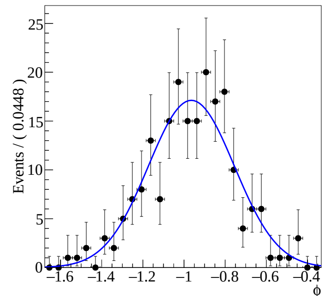

(c) $(K^{-}\pi^{0})_{V}\rho^{+}[P]$

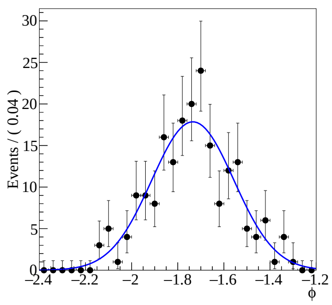

(d) $(K^{-}\pi^{0})_{V}\rho^{+}[D]$

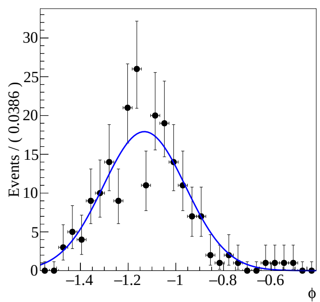

(e) $K^{*-}(\pi^{+}\pi^{0})_{V}[D]$

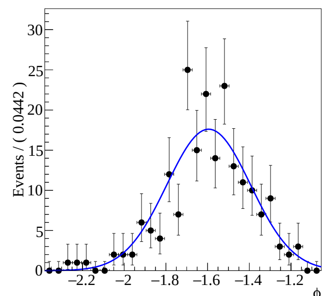

(f) $(K^{-}\pi^{0})_{V}(\pi^{+}\pi^{0})_{V}[S]$

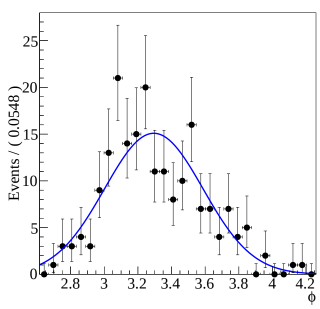

(g) $(K^{-}\pi^{+})_{S}(\pi^{0}\pi^{0})_{T}$

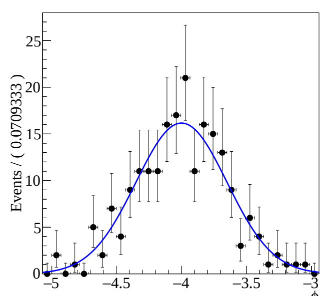

(h) $(K^{-}\pi^{0})_{S}(\pi^{+}\pi^{0})_{T}$

Figure M.12: Fits to the phase distributions (part 3).

Bibliography

[1] S. C. C. Ting *et al.*, Phys. Rev. Lett. **33**, 1404 (1974).

[2] B. Richter *et al.*, Phys. Rev. Lett. **33**, 1406 (1974).

[3] S. L. Glashow, J. Iliopoulos, and L. Maiani, Phys. Rev. D **2**, 1285 (1970).

[4] B. Bjorken and S. Glashow, Physics Letters **11**, 255257 (1964).

[5] S. W. Herb *et al.*, Phys. Rev. Lett. **39**, 252 (1977).

[6] F. Abe *et al.* (CDF Collaboration), Phys. Rev. Lett. **74**, 2626 (1995).

[7] S. Abachi *et al.* (D0 Collaboration), Phys. Rev. Lett. **74**, 2632 (1995).

[8] N. Cabibbo, Phys. Rev. Lett. **10**, 531 (1963).

[9] M. Kobayashi and T. Maskawa, Progress of Theoretical Physics **49**, 652657 (1973).

[10] G. Goldhaber *et al.*, Phys. Rev. Lett. **37**, 255 (1976).

[11] I. Peruzzi *et al.*, Phys. Rev. Lett. **37**, 569 (1976).

[12] D. Coffman *et al.* (Mark III Collaboration), Phys. Rev. D **45**, 2196 (1992).

[13] J. Adler *et al.* (Mark III Collaboration), Physics Letters B **196**, 107 (1987).

[14] S. Kopp *et al.* (CLEO Collaboration), Phys. Rev. D **63**, 092001 (2001).

[15] J. C. Anjos *et al.*, Phys. Rev. D **48**, 56 (1993).

[16] H. Muramatsu *et al.* (CLEO Collaboration), Phys. Rev. Lett. **89**, 251802 (2002).

[17] B. Aubert *et al.* (BABAR Collaboration), Phys. Rev. D **78**, 034023 (2008).

[18] H. Albrecht *et al.*, Physics Letters B **308**, 435 (1993).

[19] P. Frabetti *et al.*, Physics Letters B **331**, 217 (1994).

[20] N. Lowrey *et al.* (CLEO Collaboration), Phys. Rev. D **84**, 092005 (2011).

[21] J. Adler *et al.* (Mark III Collaboration), Phys. Rev. Lett. **64**, 2615 (1990).

[22] J. C. Anjos *et al.*, Phys. Rev. D **46**, 1941 (1992).

[23] M. Ablikim *et al.* (BESIII Collaboration), Phys. Rev. D **95**, 072010 (2017).

[24] G. Bonvicini *et al.* (CLEO Collaboration), Phys. Rev. D **78**, 052001 (2008).

[25] M. Ablikim *et al.* (BESIII Collaboration), Phys. Rev. D **89**, 052001 (2014).

[26] M. Ablikim *et al.* (BESIII Collaboration), NIM A **614**, 345 (2010).

[27] B. Zou and D. Bugg, The European Physical Journal A - Hadrons and Nuclei **16**, 537 (2003).

[28] G. J. Gounaris and J. J. Sakurai, Phys. Rev. Lett. **21**, 244 (1968).

[29] D. Aston *et al.*, Nuclear Physics B **296**, 493 (1988).

[30] M. Ablikim *et al.* (BESIII Collaboration), Chinese Physics C **37**, 123001 (2013).

[31] M. Ablikim *et al.* (BESIII Collaboration), Physics Letters B **753**, 629 (2016).

[32] M. Williams, Journal of Instrumentation **5**, P09004 (2010).

[33] S. Dobbs *et al.* (CLEO Collaboration), Phys. Rev. D **76**, 112001 (2007).

[34] P. Duan *et al.*, Talk given at BESIII 2014 Summer Collaboration meeting (2014).

[35] B.-C. Ke, O. Albayrak, R. A. Briere, and C. Liu, BESIII Doc. **446** (2015).

[36] Y. Lu and L. Dong, BESIII Doc. **416-v13** (2015).